AD-A247 233

DTIC
ELECTE
MAR 9 1992
S
C
D

AD

FATIGUE LIFE IMPROVEMENT OF AN AUTOFRETTAGED THICK-WALLED PRESSURE VESSEL WITH AN EXTERNAL GROOVE

SEUNG KEE KOH
RALPH I. STEPHENS

UNIVERSITY OF IOWA
IOWA CITY, IOWA 52242

JANUARY 1992

US ARMY ARMAMENT RESEARCH, DEVELOPMENT AND ENGINEERING CENTER
CLOSE COMBAT ARMAMENTS CENTER
BENÉT LABORATORIES
WATERVLIET, N.Y. 12189-4050

BENÉT LABS

92 3 04 087

92-05880

DISCLAIMER

The findings in this report are not to be construed as an official Department of the Army position unless so designated by other authorized documents.

The use of trade name(s) and/or manufacturer(s) does not constitute an official indorsement or approval.

DESTRUCTION NOTICE

For classified documents, follow the procedures in DoD 5200.22-M, Industrial Security Manual, Section II-19 or DoD 5200.1-R, Information Security Program Regulation, Chapter IX.

For unclassified, limited documents, destroy by any method that will prevent disclosure of contents or reconstruction of the document.

For unclassified, unlimited documents, destroy when the report is no longer needed. Do not return it to the originator.

REPORT DOCUMENTATION PAGE

Public reporting burden for this collection of information is estimated to average 1 hour per response, including the time for reviewing instructions, searching existing data sources, gathering and maintaining the data needed, and completing and reviewing the collection of information. Send comments regarding this burden estimate or any other aspect of this collection of information, including suggestions for reducing this burden to Washington Headquarters Services, Directorate for Information Operations and Reports, 1215 Jefferson Davis Highway, Suite 1204, Arlington, VA 22202-4302, and to the Office of Management and Budget, Paperwork Reduction Project (0704-0188), Washington, DC 20503.

1. AGENCY USE ONLY (Leave blank)	2. REPORT DATE January 1992	3. REPORT TYPE AND DATES COVERED Final Report

4. TITLE AND SUBTITLE
FATIGUE LIFE IMPROVEMENT OF AN AUTOFRETTAGED
THICK-WALLED PRESSURE VESSEL WITH AN EXTERNAL GROOVE

5. FUNDING NUMBERS

Contract No:
DAAA22-86-D-0278

6. AUTHOR(S)

Seung Kee Koh and Ralph I. Stephens

7. PERFORMING ORGANIZATION NAME(S) AND ADDRESS(ES)
University of Iowa
Iowa City, Iowa 52242

8. PERFORMING ORGANIZATION REPORT NUMBER

9. SPONSORING/MONITORING AGENCY NAME(S) AND ADDRESS(ES)
U.S. Army ARDEC
Benet Laboratories, SMCAR-CCB-TL
Watervliet, NY 12189-4050

10. SPONSORING/MONITORING AGENCY REPORT NUMBER
ARCCB-CR-92001

11. SUPPLEMENTARY NOTES

Joseph A. Kapp - Benet Laboratories Project Engineer

12a. DISTRIBUTION/AVAILABILITY STATEMENT
Approved for public release; distribution unlimited.

12b. DISTRIBUTION CODE

13. ABSTRACT (Maximum 200 words)

This report presents an investigation into a fatigue life improvement of an autofrettaged thick-walled pressure vessel with an external groove subjected to pulsating internal pressure, along with mean strain and mean stress effects on strain-controlled low cycle fatigue behavior. Linear elastic stress analysis of an autofrettaged thick-walled pressure vessel with an external groove is done using a finite element method. Autofrettage loading is performed using a thermal loading analogy. Change of external groove geometry is made using a quasi-optimization technique and finite element method to achieve longer fatigue life by relieving the stress concentration at the groove root. Surface treatment using shot peening is employed to produce compressive residual stresses at the vulnerable surface of the groove root to counteract the high tensile stresses. An evaluation of the fatigue life of an autofrettaged thick-walled pressure vessel with an external groove is done through a series of simulation fatigue tests using C-shaped specimens taken from the thick-walled pressure vessel.

14. SUBJECT TERMS
Autofrettage, Pressure Vessels, Thick Walls, Grooves, Fatigue Life

15. NUMBER OF PAGES
288

16. PRICE CODE

17. SECURITY CLASSIFICATION OF REPORT UNCLASSIFIED	18. SECURITY CLASSIFICATION OF THIS PAGE UNCLASSIFIED	19. SECURITY CLASSIFICATION OF ABSTRACT UNCLASSIFIED	20. LIMITATION OF ABSTRACT UL

ACKNOWLEDGMENTS

DTIC
COPY
INSPECTED
6

Accession For

NTIS GRA&I

DTIC TAB

Unannounced

Justification

By

Distribution/

Availability Codes

Avail and/or

Dist   Special

A-1

i

TABLE OF CONTENTS

LIST OF TABLES

LIST OF FIGURES

LIST OF SYMBOLS

b	Fatigue strength coefficient
c	Fatigue ductility exponent
d	Depth of groove
D'	Depth of stress relief groove
e	Nominal strain
Δe	Nominal strain range
$\Delta \varepsilon$	Strain range
$\Delta \varepsilon_e$	Elastic strain range
$\Delta \varepsilon_p$	Plastic strain range
ε_a	Strain amplitude
ε_f'	Fatigue ductility coefficient
ε_m	Mean strain ($= \varepsilon_{mean}$)
ε_θ	Tangential strain
ε_r	Radial strain
ε_z	Longitudinal strain
E	Modulus of elasticity

E_1	Modulus of elasticity from first quarter cycle of strain-controlled low cycle fatigue test
E_2	Modulus of elasticity from tensile unloading part of approximate half-life hysteresis loop
E_3	Modulus of elasticity from compressive unloading part of approximate half-life hysteresis loop
f	Objective function
F	Simulation load
g	Constraints
γ	Saw-cut opening angle
h	Height of groove
H	Design variable
H'	Height of stress relief groove
HR_c	Rockwell hardness of C scale
K	Strain-hardening coefficient
K'	Cyclic strain-hardening coefficient
K_ε	Strain concentration factor
K_f	Fatigue notch factor
K_σ	Stress concentration factor
K_t	Theoretical stress concentration factor
L	Length of pressure vessel
M	Bending moment

n	Strain-hardening exponent
n'	Cyclic strain-hardening exponent
N_f	Cycles-to-failure
$2N_f$	Reversals-to-failure
O.S.	Overstrain
P_i	Internal pressure
q	Fatigue notch sensitivity
r	Radius
ρ	Elastic-plastic radius
R	Groove root radius
R_ε	Strain ratio ($= \varepsilon_{min}/\varepsilon_{max}$)
S	Nominal stress
ΔS	Nominal stress range
$\Delta\sigma$	Stress range
σ_1	Maximum principal stress
σ_a	Stress amplitude
σ_{eq}	Equivalent stress
σ_f'	Fatigue strength coefficient
σ_m	Mean stress ($= \sigma_{mean}$)

σ_N	Nominal stress
σ_θ	Tangential stress
σ_r	Radial stress
σ_{ys}	Monotonic yield strength
σ_{ys}'	Cyclic yield strength
σ_z	Longitudinal stress
τ_{ys}	Shear yield strength
SWT	Smith-Watson-Topper parameter
t	Thickness of simulation specimen
W	Wall thickness of pressure vessel
W'	Width of stress relief groove

CHAPTER I

INTRODUCTION

1.1 Background

The design of pressure vessels for operation at very high internal pressure is a complex problem involving many considerations, including definition of permissible stress levels, criteria of failure and material behavior. A thick-walled hollow open-ended cylinder is a common configuration used in pressure vessels and is considered in this study. According to the classical Lamé solution for an elastic thick-walled cylinder under internal pressure, the largest tensile tangential stress occurs at the inside diameter. Therefore, fatigue cracks usually emanate from the inside surface of thick-walled pressure vessels subjected to internal pressure. To counteract this large tensile tangential stress at the bore, several techniques that will produce a compressive tangential residual stress in the material at the inside diameter have been developed. The compressive tangential residual stresses reduce the possibility of crack formation at the bore, and retard fatigue crack growth [1-3].

Many techniques have been used to produce favorable residual stresses, but three techniques, namely multilayer fit, wrapping, and autofrettage, have been commonly used with a certain amount of

success with thick-walled pressure vessels [4]. If a sufficiently high internal pressure is applied to the cylinder, plastic deformation will begin at the inside diameter and will extend through the cylinder wall as the pressure is increased. Due to nonuniform elastic recovery after the internal pressure is released, the outer portion of the pressure vessel attempts to resume its original size, but the inner portion of the pressure vessel which has deformed a greater amount, tries to remain permanently deformed. This process results in a tangential compressive residual stress near the inside diameter that varies logarithmically to tension through the plastically deformed region of the pressure vessel. The process of producing residual stress by means of plastic deformation of the pressure vessel is known as autofrettage [5-7].

Tangential compressive residual stresses at the inner diameter due to the autofrettage process retard crack formation and growth. It has been shown that autofrettage significantly increases the fatigue life of internally pressurized smooth thick-walled pressure vessels in which fatigue failure usually originates at the inside diameter [8-11]. However, the tangential tensile residual stresses at the outside diameter are of great concern when discontinuities such as holes, grooves, or cracks exist at the outside diameter. These discontinuities cause high stress concentrations that result in a shorter fatigue life at the discontinuities [12-15]. Therefore, for an autofrettaged thick-walled pressure vessel with an external groove subjected to internal pressure, the combination of tensile residual

stress due to autofrettage, tensile operating stress due to internal pressure, and the stress concentration of the groove causes early fatigue crack formation and fast crack growth, thus resulting in a shortened fatigue life.

Hydraulic fatigue testing has been performed on actual thick-walled cylinders with an external groove in order to find the fatigue behavior such as fatigue life, crack origins, crack growth rate, and the mode of failure, by applying the hydraulic pressure to the specimen between zero pressure and maximum operating pressure [16]. It was found in these thick-walled cylinders that all fatigue crack formation sites occurred at the roots of the external groove. The crack growth continued, linking up adjacent formation sites and finally failing by fast fracture of the shallow exterior critical crack.

1.2 Objectives

Methods of alleviating the high tensile tangential stress at the critical external groove root must be considered in order to improve the fatigue life of an autofrettaged thick-walled pressure vessel with an external groove subjected to internal pressure. It is obvious that the high stress concentration factor and tensile tangential autofrettage residual stress at the external groove root are major influencing factors in the shortened fatigue life of a thick-walled pressure vessel. Therefore, the fatigue life improvement of an autofrettaged thick-walled pressure vessel with an external groove can be achieved by design change of the groove root to relieve high

stress concentration or surface enhancement at the vulnerable groove root region to overcome the local high tensile stress. Also, the level of autofrettage overstrain, which is defined as the percentage of wall thickness subjected to plastic deformation during the application of autofrettage pressure, must be considered in order to decrease the tensile tangential residual stresses at the outer surface region without sacrificing the beneficial effect of compressive tangential residual stresses at the bore. This research will entail the following items.

In order to reduce the local high stress concentration at the conventional external groove root, a better shape of groove having a minimum stress concentration will be determined using an optimization method. Surface treatment of the locally high stressed region in the external groove by mechanical prestressing will be employed to produce beneficial compressive residual stresses at the vulnerable groove root for counteracting the high tensile stresses. Simulation specimens will be designed to best simulate the actual thick-walled pressure vessel subjected to internal pressure loading. Fatigue tests will be performed using the simulation specimens under a fatigue loading condition that is equivalent to the internal pressure loading in the actual thick-walled pressure vessel. Life estimation methodology will be made in order to predict the reasonable service life of an autofrettaged thick-walled pressure vessel prior to dangerous catastrophic failure. The local strain approach will be applied for fatigue life estimations using strain-

controlled low cycle fatigue test results, including mean stress effects.

1.3 Methods of Approach

Finite element stress analysis was employed to calculate the elastic stress distribution and theoretical stress concentration factor in the open-ended thick-walled pressure vessel subjected to internal pressure loading and autofrettage loading. Three different autofrettage loading conditions of 100, 75, and 50 percent overstrain were considered. Residual stress distributions due to autofrettage loading were calculated using a thermal loading analogy [17] and finite element methods, since this thermal loading analogy method has been applied effectively to find the residual stress distributions of complicated geometric configurations such as the presence of keyways, notches, and cracks [18].

Change of conventional groove geometry was obtained using a quasi-optimization technique with a finite element method. It was intended to increase the root radius by undercutting the groove root region to lessen the high stress concentration caused by the sharp root radius in the conventional groove. The groove root region was parameterized using a set of design variables, and a best shape that has the minimum stress concentration factor was determined from the optimization routine. Linear elastic finite element analysis was used for stress calculation in each loop of the optimization routine.

Another way of enhancing the resistance to fatigue failure is to induce compressive residual stress at the surface of the critical location. Generally, mechanical prestressing and thermal treatment are used to produce compressive residual stresses [19]. The most common mechanical prestressing methods are shot peening, surface rolling, and overloading. All of these methods produce tensile yielding near the highly stressed or vulnerable surface, thus resulting in compressive residual stress at the yielded regions due to the elastic recovery of material that was not subjected to yielding. Among heat treatment methods, carburizing, nitriding, and induction hardening are commonly used to produce the compressive residual stress. In this study, shot peening was used to induce compressive residual stresses at the changed groove root region since it is simple and has shown favorable effects for fatigue strength improvements [1-3]. The residual stresses were measured with and without shot peening using X-ray diffraction methods.

To compare the fatigue crack formation lives of the changed groove and shot peened groove with those of the conventional groove, simulation fatigue tests were performed using simulation specimens taken from an actual thick-walled pressure vessel. Three types of grooves were used for the simulation of the autofrettaged thick-walled pressure vessel under fatigue loading conditions. These were conventional groove, changed groove, and shot peened groove. For each type of specimen groove, three different simulation loads were applied to simulate three different overstrain cases, such as

100, 75 and 50 percent autofrettage or overstrain loadings. These three different simulation loads were determined from the finite element stress analysis of a simulation specimen and a thick-walled pressure vessel such that the cyclic stresses near the groove roots simulated actual stress conditions as closely as possible.

In a notched component or specimen subjected to cyclic external loads, the behavior of material near the local critical region of the notch root can be considered in terms of strain rather than stress as long as the majority of the components are elastically strained. The fatigue life of a notched component can be related to the fatigue life of a smooth test specimen subjected to the same strains as the material of the notch root. This low cycle fatigue concept, also known as local strain analysis, was applied to study the material behavior at the groove root of an autofrettaged thick-walled pressure vessel using strain-controlled fatigue test results. For an autofrettaged thick-walled pressure vessel with an external groove, the groove root is subjected to the minimum strain due to autofrettage loading and the maximum strain due to internal pressure plus autofrettage loading. This loading condition results in non-zero mean strain and non-zero mean stress, defined as $(\varepsilon_{min} + \varepsilon_{max})/2$ and $(\sigma_{min} + \sigma_{max})/2$, respectively. Strain-controlled low cycle fatigue tests were thus performed using smooth axial specimens taken from the thick-walled pressure vessel. Effect of mean stress on low cycle fatigue behavior was investigated. Several mean stress

parameters were used to describe the mean stress effect on strain-controlled low cycle fatigue behavior.

By integrating the local stresses and strains at the conventional groove, changed groove, and shot peened groove, the fatigue life of a thick-walled pressure vessel was estimated using low cycle fatigue test results. It is assumed that the fatigue life of a thick-walled pressure vessel with an external groove is approximately equal to the fatigue life of a smooth low cycle fatigue specimen, defined as the formation of small cracks in the order of a few millimeters subjected to the same local strains as the groove root. This local strain approach was used for the fatigue life estimation of a thick-walled pressure vessel with an external groove. Both linear rule and modified Neuber's rule were incorporated with this analysis in order to determine local strains at the groove roots from the elastic stress analysis results. These estimated fatigue lives were compared to the fatigue lives obtained from the simulation fatigue specimens.

CHAPTER II

MATERIAL

The thick-walled pressure vessel material tested was ASTM A723 Grade 1, Class 4 [20] with the chemical composition given in Table 2.1. Chemical composition was averaged from three separate analyses performed in the supplier's laboratory. A typical microstructure of the material taken from the outside tangential surface of the thick-walled pressure vessel is shown in Fig. 2.1, and consists of tempered martensite.

Partial monotonic stress-strain curve was obtained from the first quarter cycle of the low cycle fatigue test. Axial cylindrical specimen is shown in Fig. 2.2. The blanks for axial specimens were cut from the autofrettaged thick-walled pressure vessel such that the longitudinal axis of the blank was parallel to the tangential direction of the pressure vessel. The blanks were then machined and polished with 600 grit emery paper with final scratches in the longitudinal direction. All tests were performed using an 89 kN closed-loop electrohydraulic material testing system with hydraulic grips. Strain-controlled monotonic tensile tests with a strain rate of approximately 0.005 per minute were performed following ASTM standard method E8 [21] as a guide.

Averaged Young's modulus, E, and 0.2 percent offset yield strength, σ_{ys}, were obtained from 5 monotonic tensile tests, and these values are listed in Table 2.2. The range of E for the five tests was from 195 to 204 GPa, and the range for σ_{ys} was 1165 to 1185 MPa. The scatter for E and σ_{ys} was 2.5 and 1.3 percent compared to the averaged values of E and σ_{ys}, respectively. Values of engineering stress, S, and engineering strain, e, were taken from the X-Y plot of load versus engineering strain, and then converted to true stress, σ, and true strain, ε, using the following equations,

$$\sigma = S (1 + e), \qquad \varepsilon = \ln(1 + e) \qquad (2.1)$$

A typical true stress versus true strain curve determined from an X-Y plot of load versus engineering strain curve and Eq.(2.1) is shown in Fig. 2.3, where very little strain hardening can be observed. Since each monotonic tensile test was stopped at a certain strain for the continuation of a low cycle fatigue test, other monotonic tensile properties such as ultimate strength, σ_u, percent elongation, %EL, and percent reduction in area, %RA, could not be determined. These values, as listed in Table 2.2, were provided by the Watervliet Arsenal.

The strain hardening exponent, n, of 0.037 and the strain hardening coefficient, K, of 1483 MPa were determined from a typical true stress versus true strain curve using a log-log linear regression analysis with the following equations [22]:

$$\sigma = K (\varepsilon_p)^n \qquad (2.2)$$

where σ and ε_p are the true stress and true plastic strain, respectively. The true plastic strain was calculated from the total true strain by subtracting true elastic strain such as,

$$\varepsilon_p = \varepsilon - \varepsilon_e$$
$$= \varepsilon - \frac{\sigma}{E} \tag{2.3}$$

CHAPTER III

STRESS ANALYSIS OF AN AUTOFRETTACED
THICK-WALLED PRESSURE VESSEL

3.1 Introduction

Stress analysis of an autofrettaged thick-walled pressure vessel with/without external groove subjected to internal pressure needs to be done to understand stress distributions and find possible fatigue crack formation sites. Basically, the thick-walled pressure vessel is subjected to internal operating pressure loading and autofrettage loading. The stress due to internal pressure can be determined from the classical Lamé equation. The autofrettage process, as mentioned earlier, produces compressive tangential residual stress near the bore, and it varies to tension through the thickness of the pressure vessel. The mechanical autofrettage process, or swaging method [6], was developed to overcome the limitations of the conventional hydraulic autofrettage method, which needs extremely high hydraulic pressure for a high strength material. The swaging method consists basically of passing an oversized mandrel through the bore of the thick-walled pressure vessel to proauce the high radial forces for autofrettage by radial expansion. It was shown by Davidson et al. [4] that radial and tangential stress distributions produced by the swaging method exhibited similar behavior compared to those produced by conventional hydraulic autofrettage. They measured

residual stresses experimentally using the Sachs' boring-out technique [23]. A substantial difference in longitudinal or axial residual stress was found as the result of longitudinal shearing stress due to the tapered mandrel. The shearing stress was closely related to the lubrication and mandrel geometry, but this longitudinal residual stress component was considered insignificant in the fatigue failure of a thick-walled pressure vessel subjected to internal pressure [10].

It should be noted that residual stresses occur in the tangential, radial and longitudinal directions. However, fatigue tests of pressure vessels under synchronous pulsating triaxial stresses showed no effect of the longitudinal stress, which is an intermediate principal stress, thus supporting the Tresca or maximum shear stress criterion [24]. Internal pressure fatigue tests of thick-walled pressure vessels have shown that the maximum shear stress is a critical factor to fatigue failure [10]. Accordingly, the good agreement of this theory of failure with experiments under both static and fatigue loading conditions has led to its adoption in the design of thick-walled pressure vessels such as the American Society of Mechanical Engineers Boiler and Pressure Code for Nuclear Power Plant Components, and Pressure Vessels, Divisions 2 and 3.

If the maximum shear stress theory of failure is used as a crack formation criterion, then the radial and longitudinal residual stresses are of no concern, since the longitudinal stresses have intermediate values, and the radial stresses are zero at the free

surface of the external groove root. Therefore, only the tangential stresses are considered as an influential factor in the fatigue life of a thick-walled pressure vessel with an external groove. Thus the uniaxial fatigue failure criterion is proper, and was used in this study.

In this chapter, analytical stress distributions of autofrettaged thick-walled pressure vessels with/without an external groove under the internal pressure loading are obtained. The theoretical residual stress distributions of an autofrettaged thick-walled pressure vessel without an external groove are reviewed and compared to the results obtained from the experimental measurements. Finite element methods were used to determine the stress distribution of an autofrettaged thick-walled pressure vessel with an external groove subjected to internal pressure. These stress analysis results will be used in simulation fatigue tests and in the fatigue life estimation of a thick-walled pressure vessel with an external groove.

3.2 Stress Analysis of an Autofrettaged Thick-walled Pressure Vessel without External Groove

3.2.1 Stress Distribution due to Internal Pressure Loading

The elastic stress distribution of a thick-walled pressure vessel containing no residual stresses under an internal pressure is given by the well known Lamé equations [25].

$$\sigma_r = \frac{P_i a^2}{b^2 - a^2}\left(1 - \frac{b^2}{r^2}\right) \qquad (3.1)$$

$$\sigma_\theta = \frac{P_i\, a^2}{b^2 - a^2}\left(1 + \frac{b^2}{r^2}\right) \tag{3.2}$$

where σ_r an σ_θ denote the radial and tangential stresses; a and b are the inside and outside radius of the thick-walled pressure vessel, respectively; and P_i is the internal pressure. These equations can be derived directly by solving the differential equilibrium equations by use of stress-strain relations, strain-displacement relations, and boundary conditions. These equations can be applied regardless of the end conditions, e.g., whether they are open or closed-end conditions.

The nominal longitudinal stress for the closed-end condition of an elastic thick-walled pressure vessel is given by

$$\sigma_z = \frac{P_i\, a^2}{b^2 - a^2} \tag{3.3}$$

For the elastic pressure vessel with the open-end condition where ends of the pressure vessel are free to move in the longitudinal direction, the resulting longitudinal stress for plane-stress conditions is

$$\sigma_z = 0 \tag{3.4}$$

3.2.2 Review of Theoretical Residual Stress Distributions due to Autofrettage Loading

3.2.2.1 Elastic-plastic Stress Analysis

As mentioned earlier, the thick-walled pressure vessel was autofrettaged to produce the beneficial tangential compressive residual stress near the inside diameter. The dimensions of the

inside and outside radius are 85 and 142 mm, respectively. Theoretical solutions for the autofrettage residual stress distribution have been derived, but considerable differences exist among these solutions [4]. The differences follow from the assumptions made regarding the pressure vessel end condition, yield condition, stress-strain relations of the overstrained material, and the allowance for compressibility [5].

Most high strength steels that are currently used for high pressure vessels exhibit relatively small strain-hardening tendencies. Therefore they can be quite accurately represented by an elastic-perfectly plastic model, thus permitting a considerably more analytical and simplified approach to the elastic-plastic problem. Two yield criteria, such as the von Mises criterion and the Tresca criterion, would generally be used to predict the yielding behavior of a moderately ductile steel with a reasonable degree of accuracy. The von Mises criterion has been shown to be the most accurate under all combinations of triaxial stress [26, 27]. However, the Tresca criterion was used in this study since its application to the thick-walled pressure vessel problem results in a comparatively simple mathematical formulation, and the Tresca yield criterion used to calculate the theoretical residual stresses in a thick-walled pressure vessel has shown a good agreement with experimental results [7].

The residual stress distribution of thick-walled pressure vessels due to partial autofrettage can also be obtained by assuming the Tresca yield criterion and an elastic-perfectly plastic material [7,

28]. Since the longitudinal stress is the intermediate principal stress, the radial and tangential stresses can be obtained without any dependence on end condition and longitudinal stress distribution. Yielding occurs at the inside surface due to internal pressure when the maximum shear stress becomes equal to the shear yield stress or half of the tensile yield stress.

From the Tresca yield criterion, and Eq.(3.1) and (3.2),

$$\sigma_\theta - \sigma_r = \left[\frac{P_i\, a^2}{b^2 - a^2} \frac{2b^2}{r^2} \right]_{r=a}$$

$$= \frac{2\, P_i\, b^2}{b^2 - a^2}$$

$$= \sigma_{ys} \qquad (3.5)$$

This gives the onset of a yielding condition such as

$$\sigma_{ys} = P_i \frac{2b^2}{b^2 - a^2} \qquad (3.6)$$

As the pressure is further increased, the plastic deformation penetrates into the pressure vessel wall. If the plastic deformation penetrates into a radius, ρ, defined as the elastic-plastic radius, then from the equilibrium of an element of the wall, neglecting the body forces

$$\frac{d\sigma_r}{dr} + \frac{\sigma_r - \sigma_\theta}{r} = 0 \qquad (3.7)$$

Substituting Eq.(3.5) into Eq.(3.7) and integrating Eq.(3.7),

$$\sigma_r = \sigma_{ys} \ln r + C \qquad (3.8)$$

where the integration constant C can be determined from the boundary condition that at the inside surface the radial stress is the same as the internal pressure P_ρ required to produce yielding of the pressure vessel wall to a radius ρ.

$$[\sigma_r]_{r=a} = \sigma_{ys} \ln a + C$$
$$= P_\rho \tag{3.9}$$

Using Eq.(3.8) and (3.9),

$$\sigma_r = \sigma_{ys} \ln\left(\frac{r}{a}\right) - P_\rho \tag{3.10}$$

In particular, at $r=\rho$,

$$\sigma_\rho = \sigma_{ys} \ln\left(\frac{\rho}{a}\right) - P_\rho \tag{3.11}$$

Since the material in the region of greater than the elastic-plastic radius is elastic, and yielding just started at $r=\rho$, from Eq.(3.6) and using $-\sigma_\rho$ instead of P_i in Eq.(3.6)

$$\sigma_{ys} = -\sigma_\rho \frac{2\,b^2}{b^2 - \rho^2} \tag{3.12}$$

Eliminating σ_ρ from Eq.(3.11) and (3.12) due to the continuity in the radial pressure at $r=\rho$,

$$\frac{P_\rho}{\sigma_{ys}} = \ln\left(\frac{\rho}{a}\right) + \frac{1}{2}\left(1 - \frac{\rho^2}{b^2}\right) \tag{3.13}$$

Hence the radial stress in the plastic region of the pressure vessel due to the internal pressure P_ρ can be obtained by eliminating P_ρ from Eqs.(3.10) and (3.13)

$$\sigma_r = \sigma_{ys} \ln\left(\frac{r}{a}\right) - \sigma_{ys}\left[\ln\left(\frac{\rho}{a}\right) + \frac{1}{2}\left(1 - \frac{\rho^2}{b^2}\right)\right]$$

$$= \sigma_{ys}\left[\ln\left(\frac{r}{\rho}\right) - \frac{1}{2}\left(1 - \frac{\rho^2}{b^2}\right)\right] \qquad \text{for } a \leq r \leq \rho \qquad (3.14.a)$$

For the elastic region of the pressure vessel, using Eqs.(3.1) and (3.12),

$$\sigma_r = - \sigma_\rho \frac{\rho^2}{b^2 - \rho^2}\left(1 - \frac{b^2}{r^2}\right)$$

$$= \sigma_{ys} \frac{b^2 - \rho^2}{2 b^2} \frac{\rho^2}{b^2 - \rho^2}\left(1 - \frac{b^2}{r^2}\right)$$

$$= \sigma_{ys} \frac{\rho^2}{2 b^2}\left(1 - \frac{b^2}{r^2}\right) \qquad \text{for } \rho \leq r \leq b \qquad (3.14.b)$$

The tangential stress in the plastic region of the thick-walled pressure vessel can be determined from Eqs.(3.5) and (3.14) as

$$\sigma_\theta = \sigma_r + \sigma_{ys}$$

$$= \sigma_{ys}\left[\ln\left(\frac{r}{\rho}\right) + \frac{1}{2}\left(1 + \frac{\rho^2}{b^2}\right)\right] \qquad \text{for } a \leq r \leq \rho \qquad (3.15.a)$$

For the elastic region of the pressure vessel, using Eqs.(3.2) and (3.12)

$$\sigma_\theta = - \sigma_\rho \frac{\rho^2}{b^2 - \rho^2}\left(1 + \frac{b^2}{r^2}\right)$$

$$= \sigma_{ys} \frac{b^2 - \rho^2}{2 b^2} \frac{\rho^2}{b^2 - \rho^2}\left(1 + \frac{b^2}{r^2}\right)$$

$$= \sigma_{ys} \frac{\rho^2}{2 b^2}\left(1 + \frac{b^2}{r^2}\right) \qquad \text{for } \rho \leq r \leq b \qquad (3.15.b)$$

The above equations (3.14) and (3.15) describe the elastic-perfectly plastic stress distributions of the partially overstrained thick-walled pressure vessel due to the internal pressure, i.e., autofrettage pressure, given by Eq.(3.13). If the internal pressure is removed after the pressure vessel has been plastically deformed, a residual stress will remain in the wall due to the nonuniform elastic recovery through the wall thickness.

Assuming that the pressure vessel recovers elastically, the residual stress can be determined by subtracting the elastic stresses produced by the autofrettage pressure given by the Lamé equations from the elastic-plastic stresses given as Eqs.(3.14) and (3.15). The elastic recovery is caused by the pressure that is equal to the radial stress at r=a in Eq.(3.14.a) as

$$\sigma_{ra} = [\ \sigma_r\ ]_{r=a} = \sigma_{ys}\left[\ln\left(\frac{a}{\rho}\right) - \frac{1}{2}\left(1 - \frac{\rho^2}{b^2}\right)\right]$$ (3.16)

Therefore, the radial and tangential elastic recovery stresses can be given as

$$\sigma_r = \frac{-\sigma_{ra}\,a^2}{b^2 - a^2}\left(1 - \frac{b^2}{r^2}\right)$$

$$= -\sigma_{ys}\frac{a^2}{b^2 - a^2}\left[\ln\left(\frac{a}{\rho}\right) - \frac{1}{2}\left(1 - \frac{\rho^2}{b^2}\right)\right]\left(1 - \frac{b^2}{r^2}\right)$$ (3.17.a)

and

$$\sigma_\theta = \frac{-\sigma_{ra}\, a^2}{b^2 - a^2}\left(1 + \frac{b^2}{r^2}\right)$$

$$= -\sigma_{ys}\frac{a^2}{b^2 - a^2}\left[\ln\left(\frac{a}{\rho}\right) - \frac{1}{2}\left(1 - \frac{\rho^2}{b^2}\right)\right]\left(1 + \frac{b^2}{r^2}\right) \tag{3.17.b}$$

The final radial and tangential residual stress can be determined by subtracting Eqs.(3.17.a) and (3.17.b) from Eqs.(3.14) and (3.15), respectively [28].

$$\sigma_r = \sigma_{ys}\left\{\frac{a^2}{b^2 - a^2}\left(1 - \frac{b^2}{r^2}\right)\left[\frac{\rho^2 - b^2}{2\,b^2} - \ln\frac{\rho}{a}\right] + \left[\frac{\rho^2 - b^2}{2\,b^2} - \ln\frac{\rho}{r}\right]\right\}$$
$$\text{for } a \le r \le \rho$$

$$= \sigma_{ys}\left(1 - \frac{b^2}{r^2}\right)\left\{\frac{\rho^2}{2\,b^2} + \frac{a^2}{b^2 - a^2}\left[\frac{\rho^2 - b^2}{2\,b^2} - \ln\frac{\rho}{a}\right]\right\}$$
$$\text{for } \rho \le r \le b \tag{3.18.a}$$

and

$$\sigma_\theta = \sigma_{ys}\left\{\frac{a^2}{b^2 - a^2}\left(1 + \frac{b^2}{r^2}\right)\left[\frac{\rho^2 - b^2}{2\,b^2} - \ln\frac{\rho}{a}\right] + \left[\frac{\rho^2 + b^2}{2\,b^2} - \ln\frac{\rho}{r}\right]\right\}$$
$$\text{for } a \le r \le \rho$$

$$= \sigma_{ys}\left(1 + \frac{b^2}{r^2}\right)\left\{\frac{\rho^2}{2\,b^2} + \frac{a^2}{b^2 - a^2}\left[\frac{\rho^2 - b^2}{2\,b^2} - \ln\frac{\rho}{a}\right]\right\}$$
$$\text{for } \rho \le r \le b \tag{3.18.b}$$

If the von Mises yield criterion were used for the derivation of the autofrettage residual stresses [4], then the same equations would be obtained, except $\frac{2}{\sqrt{3}}\sigma_{ys}$ would replace σ_{ys} in Eq.(3.18).

The residual stresses were obtained based on the assumptions that the recovery is purely elastic upon the removal of the autofrettage pressure and that the residual stresses do not exceed

the compressive yield strength of the material. By equating the tangential residual stress, given in Eq.(3.18.b), to the compressive yield strength, σ_{ys}, a wall ratio, defined as b/a, of 2.2 can be obtained. Therefore, for the wall ratio of approximately greater than 2.2, the compressive tangential residual stress at the inside radius will exceed the compressive yield strength of the material and result in reverse yielding under the purely elastic recovery after the removal of autofrettage pressure. Moreover, the compressive yield strength significantly decreases due to the Bauschinger effect, and the tangential stress caused by elastic recovery may exceed the reduced compressive yield strength. The significant effect on a large wall ratio has been reported by several investigators [11, 29, 30], and it has been shown that reverse yielding would occur at the wall ratio of approximately 1.8, instead of 2.2 as theoretically predicted [7]. In this study, purely elastic recovery upon the release of autofrettage pressure without any reverse yielding was assumed for the autofrettaged pressure vessel that was used. The dimensions of the inside and outside radius of the thick-walled pressure vessel used for this study were 85 mm and 142 mm, respectively, resulting in a wall ratio of 1.67.

3.2.2.2 Equivalent Saw-cut Method

In the previous review section using elastic-plastic stress analysis, the tangential residual stress results in compression at the bore and varies logarithmically to tension through the thickness of

the wall due to autofrettage. Therefore, the radial cutting of an autofrettaged pressure vessel through thickness from the outside to inside causes a relaxation of the residual stresses analogous to the form of a pure bending moment. The theoretical residual stresses can be obtained by solving the elastic problem of a curved beam subjected to pure bending moment equivalent to the relaxation caused by the autofrettaged pressure vessel [31]. If a curved beam is subjected to couples at the ends, as shown in Fig. 3.1, the elastic stress distribution in a radial cross section can be obtained [32]. The inside and outside radii are denoted by a and b, respectively, and γ is the opening angle, as shown in Fig. 3.1.

Using a stress function and proper boundary conditions [32],

$$\sigma_r = -\frac{4\,M}{N}\left[\frac{a^2\,b^2}{r^2}\ln\frac{b}{a} + b^2\ln\frac{r}{b} + a^2\ln\frac{a}{r}\right]$$

$$= -\frac{4\,M}{N}(b^2 - a^2)\left[-\ln\frac{b}{r} - \frac{a^2}{b^2 - a^2}\left(1 - \frac{b^2}{r^2}\right)\ln\frac{b}{a}\right] \qquad (3.19.a)$$

$$\sigma_\theta = -\frac{4\,M}{N}\left[-\frac{a^2\,b^2}{r^2}\ln\frac{b}{a} + b^2\ln\frac{r}{b} + a^2\ln\frac{a}{r} + b^2 - a^2\right]$$

$$= -\frac{4\,M}{N}(b^2 - a^2)\left[1 - \ln\frac{b}{r} - \frac{a^2}{b^2 - a^2}\left(1 + \frac{b^2}{r^2}\right)\ln\frac{b}{a}\right] \qquad (3.19.b)$$

where M is the bending moment and $N = (b^2 - a^2)^2 - 4a^2b^2[\ln(b/a)]^2$. If the ends of the curved beam with an initial opening angle γ are joined by the bending moment M, then the bending moment can be calculated by considering the tangential displacement necessary to bring the ends of the curved beam together.

$$M = -\frac{\gamma E N}{16 \pi (b^2 - a^2)} \qquad (3.20)$$

Substituting Eq.(3.20) into (3.19), the stress distribution caused by bringing the ends of the curved beam with an opening angle γ together is obtained as

$$\sigma_r = \frac{\gamma E}{4 \pi}\left[-\ln\frac{b}{r} - \frac{a^2}{b^2 - a^2}\left(1 - \frac{b^2}{r^2}\right)\ln\frac{b}{a}\right] \qquad (3.21.a)$$

$$\sigma_\theta = \frac{\gamma E}{4 \pi}\left[1 - \ln\frac{b}{r} - \frac{a^2}{b^2 - a^2}\left(1 + \frac{b^2}{r^2}\right)\ln\frac{b}{a}\right] \qquad (3.21.b)$$

Similarity between Eq.(3.21) and the theoretical 100 percent autofrettage residual stresses given in Eq.(3.18) yields

$$\frac{\gamma E}{4 \pi} = \sigma_{ys} \qquad (3.22.a)$$

$$\frac{\sqrt{3}\,\gamma E}{8 \pi} = \sigma_{ys} \qquad (3.22.b)$$

where Eqs.(3.22.a) and (3.22.b) come from the similarity between Eq.(3.21) and autofrettage residual stresses based on the Tresca and von Mises yield criteria, respectively. It should be noted that Eq.(3.21) applies only for a case of 100 percent overstrain, i.e., a fully autofrettaged condition. Therefore from the opening angle γ, residual stress can be calculated by means of the moment M required to close the gap to form a closed ring. It is interesting that the opening angle γ is independent of the inside and outside diameters of the ring.

Later, the opening angle measured after the saw-cut of an autofrettaged pressure vessel will be compared to the theoretical opening angle given in Eq.(3.22) due to 100 percent autofrettage.

3.2.2.3 Thermal Loading Analogy

Stress concentration due to residual stress has been known [33-34], and it was shown that a thermal load can be used to produce thermal stresses equivalent to autofrettage residual stresses [17, 35]. This thermal loading analogy method can be effectively applied to find the residual stress distributions of complicated geometric configurations, such as the presence of keyways, notches, and cracks [18, 36-38]. Considering a thick-walled pressure vessel under the temperature, T, across the thickness, thermal stresses can be determined from the differential equilibrium equation given as Eq.(3.7), and the stress-strain and strain-displacement relations, as follows [32]:

$$\varepsilon_r = \frac{1}{E}[\sigma_r - \nu(\sigma_\theta - \sigma_z)] + \alpha T$$

$$\varepsilon_\theta = \frac{1}{E}[\sigma_\theta - \nu(\sigma_z + \sigma_r)] + \alpha T \qquad (3.23)$$

$$\varepsilon_z = \frac{1}{E}[\sigma_z - \nu(\sigma_r + \sigma_\theta)] + \alpha T$$

and

$$\varepsilon_r = \frac{du}{dr}$$

$$\varepsilon_\theta = \frac{u}{r} \qquad (3.24)$$

$$\gamma_{r\theta} = 0$$

where α is the coefficient of thermal expansion, and u is the radial displacement.

Suppose first that the ends of the pressure vessel are restrained, i.e., $\varepsilon_z = 0$, for the plane-strain condition, and then modify the solution to the free ends case for the plane-stress condition. For the case of restrained ends,

$$\sigma_z = \nu(\sigma_r + \sigma_\theta) - \alpha ET \qquad (3.25)$$

Manipulation of Eqs.(3.23), (3.24), (3.25), and (3.7) gives [32],

$$u = \frac{\alpha}{r}\left(\frac{1+\nu}{1-\nu}\right)\int_a^r Tr\ dr + C_1 r + \frac{C_2}{r}$$

$$\sigma_r = \frac{E}{1+\nu}\left[\frac{C_1}{1-2\nu} - \frac{C_2}{r^2}\right] - \frac{\alpha E}{(1-\nu)\,r^2}\int_a^r Tr\ dr$$

$$\sigma_\theta = \frac{E}{1+\nu}\left[\frac{C_1}{1-2\nu} + \frac{C_2}{r^2}\right] + \frac{\alpha E}{(1-\nu)\,r^2}\int_a^r Tr\ dr - \frac{\alpha ET}{1-\nu} \qquad (3.26)$$

$$\sigma_z = \frac{2\nu E C_1}{(1+\nu)(1-2\nu)} - \frac{\alpha E T}{1-\nu}$$

From the boundary conditions such that the radial stress is zero at the inside radius, a, and outside radius, b, the integration constants C_1 and C_2 can be determined.

If there is a steady-state heat flow such that T_a and T_ρ are the temperatures at r=a and r=ρ of the pressure vessel, respectively, then the temperature distribution becomes

$$T = \frac{T_a - T_\rho}{\ln(\rho/a)}\ln\frac{\rho}{r} \qquad \text{for } a \le r \le \rho$$

$$= T_\rho \qquad \text{for } \rho \le r \le b \qquad (3.27)$$

In this thermal loading analogy, the radius ρ corresponds to the radius of the elastic-plastic boundary in the elastic-plastic analysis of autofrettage residual stress analysis. Therefore, the final thermal

stress distribution can be obtained by substituting the expression into Eq.(3.26). Since thermal stresses result from a temperature gradient, assigning $T_\rho = 0$ for convenience,

$$\sigma_r = \frac{\alpha E}{2(1-v)} \frac{T_a}{\ln(\rho/a)} \left\{ \frac{a^2}{b^2-a^2} \left(1 - \frac{b^2}{r^2}\right) \left[\frac{\rho^2-b^2}{2\,b^2} - \ln\frac{\rho}{a}\right]\right.$$

$$\left. + \left[\frac{\rho^2-b^2}{2\,b^2} - \ln\frac{\rho}{r}\right]\right\} \quad \text{for } a \le r \le \rho$$

$$= \frac{\alpha E}{2(1-v)} \frac{T_a}{\ln(\rho/a)} \left(1 - \frac{b^2}{r^2}\right) \left\{\frac{\rho^2}{2\,b^2} + \frac{a^2}{b^2-a^2}\left[\frac{\rho^2-b^2}{2\,b^2} - \ln\frac{\rho}{a}\right]\right\}$$

$$\text{for } \rho \le r \le b \quad (3.28.a)$$

$$\sigma_\theta = \frac{\alpha E}{2(1-v)} \frac{T_a}{\ln(\rho/a)} \left\{ \frac{a^2}{b^2-a^2} \left(1 + \frac{b^2}{r^2}\right) \left[\frac{\rho^2-b^2}{2\,b^2} - \ln\frac{\rho}{a}\right]\right.$$

$$\left. + \left[\frac{\rho^2+b^2}{2\,b^2} - \ln\frac{\rho}{r}\right]\right\} \quad \text{for } a \le r \le \rho$$

$$= \frac{\alpha E}{2(1-v)} \frac{T_a}{\ln(\rho/a)} \left(1 + \frac{b^2}{r^2}\right) \left\{\frac{\rho^2}{2\,b^2} + \frac{a^2}{b^2-a^2}\left[\frac{\rho^2-b^2}{2\,b^2} - \ln\frac{\rho}{a}\right]\right\}$$

$$\text{for } \rho \le r \le b \quad (3.28.b)$$

$$\sigma_z = \frac{\alpha E}{2(1-v)} \frac{T_a}{\ln(\rho/a)} \left\{ \frac{v\,(\rho^2-a)}{b^2-a^2} - \frac{2\,v\,a^2}{b^2-a^2}\ln\frac{\rho}{a} - 2\,\ln\frac{\rho}{r}\right\} \quad \text{for } a \le r \le \rho$$

$$= \frac{\alpha E}{2(1-v)} \frac{T_a}{\ln(\rho/a)} \left\{ \frac{v\,(\rho^2-a^2)}{b^2-a^2} - \frac{2\,v\,a^2}{b^2-a^2}\ln\frac{\rho}{a}\right\} \quad \text{for } \rho \le r \le b \quad (3.28.c)$$

For the case of free ends, superposition of a uniform longitudinal stress chosen so that the resultant force on the ends is zero gives the longitudinal stress in the plane-stress condition,

$$\sigma_z = \frac{\alpha E}{1-v} \left[\frac{2}{b^2 - a^2} \int_a^r Tr\ dr - T \right]$$

$$= \frac{\alpha E}{2(1-v)} \frac{T_a}{\ln(\rho/a)} \left\{ \frac{\rho^2 - a^2}{b^2 - a^2} - \frac{2\ a^2}{b^2 - a^2}\ \ln\frac{\rho}{a} - 2\ \ln\frac{\rho}{r} \right\} \text{ for } a \le r \le \rho$$

$$= \frac{\alpha E}{2(1-v)} \frac{T_a}{\ln(\rho/a)} \left\{ \frac{\rho^2 - a^2}{b^2 - a^2} - \frac{2\ a^2}{b^2 - a^2}\ \ln\frac{\rho}{a} \right\} \text{ for } \rho \le r \le b \quad (3.29)$$

Similarity between Eqs.(3.28) and (3.18) can be easily seen. Equivalent stress distribution results if

$$\frac{\alpha E}{2(1-v)} \frac{T_a}{\ln(\rho/a)} = \sigma_{ys} \qquad (3.30)$$

Therefore, if an equivalent temperature given in Eq. (3.30) were imposed on the thick-walled pressure vessel, thermal stress distributions would be theoretically equal to the autofrettage residual stress distributions. This thermal loading analogy was employed for the autofrettage residual stress calculation of a thick-walled pressure vessel with an external groove.

3.2.3 Experimental Procedure of Autofrettage
Residual Stress Measurements

Many techniques have been developed to experimentally determine the residual stresses of components or structures in destructive or nondestructive ways [19, 39-42]. For an autofrettaged thick-walled pressure vessel, a popular technique to experimentally determine the complete residual stress distributions was developed by Sachs and Espey [23]. Davidson et al. experimentally obtained the residual stresses using the Sachs' boring-out technique by measuring

the changes in diameter and strains at the outside surface while machining out the bore [7].

In the previous sections, three methods for obtaining the theoretical residual stress distributions produced by autofrettage were presented. These were the elastic-plastic analysis, equivalent saw-cut method, and thermal loading analogy. Using the equivalent saw-cut method [39, 42], two experimental measurements of the autofrettage residual stress distributions for a 100 percent overstrain case were compared to theoretical residual stress distributions. Measurements of the relieved strains and split opening angle due to radial cutting of the autofrettaged ring were used to determine the autofrettage residual stresses. Tangential and radial residual stresses were calculated from the strain measurements and split angle by cutting rings of 20-mm thickness taken from the autofrettaged pressure vessel [31].

It was shown in section 3.2.2.2 that the theoretical stress distributions in the thick-walled pressure vessel due to 100 percent overstrain autofrettage are equivalent to the stress distributions in the curved beam due to the bending moment which is required to put the split ring together. Therefore, if an autofrettaged ring were cut through the thickness, then the cut would make a certain opening angle of the split ring due to the relaxation of tangential autofrettage residual stresses. The relaxed residual stresses are theoretically equal in magnitude, but opposite in sign, to the autofrettage residual stresses contained in the ring prior to saw-cut for the 100 percent

overstrain case, thus resulting in zero residual tangential and radial stresses after cutting. Assuming that the residual stresses contained in the pressure vessel relax elastically, then the relaxed residual stresses can be calculated from the measured strains using the generalized Hooke's law [43].

Three rings were used for measuring strains, and seven rings were used for measuring split opening angles. A typical ring used for the experiment is shown in Fig. 3.2. Both uniaxial and rosette strain gages were attached across the wall for strain measurements, and punch marks were made on the outside surface of the ring for split opening angle measurements, as shown schematically in Fig. 3.2. Strain gages, WA-09-030WR-120 and EA-06-125AA-120, from Micro-Measurements were used for strain relaxation measurements. Strain limits for WA-09-030WR-120 and EA-06-125AA-120 are 1.5% and 3% at room temperature, respectively. Prior to mounting the strain gage, the ring surface was roughened with 400-grit sandpaper and cleaned with acetone. An M-bond 200 adhesive from Micro-Measurement was used for gage bonding. The mounted strain gages and rings were then cured for at least 6 hours at room temperature. The strain gages were coated with M-Coat A to prevent environmental effects or mechanical damage.

The saw-cut between punch marks was made at the opposite side f the strain-gaged wall after installation of the strain gages, as shown in Fig. 3.2. Sudden opening with a loud breaking noise was observed before the ring was completely cut, indicating that the

residual stresses were contained inside of the ring. After the ring opened, strains and the opening angle were recorded. A digital strain indicator and a balancing unit were used for strain measurements, and a caliper with a least reading of 0.025 mm was used for opening angle measurements. Later, these rings were machined to be used for the simulation fatigue testing.

In order to measure the longitudinal stress, a 45° angle rosette was placed on the outside diameter edge surface. From the measured three strain values, two principal strains, ε_1 and ε_2, were calculated [43]. Maximum principal strain ε_1 and minimum principal strain ε_2 corresponded to the tangential strain and longitudinal strain, respectively. Two principal strains, ε_1 and ε_2, obtained from the rosette were then used to calculate the principal stresses, σ_1 and σ_2, using the following equations:

$$\sigma_1 = \frac{E}{1 - v^2} [\varepsilon_1 + v\, \varepsilon_2]$$

$$\sigma_2 = \frac{E}{1 - v^2} [\varepsilon_2 + v\, \varepsilon_1] \tag{3.31}$$

Maximum and minimum principal stresses, σ_1 and σ_2, corresponded to tangential and longitudinal principal stresses, respectively. These resulted in approximately zero longitudinal stress at the ring, thus indicating the plane-stress condition.

Uniaxial strain gages were used for strain measurements at the inside and outside edge surfaces, as shown in Fig. 3.2, since there only exist tangential relaxation stresses on those free surfaces

without longitudinal stress relaxation. Combinations of uniaxial strain gages and rosettes were used across the thickness of the wall. Locations of strain gages, measured strains, relieved stress calculations from the measured strains, and types of strain gages are listed in Table 3.1. Theoretical residual stresses in Table 3.1 were calculated using Eq.(3.18). Each measurement and the average measurements of the split opening angles compared to the theoretical opening angles calculated using Eq.(3.22) are listed in Table 3.2.

3.3 Stress Analysis of an Autofrettaged Thick-walled Pressure Vessel with Conventional External Groove using Finite Element Methods

Theoretical residual stress distributions of a smooth thick-walled pressure vessel without an external groove were mentioned in the previous section using the elastic-plastic stress analysis, equivalent saw-cut and thermal loading analogy. But in many practical cases, discontinuities such as keyway grooves, holes, and cracks are present in the thick-walled pressure vessel. These discontinuities cause a redistribution of residual stresses that may be difficult to find using elastic-plastic analysis. It was shown by Pu and Hussain [18] that an active thermal loading can be used to produce thermal elastic stresses equivalent to autofrettage residual stresses in a partially autofrettaged thick-walled pressure vessel with notches or cracks. This thermal loading analogy was applied to obtain the stress intensity factor for a radial crack in a partially autofrettaged thick-walled pressure vessel [36]. In the current

study, autofrettage residual stresses in a thick-walled pressure vessel with an external groove were found using a finite element method and thermal loading analogy.

Linear elastic stress analysis of a thick-walled pressure vessel with an external groove using the finite element method was performed. The thick-walled pressure vessel with an external groove was subjected to internal pressure of 386 MPa and thermal loading for the simulation of autofrettage loading. An internal pressure of 386 MPa is the typical operating pressure of the actual pressure vessel. The pressure vessel with a rectangular groove at the outside surface is shown in Fig. 3.3. The pressure vessel has an inside radius, a, and outside radius, b, of 85 and 142 mm, respectively. Wall thickness ratio, defined as $\frac{b}{a}$, is 1.67. Groove root radius, R, is 1.5 mm. Three autofrettage loading conditions, 100 percent, 75 percent, and 50 percent overstrain, were analyzed. The percent overstrain was defined as the percentage of wall thickness subject to plastic deformation during the application of the autofrettage pressure. In this thermal loading analogy, the equivalent temperature distribution given by Eq. (3.27) was imposed, depending on percent overstrain conditions.

Due to the symmetry of the pressure vessel, as shown in Fig. 3.3, only half a segment of pressure vessel was used for the finite element analysis. The ANSYS finite element program was employed to perform the analysis [44]. Three different types of two-dimensional plane-strain solid elements were used: a 4-node

isoparametric quadrilateral element, a 6-node isoparametric triangular element, and an 8-node isoparametric quadrilateral element. The plane-strain condition was assumed in the analysis, since the thick-walled pressure vessel is very long compared to its diameter. For each element type, convergence was checked in order to ensure correct results by avoiding possible input errors and the inherent errors in some element types.

Typical finite element meshes used to find the solution for a conventional groove are shown in Fig. 3.4. Boundary conditions are shown in Fig. 3.4.(a), where all of the nodal displacements in the y direction along the horizontal plane were restrained, and one node point at the inside radius was fixed to prevent rigid body motion due to loading. For the case of internal pressure loading, a uniform pressure of 386 MPa was applied on the inside surface. For the case of thermal loading, the temperature distribution due to steady-state heat flow was first analyzed using a finite element program, and then the nodal temperature results were transferred as an input for the thermal stress calculation. A plane-strain condition, $\varepsilon_z = 0$, where z is the longitudinal direction, was used for all loading cases in the analysis of the thick-walled pressure vessel.

To see the convergence of maximum principal stress at the root of the groove, mesh refinements were done near the groove root using three different types of element. Fig. 3.5 shows the final refined meshes for each element type using automatic mesh generation by the ANSYS program [44]. Convergence of the

theoretical stress concentration factor, K_t, due to internal pressure loading and 100 percent overstrain loading for each element type are shown in Figs. 3.6 and 3.7, respectively. The number of elements around the one quarter of the groove root circle for the 4-node quadrilateral element, 6-node triangular element, and 8-node quadrilateral element was 28, 20 and 12 elements, resulting in element sizes of 0.06, 0.12, and 0.15 mm, respectively. It should be noted that Figs. 3.6 and 3.7 were not intended to show the efficiency between different types of elements, but rather to find the convergent results for all element types. In fact, the exact comparison of efficiency between different types of element was impossible since the element size near the groove root varied in both the radial and circumferential directions.

3.4 Results and Discussion

Classical theoretical derivations using the autofrettaged smooth thick-walled pressure vessel were reviewed and the experimental measurements of autofrettaged residual stresses were done for comparison. Elastic-plastic analysis, equivalent saw-cut method, and thermal loading analogy were used to obtain the theoretical solutions of autofrettage residual stresses. Theoretical solutions were based on the assumptions of elastic-perfectly plastic material behavior, the Tresca yield criterion, and no reverse yielding nor Bauschinger effects of the pressure vessel material. The experimental strain gage method and split opening angle method due to saw-cut were

employed in this study for the residual stress measurements of an autofrettaged thick-walled pressure vessel. For the autofrettaged thick-walled pressure vessel with an external groove subjected to internal pressure, elastic stress analysis was performed using both a finite element method and the thermal loading analogy, focused on the stress concentration at the sharp root of the conventional external groove.

3.4.1 Autofrettage Residual Stress Distributions using Experimental Measurements

To measure the residual stresses in a fully autofrettaged thick-walled pressure vessel, strain gage method and split opening angle measurement were used, as shown in Fig. 3.2. Locations of strain gages, measured strains, and calculated stresses compared to the theoretical autofrettage residual stresses based on the Tresca yield criterion are listed in Table 3.1. Relieved stresses were calculated using Eq.(3.31), and the theoretical autofrettage residual stresses were calculated using Eq.(3.18). Due to the autofrettage residual stress relaxation, tensile relaxation strains were observed toward the inside surface where originally compressive autofrettage residual stresses were contained prior to saw-cut. However, compressive relaxation strains were observed toward the outside surface where tensile autofrettage residual stresses were contained prior to saw-cut. A strain gage attached to the inside surface was broken just after the cutting due to the fast high strain relaxation from a sudden opening of the autofrettaged ring.

Fig. 3.8 shows the autofrettaged stress distributions calculated from the relaxed strains by saw-cut across the thickness of the wall. The data points represent the experimental relaxation stress values with opposite signs after saw-cut, and the lines represent the theoretical residual stress values prior to saw-cut. The tangential relaxation stress data, calculated from the uniaxial strain gages using $\sigma = E\varepsilon$, were expected to be in error, which turned out to be small compared to the calculated relaxed stress data from the rosettes using generalized Hooke's law, as shown in Fig. 3.8. This was attributed to the relatively small magnitude of radial relaxation stress. Good agreement of residual stress distributions between the experimental measurements and theoretical calculations can be seen, especially for the von Mises criterion case. This good agreement implied total relaxation of the autofrettage residual stresses after saw-cut, leaving the split ring supposedly free from residual stress. Noticeable scatter in the tangential residual stress distribution between experiment and theory can be seen at both the inside and outside surfaces. This was attributed to the assumptions made on the theoretical derivation regarding elastic-perfectly plastic material behavior and yield criteria. The maximum difference in tangential residual stress between experiment and theory was approximately 28 percent for the Tresca criterion and 9 percent for the von Mises criterion. The maximum differences occurred at the inside diameter regardless of the yield criteria. One data point at the inside surface, which is closer to 1000 MPa, could be in error since the strain gage

balance checking before the saw-cut was suspicious. If this datum point were excluded from the analysis, then the difference in tangential residual stress between experiment and theory could be less than 15 percent for both criteria, which is quite a good agreement.

The distance between the punch marks measured after saw-cut was used for split angle calculation. The opening angles obtained from the seven rings taken from the autofrettaged pressure vessel are listed in Table 3.2 along with the average angle. These values can be compared to the theoretical opening angles calculated from Eq.(3.22). Young's modulus, E, of 200 GPa, and yield strength, σ_{ys}, of 1170 MPa were used for calculations. The experimental opening angle showed closer results to the theoretical opening angle based on the von Mises yield criterion than to the Tresca yield criterion.

3.4.2 Finite Element Solutions of Internal Pressure Loading

The stresses due to internal pressure loading of a thick-walled pressure vessel were given by the Lamé equations (3.1), and (3.2). Fig. 3.9 shows the finite element results with a conventional groove, for the internal pressure loading of 386 MPa, along the plane A-A' defined in Fig. 3.3, compared to the theoretical solutions from Eqs. (3.1) and (3.2). The data points represent the finite element solutions and the lines represent the Lamé solutions. Stress distribution along the plane A-A' was not influenced by the external groove on the opposite side of the pressure vessel. The difference

between the finite element results and theoretical solutions was less than 3 percent, which is considered excellent. Since the tangential stress, or maximum principal stress, has the most significant effect on the fatigue crack formation and growth in the thick-walled pressure vessel, as explained in section 3.1, the tangential stress distributions along the planes A-A', B-B', and C-C' are plotted in Fig. 3.10. It must be noted that the tangential stresses near the groove root were not equal to the maximum principal stresses, since the tangential stress direction differed from the maximum principal stress direction by some angle less than 5 degrees due to the presence of groove. But the difference between the maximum principal stress and tangential stress were less than 1 percent near the root region due to the small difference in angle. Therefore, the maximum principal stresses were used near the groove root in Fig. 3.10.

Planes B-B' and C-C' are the radial planes through the groove root where the maximum principal stress and the center of the groove occur, respectively. Theoretical stress concentration factor, K_t, defined as

$$K_t = \frac{\sigma_{max}}{\sigma_N} \qquad (3.32)$$

was calculated at both locations of the groove root and center of the groove. Nominal stress, σ_N, was defined as the stress occurring at the outside radius from the reduced wall thickness. This definition of nominal stress is analogous to a net nominal stress [45]. Therefore,

from Eq.(3.1) the nominal stress due to internal pressure P_i is given as

$$\sigma_N = \frac{2\,P_i\,a^2}{b_o^2 - a^2} \tag{3.33}$$

where b_o is the outside radius of the thick-walled pressure vessel with reduced thickness, i.e., $b_o = b - d$.

Due to a typical operating internal pressure of 386 MPa, stress concentration factors, K_t, of 3.93 and 1.72 for the B-B' and C-C' plane, respectively, are listed in Table 3.3. Theoretical elastic stress concentration factors at the root of the groove and the center of the groove, which are the points B' and C', respectively, in Fig. 3.3, were calculated from Eqs.(3.32) and (3.33). Due to the sharp radius of the groove root, the maximum principal stress was much higher at the root of the groove than at the center of groove as shown in Table 3.3. However a considerable stress concentration at the center of the groove should be noticed. Fig. 3.11 shows the maximum principal stress contours near the groove root of radius R=1.5 mm due to internal pressure loading. The maximum principal stress occurred about 18 degrees above the beginning of curvature in the groove root region, as shown in Fig. 3.11.

3.4.3 Finite Element Solutions of Autofrettage Residual Stresses using Thermal Loading Analogy

It was shown that the theoretical autofrettage residual stress distributions based on the Tresca yield criterion using an elastic-perfectly plastic material are equal to the thermal stress

distributions due to equivalent steady-state heat flow [18, 35]. A finite element method and thermal loading analogy were used to simulate the autofrettage residual stresses of a thick-walled pressure vessel with a groove at the outside surface.

In order to do a thermal stress analysis, a temperature distribution of the thick-walled pressure vessel with an external groove due to the steady-state heat flow must be found. The ANSYS finite element program was used first to determine the temperature distribution. The initial temperature input for the steady-state heat flow was calculated from Eq.(3.30) using the yield strength(σ_{ys}) of 1170 MPa, Young's modulus(E) of 210,000 MPa, thermal expansion coefficient(α) of 6.8 x 10^{-6} m/m/$^{\circ}$C, and Poisson's ratio(v) of 0.29. The initial temperature, T_a, at the inside radius r=a for each percent overstrain case is listed in Table 3.5. After performing the temperature analysis using the ANSYS program, the finite element analysis was again performed to obtain the thermal stresses from the results of temperature distributions which were calculated in the previous stage. These thermal stresses are equivalent to the autofrettage residual stresses, as discussed above.

Finite element solutions of radial and tangential stress distribution along the plane A-A' opposite to the external groove for each overstrain case are shown as open data points in Figs. 3.12 and 3.13, respectively. Three lines in Figs. 3.12 and 3.13 represent the theoretical solutions for each overstrain case from Eqs.(3.18.a) and (3.18.b), respectively. The data exhibit very close agreement with

the theoretical solutions that were derived from the thick-walled pressure vessel without an external groove. Differences between these finite element solutions and theoretical solutions were less than 3 percent, which is quite good.

Finite element stress distributions for each overstrain condition along the plane A-A', B-B', and C-C' are shown in Figs. 3.14, 3.15, and 3.16, respectively, where the data points represent the finite element solutions and the solid lines represent the interpolation curves of those finite element solutions. A very high stress concentration at the groove root can be clearly noticed for each autofrettage loading case. Just as in the case of internal pressure loading, nominal stress in the autofrettage loading was defined using a thick-walled pressure vessel with reduced wall thickness in order to be consistent with the definitions for all loading conditions. Unlike pressure loading, the nominal stress due to autofrettage loading could not be determined simply, since a change in wall thickness also causes a change in thermal loading. From Eq. (3.18), using a reduced thickness, tangential stress at the outside radius, i.e., $r=b_0=b-d$, was defined as the nominal stress by

$$\sigma_N = \sigma_{ys} \left\{ \frac{\rho^2}{b_0^2} + \frac{2\,a^2}{b_0^2 - a^2} \left[\frac{\rho^2 - b_0^2}{2\,b_0^2} - \ln\frac{\rho}{a} \right] \right\} \tag{3.34}$$

The elastic-plastic radii ρ for 75 and 50 percent overstrain cases were not changed; however, for the 100 percent overstrain case it was redefined as the changed outside radius b_0, since the original outside radius b does not exist any more at the pressure vessel with

reduced wall thickness. Nominal stress, σ_N, defined for each loading case, is listed in Table 3.4.

As shown in Figs. 3.13 through 3.16, the magnitude of compressive tangential residual stress at the inside radius increases as the percent overstrain increases. This implies that higher internal operating pressure can be applied to a smooth thick-walled pressure vessel of a larger overstrain condition for both yielding and fatigue problems. It was reported that a 100 percent overstrain condition results in the maximum fatigue life for a smooth thick-walled pressure vessel without any external grooves where cracks usually grow from the inside surface [9]. However, it can be observed that the maximum tensile stress at the external groove root increases as the percent overstrain increases, meaning that longer fatigue crack formation and growth life at the external groove root will occur for a smaller percent overstrain under the same pulsating internal pressure.

Maximum principal stresses, σ_{max}, at the locations B' and C' along with the nominal stress σ_N, and stress concentration factors, K_t, are shown in Table 3.4 for each autofrettage loading case. Significant differences in the maximum principal stresses between percent overstrain are clearly shown in Table 3.4. At the grove root, i.e., location B', the maximum principal stress in a 100 percent overstrain case was 40 and 195 percent higher than in 75 and 50 percent overstrain cases, respectively. Similar percentage differences were found at the center of the groove, or location C'. However, essentially

no differences in K_t between 75 and 50 percent overstrain cases for both the center and root of the groove can be seen in Table 3.4. Also, stress concentration factors, K_t, at the location B' and C' for a 100 percent overstrain case were only 16 and 8 percent higher, respectively, than for both 75 and 50 percent overstrain cases. The small difference in K_t, compared to the large difference in the maximum principal stress, between percent overstrain cases at both the center and root of the groove was due to the similar difference in ratio between maximum or nominal stresses.

A maximum principal stress contour plot near the groove root due to a 100 percent overstrain case is shown in Fig. 3.17. It looks very similar to the maximum principal stress contour near the groove root due to internal pressure loading. Similar contour patterns were obtained for 75 and 50 percent overstrain cases. Maximum principal stress contours from all loading conditions showed significant stress concentration at the sharp root of the groove. Maximum principal stresses along the groove root surface are plotted in Fig. 3.18. Regardless of the loading conditions, the peaks of maximum principal stress occurred at the angle θ between 15 to 20 degrees from the beginning of the root curvature, and they decreased very rapidly as the angle increased.

CHAPTER IV

GROOVE GEOMETRY CHANGE USING
A QUASI-OPTIMIZATION TECHNIQUE

4.1 Introduction

It has been noticed during the stress analysis of the thick-walled pressure vessel with a conventional external groove that a very high stress concentration occurred at the sharp root of the conventional external groove. This stress concentration at discontinuities such as notches, fillets, or holes in the structural and machine components has been a major concern in fatigue failure problems [46]. It was reported that in an autofrettaged thick-walled pressure vessel with an external groove subjected to internal pulsating pressure, fatigue failure originating from the sharp root of the external keyway groove was common [47]. Therefore, it is clear that a high stress concentration should be relieved in order to reduce the fatigue failure at the sharp root of the groove, which is necessary for engineering purposes.

In this chapter, the change of the groove root shape is considered using a quasi-optimization technique by minimizing stress concentration in order to assure a better fatigue behavior. Optimization of shape to minimize stress concentration was presented by Francavilla, Ramakrishnan, and Zienkiewicz [48]. They employed the finite element methods for an optimum fillet shape to

minimize stress concentration using a penalty function procedure. Using a finite-dimensional family of boundary shapes in terms of coordinate parameters, Tvergaard [49] presented the optimum shape of a fillet to minimize stress concentration. Schnack [50] changed the notch shapes iteratively to reduce the maximum stress by use of a finite element method to calculate the stress and displacement fields of the structure in every iteration. His conception to minimize the stress concentration was based on Neuber's idea [51] that a completely constant tangential stress distribution on a notch surface provides the minimal notch stress concentration. Yang and Choi [52] used the design sensitivity formulation [53] to determine the best fillet shape in a tension bar by use of the von Mises yield stress constraint functional. They showed improved accuracy of shape design sensitivity using isoparametric finite elements and a spline function to represent the curved boundary.

In this study of optimization of groove root shape to minimize stress concentration, an optimization module in the ANSYS finite element program was employed. This module uses approximate techniques to characterize the analysis of a design with a set of quadratic functions at each design loop. An approximate objective function is defined to be minimized and is updated at each design loop to account for the additional information. This module uses a penalty function procedure combined with a sequential unconstrained minimization technique in the optimization routine. Two-dimensional elements, such as 6-node isoparametric triangular

elements and 8-node isoparametric quadrilateral elements were used for the finite element stress analysis in optimization.

4.2 Optimization Procedure

4.2.1 Geometric Constraints on Groove Geometry Change

The objective of the shape optimization problem discussed here is to minimize stress concentration or peak maximum principal stress. Prior to optimizing the shape of the groove root, which is also called the stress relief groove, the side constraints on the geometry of stress relief groove must be considered, since those constraints will later be imposed on the design variables during the optimization routine. Instead of weakening the thick-walled pressure vessel by undercutting the conventional groove root in the radial direction, the change in groove root is restricted to the tangential direction, resulting in the shape of stress relief groove shown in Fig. 4.1. In other words, the contour of the groove root was modified in the tangential direction, allowing a smooth tangential transition curve at the root in order to relieve the high stress concentration occurring at the sharp root of the conventional groove.

Restrictions on the change in the external keyway groove root, or stress relief groove, must be specified to ensure the proper functioning of the external keyway groove, since the thick-walled pressure vessel is subjected to torsional loading, T. transmitted through a key in the keyway groove as shown in Fig. 4.2. All dimensions in Figs. 4.1 and 4.2 are the same as the dimensions of the

thick-walled pressure vessel with a conventional groove shown in Fig. 3.3, except the changes in groove root region. Fig. 4.2 shows details of the conventional and changed external keyway grooves, where F_0 is the force due to torque, d and h are the depth and height of the external groove, respectively, and t is the width of the changed groove wall. W' and D' in Fig. 4.2 are the width and depth of stress relief groove at the corner of the external keyway groove, respectively. To determine the width(W') and depth(D') of the stress relief groove, two approaches were used, namely, the theory of strength of materials and finite element analysis.

A typical torque, T, of 56,500 N·m, and a keyway groove length, L, of 54.9 mm, were provided. The key is made of 70/30 brass with yield strength of 326 MPa. The force acting on the groove wall in the changed groove as shown in Fig. 4.2(b), can be obtained as

$$F_0 = \frac{T}{r} = \frac{56500 \text{ N·m}}{0.137 \text{ m}} = 412 \text{ kN} \tag{4.1}$$

where r is the distance from the center of the thick-walled pressure vessel to the center of the changed groove wall. Assuming that the key would fail due to torque, possibilities of failure of the key due to shearing and compressive yielding were taken into consideration. First, shear stress applied to the key was calculated as

$$\tau_a = \frac{F_0}{hL} = \frac{412 \text{ kN}}{(25)(549) \text{ mm}^2}$$
$$= 30 \text{ MPa} < \tau_{ys} = 188 \text{ MPa} \tag{4.2}$$

where calculation of τ_{ys} from tensile yield strength was based on the von Mises yield criterion. This applied shear stress, τ_a, was much smaller than the shear yield stress, 188 MPa, of the 70/30 brass material, resulting in no shear failure due to the specified torque. Second, compressive yield failure due to torque was considered, assuming a uniform stress distribution along the changed keyway groove wall with dimension, t, as shown in Fig. 4.2(b). Thus compressive stress, σ_c, applied to the key due to torque becomes

$$\sigma_c = \frac{F_o}{tL} = \frac{412 \text{ kN}}{(t)(549) \text{ mm}^2} = \frac{750}{t} \text{ MPa} \qquad (4.3)$$

Therefore, in order to prevent compressive yielding failure due to torque, the compressive value given in Eq.(4.3) must be less than the compressive yield strength of the key, which yields $t \geq 2.3$ mm. However, the stress distribution is not uniform in the practical situation. Thus a safety factor of 2.0 was used, assuming a linear stress distribution along the changed keyway groove wall, resulting in the width constraint of $W' = d'$-$t \leq 5.0$ mm.

Provided that failure of the key would not occur for the width, W', less than 5 mm, the failure of the keyway groove in the pressure vessel due to torque also must be checked, since the change in shape of the groove root, or stress relief groove, may cause a fracture in the groove. Finding a reasonable geometric constraint on the depth, D', of the stress relief groove was complicated by this possibility of keyway fracture due to torque, prior to fatigue failure of the thick-walled pressure vessel across the thickness of the wall due to

internal pressure and autofrettage loading. It should be noted that a major concern in this study is the fatigue failure of a thick-walled pressure vessel across the thickness of wall emanating from the external keyway groove root. Therefore, a criterion of keyway failure must be considered, and the proper depth constraint must be imposed on the optimization of the stress relief groove to prevent keyway failure based on the criterion.

In order to study the external keyway groove failure by finding the elastic stress distribution near the keyway groove root due to torsional loading, the finite element analysis was used. An equivalent stress, defined as the von Mises stress, was calculated using the finite element method. The equivalent stress in terms of principal stresses, σ_1, σ_2, and σ_3, is given as

$$\sigma_{eq} = \frac{1}{\sqrt{2}}\left[(\sigma_1 - \sigma_2)^2 + (\sigma_2 - \sigma_3)^2 + (\sigma_3 - \sigma_1)^2\right]^{1/2} \qquad (4.4)$$

The maximum equivalent stress that occurred in the conventional groove was used as a criterion for other keyway groove designs, by allowing a changed groove whose maximum equivalent stress was less than that of the conventional groove.

The finite element mesh used for the stress analysis due to torsional loading is shown in Fig. 4.3, where nodal force F is applied to generate the equivalent torsional loading. To save computing time and effort for generating refined mesh around the groove root without affecting the accuracy of solution at the groove root region, the finite element model was simplified by eliminating one of the

groove walls, as shown in Fig. 4.3(a). Only the top side of the groove wall was assumed to be subjected to force due to torque. A typical refined mesh near the stress relief groove using 6-node isoparametric triangular elements is shown in Fig. 4.3(b).

Equivalent stress contours near the roots of the conventional and typical changed external groove due to torque obtained from the finite element analysis are plotted in Fig. 4.4. Location of the maximum equivalent stress due to torque in the conventional groove has moved toward the side wall of the groove, compared to the location of maximum principal stress due to internal pressure or autofrettage loading, as shown in Figs. 3.11 and 3.17. This maximum equivalent stress of 456 MPa, which was determined from the finite element analysis, due to torque of 56,500 N·m in the conventional groove, will be used as a reference criterion for the other changed groove geometry. A constraint on the depth, D', of the stress relief groove is to be decided from the maximum equivalent stress due to torque and variations of stress concentration due to the change of depth in some optimization results.

4.2.2 Optimization Routine

Optimization of the external groove contour in an autofrettaged thick-walled pressure vessel subjected to internal pressure is concerned with minimizing stress concentration at the external groove root. Therefore, in order to define the stress relief groove contour, a parametric representation of the contour using a set of

design variables is needed for numerical implementation such as the finite element method, which is employed in this study to calculate stresses. Representation of the groove root by a smooth curve instead of piecewise-linear segments is use for its practical application in manufacturing and to avoid inaccuracy in finite element analysis [54-55]. Just as they were used for the finite element analysis in Chapter 3, 6-node isoparametric triangular element and 8-node isoparametric quadrilateral element meshes were used for the curved boundary of the stress relief groove. Excellent accuracy in these elements with reasonable element sizes was shown in the previous chapter dealing with stress analysis of a thick-walled pressure vessel with a conventional external groove. The good accuracy of solution in a curved boundary using isoparametric elements has been shown in reference [56].

Four typical shapes of groove root are presented, as shown in Fig. 4.5, where H1, H2, and H3 denote the design parameters for representing the contours, and R is a radius of the circular groove, fixed as 2.5 mm. Cubic spline functions [57] were used in types I and II to represent the boundaries of the stress relief groove, as shown in Fig. 4.5. Cubic spline functions are among the most popular interpolation functions that fit data smoothly with little oscillatory behavior. The cubic spline function is cubic in each subinterval and has continuous first and second derivatives. A tangential line with zero slope at the left corner of the stress relief groove in Figs. 4.5(a) and (b) was specified to minimize stress concentration in the

transition region at the groove root. More than 3 design parameters in the depth of the groove were not used since it caused the failure in mesh generation due to oscillatory interpolation contour lines. Types of III and IV in Figs. 4.5(c) and (d) represent the groove root of circular shape with radius R=2.5, and of elliptic shape, respectively. Optimizations of these four types of stress relief grooves are discussed in section 4.3.

To optimize the shape of the groove root represented by design variables subject to geometric constraints through minimizing stress concentration, an optimization module in the ANSYS finite element program was employed. This optimization module uses approximation techniques to characterize the analysis of design with a set of quadratic functions at each design loop. The theoretical stress concentration factor was considered as an objective function, $f(\underline{H})$. Thus the problem can be written as,

Minimize $f(\underline{H})$

subject to $g_k(\underline{H}) \leq 0$, $k=1, 2, ..., K$ (4.5)

where $\underline{H}$ is the design variable vector, g_k is the geometric, or side, constraints, and K is the number of geometric constraints. A loading condition of internal pressure of 386 MPa plus 100 percent overstrain was used for the optimization of every type of external groove in the thick-walled pressure vessel. A loading condition of internal pressure plus 75 percent overstrain or 50 percent overstrain was used only for the stress relief groove of type IV. In order to

account for both autofrettage loading and internal pressure loading, an averaged theoretical stress concentration factor was defined as

$$K_t = \frac{\sigma_{max}}{\sigma_N} = \frac{(\sigma_{max})_A + (\sigma_{max})_P}{(\sigma_N)_A + (\sigma_N)_P} \tag{4.6}$$

where $(\sigma_{max})_A$ and $(\sigma_{max})_P$ denote maximum stresses due to autofrettage and internal pressure loading, respectively, and $(\sigma_N)_A$ and $(\sigma_N)_P$ denote nominal stresses due to autofrettage and internal pressure loading, respectively. In order to compare the averaged theoretical stress concentration factors of the changed groove, averaged theoretical stress concentration factors, K_t, for the autofrettaged thick-walled pressure vessel with a conventional external groove were calculated using Eq.(4.6) for all overstrain cases from Tables 3.3 and 3.4, and the results are listed in Table 4.1.

The procedure used in the optimization routine is shown in Fig. 4.6 [58]. In this optimization routine, a certain number of design sets are needed to form the object function approximation using the least squares curve fit. This routine requires that the number of design variables be at least equal to the number of design sets plus two before any approximations are found. The process of generating a set of design variables is random and repeated until the number of sets is sufficient for the first approximation of the objective function. The characteristics of the objective function can be determined by calculating their actual values for a variety of design variable values, since an explicit mathematical representation of any arbitrary objective function is not generally known or easily differentiated.

The approximation of the objective function can be determined by curve fit. Quadratic approximation is done by minimizing the least squares error.

The constrained optimization problem is converted to an unconstrained problem by using a penalty function to enforce the design variable constraints [59-60]. The unconstrained function, or response surface, ϕ, can be written as

$$\phi(\underline{H}, r_j) = f(\underline{H}) + r_j \sum_k P(g_k(\underline{H})) \tag{4.7}$$

where f is the objective function, r_j is the penalty function multiplier for the j-th response surface, $\underline{H}$ is the design variable vector, P is the penalty function, and g_k are the constraints.

Search for a minimum of the penalized approximate objective function, or response function, is done by the sequential unconstrained minimization technique using the steepest descent direction of the objective function [61]. After a predicted set of design variables is found by the sequential unconstrained minimization technique, a new set of design variables is determined from the best design variables and predicted design variables. The optimization routine continues until the convergence tolerance specified on the objective function or design variables are met.

A typical finite element mesh used for the optimization analysis is shown in Fig. 4.7. 8-node isoparametric quadrilateral elements or 6-node isoparametric triangular elements were used for automatic finite element mesh generation. Failure in automatic mesh

generation occurred very often in the case of the quadrilateral element   during stress analysis of the optimization routine, since the domain of the stress relief groove changes after every loop. Therefore, care was taken in mesh generation using an 8-node isoparametric quadrilateral element to avoid mesh generation failure.   Thermal loading analogy was used to simulate autofrettage residual stress, as mentioned in chapter 3, for the thick-walled pressure vessel with the external conventional groove.

4.3 Results and Discussion

4.3.1 Optimization of the Stress Relief Groove

4.3.1.1 Stress Relief Groove of Type I

The process of shape optimization for a stress relief groove of type I, shown in Fig. 4.5(a), by minimizing stress concentration is shown in Fig. 4.8.   Two design variables, depth H1 and width H2, were chosen to characterize the boundary using a smooth cubic spline function, and this is denoted as model (a) in Fig. 4.8.   First, several iterations were performed using randomly generated sets of design variables to form the approximate objective function.   Next, a set of design variables H1 and H2 were found based on that approximate function, and the peak of the maximum principal stress was obtained.   Internal pressure plus 100 percent overstrain loadings were applied to the thick-walled pressure vessel for stress analysis of type I in the optimization routine.

Since the depth constraint was not fixed, as mentioned in the previous section, a tentative constraint of $1.5 \leq H1 \leq 6.0$ was imposed on model (a) of type I to see the trend of optimization, with a known width constraint $3.0 \leq H2 \leq 5.0$ from section 4.2.1. A minimum width constraint of $H2=3.0$ mm was chosen to make the radius the same as the root radius, $R=1.5$ mm, of the conventional groove in the case of the circular stress relief groove shape. Convergence tolerances of 0.020 mm, 0.045 mm, and 10 MPa were given to design variables $H1$, $H2$, and the peak maximum principal stress, respectively, for termination of the optimization iteration. Convergence tolerances on design variables were determined from 1 percent of the constraint ranges, since they are generally limiting tolerances in machining these grooves. The tolerance of peak maximum principal stress with 10 MPa corresponds to 1 percent of the nominal stress due to 100 percent overstrain and internal pressure loading. Optimum design variables of $H1=5.21$ mm and $H2=5.00$ mm were found, and the averaged theoretical stress concentration factor, K_t, was 2.43 from Fig. 4.8, compared to a K_t of 4.25 in the conventional groove given in Table 4.1. Thus, a 43 percent decrease of K_t was obtained by introducing a stress relief groove of type I, which is a significant reduction in K_t.

The maximum equivalent stress due to torsional loading of this model was calculated to check groove failure due to torque, and it was less than that of the conventional groove. It was anticipated

that the groove failure would not occur based on the maximum equivalent stress in the conventional groove due to torsional loading.

To find the correlation between depth and stress concentration, optimization analysis was performed with each fixed width(H2) of 5, 4, and 3 mm. Groove shapes of type I with widths of 5, 4, and 3 mm are denoted as models (b), (c), and (d), respectively, and the iterative processes in optimization of these models are shown in Fig. 4.8. In Fig. 4.9, each model shows the convergent stress concentration factor at a certain depth H1 that minimizes stress concentration, and the optimum depth was essentially determined by the width. Obviously, optimum depth increases as the width increases. The optimum values of the design variables and the corresponding stress concentration factors are listed in Table 4.2. Therefore, from the results of the type I groove shape, the depth constraint of $1.5 \leq H1 \leq 6.0$ seems reasonable for a given width constraint of $3.0 \leq H2 \leq 5.0$, and this will be used for the other types of stress relief groove optimization.

For an initial shape of the stress groove in the optimization routine, a circular groove was used for each model in type I, resulting in H1=1.5 and H2=3.0 for model (a), and H1=2.5, 2.0, and 1.5 for models (b), (c), and (d), respectively. From the calculation of K_t using Eq.(4.6) and final values from Table 4.2, the final stress concentration factor of each model has dropped from 44 to 30 percent, compared to the initial K_t, which was determined from the initial circular shape of the stress relief groove of each model with initial H1 and H2. Compared to K_t of the 100 percent overstrain case

in the conventional external groove, as listed in Table 4.1, models (a), (b), (c), and (d) showed 43, 43, 38, and 29 percent decreases in final K_t, respectively, which constitute significant improvements in relieving high stress concentration at the external keyway groove root.

4.3.1.2 Stress Relief Groove of Type II

In the optimization of the stress relief groove shape of type II as shown in Fig. 4.5(b), two design variables, H1 and H2, in the direction of depth were used to parameterize the contour. Design variable H3 was initially introduced in the optimization routine, but was eliminated due to failure in mesh generation during the routine. It is attributed to the bad element shape while generating finite element meshes along the wavy boundary curves of the groove. Spline function was used to represent the contour of the stress relief groove in type II, as in type I. The optimization process by minimizing stress concentration due to internal pressure and 100 percent overstrain loading is shown for each model (a), (b) and (c) with H3=5, 4, and 3 mm, respectively, in Fig. 4.10, where quite close K_t values between models (a) and (b) can be seen. Initial values of H1=H2=2.5 mm were used for all models of type II. Final values of design variables and the averaged theoretical stress concentration factor for each model are listed in Table 4.3. Final values of K_t have dropped from 30 to 35 percent compared to the initial values of K_t, which were determined from the initial shapes of the stress relief

grooves with initial H1 and H2. Final stress concentration factors in models (a), (b), and (c) have decreased 45, 45, and 36 percent, respectively, from the conventional groove, as listed in Table 4.1. It should be noted that for a fixed width of 5 mm, model (a) in type II showed only 2 percent lower in final K_t than model (b) in type I, resulting in a negligible improvement in minimizing stress concentration. More design variables in the parameterization of the groove contour appeared to be of little importance in this type of groove. An attempt to define more design variables in the direction of depth was made, but oscillatory behavior of the stress relief groove contour shape due to many design variables caused the failure in mesh generation.

4.3.1.3 Stress Relief Groove of Type III

Recognizing that the optimized groove shape should be feasible and practical in manufacturing, a simple circular stress relief groove was considered while preserving the maximum possible root radius R=2.5 mm without violating the width constraint of 5 mm, as shown in Fig. 4.5(c). Finite element stress analysis was performed using four different depths of H1, instead of employing the optimization routine, since it is obvious that a smaller stress concentration factor will be obtained for the deeper stress relief groove. As shown in Fig. 4.11, stress concentration decreases as depth(H1) of the stress relief groove increases, and the difference in K_t between the depths of 2.5 mm and 6.0 mm was 12 percent. Table 4.4 shows the averaged

stress concentration factor due to internal pressure and 100 percent overstrain loading for each depth. Even though for the circular groove with 6 mm in depth, a 22 percent decrease in K_t relative to the conventional groove of 100 percent overstrain case as listed in Table 4.1 was achieved, the improvement is relatively little compared to the 45 percent reduction in K_t for the groove shapes of types I and II. Thus the circular groove is not recommended as a good stress relief groove.

4.3.1.4 Stress Relief Groove of Type IV

Another simple configuration of an elliptic groove of type IV, as shown in Fig. 4.5(d), was considered to minimize stress concentration using two design variables, H1 and H2, similar to type I except for the shape of contour. The optimization routine was again employed to find the best configuration with the given constraint of $3.0 \leq H1 \leq 6.0$ and $3.0 \leq H2 \leq 5.0$. Initial values of H1=H2=3 mm were used. It can be noticed in Fig. 4.12 and Table 4.5 that even the initial design for the 100 percent autofrettage case shows a quite low stress concentration factor, denoted as initial K_t, compared to other types, and the final stress concentration factor, denoted as final K_t, is the lowest value among the groove shape types considered in this study.

In addition to internal pressure plus a 100 percent overstrain loading condition, the shape optimization of the external groove root of type IV in the partially autofrettaged thick-walled pressure vessel subjected to internal pressure was performed, and these results are

shown in Fig. 4.12. Convergent K_t values were usually obtained after approximately 8 iterations. The final K_t and optimum design variables of type IV for each overstrain case are listed in Table 4.5. The final optimum design variables for 75 and 50 percent overstrain cases are very close to the 100 percent overstrain case as shown in Table 4.5. Compared to the conventional groove, the final values of K_t have dropped by 45 and 36 percent for the 75 and 50 percent overstrain cases, respectively. It must be noted that the similar values of K_t between different overstrain cases do not imply similar magnitudes of peak maximum principal stress, since the nominal stress for each overstrain case is different. In fact, the peak maximum principal stress in the 100 percent overstrain case was 14 and 26 percent higher than the 75 and 50 percent overstrain cases, respectively.

4.3.1.5 Changed Final Stress Relief Groove

Among the four types of stress relief grooves, the elliptic shape of type IV with 6.0 in depth(H1) and 4.3 in width(H2) was chosen as the best design, since it showed the lowest stress concentration factor and is practically simpler in manufacturing than a groove contour with spline function except for the circular shape of the stress relief groove. The circular groove of type III appeared to be simplest for the manufacturing process, but the stress concentration was still considerably higher than it is for the other optimum shapes. Final stress concentration factors due to internal pressure plus 100

percent overstrain loading for model (a) of type I, model (a) of type II, and type IV were 2.43, 2.33, and 2.29, respectively. These types of stress relief grooves reduced the averaged stress concentration factor of the conventional groove due to internal pressure and 100 overstrain loading of 4.25, as given in Table 4.1, by approximately 45 percent, which is a very significant improvement in minimizing stress concentration.

A computing time of approximately 500 to 900 CPU seconds per iteration of the optimization routine was generally taken on the Apollo computer, depending on the number of elements used for finite element modelling. As mentioned earlier, a 6-node isoparametric triangular element with an element size of 0.2 mm for all finite element analysis was first used to represent the curved boundary of the stress relief groove, since it has been shown in chapter 3 that this size of element resulted in good accuracy and more flexibility in automatic mesh generation compared to the 8-node isoparametric quadrilateral element. Verifications of the optimization analysis using an 8-node isoparametric quadrilateral element were done for the cases of type I, II, and IV, resulting in good agreement in final K_t values. A typical comparison for the elliptic groove of type IV is shown in Fig. 4.13, where the scatter between two elements after 4 iterations was due to the different values of the design variables, as opposed to the inaccuracy of element types. The same convergent values of K_t can be seen in Fig. 4.13. The finite element mesh used for each type of stress relief

percent overstrain loading for model (a) of type I, model (a) of type II, and type IV were 2.43, 2.33, and 2.29, respectively. These types of stress relief grooves reduced the averaged stress concentration factor of the conventional groove due to internal pressure and 100 overstrain loading of 4.25, as given in Table 4.1, by approximately 45 percent, which is a very significant improvement in minimizing stress concentration.

A computing time of approximately 500 to 900 CPU seconds per iteration of the optimization routine was generally taken on the Apollo computer, depending on the number of elements used for finite element modelling. As mentioned earlier, a 6-node isoparametric triangular element with an element size of 0.2 mm for all finite element analysis was first used to represent the curved boundary of the stress relief groove, since it has been shown in chapter 3 that this size of element resulted in good accuracy and more flexibility in automatic mesh generation compared to the 8-node isoparametric quadrilateral element. Verifications of the optimization analysis using an 8-node isoparametric quadrilateral element were done for the cases of type I, II, and IV, resulting in good agreement in final K_t values. A typical comparison for the elliptic groove of type IV is shown in Fig. 4.13, where the scatter between two elements after 4 iterations was due to the different values of the design variables, as opposed to the inaccuracy of element types. The same convergent values of K_t can be seen in Fig. 4.13. The finite element mesh used for each type of stress relief

groove is shown in Fig. 4.14. Table 4.6 shows the maximum equivalent stress due to torque for an optimum shape in each type that has a minimum stress concentration factor. All of the changed grooves were considered safe from groove failure due to torque since they had a smaller maximum equivalent stress than the conventional groove of 456 MPa, which was used as a criterion for groove failure due to torque.

4.3.2 Stress Distributions of an Autofrettaged Thick-walled Pressure Vessel with Changed External Groove

Finite element stress analysis of an autofrettaged thick-walled pressure vessel with the final optimum elliptic stress relief groove of 4.3 mm in width and 6.0 mm in depth was performed in order to compare stress distributions between the conventional and changed grooves. As explained earlier in chapter 3, a thermal loading analogy was used to simulate the autofrettage residual stress. As shown in Fig. 4.7, plane A-A' passes through the thickness opposite to the center of the groove, plane B-B' passes through the point of peak maximum principal stress at the groove root, and plane C-C' passes through the center of the groove.

Tangential stress distributions due to only internal pressure along planes of A-A', B-B', and C-C' of the thick-walled pressure vessel with the changed elliptic stress relief groove are plotted in Fig. 4.15. Stress distribution along plane A-A' was essentially the same as in the case of the conventional groove, resulting in no influence of groove root shape on stress distributions at the location away from

the groove region due to internal pressure loading. Similar behaviors in plane B-B' and C-C' between the conventional and changed groove can be observed in Figs. 3.10 and 4.15, but the magnitude of the maximum tangential stress is much lower than in the conventional groove. The maximum principal stress and theoretical stress concentration factor in the changed groove due to internal pressure loading are listed in Table 4.7. The theoretical stress concentration factors given in Table 4.7 should be distinguished from the averaged theoretical stress concentration factor used in the optimization routine since K_t in Table 4.7 was solely due to internal pressure loading. The stress concentration factor, K_t, due to internal pressure loading at the critical location B' in the changed groove has dropped by 46 percent, compared to K_t of 3.93 in the conventional groove case as listed in Table 3.3. But at location C' in the changed groove, only a 4 percent decrease in K_t was obtained, compared to K_t of 1.72 in the conventional groove. This is obvious since the stress relief groove was basically intended to reduce the local high stress concentration region at the external keyway groove root.

Tangential residual stress distributions due to 100, 75, and 50 percent overstrains along planes A-A', B-B', and C-C' in the thick-walled pressure vessel with the changed elliptic stress relief groove are shown in Figures 4.16, 4.17, and 4.18, respectively. Along plane A-A', the difference between the conventional and changed final grooves was negligible for a given percent overstrain case, indicating negligible influence on the residual stress distributions away from

the groove. Compared to the high stress concentrations noticed in the conventional groove, as shown in Figs. 3.14, 3.15, and 3.16, a relatively low stress concentration can be seen at each location of B' in Figs. 4.16, 4.17, and 4.18. Maximum principal stresses, nominal stresses and stress concentration factors due to each overstrain loading at the locations of B' and C' in the elliptic stress relief groove are shown in Table 4.8. Compared to stress concentration factors in the conventional groove, as shown in Table 3.4, stress concentration factors at the critical location B' have dropped by approximately 46 percent for all overstrain cases. At location C', a 3 to 12 percent reduction in K_t was obtained in the changed groove, compared to the conventional groove.

The maximum principal stress distribution along the elliptic stress relief groove contour due to each loading condition is shown in Fig. 4.19, where angle, θ, is defined in Fig. 4.20. Regardless of loading conditions, the maximum principal stresses were evenly distributed along the groove contour. The flattened curves of stress variations along the groove contour in Fig. 4.19 indicate a decrease in stress concentration, in contrast to the sharp stress variations along the conventional groove root, as shown in Fig. 3.18. A plot of maximum principal stress contours near the stress relief groove due to 100 percent overstrain plus internal pressure loading is shown in Fig. 4.20. In Fig. 4.20, MX and MN indicate the locations of highest and lowest maximum principal stress, respectively. Smooth stress contours can be observed and these contours are nearly parallel to

the elliptic groove boundary. This final optimized elliptic groove of 4.3 mm in width and 6.0 mm in depth was used for simulation fatigue testing to see the fatigue life improvement of an autofrettaged thick-walled pressure vessel by minimizing stress concentration.

CHAPTER V

COMPRESSIVE RESIDUAL STRESS INDUCTION
BY SHOT PEENING

5.1 Introduction

The aim of inducing compressive residual stresses in highly stressed regions such as groove roots, fillets and holes is to overcome the damaging effects of tensile stresses applied by external loads, and improve fatigue performance of the part. The fatigue strength improvement is attributed to the fact that the formation and growth of the crack is prevented by compressive residual stresses. Several methods have been used to produce beneficial compressive stresses; heat treatment and mechanical prestressing methods are most widely used. Heat treatment methods include induction hardening, carburizing, and nitriding. The most widely used methods of mechanical prestressing are shot peening, surface rolling, overloading, and coining [19].

Mechanical prestressing means that the part has been mechanically processed so that it contains a desired residual stress distribution, which must be balanced both as to forces and moments. High local stresses produce local tensile yielding at the surface of the part when a deforming tensile load is applied. When this tensile load is released, the yielded material at the surface tends to retain part of the deformation experienced under load. This is resisted by

unyielded adjacent material due to normal complete elastic recovery, resulting in a compressive residual stress state of the yielded material at the surface and a tensile residual stress state of adjacent unyielded subsurface material. To produce residual stresses by mechanical means in a part, nonuniform plastic deformation is necessary.

A local surface residual compressive stress will affect the resultant local mean stress by superimposing the residual stress on the maximum and minimum operating stresses. Obviously, it can have no effect on the amplitude of the alternating stress. Therefore, any improvement in fatigue performance due to residual stress must come from a reduction of tensile mean stress at the surface. With a given alternating stress, reduction of the mean stress will improve fatigue performance. By reducing the local surface tensile stress in the vicinity of the groove root, the damage per cycle will be reduced and a longer fatigue life will be obtained. This fatigue life improvement is attributed principally to the superimposition of a compressive residual stress upon the applied tensile stress from the external load [62]. Thus, the local tensile stress at the vulnerable surface of the part is reduced.

In this research, shot peening was used to induce compressive residual stress at the external groove root of the simulation fatigue specimen taken from the autofrettaged thick-walled pressure vessel for the simulation fatigue testing that will be discussed in the next chapter. X-ray diffraction analysis was performed on both as-

machined and shot peened-changed groove simulation specimens to determine residual stress distribution near the groove root region to the depth of approximately 0.75 mm.

5.2 Shot Peening Procedure

Shot peening was used to induce compressive residual stress at the changed external groove surface, which is the region most vulnerable to fatigue crack formation and growth due to high stress concentration. Shot peening may be defined as the process of cold working the surface of a structural or machine part by means of a driven stream of hard shot. The process is used to improve the fatigue properties of the part, and in some cases to prevent stress corrosion cracking by the introduction of compressive residual stresses in the surface layer [63].

In the shot peening process, relatively hard particles, usually spherical cast iron or steel shot, are projected against the material being peened with sufficient velocity to indent the surface. The indentations at each point of impact are the result of local plastic yielding. As the deformed regions tend to expand, they are restrained by adjacent deep material that was not plastically deformed by the shot impact. Since the plastically deformed layer seeks to occupy more space, it is compressively strained, resulting in a compressive residual stress state. Compared to other mechanical prestressing methods, the shot peening process has several

advantages, such as flexibility, control of residual stress intensity, and economy [63].

Fig. 5.1 shows the shot peened region of the changed external groove in the simulation fatigue specimen taken from an autofrettaged thick-walled pressure vessel. Detail dimensions of the changed elliptic groove are shown in Fig. 4.5(d) with 6 mm in depth(H1) and 4.3 mm in width(H2) of the stress relief groove. Other configurations of the simulation fatigue specimen will be discussed in the next chapter. As shown in Fig. 5.1, side surfaces around the external groove area were peened to prevent fatigue cracks originating from the edges of the specimen.

The magnitude of compressive residual stress induced by the shot peening is a function of the yield strength of the peened material and the peening process. It is equal to or less than approximately one-half the yield strength of the peened material with adequate coverage in the unstrained state [19]. The depth of induced compressive residual stress depends on the properties of the peened material, and the properties of the blast. The properties of the blast are defined by the hardness. size, type, shot velocity, angle of impingement on the peened surface. and exposure time [63]. To specify the shot peening intensity, standard test strips or Almen strips are used; the intensity is related to the arc height of the shot peened standard test strip [64].

The shot peening on the external grooves was performed following specifications of MIL-S-13165B [65] and SAE standard [63]

by the Metal Improvement Company. No fixture was used during the shot peening, and peening was conducted at room temperature. Shot peening was done only on the changed external groove, whose final shape was determined by a quasi-optimization process discussed in chapter 4. The peening media used was cast steel shot in spherical shape [66-67]. Two different sizes of cast steel shots, CS-550 and CS-110, with diameters of 1.4 and 0.25 mm, respectively, were used since a dual shot peening process was employed. Dual shot peening uses two different sets of conditions to gain improved fatigue life over single shot peening. The application of a smaller shot size for the second peening operation enhances the surface finish, and can provide a higher magnitude of compressive stress near the surface [63]. It must be noted that the nominal size shot used on groove surfaces shall not be greater than one-half the groove radius. Shot velocity was approximately 60 m/sec. Coverage, defined as the ratio of the indented area to total area, was checked by both visual inspection using a 10X magnifying glass and Dyescan liquid after the shot peening, resulting in full coverage.

Table 5.1 shows the data from the dual shot peening performed by the Metal Improvement Company. Peening intensities of 10-12C and 6-8A from the first and second shot peening were obtained, respectively, where "10-12C" indicates the readings of 10 to 12 in Almen gage indicator using a standard test strip of type C. Dimples in the shot peened surface taken by a scanning electron microscope can be seen in Fig. 5.2.

5.3 Residual Stress Determination
by X-ray Diffraction Method

An X-ray diffraction method was used to measure the compressive residual stresses induced at the changed groove root of the simulation fatigue specimen by the shot peening. In addition to the shot peened specimen, residual stress distribution at the changed groove of the as-machined simulation fatigue specimen was also measured to find remaining residual stresses after the saw-cut from the autofrettaged thick-walled pressure vessel and the groove machining.

The X-ray diffraction method depends on the regularity of spacing of atomic planes of the material. When a material is subjected to stress, the interplanar spacing changes. If the stress is tensile, the average interplanar spacing in the direction of the stress will increase. The change in interplanar spacing, produced by the stresses, divided by the original spacing, becomes an elastic strain which can be interpreted in terms of the corresponding stress [19, 68-69]. In the X-ray method, strain is a measure of change in the lattice spacing of the planes of atoms in the material. When using the X-ray diffraction method, first, the interplanar spacing of the planes of atoms parallel to the specimen surface is measured since the atoms are at their normal distance on the free surface. The interplanar spacing at a different angle to the specimen surface is then measured. This difference in spacing of the two planes at the inclined angle is used to determine the corresponding stress.

The two-angle technique [69] was used for X-ray diffraction residual stress measurement at the external groove of the simulation fatigue specimen. Fig. 5.3 shows the specific location where X-ray diffraction analysis was performed by the Lambda Research Laboratory. Finite element stress analysis of autofrettaged thick-walled pressure vessel with a changed external groove subjected to internal pressure, as shown in Fig. 4.20, has indicated peak maximum principal stress at this location, and it was considered as the most probable fatigue crack formation site. As shown in Fig. 5.3, the cross-hatched tongues of the changed external groove were cut for the access of X-ray analysis equipment.

Material at the analyzed location was removed electrolytically for subsurface measurement, minimizing possible alteration of the subsurface residual stress distribution as a result of material removal. Because of changes in the stress distribution due to material removal operations, additional corrections were applied to the X-ray diffraction data to account for the effect of penetration of the radiation source used to measure the strain in the material. Also, corrections to account for stress relaxation caused by layer removal were made. Residual stresses listed in Table 5.2 were determined in circumferential direction by the X-ray diffraction method for each as-machined and shot peened simulation fatigue specimen. Residual stress measurement was performed to 0.75 mm in depth with 8 readings in the direction normal to the groove surface. The compressive residual stress distributions versus depth as provided

by the Lambda Research Laboratory are shown in Fig. 5.4, where similar compressive residual stresses are observed both in the as-machined and shot peened specimens.

5.4 Results and Discussion

It was shown in Chapter 3 that autofrettage residual stress was relaxed to approximately zero when the circular rings were cut open with a saw. The relieved stresses, calculated from the experimentally measured strains and opening angles after saw-cut, were compared with the theoretical autofrettage residual stress in Fig. 3.8, resulting in close agreement, even though the actual residual stresses in the autofrettaged thick-walled pressure vessel were not measured, and the relieved stress is not necessarily the same as the actual residual stress originally present. However, the results of X-ray diffraction analysis, as shown in Fig. 5.4, indicate that the as-machined specimen with the changed groove contains compressive residual stresses similar to those of the shot peened specimen, as deep as 0.75 mm. Approximately the same values of compressive residual stresses can be observed at the examined groove surface, as shown in Fig. 5.4. Average values of compressive residual stresses for as-machined and shot peened specimens using second to fifth measurement data were taken in order to compare the subsurface compressive residual stresses at both specimens, resulting in 517 MPa and 594 MPa, respectively. Surface compressive residual stress of about 800 MPa was not considered, since the residual stress

dropped to the range of 500 to 600 MPa at a depth of 0.01 mm as given in Table 5.2. Although subsurface compressive residual stress in the shot peened specimen was about 13 percent higher than in the as-machined specimen, both values were approximately one-half the yield strength of ASTM A723 steel. The compressive residual stress in the as-machined specimen was unexpected from the previous experimental results and theoretical calculations. The experiments showed that the relieved stress distribution due to elastic recovery by saw-cut was quite close to the theoretical autofrettage residual stress distribution of a 100 percent overstrain condition.

There can be several possible causes of the difference between the expected and measured values in the residual stress of the as-machined specimen, provided that the given X-ray analyses are correct. The residual stress results using X-ray diffraction analysis done by Lambda Research were reliable from their experience. Compressive residual stress can be caused by the metal cutting operation done on the elliptic stress relief groove. But the depth of the compressive residual stress was too much compared to that of other reported sources of similar material that were cut in an abusive condition [70-71], where compressive residual stresses did not exceed about 0.25 mm in depth [72]. Thus the metal cutting process was not considered as the significant source of the compressive residual stress.

The residual stresses due to metal forming and autofrettage processes of the thick-walled pressure vessel left over after saw-cut

of the autofrettaged thick-walled pressure vessel may be the most probable source of the compressive residual stresses in the outside region of the simulation fatigue specimen. Stacey and Webster [73] calculated the redistributed residual stress field after saw-cut from the originally existing residual stresses by subtracting the stresses resulting from the recovering residual bending moment using the superposition principle. They obtained the final actual residual stress distribution before saw-cut by superimposing experimentally measured residual stresses due to previous tube forming and autofrettage processes. The resultant residual stresses after saw-cut were then determined by subtracting the residual stresses due to relieved bending moment from the measured actual residual stresses prior to saw-cut. It was found that the as-received tube prior to autofrettage contained quite high compressive residual stresses very near the outer surface due to tube forming process [73]. In this research, the same procedure was used to determine the final residual stress distributions in the simulation fatigue specimens, but theoretical residual stress distributions were assumed to be the actual residual stress distributions existing prior to saw-cut, since the actual residual stress distributions in the as-received autofrettaged thick-walled pressure vessel were not measured by any experimental method. In other words, the difference between the expected and measured residual stresses at the as-machined changed external groove in the simulation specimen was due to the lack of information about the actual existing residual stresses in the thick-walled

pressure vessel, originating from metal forming and autofrettage processes. Averaged subsurface residual stresses at the changed external grooves with/without shot peening, determined by the X-ray diffraction method, will be used for life estimation calculations of thick-walled pressure vessels and simulation specimens.

CHAPTER VI

SIMULATION FATIGUE TESTS

6.1 Introduction

Fatigue tests that simulate an autofrettaged thick-walled pressure vessel under pulsating pressure loading conditions were performed using specimens taken from the autofrettaged thick-walled pressure vessel. The fatigue life of a thick-walled pressure vessel subjected to pulsating internal pressure was assumed to be approximately equal to that of a simulation specimen if the stresses are simulated as closely as possible for both external groove roots, where fatigue cracks are expected to originate. Linear elastic finite element stress analysis was employed to calculate stresses at the external groove in the simulation specimens, since the closed-form solution was not available.

In this chapter, load-controlled simulation fatigue tests using conventional, changed, and shot peened-changed groove specimens are described. Since three different autofrettage or overstrain levels were considered, three different types of simulation fatigue loading corresponding to three different overstrain levels were applied for each type of grooved specimen. Fractographic analysis was done in order to investigate the behavior of crack formation, growth, and final fracture.

6.2 Simulation Specimens

Simulation specimens used for simulation fatigue testing were taken from the autofrettaged thick-walled pressure vessel, as shown in Fig. 6.1. Rings of 20-mm thickness were cut, followed by saw-cut and drilling holes. Grooves were then machined using a milling machine. Conventional, changed, and shot peened-changed grooved specimens were used for the simulation fatigue tests. As shown in Fig. 6.1, a conventional groove was first roughly machined using an end-mill that has a 1.5-mm tip radius and 0.5-mm undersized diameter, then finished to final dimensions using a finishing end-mill of 0.03-mm tolerance.

A keyway cutter with an elliptic contour as shown in Fig. 6.1 was specially ordered for the changed groove machining. A computerized numeric-controlled profiling machine was employed to generate the precise dimensions of the elliptic keyway cutter with a tolerance of 0.013 mm. To make a changed external groove, a slot of 25 mm in width, the same as the conventional groove, was first machined, and then a stress-relieving groove of elliptic contour was machined using the elliptic keyway cutter. In order to prevent changes in material properties and residual stress induction due to abusive machining, the groove of changed geometry was machined using an undersized rough elliptic keyway cutter, followed by the precise elliptic keyway cutter. After the final elliptic stress relief grooves were machined, shot peening was performed on the specimens with as-machined changed grooves.

The dimensions of each external groove contour after machining were measured using a 33x traveling microscope with a least reading of 0.01 mm, resulting in a difference of less than 0.10 mm compared to the exact dimensions, which were considered satisfactory. Using the same procedure as the conventional and changed-grooved specimen, the dimensions of peened-groove contours were measured, resulting in approximately the same scatter of 0.10 mm as observed in the as-machined changed groove.

6.3 Stress Analysis of Simulation Specimens

6.3.1 Stress Analysis using Finite Element Method

Stress distribution of a curved beam such as the simulation fatigue specimens shown in Fig. 6.1 can be found using a curved beam theory. Using a curved beam of reduced width of W-d without external groove, i.e., with an inside diameter of a and outside diameter of $b_o=b-d$, the tangential stress distribution along the thickness can be written as [74],

$$\sigma_\theta = -\frac{F}{A} + \frac{F(X+r')}{A\,e}\left[1 - \frac{R}{r}\right] \tag{6.1}$$

where A is the cross-sectional area of the specimen which is equal to (W-d)t and t is the thickness, r is the radius, r' is the radius to centroidal axis, R is the radius to neutral axis, which is (W-d)/ln(b/a), and e=r'-R, i.e., the distance between the centroidal and neutral axes. Therefore, Eq.(6.1) can be rewritten as

$$\sigma_\theta = -\frac{F}{(W-d)t}\left\{\frac{X+r'}{r'-R}\left(1-\frac{R}{r}\right)-1\right\} \qquad (6.2)$$

For the derivation of this equation, the plane perpendicular to the centroidal beam axis remains perpendicular to the centroidal axis subsequent to bending, i.e., the influence of shear deformation is not taken into account.

Stress analysis of the simulation specimen with external groove was done using the same finite element mesh generated for the stress analysis of the thick-walled pressure vessel, as shown in Fig. 3.4. The 8-node isoparametric quadrilateral elements were used, since this element type has shown very accurate results with respect to the stress analysis of a thick-walled pressure vessel (see Chapters 3 and 4). Plane-stress condition was used in the finite element analysis. A compressive load was applied at a nodal point in the finite element model corresponding to the location of load, F, in Fig. 6.1. The distance from the center of simulation specimen denoted as X, was 98 mm. A compressive load of 10 kN was applied for the finite element stress analysis. Two different configurations of external grooves, i.e., conventional and changed grooves, were used, as shown in Fig. 6.1.

Finite element solutions of simulation specimens with conventional and changed grooves are defined in Figs. 6.2 and 6.3, respectively. Maximum principal stresses along the conventional groove and changed-groove contours are plotted in Fig. 6.4, where angle θ was previously defined in Fig. 4.20. For each type of specimen, stress distributions along planes B-B' and C-C', as defined

in Fig. 6.1, were plotted compared to the theoretical solution of Eq.(6.2) with reduced width. Maximum principal stresses at the locations of B' and C' and nominal stresses and theoretical stress concentration factors in the simulation fatigue specimen with a conventional or a changed groove due to a compressive load of 10 kN are listed in Table 6.1. Nominal stress was calculated at the outside radius of $b_0 = b-d$, yielding

$$\sigma_N = -\frac{F}{(W-d)t}\left\{\frac{X+r'}{r'-R}\left(1-\frac{R}{b_0}\right)-1\right\}$$

$$= 234 \text{ MPa} \tag{6.3}$$

Theoretical stress concentration factors at the locations of B' and C' were calculated by dividing the maximum principal stresses by the nominal stress given in Eq.(6.3).

6.3.2 Simulation Loads

Using the finite element solutions of the simulation specimen and thick-walled pressure vessel with a conventional groove, as listed in Table 6.1 and Tables 3.3, 3.4, respectively, simulation fatigue loads were determined by equating the maximum principal stresses at location B', which is the most vulnerable to crack formation. For example, maximum and minimum simulation fatigue loads for 100 percent overstrain case were calculated as follows:

$$P_{max} = \frac{\sigma_P + \sigma_A}{\sigma_S} \times 10 = \frac{2147 + 2044}{690} \times 10 = 60.7 \quad (kN)$$

$$P_{min} = \frac{\sigma_A}{\sigma_S} \times 10 = \frac{2044}{690} \times 10 = 29.6 \quad (kN) \tag{6.4}$$

where σ_P, σ_A, σ_S are maximum principal stresses due to internal pressure, autofrettage and simulation loading, respectively. The simulation fatigue loads for each percent overstrain or autofrettage calculated similar to Eq.(6.4) are given in Table 6.2. It must be noted that the simulation fatigue loads were determined based on linear elastic stress analysis, and the simulation of linear elastic stresses at the conventional groove root in both the thick-walled pressure vessel and simulation specimen was assumed to be reasonable, even though local plastic deformation would occur at the locally high-stressed region of the groove root.

6.3.3 Experimental Verification of Finite Element Stress Analysis Results

In order to verify the linear elastic finite element solutions by experimental method, maximum principal stresses on the face of the changed external groove were determined using strain gages, as shown in Fig. 6.5. A 45° angle strain rosette with 0.76-mm gage length was placed at the middle of thickness in the center line of the changed external groove, as shown in Fig. 6.5. The strain rosette used was WA-09-030WR-120 from Micro-Measurements. A compressive load of 2.22 kN, under the elastic limit in the whole specimen without any local yielding, was applied, and the strains were then recorded as listed in Table 6.3. Two principal strains of ε_1 and ε_2 were calculated using three strains of ε_A, ε_B, and ε_C measured from a 45° angle strain rosette [43] and principal stresses were then calculated using generalized Hooke's law given in Eq.(3.31). As shown

in Table 6.3, measured ε_A and ε_C were almost the same as ε_1 and ε_2, respectively, since the strain rosette was placed such that the directions of strain ε_A and ε_C were close to the principal strain directions, i.e., hoop and longitudinal directions, respectively. A difference of about 2 degrees between strain gage and principal directions was obtained. A plane-stress condition was the result, i.e., approximately zero longitudinal stress.

Four uniaxial strain gages with 0.79-mm gage length(EA-06-031CE-350) were placed on the face of the changed external groove as shown in Fig. 6.5. The same compressive load of 2.22 kN was applied and strains from the uniaxial strain gages were measured. In the case of the uniaxial strain gage, stress was calculated using a uniaxial stress-strain relationship of $\sigma = E\varepsilon$. The maximum principal stresses calculated from the measured strains are given in Table 6.4, including the small differences compared to finite element solutions. Maximum principal stresses calculated from the measured strains using strain gages were in good agreement with the finite element solutions as shown in Table 6.4. Error was less than 5 percent, which was considered satisfactory. Uniaxial strain gages were used since the uniaxial stress state was shown from strain measurements using a strain rosette as given in Table 6.3.

6.4 Load-controlled Simulation Fatigue Testing

Simulation fatigue tests were conducted using C-shaped specimens with three different types of external groove, as explained

in section 6.2. These are conventional, changed, and shot peened-changed grooves. Three different levels of simulation loads that correspond to 100, 75, and 50 percent overstrain loadings in the actual thick-walled pressure vessel subjected to internal pressure were determined using finite element stress analysis, as mentioned in section 6.3.2, and these fatigue loads are given in Table 6.2. Each fatigue load level thus simulates a 100, 75, and 50 percent autofrettaged thick-walled pressure vessel subjected to internal pressure. Since the internal pressure does not change for all percent overstrain cases, the amplitude of simulation loads is same as that shown in Table 6.2. Eighteen specimens were used for the simulation fatigue tests, since duplication tests at three different load levels were done for three different types of simulation specimen.

Load-controlled fatigue testing was performed using an 89 kN electrohydraulic material testing system. A haversine waveform with a frequency of 0.3 to 0.9 Hz was used for the load-controlled fatigue tests performed at room temperature. Maximum and minimum loads were monitored using a digital indicator. Cracks were monitored at both sides of the specimens using 2 traveling microscopes, which have magnifications of 33x and 10x and resolutions of 0.01 mm and 0.05 mm, respectively, under stroboscope light illumination. Since four corners of the specimen groove can be possible sources of crack formation, the groove root regions were watched very carefully. A crack length of about 0.25 mm was the minimum crack length that can be observed with the

optical method. After the crack had formed, the cycles and corresponding crack lengths were recorded untii the specimen fractured.

Cycles to various crack lengths for each of the three different grooved specimens are given in Tables 6.5, 6.6, and 6.7. Fatigue cracks formed at all four corners of the groove root, and grew to several millimeters in depth, resulting in a fast ductile fracture mode. Crack lengths in Tables 6.6 and 6.7 are average values from the crack lengths monitored on both sides of the specimen, since cracks generally grew unsymmetrically for the specimens with changed and peened external grooves. Fatigue life to 2.5-mm crack length for each different type of groove and simulation load is listed in Table 6.8, where the average fatigue life means the average cycles to 2.5-mm crack length from the duplication fatigue tests. Cycles to 2.5-mm crack length in the highest compressive load in Table 6.5 could not be measured due to fast crack growth. Therefore, cycles to fracture were used for cycles to 2.5-mm crack length instead. A crack length of 2.5 mm was used as the fatigue life of the simulation specimen since a crack length less than 2.5 mm could not be detected for some tests and this value is similar to critical values in the actual pressure vessel fracture. Least squares log-log linear regression analysis was done using maximum loads and cycles to 2.5-mm crack length given in Tables 6.5, 6.6 and 6.7. The log-log linear load-life can be represented by the equation

$$F_{max} = A N^{\alpha} \qquad (6.5)$$

where Fmax is the maximum simulation load. The coefficient, A, and exponent, α, for each type of specimen are given in Table 6.9. Simulation fatigue lives to 2.5-mm crack length are plotted for three different grooved specimens in Figs. 6.6 to 6.8, and Fig. 6.9 includes all fatigue lives to 2.5-mm crack length for comparison.

6.5 Results and Discussion

6.5.1 Stress Analysis and Fatigue Tests of Simulation Specimens

Finite element solutions of simulation specimens with conventional and changed external grooves were compared to the nominal stress distribution of the specimen with reduced wall thickness in Figs. 6.2 and 6.3. Quite close stress distributions away from the external grooves along planes B-B' and C-C' were found, and stress concentrations were noticed at both points B' and C'. As given in Table 6.1, theoretical stress concentration factor, K_t, of 1.62 at the point B' of the changed groove has dropped by 45 percent compared to a K_t value of 2.96 in the conventional groove. This is a similar ratio observed in the stress analysis of the thick-walled pressure vessel with conventional and changed external grooves, as shown in Tables 3.3, 3.4 and 4.7, 4.8. Maximum principal stress distributions along both conventional and changed-groove contours, shown in Fig. 6.4 clearly indicate a stress-relieving effect by changing the shape of external groove. Angle θ in Fig. 6.4 was defined in Fig. 4.20. Magnitudes of maximum principal stresses along the contour in the

changed groove of elliptic shape were very evenly distributed compared to the high peak maximum principal stress in the conventional groove. Similar trends of maximum principal stress distributions were previously noticed in Figs. 3.18 and 4.19.

Simulation fatigue test loads were determined from the linear elastic stress analysis using finite element methods, based on the assumption that the simulation of maximum principal stresses at both the actual thick-walled pressure vessel and simulation specimen would result in approximately equal fatigue life. Compressive residual stresses remaining in the as-machined simulation specimens, measured by X-ray diffraction analysis after saw-cut, as discussed in chapter 5, were not taken into account to determine the simulation loads, thus assuming no residual stresses in the as-machined specimens. The influence of residual stresses in the specimen will be analyzed in the following chapter on fatigue life estimation.

The results of fatigue tests that simulate the autofrettaged thick-walled pressure vessel subjected to pulsating internal pressure are given in Tables 6.5-6.8. Fatigue life to 0.25 mm in the simulation specimen with a conventional groove was approximately 60 to 80 percent of the fatigue life to fracture, as shown in Table 6.5, where a 0.25-mm crack length was the smallest crack length that could be observed by a 33x traveling microscope of 0.01-mm resolution. The difference in cycles from 2.5-mm crack length to final fracture in the conventional groove was less than 20 percent of

the fatigue life to fracture, depending upon the simulation load level. The higher load level showed a smaller difference between cycles to 2.5-mm crack length and fracture than the lower load level due to a smaller critical crack length under higher load level. In the case of the highest load level, or the 100 percent overstrain case, cycles to crack lengths of 1.5 and 2.5 mm were not recorded due to fast crack growth after 1-mm crack length. Cycles to final fracture were used instead since the cycles to 2.5-mm crack length must be within 4 percent range of cycles to fracture.

Cycles to crack length of less than 2.5 mm in the specimens with changed and shot peened grooves were difficult to monitor since cracks of sizes of 1 to 2 mm appeared suddenly on the side surface of specimen. Therefore cycles to 2.5-mm crack length were defined as fatigue life of the simulation specimen in this research since the cycles to crack length of 2.5 mm for all types of specimens could be obtained and were also similar to the actual case of the thick-walled pressure vessel. It can be found in Table 6.6 and 6.7 that the percentage of crack growth life to fatigue life of fracture in both the changed and shot peened grooves is smaller than that of the conventional groove. This is attributed to the longer crack formation life in changed and shot peened grooves under a similar crack growth rate in all types of groove for a given load level. From Table 6.8, increases in fatigue life, i.e, cycles to 2.5-mm crack length, of 26 and 42 percent were obtained for 75 and 50 percent overstrain cases, respectively, compared to a 100 percent overstrain case of the

conventional-grooved specimen. In the case of the changed groove, 46 and 115 percent longer fatigue life were obtained for 75 and 50 percent overstrain cases, respectively, than for the 100 percent overstrain case. In the case of the shot peened groove, 80 and 430 percent longer fatigue life were obtained for 75 and 50 percent overstrain cases, respectively, than for 100 percent overstrain case. Changes in fatigue life under the different levels of simulation load for each type of groove were clearly due to the mean stress or maximum stress, since the simulation load amplitude was fixed for all fatigue tests, as given in Table 6.2. Approximately 1 to 20 percent difference in fatigue life between cycles to 2.5 mm to final fracture was obtained in the conventional groove, and 1 to 10 percent difference in the changed and shot peened-changed grooves was obtained.

Simulation fatigue test results are plotted in Figs. 6.6-6.8 for each type of groove, and all test data points are superimposed in Fig. 6.9, including log-log linear least squares fit lines. Both changed and shot peened grooves exhibit considerably improved fatigue lives compared to the conventional groove. In 100 percent overstrain case, both changed and shot peened grooves showed 3.5 times longer fatigue lives than the conventional groove. The negligible difference between changed and shot peened grooves in the 100 percent overstrain case, as shown in Fig. 6.9, was attributed to the high simulation load level, which reduced the influence of surface roughness caused by groove machining and washed out compressive

residual stresses by shot peening. In the 75 percent overstrain case, the changed and shot peened grooves showed 4 and 5 times longer fatigue lives than the conventional groove, respectively. Significant fatigue life improvements were obtained in the 50 percent overstrain case, i.e., the lowest simulation load level, where the changed and shot peened grooves showed 5 and 13 times longer fatigue lives than the conventional groove, respectively. Comparisons between different types of groove for each simulation load level are shown in Fig. 6.9. However, the fatigue improvement of the shot peened groove case, compared to the changed groove was not completely due to the influence of compressive residual stresses by shot peening, since X-ray residual stress analysis indicated a magnitude of compressive residual stresses in the as-machined changed groove similar to that of the shot peened groove, resulting in a small difference of compressive residual stress of about 80 MPa. Improved surface roughness by shot peening was therefore regarded as one of the influential factors of fatigue life improvement of the simulation specimen with the shot peened-changed groove. Conclusively, 3.5 to 13 times longer fatigue lives, depending upon the percent overstrain levels were obtained in the changed and the shot peened groove, compared to that of the conventional groove. This was considered a significant improvement in the fatigue life of the simulation fatigue specimen and thus of the autofrettaged thick-walled pressure vessel subjected to internal pressure.

6.5.2 Fractographic Analysis

The fracture surfaces used in this analysis were cut from simulation specimens using a band saw. For each type of groove, three samples from three different simulation load levels were chosen, resulting in a total of 9 fracture surface samples used for the analysis of simulation fatigue specimens. In order to use a scanning electron microscope(SEM), these fracture surface samples were cleaned by placing them in the ultrasonic cleaner container filled with acetone since enamel was sprayed on the fractured surfaces right after each testing to prevent corrosion.

Macroscopic fracture surface examinations were done to find the crack formation features and general fracture behaviors, using a 10x magnifying glass. It was noticed during fatigue tests that cracks usually started from the machining tool marks on the simulation specimen surfaces, and final fracture mode was characterized by a shearing failure.

Fig. 6.10 shows the macroscopic fracture surfaces of simulation specimens with conventional grooves subjected to 100, 75, and 50 percent autofrettage load levels, respectively. All three fracture surfaces can be clearly distinguished by the size of the smooth textured crack growth region. The highest simulation load level of the 100 percent overstrain case exhibited the smallest crack growth region, which was evident from the shortest critical crack length among the three simulation load levels. Macrocracks originated from about 10 to 20 locations along the thickness and propagated

separately, but finally joined together. Crack growth regions for all three fracture surfaces exhibited smooth textures at the beginning area under slow crack growth rate but became rougher as the cracks lengthened under faster crack growth rate. Crack tunneling was observed in contrast to final fracture surface appearance. Final fracture regions for all three fracture surfaces in Fig. 6.10 show large shear lips, indicating the ductile mode of fracture.

Fig. 6.11 shows three macroscopic fracture surfaces from simulation specimens with changed grooves subjected to 100, 75, and 50 percent autofrettage load levels, respectively. It is easily noticed that the appearance of the crack formation regions for all three fracture surfaces is quite different from the fracture surfaces of the simulation specimens with a conventional external groove, as shown in Fig. 6.10. These crack formation regions along the thickness of the groove root were not flat, as shown in Fig. 6.11. The irregular appearance of the crack formation region can be explained by the effect of tool marks due to stress relief groove machining and the wide area of the evenly distributed stressed region along the contour of the elliptic stress relief groove, which make cracks originate at 5 to 8 different positions in height, as shown clearly in Fig. 6.11(b). The irregularity in height of crack formation region cannot be found in the conventional-grooved specimens, as shown in Fig. 6.10, since the crack formation regions of the sharp groove roots were locally high stressed with a very high stress gradient. In Fig. 6.11, the smooth textured area due to slower crack growth rate at the initial

stage of crack growth can be seen, even though it is not at the same height.

Fracture surfaces from the shot peened simulation specimens with changed grooves are shown in Fig. 6.12. The macroscopic features of fracture surfaces are similar to those in Fig. 6.11, with more smooth crack formation sites. Along the machined and shot peened-groove faces, about 10 to 20 microcrack formation sites were observed. The irregular positions in height at the crack formation regions as seen in the unpeened-changed grooves were not observed. This was attributed to the elimination of sharp tool marks on the groove surfaces by the shot peening operation, resulting in improved surface roughness. No difference in the final fracture mode between all fracture surfaces was found, regardless of the groove shape and shot peening operation.

Microscopic analysis of the fractured surfaces of the simulation specimens was performed using a scanning electron microscope. Crack formation sites along the groove surfaces and crack growth and final fracture behavior were examined using the same fracture samples used in the macroscopic analysis of fracture surfaces. SEM photos of the simulation specimens with the conventional, changed, and shot peened-changed groove are shown in Figs. 6.13, 6.14 and 6.15, respectively. Fracture surface samples of all simulation load levels for each type of grooved specimen were examined, but they were basically the same in microscopic fracture appearance. Therefore, only typical fractographs from the highest load level, i.e.,

100 percent overstrain loading case, are shown in the figures, and these were taken at the crack formation regions of the groove root. Each of the Figures 6.12-6.15 consists of a macrophoto of crack formation region at the groove root surface and a higher magnification view of the microcrack formation site in square box in the macrophoto.

The fracture surface appearance of the crack formation and the early stage of the crack growth regions from the conventional and changed groove were very similar, as shown in Figs. 6.13 and 6.14, respectively, while those from the shot peened-changed groove exhibited a smoother texture, as shown in Fig. 6.15. Lower parts of SEM fractographs in Figs. 6.13-6.15 show the machined or shot peened groove surfaces. Fractographs on the right-hand side of Figs. 6.13-6.15 were magnified from the square boxed regions of macro-SEM fractographs and showed crack formation sites, resulting in essentially the same appearance of fracture surface. Fig. 6.16 shows a typical region of transcrystalline crack growth, where secondary cracks and the formation of striations can be found. Typical final fracture surfaces are shown in Fig. 6.17 with different magnifications. A typical transgranular fracture surface of martensite steel [75] is shown at the bottom of Fig. 6.17, where widely distributed inclusion stringers are found. A fractograph of higher magnification view at the top of Fig. 6.17 shows the ductile dimples that represent the coalesced microvoids, and also several inclusion-nucleated voids are seen on the left side of the same figure.

CHAPTER VII

MEAN STRESS EFFECTS ON LOW CYCLE FATIGUE BEHAVIOR

7.1 Introduction

In manufacturing mechanical components or structures, residual stresses are introduced due to the nature of the manufacturing process or for the purpose of the beneficial effects of residual stresses. When these components or structures are subjected to cyclic loadings or deformations, premature failure or prolonged fatigue life can occur due to the residual stress. The presence of the residual stress implies mean stress in components or structures under cyclic loadings.

The effect of mean stress on fatigue life was investigated earlier by Gerber and Goodman [46]. Their empirical relationships were based on stresses. Various combinations of stress amplitude and mean stress were applied to smooth laboratory specimens, and plots of stress amplitude versus mean stress for various values of cycles to failure were produced. These approaches had limitations in that a great amount of data were required to cover all the possible stress ratios which could occur in service. Later, many proposals to reduce the data with various stresses and stress ratios to a single line on a log-log plot were made. Morrow [76] proposed that a combination of stress amplitude and mean stress could be

represented by an equivalent completely reversed stress amplitude. He claimed that the equivalent completely reversed stress amplitude for a nonzero mean stress test and the same magnitude of stress amplitude for a zero mean stress test would result in the same fatigue life. A parametric approach similar to Morrow's was suggested by Topper and Sandor [77], and various attempts were made to correlate mean stress and completely reversed fatigue test data using a parameter called the equivalent-completely reversed strain amplitude. Another approach was developed by Smith, Watson, and Topper from the well-known Neuber rule [78].

Numerous proposals have been made for treating mean stress effects in low cycle fatigue. Nihei et al. [79] reviewed the capability and accuracy of several damage parameters to predict the mean stress effects on fatigue life of unnotched specimens using strain-controlled fatigue tests. Fatemi and Stephens [80] showed the effects of tensile mean stress and strain on axial fatigue and cyclic deformation behavior of SAE 1045 HR steel using Morrow's parameter and the Smith, Watson, and Topper(SWT) parameter, which are the most commonly used methods to deal with the mean stress effects on fatigue life involving low cycle fatigue concepts. It was also found by Fatemi and Stephens that mean strain was not detrimental to fatigue life unless it produced a mean stress. The effect of mean stress in stress and strain controlled fatigue tests on the cyclic stress-strain curves was presented by Kliman and Bily [81], showing that the stress-controlled cyclic stress-strain curves

were clearly influenced by the mean stress level, whereas the strain-controlled cyclic stress-strain curves for various mean strains were identical. Lorenzo and Laird [82] suggested that the stress-controlled fatigue life data with mean stress could be adequately described by the Manson-Coffin relationship. A modified stress-strain parameter based on the SWT parameter was proposed by them.

The fatigue life of components is generally considered to be composed of a crack formation(or initiation) life and a crack propagation life. Fatigue cracks usually originate from the critical location containing a stress and strain raiser such as fillets, holes, notches, keyways, seams, and tool marks which are subjected to an essentially local strain cycling condition due to the constraint of surrounding elastic material. Therefore, the cyclic stress-strain relationship and strain-life relationship obtained from smooth axial specimens are generally incorporated with the local strain approach to evaluate the fatigue crack initiation life, or formation life, to crack sizes of about 0.25 to 5 mm [46], of the components or structures. Crack propagation life can be evaluated using the fracture mechanics approach from the stress intensity factor known for the geometry of the component.

An autofrettaged thick-walled pressure vessel with an external groove experiences fluctuating internal pressure in addition to the prestrain/prestress during the overstraining process. A keyway groove at the outside diameter of an autofrettaged thick-walled pressure vessel serves as a stress raiser. Therefore, in order to

investigate the low cycle fatigue behavior of the thick-walled pressure vessel with an external groove, strain-controlled low cycle fatigue testing with mean strain was conducted using specimens taken from the pressure vessel. Based on these experiments, the fundamental smooth specimen low cycle fatigue properties and the tensile and compressive mean strain and stress effects on low cycle fatigue behavior of a high strength pressure vessel steel ASTM A723 were investigated using several mean stress parameters.

7.2 Experimental Procedure

7.2.1 Specimen Preparation

High strength pressure vessel steel ASTM A723 was used for the experiment. The chemical composition and monotonic tensile properties of the material are shown in Tables 2.1 and Table 2.2, respectively.

The specimens for the low cycle fatigue tests were taken from the autofrettaged thick-walled pressure vessel. Specimen I.D. was marked to distinguish each other. Uniaxial fatigue specimens with a gage section diameter of 6 mm and a gage section length of 15.2 mm, as shown in Fig. 2.2, were used. The specimens were polished with final polishing marks in the longitudinal direction using a fine emery paper of 600 grit. The diameter of the gage section of each smooth axial low cycle fatigue specimen was averaged from six measurements at three positions along its longitudinal axis using a 33X travelling microscope to prevent the surface of the specimens

from being scratched. The specimens were kept in the desiccator after vaseline was applied to the surface for protection against corrosion.

Before the fatigue test, epoxy dots were applied on the surfaces of the low cycle fatigue specimens to prevent the knife edge of the extensometer from cutting into the polished surfaces. Epoxy dots of approximately 2 to 3 mm in diameter were applied to the specimen surfaces. Curing was done for about 24 hours at room temperature. After the epoxy dots were cured, the tops of the dots were filed flat in order to mount an extensometer of gage length 12.5 mm. Care was used not to nick the test specimen during the filing. Rubber bands were used to support an extensometer on a test specimen. Fatigue tests were started after the extensometer knife edges were allowed to cut into the hardened epoxy dots for about 10 minutes.

7.2.2 Strain-Controlled Low Cycle Fatigue Testing

Low cycle fatigue tests were performed with an 89 kN closed-loop electrohydraulic material testing system with hydraulic grips. Strain-controlled low cycle fatigue tests were performed using ASTM standard practice E606 as a guide [83]. System alignment for the low cycle fatigue tests was done following ASTM standard practice E1012 [84]. A specimen with eight strain gages attached was used to achieve the alignment of the system. Four strain gages centered in the middle of the test section and the other four strain gages near the root of the curvature were applied to the specimen to determine

the strain due to bending. The maximum bending strain measured in the alignment system was below 5% of the maximum axial strain, as suggested in ASTM standard practice E606.

Five different strain ratios, R=-2, -1, 0, 0.5, 0.75, which is defined as $\frac{\varepsilon_{min}}{\varepsilon_{max}}$, were used to investigate the mean strain and mean stress effects on the low cycle fatigue behavior. For the completely reversed test, i.e., R=-1, 10 different strain amplitudes ranging from 0.0025 to 0.03 were used. In addition, three duplication tests were done for the strain amplitudes of 0.003, 0.005, and 0.01 that showed very close reversals to failure. For the mean strain test, i.e., R≠-1, six to seven different strain amplitudes ranging from 0.015 to 0.002 were selected for use of the SWT parameter and the cyclic stress-strain curve to make the data evenly distributed with respect to the reversals to failures for the later purpose of comparison. The SWT parameter will be explained in a later section.

A triangular waveform with a frequency ranging from 0.0625 to 1.25 Hz was used. The strain rate varied from 0.006 sec^{-1} to 0.02 sec^{-1}, but most of the tests were done using a strain rate of 0.01 sec^{-1} except for 6 tests out of the total of 38 tests. All tests except one were run in strain control throughout the test at room temperature, i.e., of about 25° C. One specimen slipped out of the hydraulic grip during strain control, and the remainder of the test was carried out using a load control because the strain amplitude was within the elastic limit of the material. Strains and loads during the tests were monitored using a strip chart recorder and a digital indicator. After

recording several initial hysteresis loops of load versus strain, additional single hysteresis loops were recorded periodically on an analog X-Y plotter. The sign of strain at the first quarter cycle was tensile for the tests with a strain ratio greater than or equal to -1, and compressive for tests with strain ratio of -2.

A 20% drop in the maximum load or fracture were first defined as failure criteria, but these criteria were changed since they were not appropriate to the mean strain tests. The low cycle fatigue test with high tensile mean strain showed significant mean stress relaxation at the early portion of the life. The relaxation caused a confusion in the load drop due to crack formation. Based on the observation of crack formation at the specimen surface, final fracture or a 25% drop in the maximum tensile load were considered as the appropriate criteria for specimen failure. Even though the tensile load dropped below 25% of maximum load, tests were continued until the specimen fractured into two parts.

The replication tests were done only for the completely reversed fatigue tests. Assuming that the purpose of this testing was of a preliminary and exploratory nature, ASTM standard practice E739 [85] requires that there be percent replication from 17% to 33%, where percent replication has been defined by the relation

$$\% \text{ Replication} = [1 - x/y] \times 100 \qquad (7.1)$$

where　　x = total number of strain amplitudes

　　　　　y = total number of specimens tested

The percent replication of 23% for the completely reversed tests with zero mean strain satisfied the ASTM recommendation.

7.3 Fractographic Analysis

7.3.1 Sample Preparation

Fractured surfaces used in the fractographic analysis were cut from axial low cycle fatigue test specimens. Two typical specimens were selected from each of R=-2, R=-1, and R≥0. These three types of strain ratios represent compressive, zero, and tensile mean stresses in low cycle fatigue testings. One of two specimens from each type was from low strain amplitude tests and the other from high strain amplitude tests. All of the fractured surfaces were examined macroscopically using a 10X magnifying glass, and then a Scanning Electron Microscope(SEM) was used to do microscopic examination of fractured surfaces. For SEM fractographic analysis, the fracture surface samples were cleaned with acetone using an ultrasonic cleaner. Approximately 3 minutes were taken to clean one fracture surface sample.

7.3.2 Crack Formation, Growth, and Final Fracture

Macroscopic examinations of the fractured surfaces were done to find the location of crack formation, and the region of crack growth and final fracture. Generally, cracks started at the surface without any surface flaw or subsurface defect of the specimen being

noticed. The final fracture was characterized by a shearing mode, i.e., a slant fracture, regardless of strain ratios.

The locations of the crack formation for strain amplitudes smaller than approximately 0.005 for all strain ratios were easily observed macroscopically, since the smooth crack propagation region and the final slant shearing fracture region could be clearly recognized using just a 10X magnification. For high strain amplitudes, approximately greater than or equal to 0.005, the fractured surfaces were too rough to find the locations of crack formation, even though the final tearing regions were easily observed. Microscopic observations were needed to find the crack formation region.

Fig. 7.1 shows fracture surfaces of completely reversed low cycle fatigue testings, R=-1, that indicate zero mean strain and approximately zero mean stress In Fig. 7.1(a) the existence of a smooth region made finding the crack formation region easy, as marked with an arrow. It is very difficult in Fig. 7.1(b) to find the crack formation region. This was attributed to the fast crack growth under the high strain amplitude as soon as the crack had formed, as was noticed during the low cycle fatigue testing. The final sheared fracture region can be seen at the opposite side of the crack formation location in Fig. 7.1(a).

Fig. 7.2 and Fig. 7.3 show the fractured surfaces for the negative and positive mean strain tests, respectively. Figs. 7.2(a) and 7.3(a) are from low cycle fatigue tests with low strain amplitude, and

Figs. 7.2(b) and 7.3(b) are from low cycle fatigue tests with high strain amplitude. The fracture surfaces of negative mean strain testing with low strain amplitude in Fig. 7.2(a) look very similar to those in Fig. 7.1(a), and crack formation location is marked with an arrow. However significant differences in fracture surface appearance between negative and positive mean strain test specimens can be observed in the relatively small strain amplitude testings such as those shown in Fig. 7.2(a) and Fig. 7.3(a). The fracture surface of the negative mean strain testing as shown in Fig. 7.2(a), looks brighter and smoother in appearance than those of the positive or zero mean strain test specimens. This is due to rubbing or fretting of the cracked surfaces under the compressive loading. In the fracture surfaces from the positive mean strain testings, several crack formation locations were found, especially for R=0.75. This is attributed to large stretching of the specimen under high mean strain. In Fig. 7.3(a) three crack formation locations were found, as indicated by the arrows. Regardless of sign of mean strain, high strain amplitude tests as shown in Figs. 7.1(b), 7.2(b), and 7.3(b) showed very rough fracture surfaces, and crack formation locations were not easily found in low magnification with the SEM.

Typical fatigue crack formation locations can be seen in Figs. 7.4 and 7.5 that were taken from low and high strain amplitude low cycle fatigue testings, respectively. In Fig. 7.4, inclusions, considered as stress concentrators, are found near the surface. Many inclusions were observed in SEM examination, and they mostly consisted of

aluminum and calcium. These chemical compositions were obtained using X-ray analysis equipment in a scanning electron microscope. A fractograph of higher magnification from the fracture surface with high strain amplitude low cycle fatigue testing is shown in Fig. 7.5, where the location of the crack formation site is still not clear.

Basically, similar fatigue crack growth and final fracture surface were observed in all types of fracture samples from the low cycle fatigue testings. Depending upon strain amplitudes, the crack growth .egion showed fine or rough striations. Generally, lower strain amplitude testing($\Delta\varepsilon/2 < 0.005$) or negative mean strain testing(R=-2) showed a finer surface in fatigue crack growth regions than high strain amplitude($\Delta\varepsilon/2 \geq 0.005$) or positive mean strain testings(R$\geq$0). A typical fatigue crack growth region taken at the middle of the sample in Fig. 7.2 is shown in Fig. 7.6. The final fracture surface of ASTM A723 steel used in this study can be characterized as a ductile mode of fracture. Dimples in the final fracture region are seen in Fig. 7.7, and essentially the same fracture appearances were observed in all samples.

7.4 Results and Discussion

7.4.1 Variations of Mean Stresses

Representative hysteresis loops for each strain ratio under both large and small strain-controlled amplitudes are shown in Figs. 7.8-7.12. For a negative mean strain test, R=-2, with a relatively large strain amplitude of 0.008, as shown in Fig. 7.8(a), the

continuous increase of minimum stress results in significant relaxation of negative mean stress. However, for a negative mean strain test with a relatively small strain amplitude of 0.004, as shown in Fig. 7.8(b), the cyclic stress and strain response is essentially elastic, and no significant compressive mean stress relaxation is seen. Very similar mean stress behavior was observed in the tensile mean strain tests. Figs. 7.10(a), 7.11(a), and 7.12(a) show the obvious tensile mean stress relaxation during the initial cycles and throughout the fatigue life for the larger strain amplitudes. The tests of high mean strain but with a relatively small strain amplitude in Figs. 7.10(b), 7.11(b), and 7.12(b) show the same mean stress relaxation at the very beginning of the test followed by stabilized behavior.

Maximum, minimum, and mean stress variations of each specimen for all strain ratios are shown in Figs. 7.13-7.17. Mean stress relaxation can be seen in these figures, particularly for the large strain amplitude tests, due primarily to the fact that both maximum and minimum stresses increased for the negative or compressive mean strain tests of $R=-2$, while both maximum and minimum stresses decreased for the positive or tensile mean strain tests. The larger the strain amplitude, the more the significant amount of mean stress relaxation. It is interesting that mean stress relaxation occurred for strain amplitudes greater than 0.005, regardless of tensile or compressive mean strain. Only small differences in the fatigue lives between strain ratios were found for

the strain amplitudes greater than 0.005, indicating that the mean strain was not detrimental to the fatigue life unless it produced a mean stress. This finding will be discussed later.

It was noticed during the testing that, for all R ratios, the hysteresis loops of the strain amplitudes below 0.005 were essentially elastic. At the strain amplitude of 0.005, a small plastic strain appeared. This will also be seen in the cyclic stress-strain curve in the following section. This confirms that mean or residual stress is relaxed out by plastic deformation [86]. Also it can be seen in Figs. 7.13-7.17 that mean stresses in higher strain amplitude tests dropped quickly to a steady-state low value of mean stress.

7.4.2 Cyclic Stress-strain Behavior

Table 7.1 shows the results of low cycle fatigue tests that include the number of reversals to failure and approximate half-life data, such as total, elastic and plastic strain amplitude, mean strain, stress amplitude, maximum and mean stress, and whether the specimen failed inside or outside of the gage length of the extensometer. Young's modulus(E_t) in Table 7.1 was taken from the first quarter cycle of the hysteresis loops. Six out of a total of 38 specimens fractured out of gage length, i.e., outside the knife edge, but five specimens among them were considered valid since the failure occurred between the knife edge and the root of the curvature of the axial low cycle fatigue specimen. One invalid test was excluded from the analysis. Macroscopic observation showed

that no failure occurred at obvious macroscopic discontinuities or flaws on the surface.

It is generally accepted that the governing parameter of the fatigue process is cyclic plastic strain. Therefore, it is important to find out the material response to the cyclic loading. The cyclic stress-strain curve which represents the cyclic properties of a material was obtained using the companion specimen method that connects the maximum stress of the stabilized half-life hysteresis loops of the completely reversed, R=-1, low cycle fatigue tests. Difficulties were found when calculating the plastic strain amplitudes at the half-lives, since a substantial difference between Young's modulus of loading and unloading during the cycle was noticed. The difference of 5 to 15 percent between Young's modulus from the first quarter cycle(E_1) and that of the unloading cycle from the maximum tensile stress at approximate half-life(E_2), as shown in Fig. 7.8(a), was found. This phenomenon of decrease in Young's modulus can be seen clearly in the first several hysteresis loops, as shown in Figs. 7.8-7.12. Careful examination of the plastic strains directly measured from the stable hysteresis loops at approximate half-life provided very close values of the plastic strains calculated using Young's modulus(E_3) taken from the unloading cycle at the maximum compressive stress of the same approximate half-life hysteresis loops as shown in Fig. 7.8(a). The error between these plastic strains was less than 3 percent and E_3 obtained from each test was used for the analysis.

The elastic strain amplitude was calculated using the Young's modulus(E_3) taken from the unloading cycle of the hysteresis loop at approximate half-life, and the plastic strain amplitude was directly measured from the same hysteresis loop.

$$\frac{\Delta\varepsilon_e}{2} = \frac{\Delta\sigma}{2E_3} \qquad (7.2)$$

The cyclic stress-strain curve is represented by the relationship

$$\frac{\Delta\varepsilon}{2} = \frac{\Delta\varepsilon_e}{2} + \frac{\Delta\varepsilon_p}{2} \qquad (7.3)$$

$$= \frac{\Delta\sigma}{2E_3} + \left(\frac{\Delta\sigma}{2K'}\right)^{1/n'} \qquad (7.4)$$

where
$\Delta\varepsilon/2$ = total strain amplitude

$\Delta\varepsilon_e/2$ = elastic strain amplitude at approximate half-life

$\Delta\varepsilon_p/2$ = plastic strain amplitude at approximate half-life

$\Delta\sigma/2$ = stress amplitude at approximate half-life

K' = cyclic strength coefficient

n' = cyclic strain-hardening exponent

E_3 = Young's modulus at approximate half-life

Values for K' and n', given in Table 7.2. were obtained from the log-log linear regression analysis using plastic strain amplitudes and corresponding stress amplitudes of the completely reversed fatigue tests at approximate half-life. The cyclic stress-strain curve using the completely reversed low cycle fatigue test data of approximate half-life exhibits cyclic strain softening behavior compared to the monotonic stress-strain curve, as shown in Fig. 7.18. Direct

comparison of monotonic yield strength with cyclic yield strength gives a quantitative idea of cyclic softening. Cyclic yield strength, σ_{ys}', in Table 7.2, was obtained from the intersection of the cyclic stress-strain curve and the 0.2% offset line with the same initial slope. A difference of 13 percent between monotonic and cyclic yield strength was obtained. As mentioned in the previous section, the cyclic stress-strain curve appears linear below the strain amplitude of 0.005, above which significant mean stress relaxation was noticed for $R \neq -1$ tests.

The cyclic stress-strain curve, including all data points from the mean strain tests, is shown in Fig. 7.19. Pair values of strain amplitude and stress amplitude at the approximate half-life from the five different strain ratios are plotted, including the cyclic stress-strain curve generated by Eq.(7.4). All data points with nonzero mean strain show a similar behavior to the cyclic stress-strain curve obtained from completely reversed low cycle fatigue testing. Data from large mean strain values, such as $R=0.5$ or 0.75, show a little more cyclic softening behavior than the other data. This was the influence of mean stress relaxation observed in the mean strain tests with large strain amplitudes. The influence of the mean stress and strain was studied by Kliman and Bily [81]. They showed that the strain-controlled cyclic stress-strain curve was not affected by the mean strain.

7.4.3 Completely Reversed Low Cycle Fatigue Behavior

The total strain amplitude versus reversals-to-failure for the tests without mean strain, i.e., R=-1 is shown in Fig. 7.20. The elastic and plastic components of strain amplitude versus reversals-to-failure are shown in Figs. 7.21 and 7.22. The fatigue life consists of the elastic and plastic strain-life, and each life is mathematically modelled using

$$\frac{\Delta\varepsilon}{2} = \frac{\Delta\varepsilon_e}{2} + \frac{\Delta\varepsilon_p}{2} \tag{7.5}$$

$$= \frac{\sigma_f'}{E_3}(2N_f)^b + \varepsilon_f'(2N_f)^c \tag{7.6}$$

where σ_f' =   fatigue strength coefficient

ε_f' =   fatigue ductility coefficient

b   =   fatigue strength exponent

c   =   fatigue ductility exponent

The low cycle fatigue properties, σ_f', b, ε_f', and c, listed in Table 7.3, were determined from the y-intercepts and slopes of log-log linear regression lines of elastic and plastic strain-life. The averaged Young's modulus, E_3, of 193 GPa taken from the unloading cycle of the approximate half-life hysteresis loop, as shown in Fig. 7.8(a), was used and averaged Young's moduli from different definitions are given in Table 7.2. These values were used to plot the lines in Figs. 7.20-7.22. Elastic, plastic, and total strain components versus reversals-to-failure curves are superimposed in Fig. 7.23 using the low cycle fatigue properties. The transition fatigue life where the

total strain-life consists of equal elastic and plastic strain-life is shown at about 250 reversals with a strain amplitude of about 0.006.

Figs. 7.20 and 7.23 show that the conventional low cycle fatigue model gives nonconservative predictions for the short life region less than 100 reversals and the long life region greater than 5×10^5 reversals. This nonconservatism can be explained by the characteristics of nonlinearity of the elastic and plastic strain-life curves. Close examination of the cyclic stress-strain curve in Fig. 7.18 shows that there is little change in the stress amplitude for the strain amplitude with $\Delta\varepsilon/2 < 0.015$, as expected from low cyclic strain hardening exponent n' of 0.071, as listed in Table 7.2. The change of total strain amplitude at the high strain region of the cyclic stress-strain curve caused little change in stress amplitude and the corresponding elastic strain amplitude for $\Delta\varepsilon/2 \geq 0.015$, resulting in the nonlinearity of the log-log elastic strain-life curve. The shorter life region data of the elastic strain-life curve appears almost horizontal in Fig. 7.21. The nonlinearity of the plastic strain-life can be explained by the sharp decrease in plastic strain amplitude in the long life region. Thus the mathematical model predicts a fatigue life at both small and large strain amplitudes that is longer than the actual fatigue life.

A linear log-log total strain-life model used by Stephens and Koh [87] for A356-T6 cast aluminum alloy was used in order to improve the conventional strain-life model given by Eq.(7.6).

$$\frac{\Delta\varepsilon}{2} = M(2N_f)^m \tag{7.7}$$

The values of coefficient M and exponent m, as listed in Table 7.4, were obtained by the linear regression analysis. As shown in Fig. 7.24, the linear log-log total strain-life model eliminates the nonconservatism.

7.4.4 Mean Stress Effects on Low Cycle Fatigue Behavior

The fact that a continuous and significant mean stress relaxation was shown for the tests of large strain amplitudes greater than 0.005 caused the difficulty in deciding the life-to-failure and finding a stable hysteresis loop. Mean stress versus the applied cycles plot for R=0.75 and $\Delta\varepsilon/2$=0.08 in Fig. 7.12 shows a typical tensile mean stress relaxation throughout the life. The life-to-25 percent drop in maximum tensile load was defined as the life-to-failure because a crack of observable size, i.e., 3 to 5 mm in circumferential dimension, was seen, and the maximum tensile load was beginning to drop rapidly afterwards. For strain amplitudes larger than 0.005, the difference between the fatigue life-to-25 percent maximum load drop and the fatigue life-to-fracture was less than 15 percent.

Total strain-life curves of low cycle fatigue tests for each strain ratio are shown in Fig. 7.25. It is easily observed that all data points fall nicely into the log-log linear least squares fitting lines. This log-log linear model was already noticed in the completely reversed low cycle fatigue testing. The coefficients and exponents in Eq.(7.7) for

each R ratio are listed in Table 7.4. Values from the tensile mean strain test results, i.e., R>-1, are very close, especially for R=0 and 0.75.

Fig. 7.26 shows the superposition of data points from all strain ratios. Little difference in fatigue life for strain amplitudes greater than 0.005 can be found. But care must be used in the analysis, since three data points from R=-1 whose strain amplitudes are greater than 0.015 may mislead the understanding of strain-life behavior. A recognizable difference in fatigue life starts from the strain amplitude of 0.005, and the difference gets bigger for the lower strain amplitudes. Three trends that consist of the negative mean strain, zero mean strain, and positive mean strain data are observed. Data from the negative mean strain tests, with compressive mean stresses as listed in Table 7.1, show a longer life than the others, while data from positive mean strain tests with tensile mean stresses show a shorter life. Little difference in fatigue life between the positive mean strain data can be found. Zero mean strain test data from R=-1, which showed approximately zero mean stress, are between the negative and positive mean strain data.

This influence of mean strain/stress on the fatigue life can be explained in Fig. 7.27, which shows the sign and relative magnitude of mean stress at the approximate half-life. The difference in fatigue life for the same strain amplitude can be attributed to the mean stress. Compressive mean stresses cause longer lives than zero or tensile mean stresses, as shown in Fig. 7.27. The mean stress with a

magnitude less than 5 percent of the yield strength of high strength pressure vessel steel ASTM A723 was defined as essentially zero mean stress. Mean stress relaxation shown in higher strain amplitudes causes no difference in fatigue life, regardless of the sign or magnitude of mean strain. The larger the magnitude of mean stress, the greater the difference in the fatigue life of the same strain amplitude, as shown in Fig. 7.27(b). In other words, mean strain with zero mean stress did not significantly affect the fatigue life, while mean strain with considerable mean stress did affect the fatigue life significantly. Mean strain did not affect the fatigue life if it did not accompany the mean stress. Therefore, the mean stress can be considered as a major important factor in the fatigue life. Tensile mean stress at longer lives was detrimental to the fatigue life, while the compressive mean stress at longer lives was beneficial.

To account for the mean stress effects on the fatigue life, several early investigations using the stress-based high cycle fatigue data were made by Gerber and Goodman [46]. Later Morrow [76] introduced the mean stress into the Basquin equation [88], suggesting that the mean stress effect could be taken into account by modifying the elastic term in the conventional strain-life Eq.(7.6) by the mean stress σ_m

$$\frac{\Delta\varepsilon}{2} = \frac{\sigma_f'-\sigma_m}{E} (2N_f)^b + \varepsilon_f'(2N_f)^c \tag{7.8}$$

If only the elastic term is considered,

$$\sigma_a = (\sigma_f'-\sigma_m) (2N_f)^b \tag{7.9}$$

Morrow's Eq.(7.8) implies that the mean stress has influence only on the elastic strain-life relationship. It is quite interesting that in Fig. 7.27 this mean stress influence can be clearly seen in longer lives where the elastic strain-life is the major contributing part of the total strain-life. As shown in Table 7.1, a relatively small amount of plastic strain was observed in longer lives of strain amplitudes equal to or lower than 0.005.

For a fixed value of σ_m, Eq.(7.9) represents a straight line on a log-log plot parallel to the line $\sigma_m = 0$. Rearranging Eq.(7.9),

$$2N_f = \left(\frac{\sigma_a}{\sigma_f' - \sigma_m}\right)^{1/b} \tag{7.10}$$

Eq.(7.10) can be used to derive a useful form by introducing σ_{cr} [76], the equivalent completely reversed stress amplitude for a given life $2N_f$.

$$2N_f = \left(\frac{\sigma_a}{\sigma_f' - \sigma_m}\right)^{1/b} = \left(\frac{\sigma_{cr}}{\sigma_f'}\right)^{1/b} \tag{7.11}$$

Therefore,

$$\sigma_{cr} = \sigma_f' \left(\frac{\sigma_a}{\sigma_f' - \sigma_m}\right) \tag{7.12}$$

$$\frac{\sigma_a}{\sigma_{cr}} + \frac{\sigma_m}{\sigma_f'} = 1 \tag{7.13}$$

where σ_a and σ_m are stress amplitude and mean stress, respectively. The value of σ_f' is the intercept at $2N_f = 1$ on a log-log plot of σ_a versus $2N_f$ from $R = -1$ testing, i.e., completely reversed fatigue testing. Eq.(7.13) is similar in form to the modified Goodman relation. It represents the equation of a line in σ_a versus σ_m plot whose

intercepts of the vertical and horizontal axes are σ_f' and σ_{cr}, respectively. If the values of σ_f', σ_m and σ_a are given for a mean stress test, σ_{cr} can be easily calculated from Eq.(7.13), and its fatigue life is the same as the fatigue life of the completely reversed test, R=-1, with the stress amplitude of σ_{cr}. Therefore, fatigue life with mean stress can be estimated from the conventional σ_a-$2N_f$ curve of completely reversed fatigue testing.

Reasonably close agreement of SAE 1045 steel with the prediction based on (7.10) was shown by Landgraf [89]. Correlation between the test result of this ASTM A723 steel and the prediction using an elastic strain part in the Morrow's parameter given as Eq.(7.10) is shown in Fig. 7.28. This parameter does not show a satisfactory correlation. This is attributed to the same fact of the nonlinearity of log-log linear elastic strain-life of the completely reversed tests. It did not appear proper to estimate the efficiency of the Morrow's parameter for mean stress effect by just using one elastic term of Morrow's equation.

Comparison of fatigue lives using Morrow's equation (7.8) with actual fatigue lives is shown in Fig. 7.29. Actual fatigue life for a strain amplitude was taken directly from the fatigue testing. The fatigue life predicted by Morrow's equation for a given strain amplitude was obtained by solving the nonlinear equation (7.8) using a measured mean stress at approximate half-life and the known low cycle fatigue properties determined from R=-1 testing given in Table 7.3. Averaged Young's modulus E_3 was used for calculation. Fairly

good correlation between actual life and predicted life can be seen, even though Morrow's equation seems to overestimate the fatigue lives in the longer life region at 10^5 reversals and to underestimate the fatigue lives between 5×10^2 and 2×10^4 reversals. Scatter in Fig. 7.29 appears to be less than a factor of ± 2. Nonconservatism of Morrow's equation at both shorter and longer life regions can be seen in Fig. 7.29. Similar phenomenon is shown in Fig. 7.28. Since the plastic strain-life dominated the shorter fatigue life, nonlinearity at the shorter life region caused mainly by the elastic strain-life looks less significant in Fig. 7.29 than in Fig. 7.28.

The elastic and plastic strain amplitudes at approximate half-lives versus reversals-to-failure for all strain ratios are shown in Figs. 7.30-7.31. Elastic strain-lives in Fig. 7.30 are significantly influenced by the mean stress, but the Manson-Coffin relationship in Fig. 7.31 represented by the plastic strain-life of the completely reversed strain-controlled test is not affected by the mean stress, confirming Morrow's proposal. On the other hand, Lorenzo and Laird [82], using data from Pokluda and Stanek [90], showed that the Manson-Coffin plot in stress-controlled cyclic creep tests exhibited considerable scatter and a tendency for lives in cyclic creep to fall below those under zero mean stress.

The most popular and promising parameter that accounts for the effects of mean stress was proposed by Smith, Watson, and Topper [78]. The SWT mean stress parameter has the form

$$\sqrt{\sigma_{max}\varepsilon_a E} = f(2N_f) \tag{7.14}$$

where σ_{max} is the maximum stress at the half-life of each test. This stress-strain function can be derived by manipulation of the basic low cycle fatigue equations

$$\varepsilon_a = \frac{\sigma_f'}{E} (2N_f)^b + \varepsilon_f'(2N_f)^c \qquad (7.6)$$

$$\sigma_a = \sigma_f'(2N_f)^b \qquad (7.15)$$

According to SWT, $\sigma_a\varepsilon_a$ for a completely reversed test is equal to $\sigma_{max}\varepsilon_a$ for a mean stress test at a given life

$$\sigma_{max}\varepsilon_a = \sigma_f'(2N_f)^b \left[\frac{\sigma_f'}{E}(2N_f)^b + \varepsilon_f'(2N_f)^c \right] \qquad (7.16)$$

$$= \frac{(\sigma_f')^2}{E} (2N_f)^{2b} + \sigma_f'\varepsilon_f'(2N_f)^{b+c} \qquad (7.17)$$

$$= A(N_f)^\alpha + B(N_f)^\beta \qquad (7.18)$$

A satisfactory correlation of mean strain data from the strain-controlled tests was obtained using the SWT parameter by many authors [77, 79, 91-92]. Using the SWT parameter, a single graphical representation of both load and strain-controlled fatigue tests from the grey cast iron was found by Fash and Socie [91].

Plots of SWT parameter versus number of reversals-to-failure for each different strain ratio are shown in Fig. 7.32. A single function governing the fatigue life under mean stress in the finite regime less than 10^6 reversals-to-failure can be obtained from Eq.(7.16), and the low cycle fatigue properties of a completely reversed test are given in Table 7.3,

$$\sigma_{max}\varepsilon_a = \frac{(\sigma_f')^2}{E_3}(2N_f)^{2b} + \sigma_f'\varepsilon_f'(2N_f)^{b+c}$$

$$= 161(2N_f)^{-0.220} + 1037(2N_f)^{-0.893} \qquad (7.19)$$

This log-log bilinear model did not seem to represent the good correlation as shown in Fig. 7.33. Instead of the log-log bilinear equation, a log-log linear model was employed. Linear regression analysis of the SWT model using R=-1 data resulted in the equation

$$\sigma_{max}\varepsilon_a = C(2N_f)^{\gamma} \qquad (7.20)$$

$$= 117(2N_f)^{-0.369} \qquad (7.21)$$

This linear model of Eq.(7.21) was plotted in Fig. 7.33, compared to the bilinear model of Eq.(7.19) from R=-1 low cycle fatigue properties. Very nice correlation between SWT parameter versus reversals-to-failure in the linear model can be seen, regardless of the completely reversed test data and mean strain test data, resulting in a single line, as shown in Fig. 7.33. The values of coefficients and exponents for each strain ratio and all strain data from all strain ratios calculated using Eq.(7.20) are given in Table 7.5. These values are used to plot the lines in Fig. 7.32. Reversals-to-failure calculated using the SWT parameter from test data at approximate half-life were compared to the reversals-to-failure determined in experiment. All data fell nicely into the scatter with a factor of ±2. Better correlation can be observed in the SWT parameter than in Morrow's parameter, as shown in Figs. 7.34 and 7.29, respectively. Fig. 7.35 shows the plots of SWT versus reversals-to-failure with the sign and magnitude of mean stress from all tests where all data points fall

into a single line regardless of the mean stresses. In Fig. 7.35, mean stress of magnitude less than 5 percent of yield strength was considered as essentially zero mean stress.

Lorenzo and Laird [82] proposed a modified low cycle fatigue stress-strain parameter based on the SWT parameter to deal with mean stress effects. It was assumed that the same fatigue life would be observed if $\sigma_a \Delta \varepsilon_p/2$ from the completely reversed test were equal to $\sigma_{max} \varepsilon_{ap}$ from the mean stress test, where ε_{ap} is the plastic strain amplitude at the approximate half-life associated with the mean stress test. Therefore, a relationship can be written for a given life N_f as

$$\sigma_a (\Delta \varepsilon_p/2) = \sigma_{max} \varepsilon_{ap} = \text{constant} \qquad (7.22)$$

As seen in Eq.(7.22), this parameter is only applicable where plastic strain amplitude exists. The parameter proposed by Lorenzo and Laird versus number of reversals-to-failure is plotted in Fig. 7.36. Similar to the SWT parameter, the completely reversed and mean strain data can be collapsed to a single scatter band within a fatigue life of finite regime less than 10^6 reversals-to-failure. The log-log linear regression analysis was done using the total 21 test data points of $\Delta \varepsilon/2 \geq 0.005$, and is given as

$$\sigma_{max} \varepsilon_{ap} = 1061(2N_f)^{-0.898} \qquad (7.23)$$

The exponent and coefficient in Eq.(7.23) determined from the linear regression analysis using only R=-1 data were -0.825, and 673 MPa, respectively. Two lines determined from total and R=-1 data in Fig.

7.36 look similar in the finite region of 10^2 to 10^4 reversals-to-failure.

In this chapter the strain-controlled low cycle fatigue testing procedure was described in detail and test results were analyzed to find the low cycle fatigue behavior under the mean stress. The fatigue lives of strain-controlled low cycle fatigue tests with nonzero mean strains were significantly influenced by the mean stresses. Several mean stress parameters such as Morrow's equation, the SWT parameter, and the Lorenzo-Laird parameter were introduced to account for the effect of mean stress on the low cycle fatigue life. The SWT log-log linear parameter appeared to provide a better correlation than the Morrow's parameter or Lorenzo-Laird parameter in the finite life region less than 10^6 reversals, and it will be recommended for the fatigue life estimation of thick-walled pressure vessels with an external groove.

CHAPTER VIII

LIFE ESTIMATION OF THE AUTOFRETTAGED THICK-WALLED PRESSURE VESSEL WITH AN EXTERNAL GROOVE

8.1 Introduction

A fatigue life estimation method based on a local strain approach is considered in this chapter. The local strain approach is a method to access the crack formation life of a component that has a critical region such as a groove and notch where fatigue cracks are formed at the roots eventually due to local high strain, while the majority of the part is elastically strained by the cyclic loading. Therefore, the fatigue life of a notched component can be related to the fatigue life of small unnotched specimen that is cycled to the same strain as the material at the notch root. The local strain approach is based on three fundamentals: load-notch strain relation, cyclic stress-strain relation, and fatigue damage evaluation. The load-notch strain and cyclic stress-strain relation are used to determine the local strain history of a component subjected to an arbitrary load history.

In this chapter, the fatigue life of the autofrettaged thick-walled pressure vessel with an external groove subjected to internal pressure will be estimated by using the local strain approach. Several methods of determining the load-notch strain relation are used: experimental tests, the finite element method, and an

approximation formula. Among these, an approximation formula of linear and Neuber's rule [46, 93-94] will be used. A cyclic stress-strain relation and fatigue damage model such as SWT and Morrow's models, which were determined previously from the strain-controlled low cycle fatigue tests reported in chapter 7, will be employed to estimate the fatigue life of the autofrettaged thick-walled pressure vessel with an external groove.

8.2 Local Strain Approach

Analyses by Stowell [95] and Neuber [93] were done to describe the nonlinear stress-strain behavior of notches. Their work has been applied to fatigue problems of notched components by numerous investigators [96-99], who tried to relate the cyclic load on a notched component to the actual stress and strain at the notch root and then estimate the fatigue life of the notched component from stress-life or strain-life curves obtained from smooth specimen tests.

Two different approaches, namely, linear and Neuber's rules, to determine the local stress and strain were considered in this research. In the linear rule, the strain concentration factor is assumed to be the same as the theoretical stress concentration factor, K_t, and given as

$$\frac{\varepsilon}{e} = K_\varepsilon = K_t \tag{8.1}$$

The local strain can be directly calculated, and local stress is then obtained from the local strain and cyclic stress-strain curve, given as

$$\varepsilon = \frac{\sigma}{E} + \left(\frac{\sigma}{K}\right)^{1/n'} \qquad (8.2)$$

where σ, ε and S, e are local stress, local strain and nominal stress, and nominal strain, respectively. The equation proposed by Neuber is

$$K_t = (K_\sigma K_\varepsilon)^{1/2}$$

$$\text{where} \quad K_\sigma = \frac{\sigma}{s}, \quad K_\varepsilon = \frac{\varepsilon}{e} \qquad (8.3)$$

This rule means that the theoretical stress concentration factor, K_t, is equal to the geometric mean of the actual stress concentration factor, K_σ, and the strain concentration factor, K_ε. Since it has been known that sharp notches have less effect in fatigue than indicated by K_t, a fatigue notch factor, K_f, is used instead of K_t when dealing with fatigue problems.

The fatigue notch factor can be determined by taking the ratio of fatigue strength of the smooth specimen to the fatigue strength of the notched specimen at a given life level.

$$K_f = \frac{S_{smooth}}{S_{notched}} \qquad (8.4)$$

and often a notch sensitivity index is defined as

$$q = \frac{K_f - 1}{K_t - 1} \qquad (8.5)$$

which varies from 0 to 1, depending on no notch effect or full theoretical effect. It is known that the value of q is dependent on material and the notch root radius. Many attempts have been made

to determine the values of K_f analytically. Neuber [51] proposed the following equation:

$$K_f = 1 + \frac{K_t - 1}{1 + \sqrt{a/r}} \qquad (8.6)$$

where a is the material constant and r is the notch root radius. Another approximate formula by Peterson [45] is

$$K_f = 1 + \frac{K_t - 1}{1 + p/r} \qquad (8.7)$$

where p is the material constant determined from long-life fatigue data for notched and unnotched specimens, given in the following form:

$$p = 0.00254 \left(\frac{2068 \ MPa}{\sigma_u}\right)^{1.8} mm \qquad (8.8)$$

The fatigue notch factor, K_f, by Peterson in Eq(8.7), which is assumed to be constant for a given material and geometry, is employed in applying Neuber's rule to account for local plasticity action in this research. Therefore, Neuber's rule in Eq(8.3) can be rewritten in terms of stress and strain ranges

$$\Delta\sigma \ \Delta\varepsilon = K_f^2 \ \Delta S \ \Delta e \qquad (8.9)$$

If the nominal stress and strain are limited to the elastic region, Eq(8.9) can be reduced to

$$\Delta\sigma \ \Delta\varepsilon = \frac{(K_f \ \Delta S)^2}{E} \qquad (8.10)$$

The above equation relates the nominal stress-strain behavior of a notched component to the actual stress-strain behavior at the critical location.

Fig. 8.1 shows the method to determine local stresses and strains using the Neuber parabola given in Eq(8.10) and the cyclic stress-strain curve in Eq.(8.2) for a given nominal stress-time sequence [100-101]. Rewriting Eq(8.2) in terms of stress and strain ranges,

$$\frac{\Delta\varepsilon}{2} = \frac{\Delta\sigma}{2E} + \left(\frac{\Delta\sigma}{2K'}\right)^{1/n'} \tag{8.11}$$

Since two nonlinear equations of Eq(8.10) and (8.11) are given, the two unknowns of $\Delta\sigma$, and $\Delta\varepsilon$ can be determined by using numerical iteration techniques such as the Newton-Raphson or secant methods. From Eqs.(8.10) and (8.11), the following equation can be obtained:

$$\frac{(K_f \Delta S)^2}{4E} = \frac{(\Delta\sigma)^2}{4E} + \frac{\Delta\sigma}{2}\left(\frac{\Delta\sigma}{2K'}\right)^{1/n'} \tag{8.12}$$

It is important to note that in Fig. 8.1, the line from point 0 to a represents the cyclic stress-strain curve, and that the lines from point a to b and b to c represent the hysteresis loop that is equal to two times the cyclic stress-strain curve [97]. Mean stress, σ_m, was then calculated from σ_{max} and σ_{min} determined from Eqs.(8.10) and (8.11) using $\sigma_m = (\sigma_{max} + \sigma_{min})/2$. In Fig. 8.1, σ_0 indicates the residual stress existing before the load is applied.

Local stresses and strains using both linear and Neuber's rule were obtained at the three different types of external grooves in the

thick-walled pressure vessels and simulation specimens. These are conventional, changed, and shot peened-changed grooves as used in the simulation fatigue tests. However, simulation loads were determined without considering the compressive residual stresses existing in the simulation specimens. For this reason, the local stresses and strains in the simulation specimens were evaluated again including the initial residual stresses at the groove roots as determined from X-ray analysis results. It should be noted that the autofrettaged residual stresses are already included in the simulation fatigue loading. To account for the residual stresses measured by X-ray diffraction analysis, denoted as σ_0, in the specimen when estimating local stress and strain, the residual stress was superimposed in the case of linear rule,

$$\Delta\varepsilon = \frac{(K_t\Delta S + \sigma_0)}{E} \qquad (8.13)$$

and in the case of Neuber's rule from Lawrence et al. [102],

$$\Delta\sigma \, \Delta\varepsilon = \frac{(K_f\Delta S + \sigma_0)^2}{E} \qquad (8.14)$$

The nominal stress term in the Neuber's parabola of Eq.(8.10) was modified to Eq.(8.14) by introducing the residual stress σ_0, thus accounting for the residual stress effect in the calculation of local stress and strain.

The local strains and stresses determined by using linear and Neuber's rules are listed in Tables 8.1 through 8.10. In Tables 8.1 and 8.2, theoretical elastic stresses were determined by linear elastic

finite element stress analysis. The maximum and minimum nominal stress, denoted as Smax and Smin, includes the nominal stresses due to internal pressure plus autofrettage loading and autofrettage loading only, respectively. These nominal stresses due to internal pressure and autofrettage loadings are given by Eqs.(3.33) and (3.34), respectively. The theoretical stress concentration factor, K_t, was obtained by dividing the maximum theoretical elastic stress by the maximum nominal stress. The fatigue notch factor, K_f, was based on the Peterson's equation given in Eq.(8.7). For the changed grooves, K_f was essentially the same as K_t, as shown in Table 8.2, due to the large root radius in the changed groove. The elliptic root radius is a variable and a realistic value in the crack growth region was approximately 8 mm. In Table 8.1, ε_{max} is the maximum local strain determined from the linear or Neuber's rule, which corresponds to σ_{max}, given as points a or c in Fig. 8.1 for the case of Neuber's rule, and $\Delta\varepsilon/2$ was obtained from the previously determined values of ε_{max} and ε_{min} from the linear or Neuber's rule.

Induced residual stress, σ_0, at each type of external groove in the simulation fatigue specimen is given in Table 8.5, where σ_0 in the changed and shot peened groove specimens was averaged from the residual stress of 0.010 to 0.125 mm in depth obtained by X-ray diffraction analysis, as shown in Fig. 5.4, and Table 5.2. Because the residual stresses at the conventional external groove of the simulation specimen were not measured, the same value as the changed groove was assumed. Since the residual stresses, σ_0,

resulted from the shot peening operation or from the remaining residual stresses in the simulation specimen after saw-cut of the autofrettaged thick-walled pressure vessel, the local stress and strain in the thick-walled pressure vessel with a conventional and changed groove as given in Tables 8.1 and 8.2, did not have to account for these residual stresses. In the shot peened-changed groove of the thick-walled pressure vessel, the residual stresses due to shot peening were included for the calculation of local stress and strain, as shown in Table 8.3.

To estimate the fatigue life of the autofrettaged thick-walled pressure vessel, including the simulation specimen, two mean stress parameters determined in the low cycle fatigue tests were used. These are SWT parameter [78] and Morrow's parameter [76]. The strain-life and Lorenzo-Laird models mentioned in Chapter 7 will not be used for fatigue life estimation since the strain-life model determined from 5 different strain ratios could not differentiate many strain ratios obtained from the linear or Neuber's rule, as shown in Tables 8.1-8.10, and the Lorenzo-Laird model could not be applied to the case of zero local plastic strain amplitude. The log-log linear SWT model was given in Eq.(7.20) as

$$\sigma_{max} \, \varepsilon_a = C(2N_f)^{\gamma} \qquad (7.20)$$

Fatigue life, $2N_f$, can be directly computed from σ_{max} and ε_a determined from the linear or Neuber's rules. The coefficient, C, of 105 MPa and exponent, γ, of -0.352 determined from linear regression using all low cycle fatigue test data were used for fatigue

life estimation in this chapter. Morrow's model was given in Eq.(7.8) as

$$\frac{\Delta\varepsilon}{2} = \frac{(\sigma_f'-\sigma_m)}{E} (2N_f)^b + \varepsilon_f'(2N_f)^c \qquad (7.8)$$

Therefore, fatigue life, $2N_f$, can be evaluated for a given $\Delta\varepsilon/2$ and σ_m, and low cycle fatigue properties by solving the nonlinear equation (7.8) using numerical iteration techniques. The mean stress, σ_m, included the residual stresses, σ_o, if they existed. Fatigue lives of the thick-walled pressure vessels and simulation specimens using the SWT and Morrow's parameters are shown in Tables 8.11 and 8.12, respectively.

8.3 Results and Discussion

Local strains and stresses at the conventional, changed, and shot peened changed groove of the thick-walled pressure vessel for each overstrain level are given in Tables 8.1 through 8.3. The linear rule predicted smaller local strain and stress than the Neuber's rule. However, local strain amplitudes were similar. These similar local strain amplitudes from both linear and Neuber's rules can be attributed to the essentially elastic cyclic loading and unloading behavior caused by the pulsating internal pressure. For both linear and Neuber's rules, an almost 50 percent decrease in local maximum stress and strain amplitude at the changed groove root of the thick-walled pressure vessel can be observed, compared to the conventional groove, from Tables 8.1 and 8.2. Due to the compressive residual stresses by shot peening, the maximum local

strains at the shot peened-changed groove dropped by 25 to 50 percent, compared to the changed groove, depending upon the percent overstrain and local strain calculation rule used. However, local strain amplitudes for both changed and shot peened-changed grooves were the same from Tables 8.2 and 8.3. Small differences in maximum local stresses between different types of groove and different percent overstrain levels can be explained from the small changes of stress in the cyclic stress-strain curve beyond the strain of 0.02, as shown in Fig. 7.19.

Lower local mean stress σ_m was obtained in the linear rule than in the Neuber's rule due to higher σ_{max} from the Neuber's rule. Differences in mean stress between the linear and Neuber's rules were larger in the conventional groove than in the changed or shot peened changed groove. Due to similar σ_{max} and smaller $\Delta\sigma/2$, mean stresses σ_m at the changed groove were much higher for any percent overstrain level than at the conventional groove, as shown in Tables 8.1 and 8.2. The high mean stresses in the changed groove were reduced by 10 to 40 percent by shot peening, from Tables 8.2 and 8.3. A larger decrease in σ_m was observed in the lower percent overstrain case.

Local strains and stresses of the conventional and changed grooves of simulation specimens without induced residual stresses at the groove surfaces are shown in Tables 8.6 and 8.8, respectively, resulting in essentially the same local strain and stress results as the thick-walled pressure vessel as given in Table 8.1 and 8.2. This is

attributed to the fact that the simulation loads, which caused the local strains and stresses, were determined from the stresses near the groove roots in order to simulate the stresses at both groove roots as closely as possible.

In order to account for residual stresses in the groove roots, local stress and strain were computed by including the residual stresses, and are given in Tables 8.7 and 8.9. From Tables 8.6 and 8.7, a 5 to 10 percent decrease in σ_{max} and a 25 to 70 percent decrease in σ_m in the conventional groove with induced residual stresses, compared to the conventional groove without residual stresses, were found. A similar decrease of σ_{max} and 10 to 30 percent decrease in σ_m were found in the changed groove with induced residual stresses, compared to the changed groove without residual stresses. Higher mean stresses were noticed in the changed groove than in the conventional groove due to the smaller local strain amplitude in the changed groove. Essentially the same stress and strain resulted in the shot peened-changed groove specimen as the thick-walled pressure vessel with shot peened-changed groove, as given in Tables 8.3 and 8.10, respectively.

Based on local strains and local stresses using linear and Neuber's rules, fatigue life estimation of the thick-walled pressure vessel was made. In Chapter 7, several models to evaluate the fatigue life were mentioned. These are strain-life, SWT, Morrow, and Lorenzo-Laird models. The strain-life model as shown in Fig. 7.26 was determined from the low cycle fatigue tests with 5 different

strain ratios. However, this was difficult to employ in life estimation since the local strain calculations resulted in various strain ratios and the strain-life curves for strain ratios with $R_\varepsilon \le 0$ were too similar to differentiate them. The Lorenzo-Laird model as shown in Fig. 7.36 describes the fatigue life in terms of $\sigma_{max}\,\varepsilon_{ap}$, where σ_{max} is the true maximum stress and ε_{ap} is the true plastic strain amplitude. However the local plastic strain amplitude calculated by using the local strain amplitude, local maximum stress, local mean stress, and equation of

$$\frac{\Delta\varepsilon_p}{2} = \frac{\Delta\varepsilon}{2} - \frac{\Delta\sigma}{2E}$$
$$= \frac{\Delta\varepsilon}{2} - \frac{(\sigma_{max}-\sigma_m)}{2E} \qquad (8.15)$$

showed plastic strain amplitude of 10^{-4} or less, which is very small and not a confident value. From these reasons, two models from the strain-life and Lorenzo-Laird were not used for fatigue life estimation of thick-walled pressure vessel and simulation specimens.

Life estimations of thick-walled pressure vessels and simulation fatigue specimens with different types of external grooves by using SWT and Morrow's parameters are given in Tables 8.11 and 8.12, respectively. The fatigue life that accounts for induced residual stresses in the specimens measured by X-ray diffraction analysis was included. Estimated fatigue lives determined by SWT parameter using local stress/strain from Neuber's rule were 40 percent, 15 to 20 percent, and 10 to 20 percent shorter than those using linear rule in the conventional, changed, and shot peened-changed grooves,

respectively, for both the thick-walled pressure and simulation specimens from Table 8.11 and 8.12, thus resulting in a more conservative life estimation.

The estimated fatigue lives using SWT parameter versus experimental fatigue lives are plotted in Figs. 8.2 to 8.4, where lines indicate the life estimation factors of 2 and 4. The average fatigue life, as defined by the cycles to 2.5-mm crack length, determined by simulation fatigue tests and given in Table 6.8 for each percent overstrain and type of groove, was used as the experimental fatigue life. Therefore, three data points from three different overstrain or simulation load levels for each type of groove using linear or Neuber's rule are shown. The estimated fatigue lives of thick-walled pressure vessels and simulation specimens without considering residual stresses were essentially the same, since the same stresses at both groove roots were simulated. Life estimation factors of 2 to 4 can be observed in Figs. 8.2 and 8.3, where conservative fatigue life estimations by the Neuber's rule are seen compared to the linear rule. A large difference in the fatigue life of conventional groove between estimations and experiments can be noticed in Figs. 8.2 and 8.3. This was attributed to the large percentage of crack growth life to 2.5-mm crack length in the fatigue life, compared to other types of groove, as mentioned in chapter 6. For example, crack growth life from 1.0-mm to 2.5-mm crack length in the conventional groove was 15 to 30 percent of the fatigue life to 2.5-mm crack length, compared to 2 to 10 percent in the changed and shot peened-changed grooves.

In other words, the difference between small fatigue crack formation life and fatigue crack to 2.5-mm crack length appeared to be larger in the case of the conventional groove compared with other types of groove. In the 100 and 75 percent overstrain cases from Table 8.11, both the changed and shot peened-changed grooves showed 7 to 12 times longer estimated fatigue lives than the conventional groove, depending on the local strain calculation methods used. Life estimation based on the Neuber's rule showed larger difference in fatigue lives between the conventional and changed or shot peened-changed grooves. Significant differences in the estimated fatigue lives were obtained for the 50 percent overstrain case, where the changed and shot peened-changed grooves showed 8 to 20 times longer fatigue lives than the conventional grooves, depending on the local strain calculation methods used.

By including the residual stresses in the groove roots of specimens, a slightly better correlation with the experimental fatigue life can be obtained, as shown in Fig. 8.4. A slight change in fatigue life by including the compressive residual stresses of approximately 500 to 600 MPa in the simulation specimens can be attributed to the fact that the addition of residual stresses caused only small changes in σ_{max} and almost similar strain amplitudes, especially in higher percent overstrain or higher simulation load levels, resulting in small changes of SWT parameter $\sigma_{max}\varepsilon_a$. Also, conservative fatigue life estimation of the shot peened-changed groove can be seen in Figs. 8.2 and 8.4, resulting in scatter with a factor of 3.

Estimated fatigue lives using the Morrow's parameter are given in Table 8.12, showing basically similar behavior between linear and Neuber's rules to the fatigue lives estimated using the SWT parameter. Estimated fatigue lives versus experimental fatigue lives from the simulation fatigue tests are shown in Figs. 8.5 to 8.7, resulting in similar trends to the results from the SWT parameter. A small difference between estimated and experimental lives was obtained by taking the residual stresses into consideration.

Life estimation of the autofrettaged thick-walled pressure vessel with an external groove was made by integrating the linear elastic finite element stress analysis, and the fatigue properties of the material determined from the low cycle fatigue tests including mean stress effects, and a local strain approach. Fatigue life estimations of autofrettaged thick-walled pressure vessels and simulation specimens by both SWT and Morrow's parameters using the local stresses and strains determined from the linear and Neuber's rules showed quite satisfactory correlation with the simulation fatigue life results. For both the SWT and Morrow's parameters, the estimated fatigue lives of the changed and shot peened-changed grooves were approximately 7 to 20 times longer than the conventional groove. A life estimation factor of 2 to 4 was observed in the conventional groove and a factor of less than 2 was observed in the changed and shot peened-changed grooves, compared to the experimental fatigue lives determined from the simulation fatigue tests.

CHAPTER IX
SUMMARY/CONCLUSIONS AND RECOMMENDATIONS

9.1 Summary/Conclusions

In order to improve fatigue life of the autofrettaged thick-walled pressure vessel with an external groove subjected to internal pressure of 386 MPa, several approaches were considered and simulation fatigue tests were conducted to compare the fatigue lives to the conventional autofrettaged thick-walled pressure vessel. The low cycle fatigue behavior of the autofrettaged thick-walled pressure vessel material was investigated through a series of low cycle fatigue tests including mean stress effects and these results were used for the life estimations.

The stress analysis of the autofrettaged thick-walled pressure vessel with a conventional external groove was done by using a linear elastic finite element analysis. A thermal loading analogy was introduced to simulate autofrettage residual stress distributions along with the finite element methods. Due to the sharp root radius of 1.5 mm in the conventional external groove, very high theoretical stress concentration factors, K_t, were found, resulting in K_t of 3.9 for the internal pressure loading and 4.7, 4.0, and 4.0 for the 100, 75, and 50 percent overstrain loadings, respectively. The local high stresses at the sharp root radius of the conventional groove were

mitigated by changing the shape of groove root using a quasi-optimization technique. The final shape of the elliptic stress relief groove reduced the theoretical stress concentration factor, K_t, by a factor of 2, compared to the conventional groove, regardless of loading conditions and percent overstrain levels.

Compressive residual stresses by peening with cast steel shot were induced at the vulnerable surface of the changed groove root region of the simulation specimen in order to alleviate high tensile stresses in that region due to the autofrettage and internal pressure loadings. The magnitude of the residual stress at the groove root by shot peening was measured to a depth of approximately 0.8 mm using X-ray diffraction analysis. The resulting average compressive residual stress was 594 MPa. An average compressive residual stress of 517 MPa in the as-machined changed groove of the simulation specimen was also determined by X-ray analysis. However, the residual stress remaining in the simulation specimen after the saw-cut of a ring taken from a fully autofrettaged, i.e., 100 percent overstrained, thick-walled pressure vessel should be theoretically about zero due to the equivalence of stress fields between autofrettage residual stress and bending of curved beams due to the relieving moment. The compressive residual stress at the groove of the simulation specimen with an as-machined changed groove was explained by the metal forming process prior to the autofrettage process.

Simulation fatigue tests using specimens with the conventional, changed, and shot peened-changed grooves were performed by controlling loads determined from the finite element analysis for each percent overstrain level. The fatigue life, defined as the cycles to 2.5 mm-crack length, increased by 3 to 5 times for the changed groove and 3 to 13 times for the shot peened-changed groove, compared to the conventional groove. Similar fatigue lives in 100 and 75 percent overstrain levels for both the changed and shot peened-changed grooves were observed. However, a significant increase in fatigue life of the shot peened-changed groove for 50 percent overstrain level indicated influences of the low stress level and the better surface finish in the shot peened groove than in the as-machined groove, under the similar magnitudes compressive residual stresses existing in both types of groove surfaces determined by the X-ray analysis.

Mean stress effects on the low cycle fatigue behavior were investigated using the strain-controlled low cycle fatigue tests of smooth axial specimens taken from an autofrettaged thick-walled pressure vessel. Five different strain ratios were chosen to account for compressive, zero, and tensile mean stresses. For the low cycle fatigue tests with strain amplitudes less than approximately 0.005, essentially linear hysteresis loops, i.e., negligible plastic strain amplitudes in the hysteresis loops, were found, and noticeable mean stress relaxation was not seen even in the high strain ratio of $R=0.75$. However, for the low cycle fatigue tests with strain amplitudes

greater than or equal to about 0.005, plastic strains were observed in the hysteresis loops and significant mean stress relaxation was noticed, especially at the beginning stage of the low cycle fatigue tests. The larger the strain amplitude, the larger the plastic strains in the hysteresis loops and the more significant mean stress relaxation. This indicated the strong influence of the plastic strain amplitude on the mean stress relaxation. A longer fatigue life was obtained with the strain ratio of R=-2 than with R≥-1 for a given strain amplitude below 0.005 due to the compressive mean stress. Only small differences in fatigue lives with R≥0 were observed for a given strain amplitude.

Mean stress parameters from SWT, Morrow, and Lorenzo-Laird were used to adequately account for the effects of mean stress on the low cycle fatigue life. Each mean stress parameter reduced the low cycle fatigue data with various mean stress and mean strains into a single function, enabling one to predict fatigue life of a component with nonzero mean stress from the completely reversed low cycle fatigue data. All mean stress parameters showed quite good correlations with the data.

Fractographic analysis of fractured surface samples from the simulation and low cycle fatigue specimens using a scanning electron microscope enhanced the understanding of crack formation, growth, and final fracture behavior. Approximately 10 to 20 microcrack formation sites from the machined or shot peened external groove of the simulation specimens were found. The initiated cracks coalesced

and grew in a transgranular manner, resulting in a final ductile mode of failure. The final microscopic fracture appearance consisted mainly of ductile dimples from microvoid coalescence, and inclusions oriented to the metal-forming direction. In the fracture surfaces of the low cycle fatigue test specimens, subsurface defects of inclusions, consisting of aluminum and calcium, were the main source of crack formations. These were clearly noticed at every highly magnified fractograph of fracture samples from the low cycle fatigue tests with low strain amplitudes. Basically the same fracture appearance in the crack growth or final fracture region was observed in both low cycle fatigue and simulation specimens.

Life estimations of the autofrettaged thick-walled pressure vessels, including the simulation specimens, were made by using a local strain approach, which is based on a local strain calculation and a fatigue damage relation. Two extreme cases of approximate methods, namely linear and Neuber's rules, were used to evaluate the local stress and strain at the groove root of the autofrettaged thick-walled pressure vessel. The SWT and Morrow's mean stress parameters determined from the low cycle fatigue tests were then employed to estimate the fatigue life. Larger local stresses and strains were obtained from the Neuber's rule, which led to the conservative fatigue life estimations. Similar estimated fatigue lives for the two mean stress parameters were obtained within factors of 2 to 4, compared to the experimental fatigue lives determined from the simulation fatigue tests. For both the SWT and Morrow's

parameters, the estimated fatigue lives of the changed and shot peened-changed grooves were approximately 7 to 20 times longer than the conventional groove.

9.2 Recommendations

It is recommended to change the shape of the conventional external groove in the autofrettaged thick-walled pressure vessel to the elliptic shape of 4.3 x 6.0-mm width and depth, respectively, in order to reduce the high stress concentration factor at the conventional groove root and increase fatigue life. Other simpler and more practical stress relief groove geometries such as a circular shape can be considered, if the elliptic shape of stress relief groove cannot be introduced due to manufacturing or economic problems.

Compressive residual stress effects by shot peening in the simulation fatigue tests were clouded by the residual stresses existing in the simulation specimens after saw-cut of an autofrettaged pressure vessel. The residual stresses determined by X-ray diffraction analysis indicate the necessity of re-evaluation of residual stress distributions prior to and after the autofrettage process since the residual stresses in the as-received thick-walled pressure vessel will alter the final residual stress distributions after autofrettage.

As noticed in simulation fatigue tests, a 50 percent overstrain level produced the largest increase in the fatigue life, compared to the higher overstrain levels. Therefore the level of overstrain is

recommended to be reduced in the case of the autofrettaged thick-walled pressure vessel with an external groove, and more study is needed to determine the optimum percent overstain level.

REFERENCES

1. Fuchs, H. O., "The Effect of Self-Stresses on High Cycle Fatigue," Journal of Testing and Evaluation, Vol. 10, No. 4, July 1982, pp. 168-173.

2. Gerber, T. L., and Fuchs, H. O., "Improvement in the Fatigue Strength of Notched Bars by Compressive Self-Stresses," in Achievement of High Fatigue Resistance in Metals and Alloys, ASTM STP 467, 1970, pp. 276-295.

3. Gerber, T. L., and Fuchs, H. O., "Analysis of Nonpropagating Fatigue Cracks in Notched Parts with Compressive Mean Stress," Journal of Materials, Vol. 3, No. 2, June 1968, pp. 359-374.

4. Davidson, T. E., and Kendall, D. P.. "The Design of High Pressure Containers and Associated Equipment," The Mechanical Behavior of Materials Under Pressure, Pugh, H. Ll. D., Editor, Elsevier Publishing, Amsterdam, 1970, pp. 54-118.

5. Franklin, G. J., and Morrison, J. L. M., "Autofrettage of Cylinders: Prediction of Pressure/External Expansion Curves and Calculation of Residual Stresses," Proceedings of Institution of Mechanical Engineers, Vol. 174, No. 35, 1960, pp. 947-974.

6. Davidson, T. E., Barton, C. S., Reiner, A. N., and Kendall, D. P., "New Approach to the Autofrettage of High-Strength Cylinders," Experimental Mechanics, Vol. 2, No.2, February 1962, pp. 33-40.

7. Davidson, T. E., Kendall, D. P., and Reiner, A. N., "Residual Stresses in Thick-Walled Cylinders Resulting from Mechanically Induced Overstrain," Experimental Mechanics, Vol. 3, No. 11, November 1963, pp. 253-262.

8.   Sachs, G., and Espey, G.,   "The Measurement of Residual Stresses in Metal," Iron Age, Vol. 148, No. 12, 1941, pp. 63-71.

9.   Davidson, T. E., Eisenstadt, R., and Reiner, A. N.,   "Fatigue Characteristic of Open-End Thick-Walled Cylinders Under Cyclic Internal Pressure," Journal of Basic Engineering, December 1963, pp. 555-565.

10.   Morrison, J. L. M., Crossland, B, and Parry, J. C. S.,   "Strength of Thick Cylinders Subjected to Repeated Internal Pressure," Journal of Engineering for Industry, May 1960, pp. 143-153.

11.   Findley, W. N., and Reed, R. M.,   "Fatigue of Autofrettaged Thick Tubes: Closed and Open Ended; As-Received and Honed," Journal of Engineering Materials and Technology, Vol. 105, July 1983, pp. 105-201.

12.   Kapp, J. A.,   "Predicting Catastrophic Outside Diameter Initiated Failure of Thick-Walled Cylinder Using Low Cycle Data," Material Research Society Symposium Proceedings, Vol. 22, Elsevier Science Publishing   Co., 1984, pp. 243-248.

13.   Kapp, J. A., Greco, V. P., and Abbott, R.T.,   "Simulation Fatigue Testing of an Autofrettaged Cylinder with an Outside Diameter Notch: The Effects of Root Radius and Surface Condition, Part I - Very Low Cycle Applications," Technical Report ARCCB-TR-86022, Benet Weapons Lab, Watervliet, N.Y., June 1986.

14.   Kapp, J. A., and Underwood, J. H.,   'Service-Simulation Tests to Determine the Fatigue Life of Outside-Diameter-Notched Thick-Walled Cylinders," Experimental Mechanics, Vol. 22, No. 3, March 1982, pp. 96-100.

15.   Kapp, J. A., and Pu, S. L.   "Fatigue Design of Thick- alled Cylinders Considering the OD as a Failure Site," Pressure Vessel Design, PVP-57, American Society of Mechanical Engineers, 1982.

16. Brown, B., "155-mm Howitzer Tube M185 Fatigue Test," Technical Report BWL 84-4, Benet Weapons Laboratory, Watervliet, N.Y., June 1984.

17. Hussain, M. A., Pu, S. L., Vasilakis, J. D., and O'Hara, P., "Simulation of Partial Autofrettage by Thermal Loads," Journal of Pressure Vessel Technology, 1980, pp. 314-318.

18. Pu, S. L., and Hussain, M. A., "Residual Stress Redistribution Caused by Notches and Cracks in a Partially Autofrettaged Tube," Journal of Pressure Vessel Technology, Vol. 103, November 1981, pp. 302-306.

19. Almen, J. O., and Black, P. E., Residual Stresses and Fatigue in Metals, McGraw-Hill, N.Y., 1963.

20. Standard A723, "Alloy Steel Forgings for High-Strength Pressure Component Application," 1988 Annual Book of ASTM Standards, Vol. 01.04.

21. Standard E8, "Tension Testing of Metallic Materials," 1988 Annual Book of ASTM Standards, Vol. 03.01.

22. Standard E646, "Tensile Strain-Hardening Exponents of Metallic Sheet Materials," 1988 Annual Book of ASTM Standards, Vol. 03.01.

23. Sachs, G., and Espey, G., "The Measurement of Residual Stresses in Metal," Iron Age, Vol. 148, No. 12, 1941, pp. 63-71.

24. Findley, W. N., and Tracy, J. F., "The Effect of the Intermediate Principal Stress on Triaxial Fatigue of 7075-T6 Aluminum Alloy," Journal of Testing and Evaluation, Vol. 1, No. 5, September 1973, pp. 432-434.

25. Ugural, A. C., and Fenster, S. K., Advanced Strength and Applied Elasticity, Elsevier Publishing Co., N.Y., 1981.

26. Hill, R. Theoretical Theory of Plasticity, Oxford Press, London, 1950.

27. Prager, W., and Hodge, P. C., Theory of Perfectly Plastic Solids, John Wiley and Sons, N.Y., 1951.

28. Johnson, W., and Mellor, P. B., Engineering Plasticity, Van Nostrand Co., London, 1973.

29. Sidebottom, O. M., Chu, S. C., and Lamba, H. S., "Unloading of Thick-Walled Cylinders That Have Been Plastically Deformed," Experimental Mechanics, Vol. 16, No. 12, December 1976, pp. 454-460.

30. Chen, P. C. T., "The Bauschinger and Hardening Effect on Residual Stresses in an Autofrettaged Thick-Walled Cylinder," ASME Paper 84-PVP-113, 1984.

31. Parker, A. P., and Farrow, J. R., "On the equivalence of Axisymmetric Bending, Thermal, and Autofrettage Residual Stress Fields," Journal of Strain Analysis, Vol. 15, No. 1, 1980, pp. 51-52.

32. Timoshenko, S. P., and Goodier, J. N., Theory of Elasticity, McGraw-Hill, N.Y., 1970.

33. Todd, R. H., and Fuchs, H. O., "Self-Stress Concentrations," Experimental Mechanics, Vol. 11, No. 12, December 1971, pp. 548-553.

34. Emery, A. F., Williams, J. A., and Avery, J., "Thermal-Stress Concentration Caused by Structural Discontinuities," Experimental Mechanics, Vol. 9, No. 12, December 1969, pp. 558-564.

35. Kapp, J. A., and Pflegl, G. A., "Stress Analysis of O.D. Notched Thick-Walled Cylinders Subjected to Internal Pressure or Thermal Loads," Journal of Pressure Vessel Technology, Vol. 103, February 1981, pp. 76-84.

36. Pu, S. L., and Hussain, M. A., "Stress Intensity Factor for Radial Cracks in a Partially Autofrettaged Thick-Walled Cylinder," in <u>Fracture Mechanics: Fourteenth Symposium - Vol I: Theory and Analysis</u>, ASTM STP 791, Lewis, J. C., and Sines, G., Editors, 1983, pp. I-194-I-215.

37. Pu, S. L., and Chen, P. C. T., "Stress Intensity Factors for Radial Cracks in a Pre-Stressed, Thick-Walled Cylinder of Strain-Hardening Materials," <u>Journal of Pressure Vessel Technology</u>, Vol. 105, May 1983, pp. 117-123.

38. Kapp, J. A., and Eisenstadt, R., "Crack Growth in Externally Flawed, Autofrettaged Thick-Walled Cylinders and Rings," in <u>Fracture Mechanics</u>, ASTM STP 677, Smith, C. W., Editor, 1979, pp. 736-756.

39. Throop, J. F., Underwood, J. H., and Leger, G. S., "Thermal Relaxation in Autofrettaged Cylinders," in <u>Residual Stress and Stress Relaxation</u>, Edited by Kula, E. and Weiss, V., Sagamore Army Material Research Conference Proceedings, Plenum Press, N.Y., 1982, pp. 205-226.

40. Young, W. B., <u>Residual Stress in Design, Process and Material Selection</u>, Editor, Proceedings of ASM's Conference on Residual Stress-In Design, Process and Material Selection, Cincinnati, Ohio, USA, April 1987.

41. Kula, E., and Weiss, V., <u>Residual Stress and Stress Relaxation</u>, Editors, Sagamore Army Material Research Conference Proceedings, Plenum Press, 1982.

42. Rosenthal, D., "Measurement of Residual Stress," in <u>Residual Stresses in Metals and Metal Construction</u>, Osgood, W. R., Editor, Reinhold Publishing Co., N.Y., 1954.

43. Dally, J. W., and Riley, W. F., <u>Experimental Stress Analysis</u>, McGraw-Hill, N.Y., 1978, pp. 318-328.

44. DeSalvo, G., and Swanson, J. A., <u>ANSYS User's Manual</u>, Swanson Analysis Systems Inc., June 1985.

45. Peterson, R. E., Stress Concentration Factors, John Wiley and Sons, N.Y., 1974.

46. Fuchs, H. O., and Stephens, R. I., Metal Fatigue in Engineering, John Wiley and Sons, New York, 1980.

47. Brown, B., "155 mm Howitzer Tube M185 Fatigue Test," Technical Report BWL 84-4, Benet Weapons Laboratory, Watervliet, N.Y., June 1984.

48. Francavilla, A., Ramakrishnan, C. V., and Zienkiewicz, O. C., "Optimization of Shape to Minimize Stress Concentration," Journal of Strain Analysis, Vol. 10, No. 2, 1975, pp. 63-70.

49. Tvergaard, V., "On the Optimum Shape of Fillet in a Flat Bar with Restrictions," in Optimizations in Structural Design, Edited by Sawczuk, A., and Mroz, M., Springer-Verlag, Berlin, 1975, pp. 181-195.

50. Schnack, E., "An Optimization Procedure for Stress Concentrations by the Finite Element Technique," International Journal for Numerical Methods in Engineering, Vol. 14, 1979, pp. 115-124.

51. Neuber, H., Kerbspannungslehre, Springer-Verlag, Berlin, 1958, Translation Theory of Notch Stress, U.S. Office of Technical Services, 1961.

52. Yang, R. J., and Choi, K. K., "Accuracy of Finite Element Based Shape Design Sensitivity Analysis," Journal of Structural Mechanics, Vol. 12, No. 3, 1985, pp. 223-239.

53. Haug, E. J., Choi, K. K., and Komkov, V., Design Sensitivity Analysis of Structural Systems, Academic Press, Orlando, 1986.

54. Babuska, I., "The Rate of Convergence for the Finite Element Method," Journal on Numerical Analysis, Vol. 8, No. 2, 1971, pp. 304-315.

55. Strang, G., and Fix, G. J., _An Analysis of the Finite Element Method_, Prentice-Hall, Englewood Cliffs, New Jersey, 1973.

56. Krauthammer, T., "Accuracy of the Finite Element Method Near a Curved Boundary," _Computers and Structures_, Vol. 10, pp. 921-929.

57. Atkinson, K. E., _An Introduction to Numerical Analysis_, John Wiley and Sons, New York, 1978.

58. Kohnke, P. E., _ANSYS Theoretical Manual_, Swanson Analysis Systems Inc., Houston, Pennsylvania, 1986.

59. Ramakrishnan, C. V., and Francavilla, A., "Structural Shape Design Optimization Using Penalty Functions," _Journal of Structural Mechanics_, Vol. 3, No. 4, 1975, pp. 403-422.

60. Moe, J., "Penalty-Function Methods," in _Optimum Structural Design_, Edited by Gallagher, R. H., and Zienkiewicz, O. C., John Wiley and Sons, New York, 1973, pp. 143-177.

61. Fiacco, A. V., and McCormick, G. P., _Nonlinear Programming: Sequential Unconstrained Minimization Technique_, John Wiley and Sons, New York, 1968.

62. Fuchs, H. O., "Shot Peening," Chapter 32, in _Mechanical Engineers' Handbook_, Edited by Kutz, M., John Wiley and Sons, New York, 1986.

63. _Manuals on Shot Peening_, J808a, Society of Automotive Engineers, Warrendale, PA, 1967.

64. Standard J442, "Test Strip, Holder and Gage for Shot Peening," _1988 SAE Handbook._, Vol. 1.

65. _Shot Peening of Metal Parts_, MIL-S-13165B, amended 1979.

66. Recommended Practice J444, "Cast Shot and Grit Size Specifications for Peening and Cleaning," 1988 SAE Handbook, Vol. 1.

67. Recommended Practice J827, "Cast Steel Shot," 1988 SAE Handbook, Vol. 1.

68. Heindlhofer, K., Evaluation of Residual Stress, McGraw-Hill. New York, 1948.

69. Noyan, I. C., and Cohen, J. B., Residual Stress, Springer-Verlag, New York, 1987.

70. Koster, P. K., et al., "Surface Integrity of Machined Structural Components," AFML-TR-70-11, March 1970.

71. Koster, P. K., et al., "Manufacturing Methods for Surface Integrity of Machined Structural Components," AFML-TR-71-258, April 1972.

72. Cammett, J. T., Private communication.

73. Stacey, A., and Webster, G. A., "Influence of Residual Stress on Fatigue Crack Growth in Thick-Walled Cylinders," in Analytical and Experimental Methods for Residual Stress Effects in Fatigue, Edited by Champoux, R. L., Underwood, J. H., and Kapp, J. A., ASTM STP 1004, pp. 107-121.

74. Boresi, A. P., and Sidebottom, O. M., Seeley, F. B., and Smith, J. O., Advanced Mechanics of Materials, John Wiley and Sons, New York, 1978.

75. Sailors, R. H., "Fracture Feature Anisotropy in a Martensitic Steel Plate," in Fractography-Microscopic Cracking Processes, ASTM STP 600, 1976, pp. 172-189.

76. Graham, J. A., Ed., Chapter 3 in Fatigue Design Handbook, Vol. 4, Society of Automotive Engineers, 1968.

77. Topper, T. H., and Sandor, B. I., "Effects of Mean Stress and Strain on Fatigue Damage Summation," in Effects of Environment and Complex Load History on Fatigue Life, ASTM STP 462, 1970, pp. 93-104.

78. Smith, K. N., Watson, P., and Topper, T. H., "A Stress-Strain Function for the Fatigue of Metals," Journal of Materials, Vol. 5, No. 4, 1970, pp. 767-778.

79. Nihei, M, Heuler, P., Boller, C., and Seeger, T, "Evaluation of Mean Stress Effect on Fatigue Life by Use of Damage Parameters," International Journal of Fatigue, Vol. 8, No. 3, July 1986, pp. 119-126.

80. Fatemi, A., and Stephens, R. I., "Tensile Mean Stress Effects on Uniaxial Fatigue Behavior of 1045 HR Steel," in Fatigue 87, Vol. I, Proceedings of the Third International Conference on Fatigue and Fatigue Thresholds, Edited by Ritchie, R. O., and Starke, E. A., Jr., Charlottesville, VA., 1987, pp. 537-546.

81. Kliman, V., and Bily, M., "Influence of Mode Control, Mean Value and Frequency of Loading on the Cyclic Stress-Strain Curve," Materials Science and Engineering, Vol. 44, 1980, pp. 73-79.

82. Lorenzo, F., and Laird, C., "A New Approach to Predicting Fatigue Life Behavior Under the Action of Mean Stresses," Materials Science and Engineering, Vol. 62, 1984, pp. 205-210.

83. Standard E606, "Constant-Amplitude Low-Cycle Fatigue Testing," 1988 Annual Book of ASTM Standards, Vol. 03.01, American Society for Testing and Materials, 1988, pp. 596-606.

84. Standard E1012, "Verification of Specimen Alignment Under Tensile Loading" 1988 Annual Book of ASTM Standards, Vol. 03.01, American Society for Testing and Materials, 1988, pp. 757-763.

85. Standard E739, "Statistical Analysis of Linear or Linearized Stress-Life(S-N) and Strain-Life(ε-N) Fatigue Data," <u>1988 Annual Book of ASTM Standards, Vol. 03.01,</u> American Society for Testing and Materials, 1988, pp. 655-661.

86. Rosenthal, D., "Influence of Residual Stress on Fatigue," in <u>Metal Fatigue,</u> Edited by Sines, G., and Waisman, J. L., McGraw-Hill, 1959, pp. 171-196.

87. Stephens, R. I., and Koh, S. K., "Improvements in Empirical Representation of A356-T6 Cast Aluminum Alloy," SAE Paper No. 881702, in <u>Fatigue and Fracture Toughness of A356-T6 Cast Aluminum Alloy,</u> Edited by R. I. Stephens, SAE SP-760, 1988, pp. 29-38.

88. Basquin, H. O., "The Experimental Law of Endurance Tests," <u>Proceedings of ASTM,</u> Vol. 10, Part II, 1910, p. 625.

89. Landgraf, R. W., "The Resistance of Metals to Cyclic Deformation," in <u>Achievement of High Fatigue Resistance in Metals and Alloys,</u> ASTM STP 467, 1970, pp. 3-36.

90. Pokluda, J., and Stanek, P., <u>Kovove Materialy,</u> Vol. 16, No. 5, October 1978, pp. 583-599.

91. Fash, J., and Socie, D. F., "Fatigue Behavior and Mean Effects in Grey Cast Iron," <u>International Journal of Fatigue,</u> July 1982, pp. 137-142.

92. Cordes, T. S., Berns, H. D., Lingenfelser, D. J., Mahoney, B. J., and Testin, R. A., "A SWT Fatigue Mean Stress Model for A356-T6 Cast Aluminum Alloy," SAE Paper No. 881703, in <u>Fatigue and Fracture Toughness of A356-T6 Cast Aluminum Alloy,</u> Edited by R. I. Stephens, SAE SP-760, 1988, pp. 39-47.

93. Neuber, H., "Theory of Stress Concentration for Shear-Strained Prismatic Bodies with Arbitrary Nonlinear Stress-Strain Law," <u>Journal of Applied Mechanics,</u> December 1961, pp. 544-550.

94. Topper, T. H., Wetzel, R. M., and Morrow, JoDean, "Neuber's Rule Applied to Fatigue of Notched Specimens," Journal of Materials, Vol. 4, No. 1, March 1969, pp. 200-209.

95. Stowell, E. Z., "Stress and Strain Concentration at a Circular Hole in an Infinite Plate," NACA Technical Note 2073, National Advisory Committee for Aeronautics, April 1950.

96. Crews, J. H., Jr., and Hardrath, H. F., "A Study of Cyclic Plastic Stresses at a Notch Root," Experimental Mechanics, Vol. 6, No. 6, June 1966, pp. 313-320.

97. Wetzel, R. M., "Smooth Specimen Simulation of Fatigue Behavior of Notches," Journal of Materials, Vol. 3, No. 3, September 1968, pp. 646-657.

98. Topper, T. H., Sandor, B. I., and Morrow, JoDean, "Cumulative Fatigue Damage Under Cyclic Strain Control," Journal of Materials, Vol. 4, No. 1, March 1969. pp. 189-199.

99. Morrow, JoDean, Wetzel, R. M., and Topper, T. H., "Laboratory Simulation of Structural Fatigue Behavior," in Effects of Environmental and Complex Load History on Fatigue Life, ASTM STP 462, 1970, pp. 74-91.

100. Socie, D. F., "Fatigue Life Prediction Using Local Stress-Strain Concepts," Experimental Mechanics, Vol. 17, No. 2, February 1977, pp. 50-56.

101. Dowling, N. E., "Fatigue Life Prediction for Complex Load versus Time Histories," Journal of Engineering Materials and Technology, Vol. 105, July 1983, pp. 206-214.

102. Lawrence, F. V., Jr., Burk, J. D., and Yung, J-Y, "Influence of Residual Stress on the Predicted Fatigue Life of Weldments," in Residual Stress Effects in Fatigue, ASTM STP 776, 1982, pp. 33-43.

APPENDIX A. TABLES

Table 2.1 Chemical compositions in weight %

C	Mn	P	S	Si	Cu	Ni	Cr	V	Mo	Fe
.332	.629	.009	.011	.205	.097	2.22	1.15	.126	.643	base

* Averaged value of 3 separate analyses provided by Watervliet Arsenal

Table 2.2 Averaged monotonic tensile properties and hardness

Young's Modulus, E (GPa)	200
0.2% Offset Yield Strength, σ_{ys} (MPa)	1170
Ultimate Tensile Strength, σ_u (MPa)	1262 *
% Elongation	13 *
% Reduction in Area	50 *
Strain-Hardening Coefficient, K (MPa)	1483
Strain-Hardening Exponent, n	0.037
Rockwell Hardness (HR_C)	40

* Averaged value of 2 test results provided by Watervliet Arsenal

Table 3.1 Strain measurement and relieved stresses calculated from the saw-cut of autofrettaged ring

Location r (mm)	Relieved strain ε_r (με)	ε_θ (με)	Relieved stress σ_r (MPa)	σ_θ (MPa)	Theoretical stress σ_r (MPa)	σ_θ (MPa)	Strain gage type
85		4028		806	0	-701	Uniaxial
85		4670		934	0	-701	Uniaxial
99	-88	1486	79	321	-68	-277	45° Rosette
104		734		147	-75	-154	Uniaxial
113.5		-348		-70	-73	48	Uniaxial
115	540	-547	83	-85	-71	77	45° Rosette
123		-1200		-240	-56	220	Uniaxial
128	746	-1728	50	-331	-44	301	45° Rosette
142		-2688		-538	0	500	Uniaxial
142		-3008		-602	0	500	Uniaxial
142		-3060		-612	0	500	Uniaxial

Table 3.2 Split opening angles from the saw-cut of autofrettaged rings

Experimental opening angle (Degree)*	Theoretical opening angle (Degree)
4.98, 4.97, 4.68, 5.05	4.21 (Tresca)
4.84, 5.04, 5.25	4.86 (von Mises)

* Average value: 4.97

Table 3.3 Nominal stresses, and finite element solutions of maximum principal stresses and theoretical stress concentration factors for pressure-loading condition

Loading condition	σ_{max} @ B' (MPa)	σ_{max} @ C' (MPa)	σ_N (MPa)	K_t	
				@ B'	@ C
Internal pressure[*]	2147	938	547	3.93	1.72

* P_i = 386 MPa

Table 3.4 Nominal stresses, and finite element solutions of maximum principal stresses and theoretical stress concentration factors for autofrettage-loading condition

Loading condition		σ_{max} @ B' (MPa)	σ_{max} @ C' (MPa)	σ_N (MPa)	K_t	
					@ B'	@ C
Percent	100	2044	825	440	4.65	1.88
overstrain	75	1462	633	368	3.97	1.72
	50	692	299	170	4.07	1.76

Table 3.5 Temperature at the inside surface, T_a, for each thermal loading

Percent overstrain	T_a (°C)
100	589
75	467
50	332

Table 4.1 Averaged theoretical stress concentration factors in the conventional groove

Percent overstrain (%)	σ_N (MPa)	σ_{max} (MPa)	K_t
100	987	4191	4.25
75	915	3609	3.94
50	717	2839	3.96

Table 4.2 Averaged theoretical stress concentration factors in the optimized stress relief groove shape of type I

Model	Design variables*	Constraints*	Optimum design variables*	Initial K_t	Final K_t
a	H1, H2	$1.5 \leq H1 \leq 6.0$ $3.0 \leq H2 \leq 5.0$	H1=5.21 H2=5.00	4.33	2.43
b	H1 (H2=5.0)	$2.5 \leq H1 \leq 6.0$	H1=5.61	3.71	2.41
c	H1 (H2=4.0)	$2.0 \leq H1 \leq 6.0$	H1=4.84	3.95	2.65
d	H1 (H2=3.0)	$1.5 \leq H1 \leq 6.0$	H1=3.61	4.33	3.04

* unit: mm

Table 4.3 Averaged theoretical stress concentration factors in the optimized stress relief groove shape of type II

Model	Design variables*	Constraints*	Optimum design variables*	Initial K_t	Final K_t
a	H1, H2 (H3=5.0)	2.5≤H1≤6.0 2.5≤H2≤6.0	H1=6.00 H2=4.54	3.60	2.33
b	H1, H2 (H3=4.0)	2.5≤H1≤6.0 2.5≤H2≤6.0	H1=5.15 H2=5.97	3.38	2.36
c	H1, H2 (H3=3.0)	2.5≤H1≤6.0 2.5≤H2≤6.0	H1=3.23 H2=4.20	4.22	2.73

* unit: mm

Table 4.4 Averaged theoretical stress concentration factors in the optimized stress relief groove shape of type III

Depth (mm)	K_t
2.5	3.73
4.0	3.42
5.0	3.38
6.0	3.30

Table 4.5 Averaged theoretical stress concentration factors in the optimized stress relief groove shape of type IV

Percent O.S.	Design variables*	Constraints*	Optimum design variables*	Initial K_t	Final K_t
100	H1, H2	3.0≤H1≤6.0 3.0≤H2≤5.0	H1=6.00 H2=4.13	2.98	2.29
75	H1, H2	3.0≤H1≤6.0 3.0≤H2≤5.0	H1=6.00 H2=4.15	2.76	2.13
50	H1 H2	3.0≤H1≤6.0 3.0≤H2≤5.0	H1=6.00 H2=4.14	3.01	2.32

* unit: mm

Table 4.6 Maximum equivalent stress of each groove due to torque*

Groove shape		σ_{eq} (MPa)
Conventional groove		456
Changed groove	Type I	336
	Type II	402
	Type III	363
	Type IV	328

* Torque = 56,500 N·m

Table 4.7 Nominal stresses and finite element solutions of maximum principal stresses and theoretical stress concentration factors for pressure-loading condition in the changed groove

Loading condition	σ_{max} @ B' (MPa)	σ_{max} @ C' (MPa)	σ_N (MPa)	K_t	
				@ B'	@ C
Internal pressure *	1157	902	547	2.12	1.65

* P_i = 386 MPa

Table 4.8 Nominal stresses and finite element solutions of maximum principal stresses and theoretical stress concentration factors for autofrettage-loading condition in the changed groove

Loading condition		σ_{max} @ B' (MPa)	σ_{max} @ C' (MPa)	σ_N (MPa)	K_t	
					@ B'	@ C
Percent	100	1116	793	440	2.54	1.65
overstrain	75	788	613	368	2.14	1.67
	50	359	280	170	2.11	1.65

Table 5.1 Shot peening data

Peening	Shot size	Shot diameter (mm)	Intensity
First shot	CS-550	1.40	10 - 12C
Second shot	CS-110	0.28	6 - 8A

Table 5.2 Residual stress determination by X-ray diffraction method

Specimen type	Depth (mm)	Residual stress (MPa)
As-machined	0.000	-804
	0.015	-464
	0.028	-526
	0.048	-508
	0.124	-570
	0.269	-584
	0.378	-522
	0.739	-509
Shot peened	0.000	-802
	0.010	-569
	0.020	-565
	0.046	-627
	0.127	-614
	0.251	-398
	0.384	-640
	0.744	-375

Table 6.1 Finite element stress analysis results of conventional and changed external grooved simulation specimens due to compressive load*

Groove type	σ_{max} @ B' (MPa)	σ_{max} @ C' (MPa)	σ_N (MPa)	K_t @ B'	K_t @ C'
Conventional	690	294	234	2.96	1.26
Changed	379	271	234	1.62	1.16

* Applied compressive load, F = 10 kN

Table 6.2 Fatigue simulation loads for each percent overstrain level

Percent overstrain	Simulation compressive load (kN) Maximum load	Minimum load	Load amplitude
100	60.7	29.6	31.1
75	52.3	21.2	31.1
50	41.1	10.0	31.1

Table 6.3 Experimental strains and stresses from a strain rosette

Load (kN)	Strain ($\mu\varepsilon$) Measured ε_A	ε_B	ε_C	Experimental ε_1	ε_2	Experimental stress (MPa) σ_1	σ_2
-2.22	278	106	-86	278.3	-86.3	58.3	

Table 6.4 Maximum principal stresses along the changed external groove of simulation specimen due to compressive load[1] using strain measurements

Strain gage location[2]	Measured strain ($\mu\varepsilon$)	Experimental stress (MPa)	Stress from FEM (MPa)	Error[3] (%)	Gage type
0	278	58.3	60.1	3.0	Rosette
8.6	294	61.7	62.2	0.8	Uniaxial
12.5	360	75.6	72.2	4.5	Uniaxial
15.0	386	81.1	82.5	1.7	Uniaxial
16.5	380	79.8	83.9	4.9	Uniaxial

[1] Applied compressive load, F=2.22 kN

[2] Distance from the center of changed external groove

[3] $\text{Error}(\%) = \left| \dfrac{\sigma_{FEM} - \sigma_{gage}}{\sigma_{FEM}} \right| \times 100$

Table 6.5 Cycles to various crack lengths for simulation specimen with conventional groove

Simulation load max/min (kN)	Specimen I.D.	Cycles to crack length(mm)					
		0.25	0.50	1.00	1.50	2.50	Fracture
60.7/29.6	G-1	1971	2405	2743	-	-	2840
(100% O.S.)	G-4	2177	2474	2666	-	-	2718
52.3/21.2	G-2	2174	2699	2987	3343	3580	3587
(75% O.S.)	G-5	2549	2698	2930	3154	3494	3700
41.1/10.0	G-3	2803	3114	3347	3460	3805	4666
(50% O.S.)	G-6	3245	3463	3683	3854	4156	4743

Table 6.6 Cycles to various crack lengths for simulation specimen with changed groove

Simulation load max/min (kN)	Specimen I.D.	Cycles to crack length(mm)				
		0.50	1.00	1.5	2.5	Fracture
60.7/29.6	G-11	12237	12309	12375	12490	12650
(100% O.S.)	G-12	5990	6297	6523	6800	7068
52.3/21.2	G-13	-	12844	13033	13387	14297
(75% O. S.)	G-14	-	-	14606	14847	16034
41.1/10.0	G-15	-	-	-	23760	26365
(50% O.S.)	G-16	-	-	-	17630	18998

Table 6.7 Cycles to various crack lengths for simulation specimen with shot peened-changed groove

Simulation load max/min (kN)	Specimen I.D.	Cycles to crack length(mm)				
		0.50	1.00	1.5	2.5	Fracture
60.7/29.6	G-21	-	7653	7890	8054	8100
(100% O.S.)	G-25	-	-	11004	11751	13177
52.3/21.2	G-23	-	-	-	20471	20960
(75% O.S.)	G-26	14770	14810	14848	14921	15115
41.1/10.0	G-24	-	-	-	37157	38667
(50% O.S.)	G-27	65794	65885	65975	67293	72951

Table 6.8 Average simulation fatigue life to 2.5-mm crack length for each type of specimen

Simulation load max/min (kN)	Percent O. S. (%)	Specimen type		
		Conventional	Changed	Shot peened
60.7/29.6	100	2,799	9,645	9,903
52.3/21.2	75	3,537	14,117	17,696
41.1/10.0	50	3,978	20,695	52,225

Table 6.9 Log-log linear load-life of simulation fatigue tests for each type of specimen

Specimen type	Coefficient, A (kN)	Exponent, α
Conventional	695,113	-1.172
Changed	6,843	-0.514
Peened	569	-0.244

Table 7.1 Low cycle fatigue test data

Specimen I.D.	R_ε	$\Delta\varepsilon/2$	$2N_f$	$\Delta\varepsilon_e/2$	$\Delta\varepsilon_p/2$	ε_{mean}	$\Delta\sigma/2$ (MPa)	σ_{max} (MPa)	σ_{mean} (MPa)	E_1 (GPa)
O-13	-2	0.010	480	.0056	.0043	-.0033	1090	1078	-12	206
O-14	-2	0.008	1310	.0053	.0026	-.0027	1019	1001	-18	201
0-18	-2	0.006	2320**	.0052	.0026	-.0020	997	948	-49	201
O-15	-2	0.005	10968	.0047	.0005	-.0017	900	838	-62	201
0-16	-2	0.004	29320	.0040	-	-.0013	805	700	-104	205
O-17	-2	0.003	195568*	.0030	-	-.0010	600	485	-115	202
I-4	-1	0.030	29	.0065	.0231	.0000	1218	1207	-11	196
I-6	-1	0.020	78	.0063	.0135	.0000	1186	1170	-16	194
M-3	-1	0.015	160	.0061	.0088	.0000	1129	1123	-6	193
O-2	-1	0.010	640	.0058	.0042	.0000	1065	1049	-16	196
I-7	-1	0.010	672	.0056	.0044	.0000	1047	1039	-8	195
I-2	-1	0.008	1028	.0053	.0027	.0000	1029	1027	-2	203
O-3	-1	0.006	3740	.0049	.0011	.0000	948	963	15	199
I-5	-1	0.005	7500*	.0047	.0003	.0000	915	952	37	206
I-10	-1	0.005	6520	.0046	.0004	.0000	903	957	54	200
I-3	-1	0.004	20962*	.0040	-	.0000	789	822	33	202
O-4	-1	0.003	81262*	.0030	-	.0000	602	599	3	198
I-8	-1	0.003	80500*	.0030	-	.0000	596	611	15	197
O-5	-1	0.0025	152328	.0025	-	.0000	498	516	18	201
I-12	0	0.015	156	.0059	.0084	.0150	1140	1142	2	194
I-13	0	0.007	1600	.0050	.0017	.0070	975	1019	45	197
I-14	0	0.005	4010	.0046	.0003	.0050	889	1074	185	198
1-15	0	0.0035	12522	.0035	-	.0035	672	1155	483	198
I-16	0	0.0025	45840	.0025	-	.0025	483	965	482	196
I-17	0	0.0020	88720	.0020	-	.0020	434	824	390	195

Table 7.1 -- continued

Specimen I.D.	R_ε	$\Delta\varepsilon/2$	$2N_f$	$\Delta\varepsilon_e/2$	$\Delta\varepsilon_p/2$	ε_{mean}	$\Delta\sigma/2$ (MPa)	σ_{max} (MPa)	σ_{mean} (MPa)	E_1 (GPa)
O-10	0.5	0.009	1004	.0052	.0030	.0270	1009	1034	25	198
O-9	0.5	0.006	2780	.0048	.0009	.0180	921	1031	110	195
M-1	0.5	0.005	5620	.0044	.0003	.0150	850	1099	251	198
O-8	0.5	0.004	10348	.0037	-	.0120	711	1182	471	193
I-9	0.5	0.003	16120	.0030	-	.0090	560	1192	632	194
O-11	0.5	0.0025	37540	.0025	-	.0075	474	1140	666	200
O-12	0.5	·0.0020	74100	.0020	-	.0060	382	1187	805	204
I-18	0.75	0.008	768	.0050	.0019	.0400	966	1056	90	197
I-19	0.75	0.006	2960	.0045	.0008	.0300	874	1038	164	193
I-11	0.75	0.004	6440	.0040	.0002	.0200	772	1228	456	189
M-2	0.75	0.003	22760	.0030	-	.0150	506	1201	695	194
O-19	0.75	0.0025	26090	.0025	-	.0125	452	1219	767	195
I-20	0.75	0.0020	70480	.0020	-	.0100	336	1197	861	194

* Failed outside gage length but not in the fillet, considered valid

** Failed outside gage length and in the fillet, considered invalid

Table 7.2 Cyclic stress-strain properties from R=-1

Cyclic Strength Coefficient, K' (MPa)	1581
Cyclic Strength Exponent, n'	0.071
0.2% Offset Cyclic Yield Strength, σ_{ys}' (MPa)	1014

Table 7.3 Low cycle fatigue properties from R=-1

Fatigue Strength Coefficient, σ_f' (MPa)	2123
Fatigue Strength Exponent, b	-0.110
Fatigue Ductility Coefficient, ε_f'	0.489
Fatigue Ductility Exponent, c	-0.783
Averaged Young's Modulus, E_1 (GPa)	200
Averaged Young's Modulus, E_2 (GPa)	175
Averaged Young's Modulus, E_3 (GPa)	193

Table 7.4 Log-log linear strain-life low cycle fatigue
properties for each strain ratio

Strain ratio, R	Coefficient, M	Exponent, m
-2	0.035	-0.206
-1	0.065	-0.281
0	0.072	-0.317
0.5	0.104	-0.355
0.75	0.073	-0.324

Table 7.5 Log-log linear SWT model for each strain ratio

Strain ratio, R	Coefficient, C (MPa)	Exponent, γ
-2	89	-0.335
-1	117	-0.369
0	105	-0.357
0.5	85	-0.321
0.75	59	-0.286
All	105	-0.352

Table 8.1 Local strains and local stresses for each overstrain level in the thick-walled pressure vessel with a conventional external groove

Percent O.S. (%)	Theoretical elastic stress(MPa)		Nominal stress, S(MPa)		K_t	K_f
	Maximum	Minimum	Smax	Smin		
100	4191	2044	987	481	4.25	4.12
75	3069	1462	915	371	3.94	3.82
50	2839	692	717	175	3.96	3.84

1) Linear rule

Percent O.S. (%)	Local strain, ε		Local stress, σ (MPa)		Strain ratio, R_ε
	ε_{max}	$\Delta\varepsilon/2$	σ_{max}	σ_m	
100	0.0210	0.0054	1172	130	0.49
75	0.0181	0.0054	1153	111	0.40
50	0.0142	0.0054	1124	82	0.24

2) Neuber's rule

Percent O.S. (%)	Local strain, ε		Local stress, σ (MPa)		Strain ratio, R_ε
	ε_{max}	$\Delta\varepsilon/2$	σ_{max}	σ_m	
100	0.0663	0.0059	1293	334	0.82
75	0.0501	0.0059	1264	307	0.77
50	0.0322	0.0059	1218	260	0.63

Table 8.2 Local strains and local stresses for each overstrain level in the thick-walled pressure vessel with a changed external groove

Percent O.S. (%)	Theoretical elastic stress(MPa)		Nominal stress, S(MPa)		K_t	K_f
	Maximum	Minimum	Smax	Smin		
100	2273	1106	987	481	2.30	2.30
75	1945	790	915	371	2.13	2.13
50	1516	369	717	175	2.11	2.11

1) Linear rule

Percent O.S. (%)	Local strain, ε		Local stress, σ (MPa)		Strain ratio, R_ε
	ε_{max}	$\Delta\varepsilon/2$	σ_{max}	σ_m	
100	0.0114	0.0029	1093	533	0.49
75	0.0097	0.0029	1069	509	0.40
50	0.0076	0.0029	1024	464	0.24

2) Neuber's rule

Percent O.S. (%)	Local strain, ε		Local stress, σ (MPa)		Strain ratio, R_ε
	ε_{max}	$\Delta\varepsilon/2$	σ_{max}	σ_m	
100	0.0217	0.0029	1175	606	0.73
75	0.0164	0.0029	1142	576	0.65
50	0.0105	0.0029	1082	521	0.45

Table 8.3 Local strains and local stresses for each overstrain level
in the thick-walled pressure vessel with a shot peened-
changed external groove

1) Linear rule

Percent O.S. (%)	Local strain, ε		Local stress, σ (MPa)		Strain ratio, R_ε
	ε_{max}	$\Delta\varepsilon/2$	σ_{max}	σ_m	
100	0.0084	0.0029	1043	483	0.31
75	0.0068	0.0029	998	438	0.15
50	0.0046	0.0029	842	282	-0.26

2) Neuber's rule

Percent O.S. (%)	Local strain, ε		Local stress, σ (MPa)		Strain ratio, R_ε
	ε_{max}	$\Delta\varepsilon/2$	σ_{max}	σ_m	
100	0.0124	0.0029	1106	537	0.53
75	0.0085	0.0029	1046	480	0.32
50	0.0047	0.0029	869	308	-0.23

Table 8.4 Nominal stresses for each overstrain level in the
simulation fatigue specimen

Simulation load, F(kN)		Percent	Nominal stress, S(MPa)	
Maximum	Minimum	O.S. (%)	S_{max}	S_{min}
60.7	29.6	100	1418	692
52.3	21.2	75	1221	495
41.1	10.0	50	960	234

Table 8.5 Induced residual stresses at each type of external groove
in the simulation fatigue specimen

Groove type	Residual stress, σ_0 (MPa)	K_t	K_f
Conventional	-517	2.96	2.88
Changed	-517	1.62	1.62
Shot peened	-594	1.62	1.62

Table 8.6 Local strains and local stresses for each overstrain level in the simulation fatigue specimen with a conventional external groove without considering induced residual stresses

1) Linear rule

Percent O.S. (%)	Local strain, ε		Local stress, σ (MPa)		Strain ratio, R_ε
	ε_{max}	$\Delta\varepsilon/2$	σ_{max}	σ_m	
100	0.0210	0.0054	1172	130	0.49
75	0.0181	0.0054	1153	111	0.40
50	0.0142	0.0054	1124	82	0.24

2) Neuber's rule

Percent O.S. (%)	Local strain, ε		Local stress, σ (MPa)		Strain ratio, R_ε
	ε_{max}	$\Delta\varepsilon/2$	σ_{max}	σ_m	
100	0.0668	0.0059	1293	333	0.82
75	0.0506	0.0059	1265	305	0.77
50	0.0325	0.0059	1219	259	0.63

Table 8.7 Local strains and local stresses for each overstrain level in the simulation fatigue specimen with a conventional external groove including induced residual stresses

1) Linear rule

Percent O.S. (%)	Local strain, ε		Local stress, σ (MPa)		Strain ratio, R_ε
	ε_{max}	$\Delta\varepsilon/2$	σ_{max}	σ_m	
100	0.0163	0.0054	1141	99	0.34
75	0.0134	0.0054	1115	73	0.19
50	0.0095	0.0054	1065	23	-0.14

2) Neuber's rule

Percent O.S. (%)	Local strain, ε		Local stress, σ (MPa)		Strain ratio, R_ε
	ε_{max}	$\Delta\varepsilon/2$	σ_{max}	σ_m	
100	0.0411	0.0059	1244	284	0.71
75	0.0285	0.0059	1205	245	0.59
50	0.0152	0.0059	1132	172	0.22

Table 8.8 Local strains and local stresses for each overstrain level in the simulation fatigue specimen with a changed external groove without considering induced residual stresses

1) Linear rule

Percent O.S. (%)	Local strain, ε		Local stress, σ (MPa)		Strain ratio, R_ε
	ε_{max}	$\Delta\varepsilon/2$	σ_{max}	σ_m	
100	0.0115	0.0029	1095	535	0.50
75	0.0099	0.0029	1072	512	0.42
50	0.0078	0.0029	1028	468	0.26

2) Neuber's rule

Percent O.S. (%)	Local strain, ε		Local stress, σ (MPa)		Strain ratio, R_ε
	ε_{max}	$\Delta\varepsilon/2$	σ_{max}	σ_m	
100	0.0224	0.0030	1178	601	0.73
75	0.0170	0.0030	1146	569	0.65
50	0.0111	0.0030	1090	513	0.45

Table 8.9   Local strains and local stresses for each overstrain level
in the simulation fatigue specimen with a changed
external groove including induced residual stresses

1) Linear rule

Percent O.S. (%)	Local strain, ε		Local stress, σ (MPa)		Strain ratio, R_ε
	ε_{max}	$\Delta\varepsilon/2$	σ_{max}	σ_m	
100	0.0089	0.0029	1054	494	0.35
75	0.0073	0.0029	1017	457	0.21
50	0.0052	0.0029	916	356	-0.12

2) Neuber's rule

Percent O.S. (%)	Local strain, ε		Local stress, σ (MPa)		Strain ratio, R_ε
	ε_{max}	$\Delta\varepsilon/2$	σ_{max}	σ_m	
100	0.0140	0.0030	1121	544	0.57
75	0.0098	0.0030	1071	494	0.39
50	0.0056	0.0030	943	366	-0.07

Table 8.10 Local strains and local stresses for each overstrain level in the simulation fatigue specimen with a shot peened-changed external groove

1) Linear rule

Percent O.S. (%)	Local strain, ε		Local stress, σ (MPa)		Strain ratio, R_ε
	ε_{max}	$\Delta\varepsilon/2$	σ_{max}	σ_m	
100	0.0085	0.0029	1046	486	0.32
75	0.0069	0.0029	1005	445	0.16
50	0.0048	0.0029	872	312	-0.21

2) Neuber's rule

Percent O.S. (%)	Local strain, ε		Local stress, σ (MPa)		Strain ratio, R_ε
	ε_{max}	$\Delta\varepsilon/2$	σ_{max}	σ_m	
100	0.0129	0.0030	1111	534	0.53
75	0.0089	0.0030	1055	478	0.32
50	0.0050	0.0030	898	321	-0.23

Table 8.11 Life estimations of thick-walled pressure vessel and simulation fatigue specimen with different types of external groove for each overstrain level by using SWT parameter

1) Thick-walled pressure vessel

Groove type	O.S.(%)	Estimated fatigue life (cycles)	
		Linear rule	Neuber's rule
Conventional	100	1461	859
	75	1530	916
	50	1645	1018
Changed	100	10415	8480
	75	11093	9195
	50	12534	10718
Shot peened-changed	100	11897	10071
	75	13484	11800
	50	21855	19980

2) Simulation fatigue specimen without induced residual stresses

Groove type	O.S.(%)	Estimated fatigue life (cycles)	
		Linear rule	Neuber's rule
Conventional	100	1461	859
	75	1530	916
	50	1645	1018
Changed	100	10361	7646
	75	11005	8268
	50	12396	9533

Table 8.11 --- continued

3) Simulation fatigue specimen including induced residual stresses

Groove type	O.S.(%)	Fatigue life (cycles)		
		Estimated		Experimental
		Linear rule	Neuber's rule	(cycles)
Conventional	100	.1576	959	2799
	75	1683	1050	3537
	50	1917	1254	3978
Changed	100	11547	8803	9645
	75	12781	10021	14117
	50	17203	14386	20695
Shot peened-changed	100	11800	9030	9903
	75	13219	10459	17696
	50	19786	16530	52225

Table 8.12 Life estimations of thick-walled pressure vessel and simulation fatigue specimen with different types of external groove for each overstrain level by using Morrow's equation

1) Thick-walled pressure vessel

Groove type	O.S. (%)	Estimated fatigue life (cycles)	
		Linear rule	Neuber's rule
Conventional	100	1285	685
	75	1326	710
	50	1394	756
Changed	100	11955	9055
	75	13125	10138
	50	15669	12525
Shot peened-changed	100	14535	11772
	75	17378	14708
	50	32692	29401

2) Simulation fatigue specimen without induced residual stresses

Groove type	O.S. (%)	Estimated fatigue life (cycles)	
		Linear rule	Neuber's rule
Conventional	100	1285	930
	75	1327	970
	50	1394	1041
Changed	100	11863	9227
	75	12972	10412
	50	15423	12921

Table 8.12 --- continued

3) Simulation fatigue specimen including induced residual stresses

| Groove type | O.S.(%) | Fatigue life (cycles) | | Experimental |
| | | Estimated | | (cycles) |
		Linear rule	Neuber's rule	
Conventional	100	1354	1002	2799
	75	1416	1065	3537
	50	1546	1198	3978
Changed	100	13919	11454	9645
	75	16111	13919	14117
	50	24185	23223	20695
Shot peened-changed	100	14364	11910	9903
	75	16899	14825	17696
	50	28926	27884	52225

APPENDIX B. FIGURES

20 μm
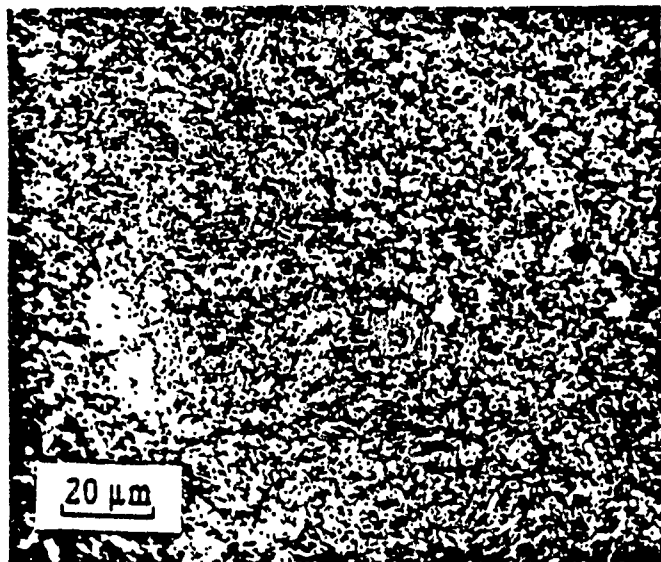
Figure 2.1 Microstructure of ASTM A723 steel
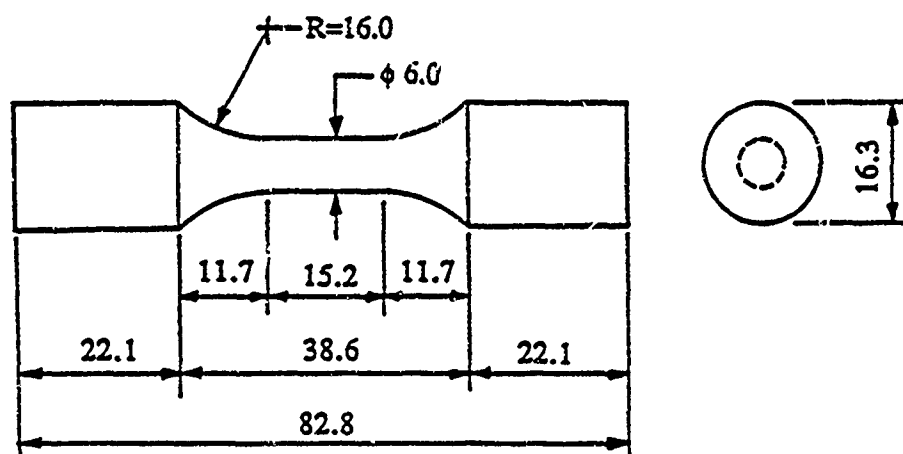
Figure 2.2 Axial test specimen (unit: mm)
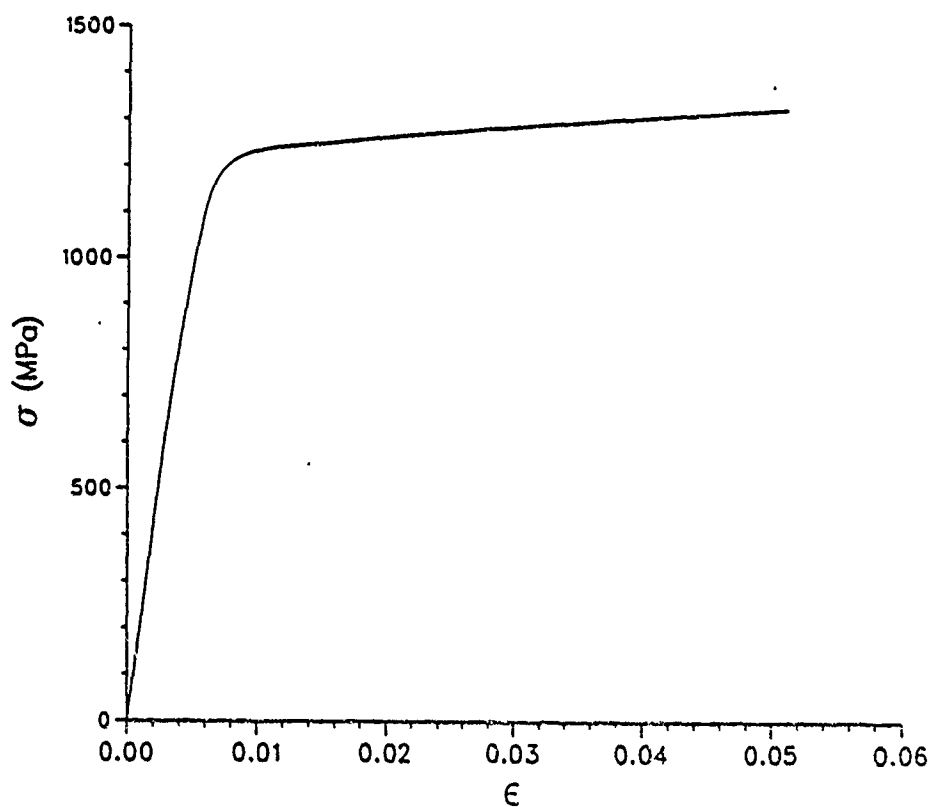
Figure 2.3 Partial monotonic true stress-true strain curve
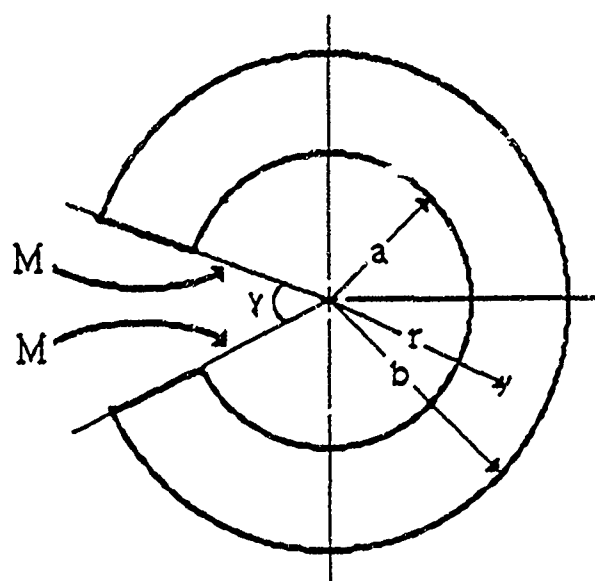
Figure 3.1 Curved beam subjected to pure bending moment
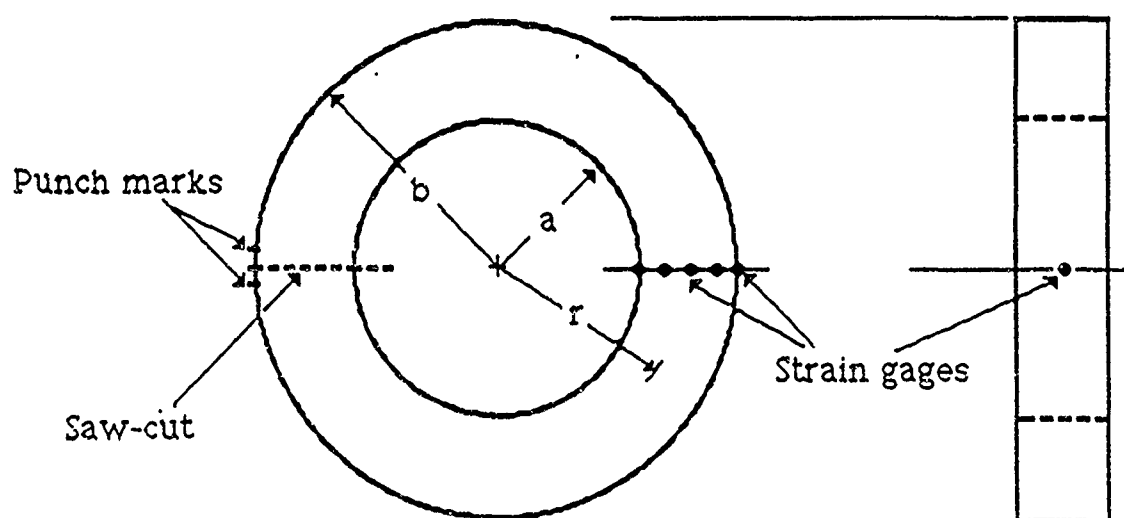
Figure 3.2 Saw-cut of autofrettaged ring
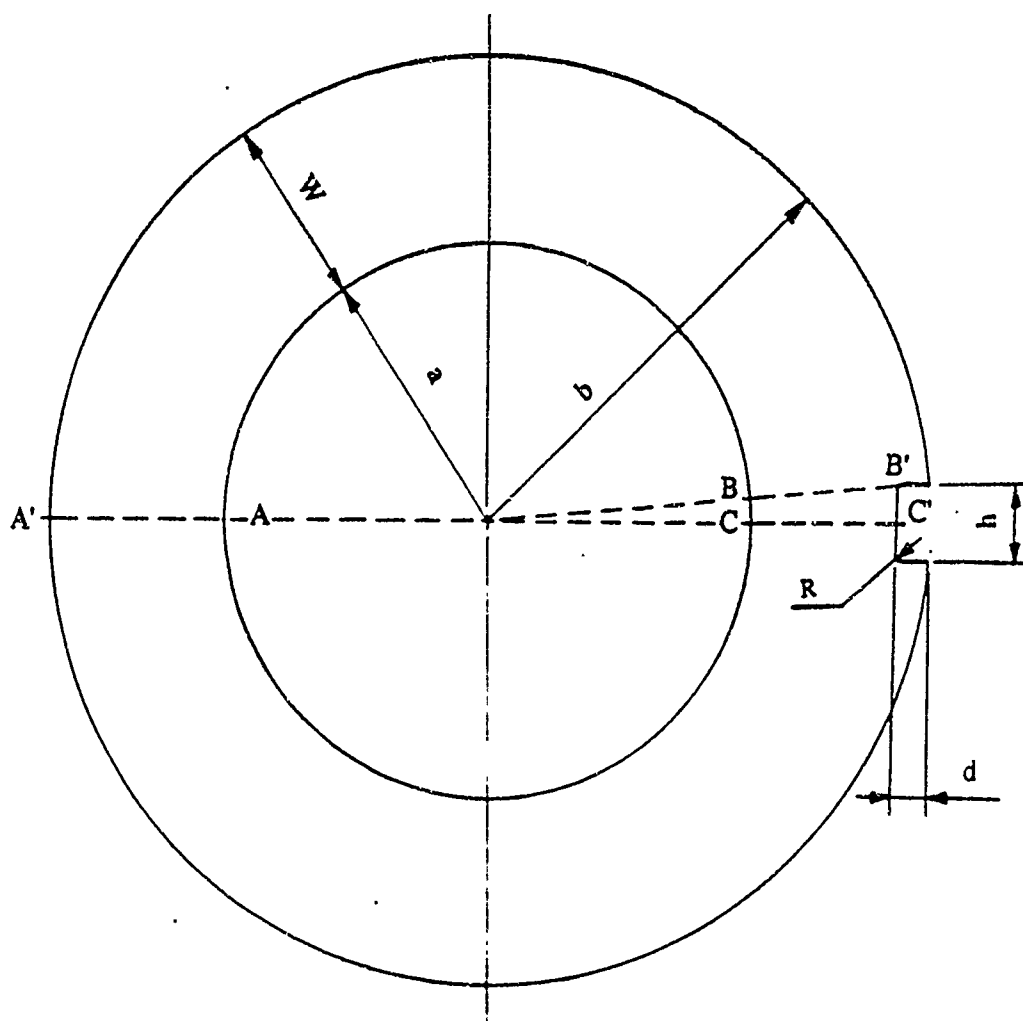
Figure 3.3 Thick-walled pressure vessel with a conventional external groove (a=85, b=142, d=10, h=25, W=57, R=1.5, unit: mm)
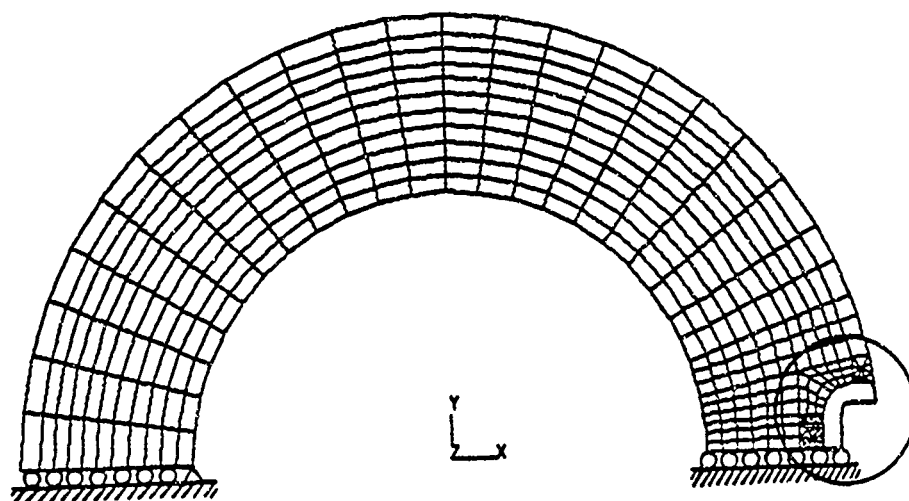
(a) Generated mesh
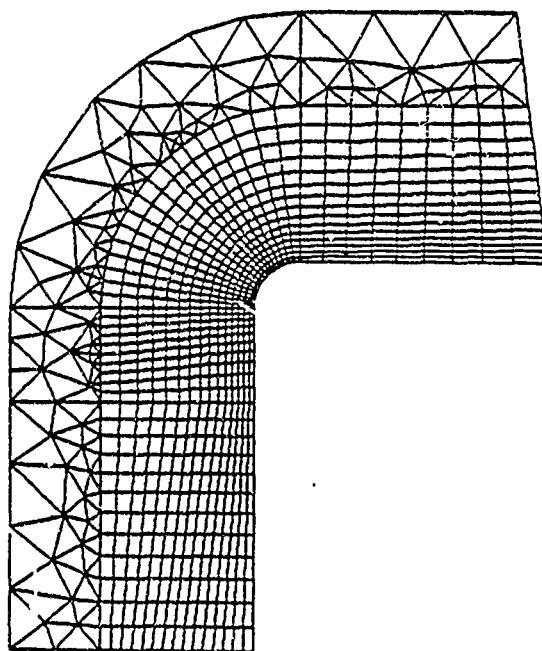
(b) Refined mesh near the root of groove

Figure 3.4 Finite element mesh used for a conventional groove

(a) 4-node isoparametric quadrilateral element

(b) ·6-node isoparametric triangular element

(c) 8-node isoparametric quadrilateral element
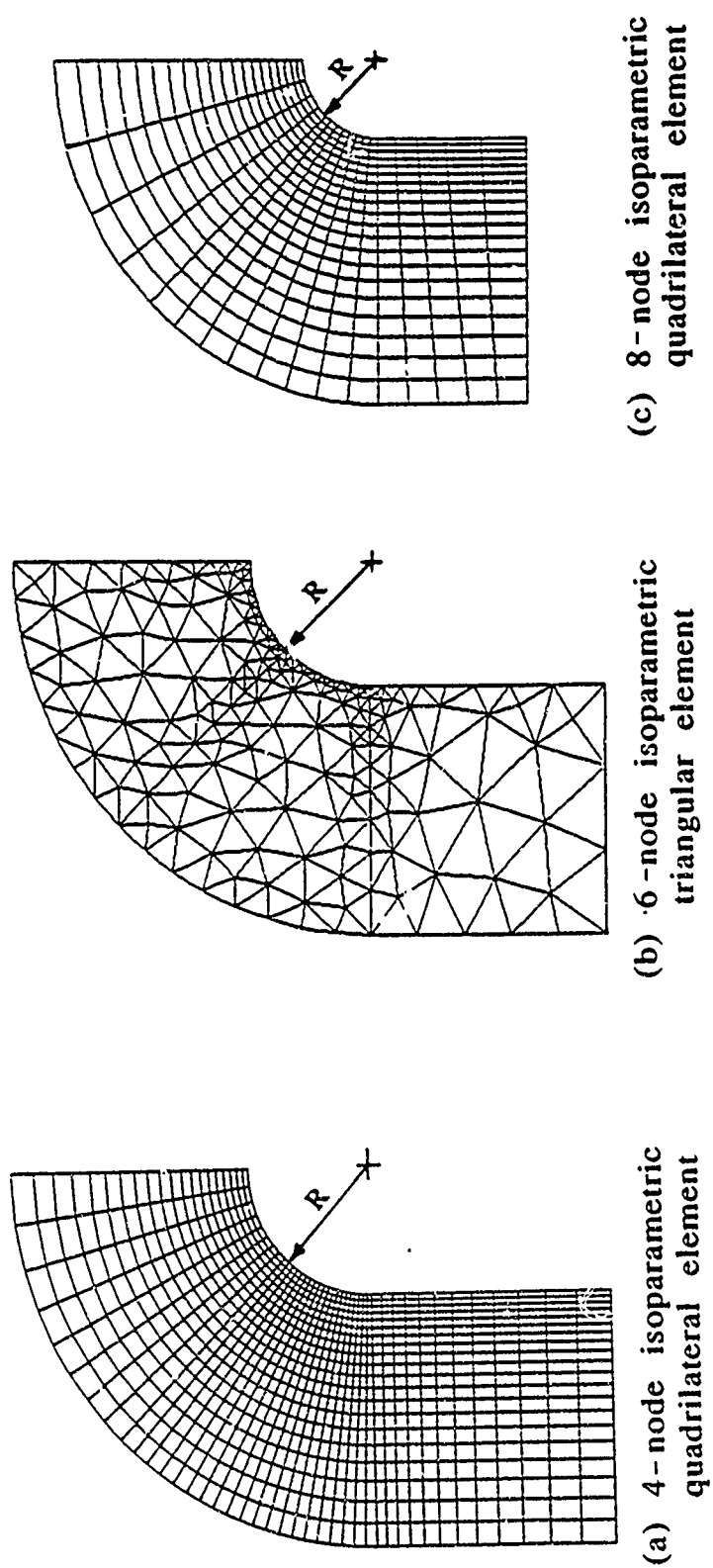
Figure 3.5 Refined finite element mesh near the root of a conventional groove using different element types
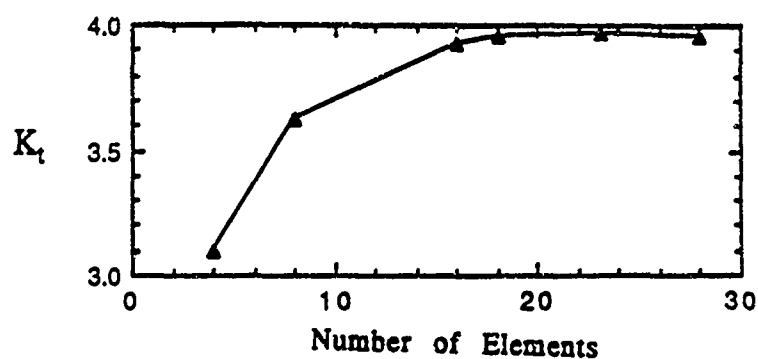
(a) 4-node isoparametric quadrilateral element
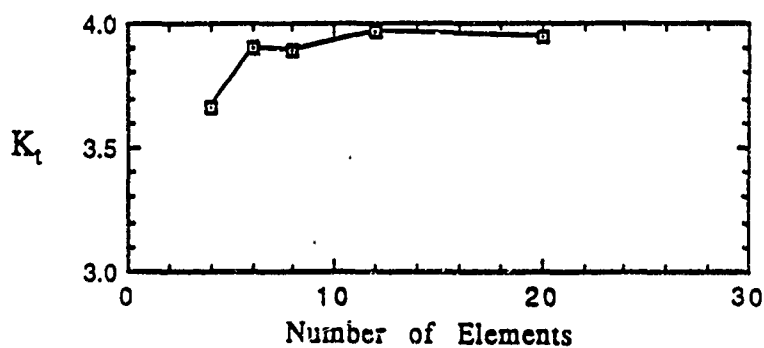
(b) 6-node isoparametric triangular element
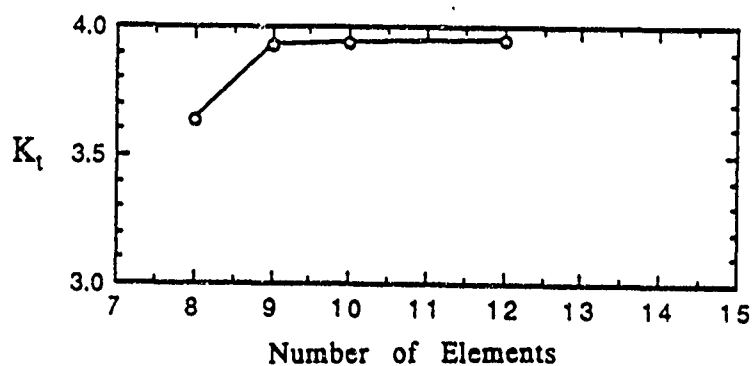
(c) 8-node isoparametric quadrilateral element

Figure 3.6 Convergence of theoretical stress concentration factor K_t due to internal pressure loading for three different element types used for conventional groove
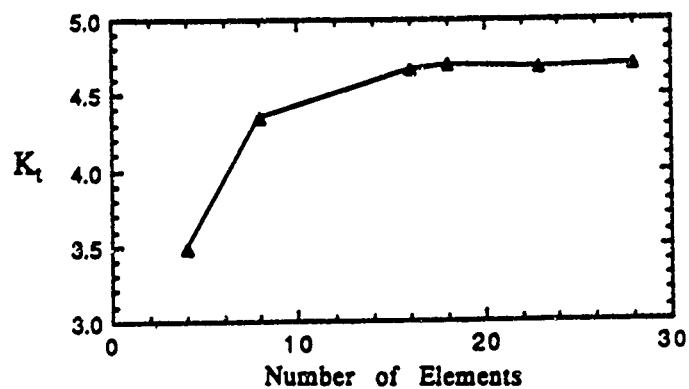
(a) 4-node isoparametric quadrilateral element
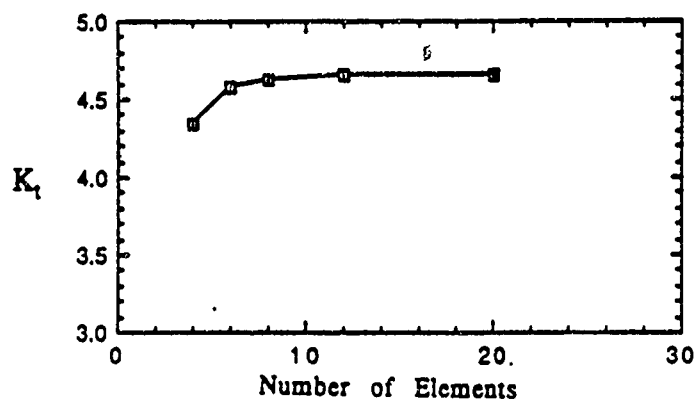
(b) 6-node isoparametric triangular element
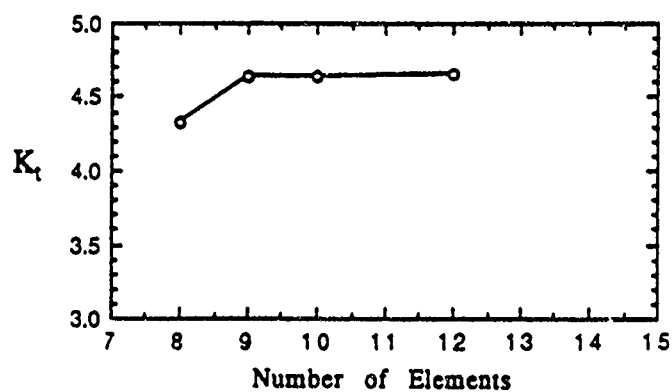
(c) 8-node isoparametric quadrilateral element

Figure 3.7 Convergence of theoretical stress concentration factor K_t due to 100 percent overstrain loading for three different element types used for conventional groove
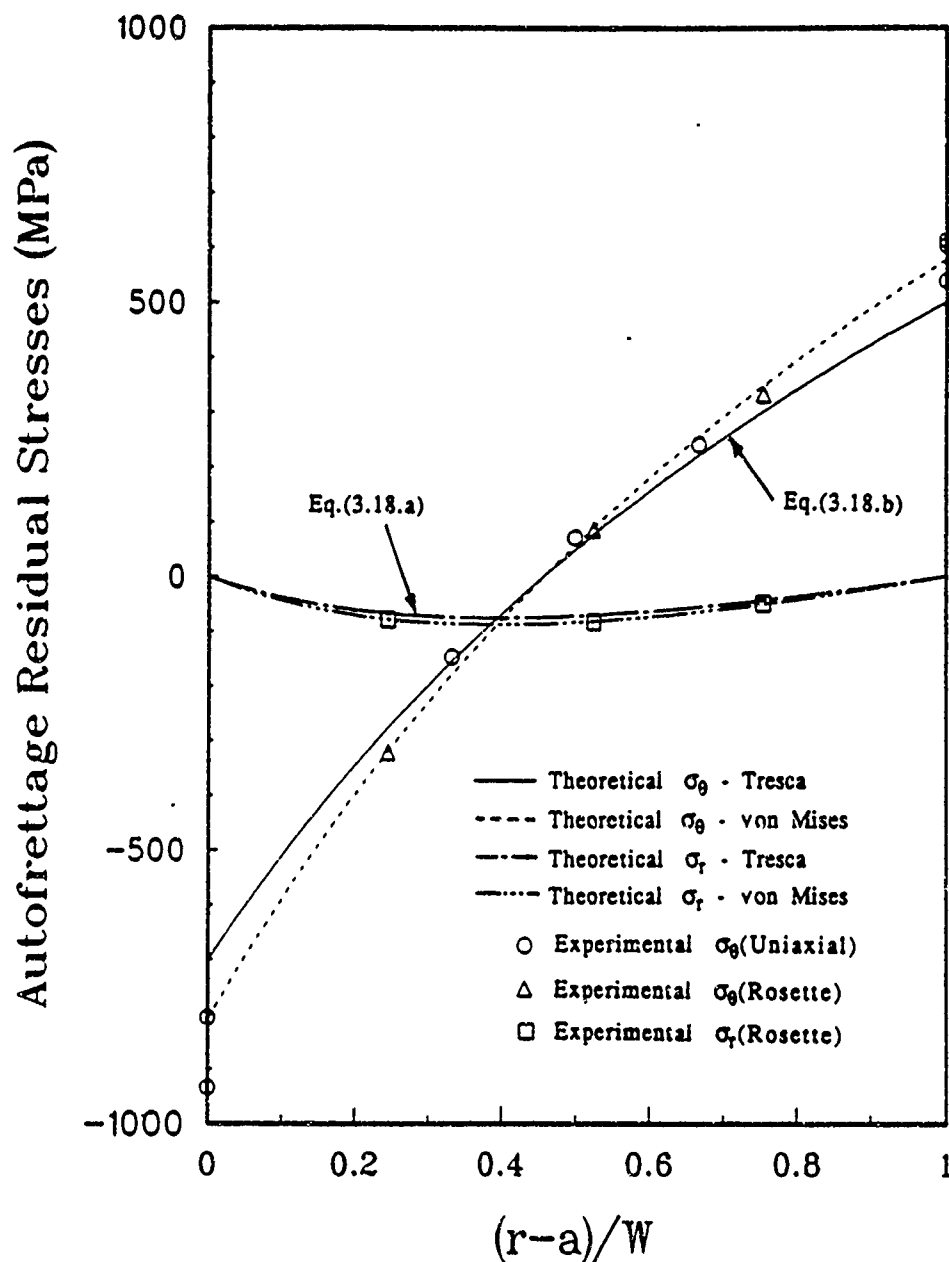
Figure 3.8 Autofrettage residual stress distributions across the thickness for a 100 percent overstrained thick-walled pressure vessel of wall ratio 1.67
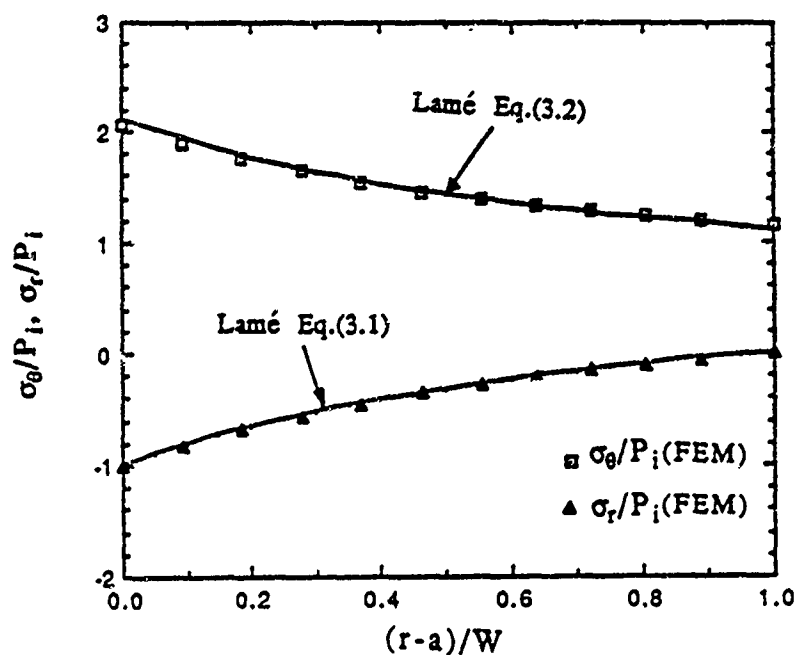
Figure 3.9 Tangential and radial stress distributions due to internal pressure along plane A-A' in a thick-walled pressure vessel with a conventional groove
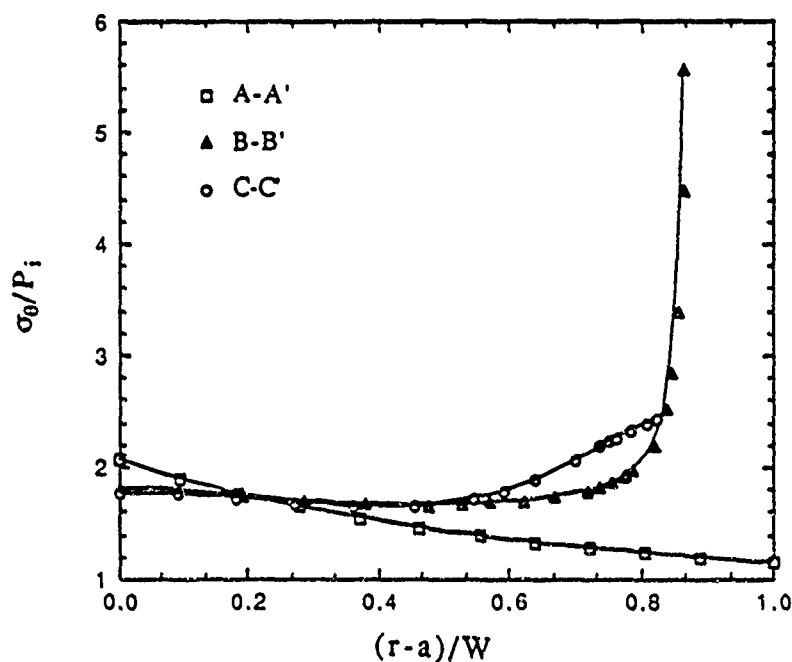
Figure 3.10 Tangential stress distributions due to internal pressure along A-A', B-B', and C-C' in a thick-walled pressure vessel with a conventional groove
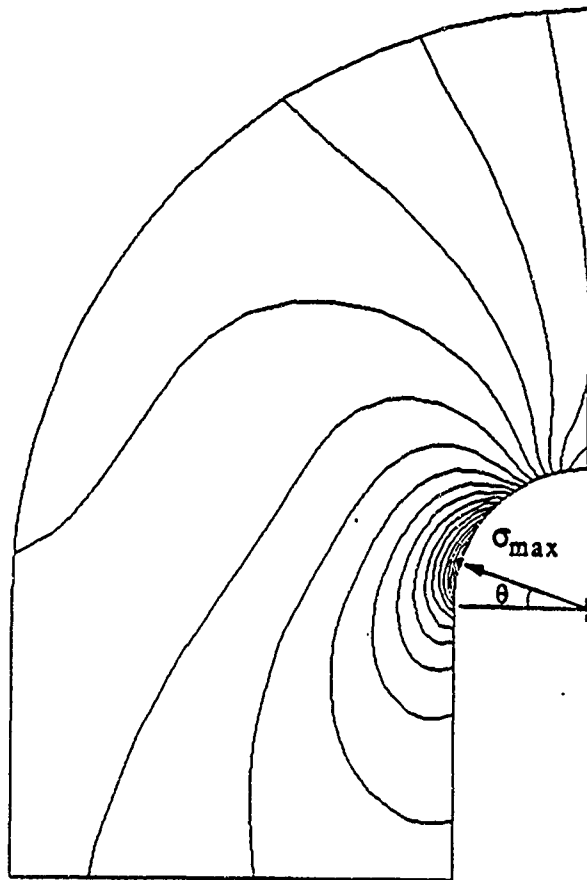
Figure 3.11 Maximum principal stress contours near the root of a
conventional groove due to internal pressure loading
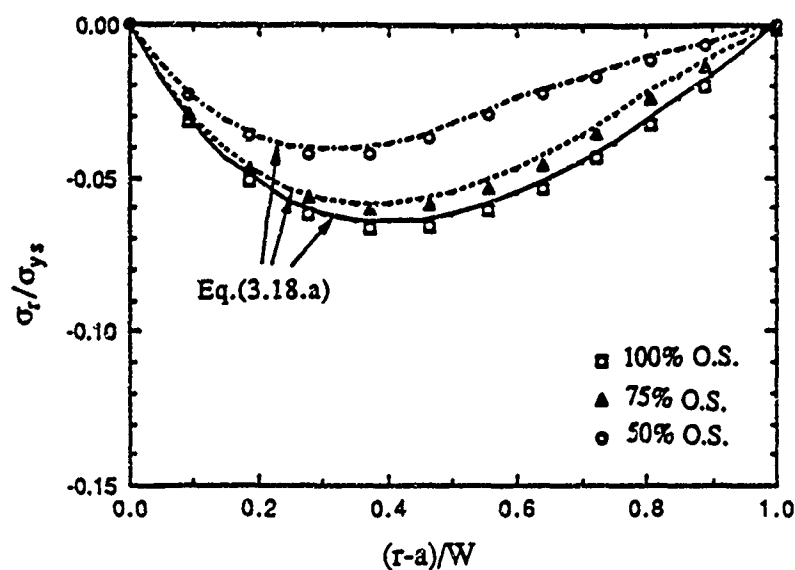
Figure 3.12 Radial residual stress distributions due to 100, 75, and 50 percent overstrain along plane A-A' in a thick-walled pressure vessel with a conventional groove
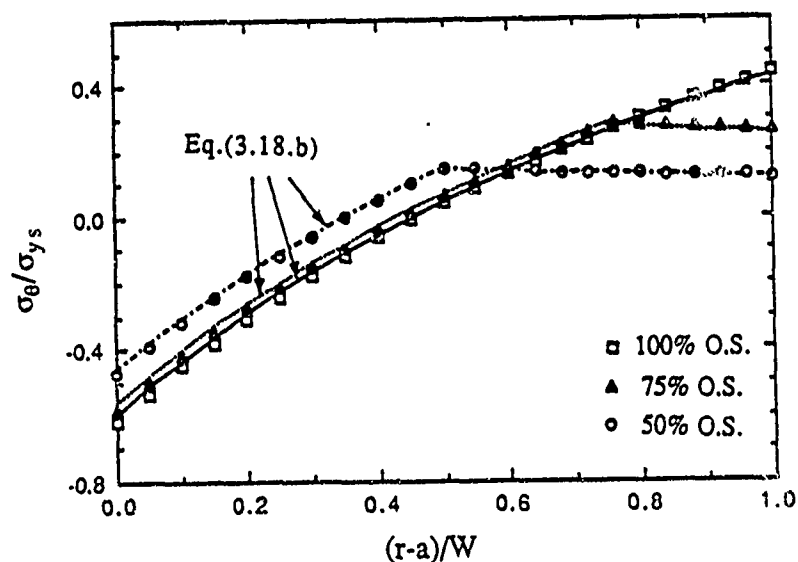
Figure 3.13 Tangential residual stress distributions due to 100, 75, and 50 percent overstrain along plane A-A' in a thick-walled pressure vessel with a conventional groove
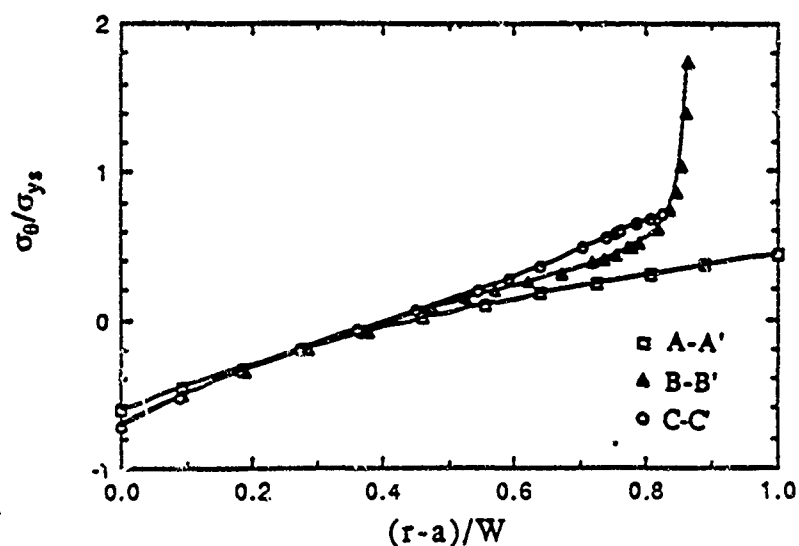
Figure 3.14 Tangential residual stress distributions due to 100 percent overstrain along plane A-A', B-B', and C-C' in a thick-walled pressure vessel with a conventional groove
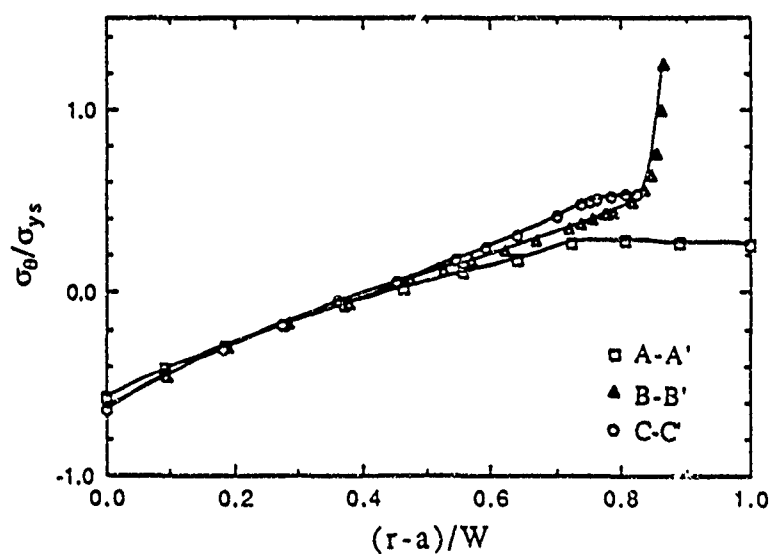
Figure 3.15 Tangential residual stress distributions due to 75 percent overstrain along plane A-A', B-B', and C-C' in a thick-walled pressure vessel with a conventional groove
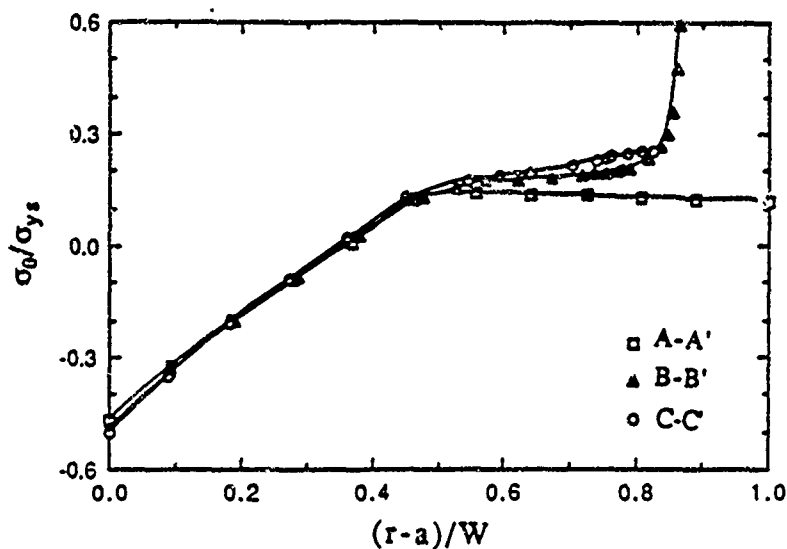
Figure 3.16 Tangential residual stress distributions due to 50 percent overstrain along plane A-A', B-B', and C-C' in a thick-walled pressure vessel with a conventional groove
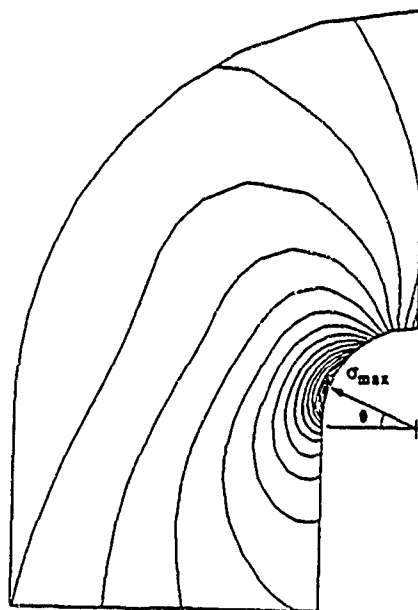
Figure 3.17 Maximum principal stress contours near the root of a conventional groove due to 100 percent overstrain
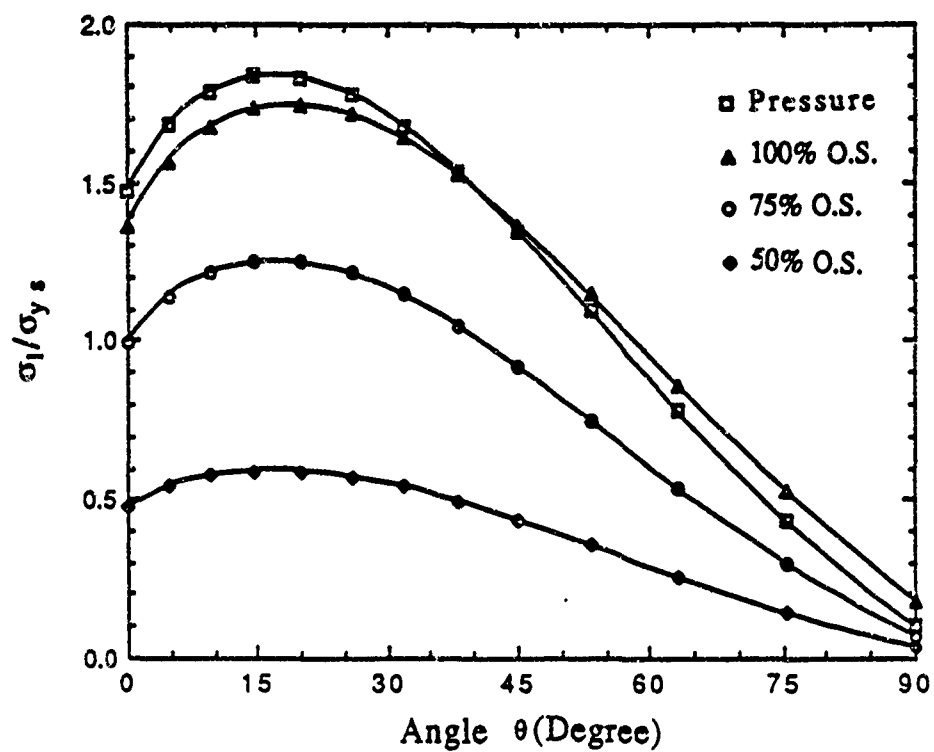
Figure 3.18 Maximum principal stress variations along the root of a conventional groove due to each loading condition
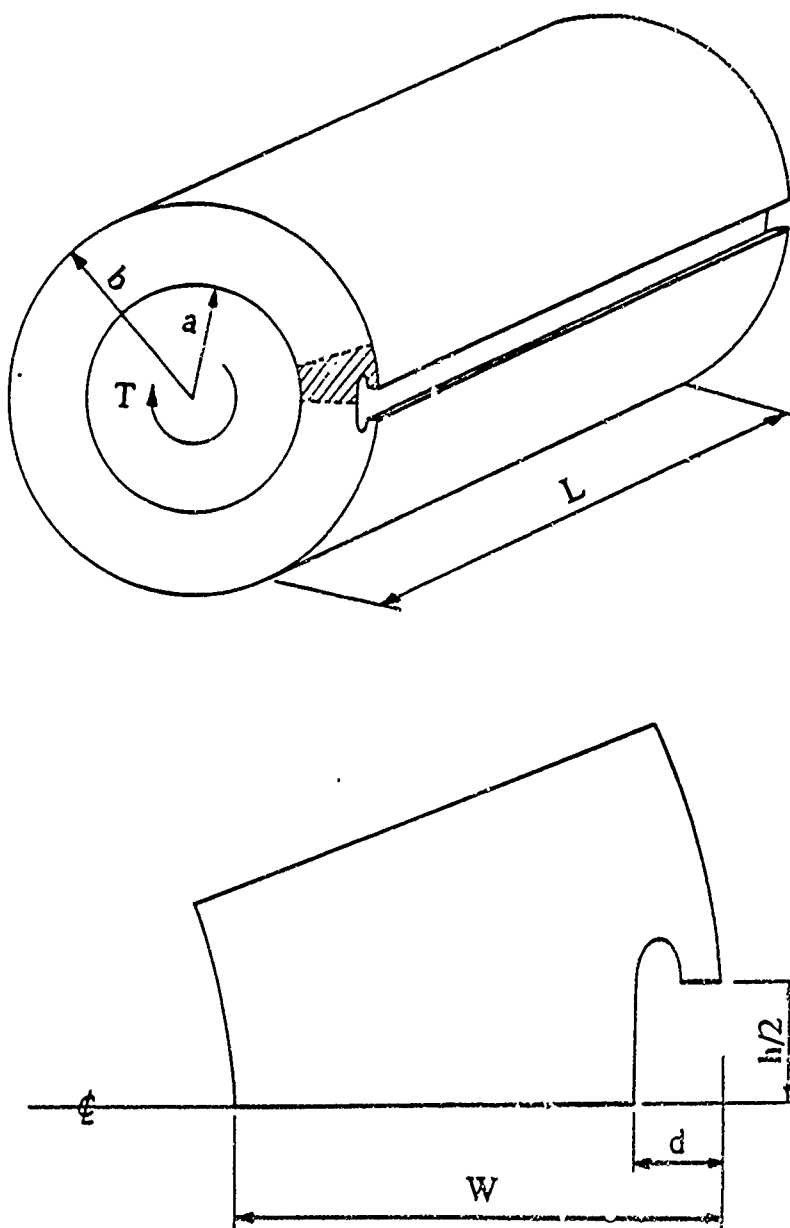
Figure 4.1 Thick-walled pressure vessel with an external groove subjected to torque (a=85, b=142, d=10, h=25, W=57, L=549, unit: mm)
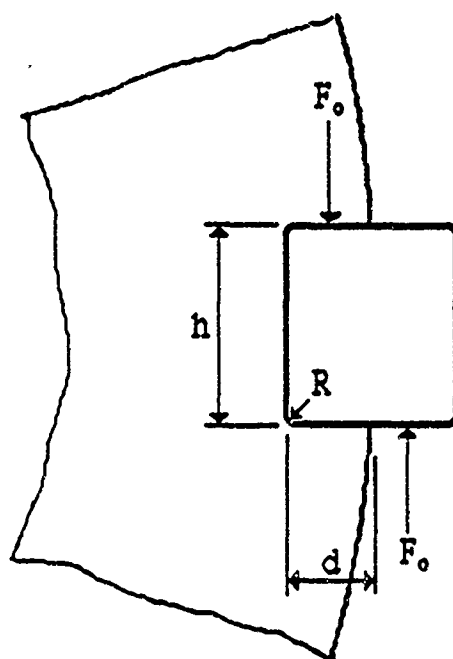
(a) Conventional groove
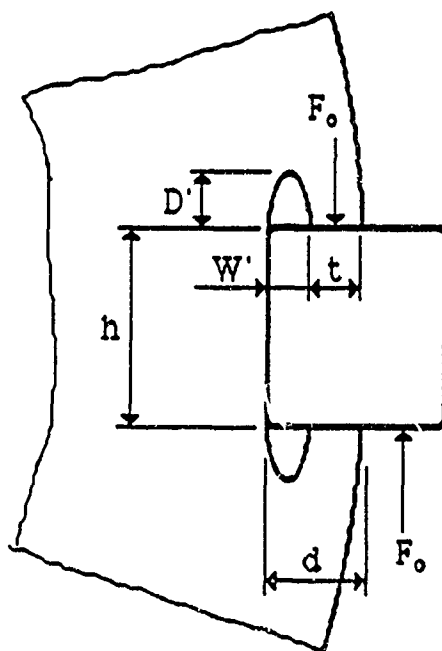
(b) Changed groove

Figure 4.2 Keyway and keyway groove in the thick-walled pressure vessel subjected to torque
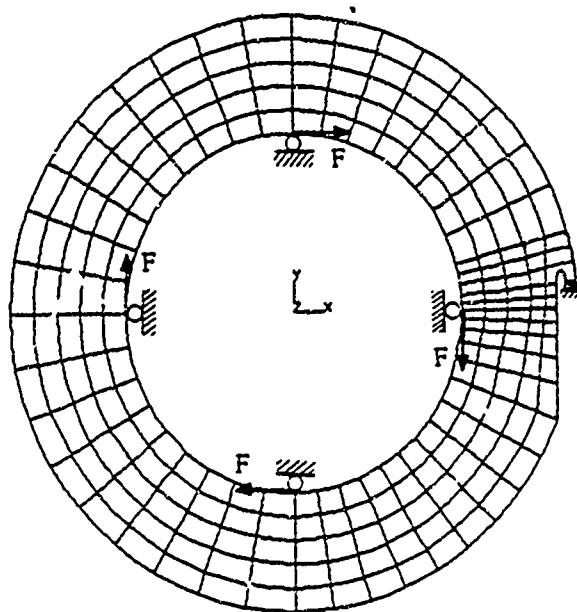
(a) Finite element mesh and boundary conditions
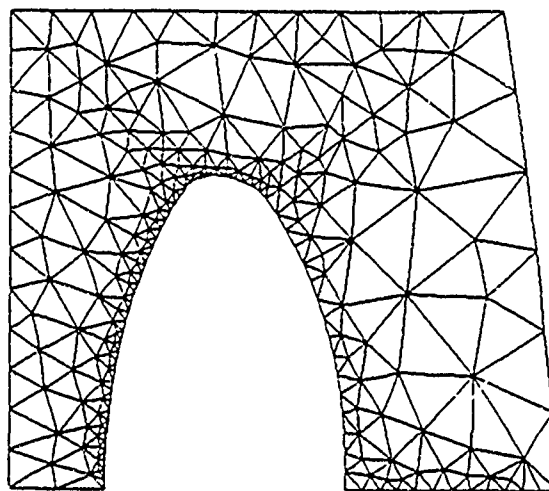
(b) Refined finite element mesh near the changed groove

Figure 4.3 Finite element model of thick-walled pressure vessel with
a changed external groove
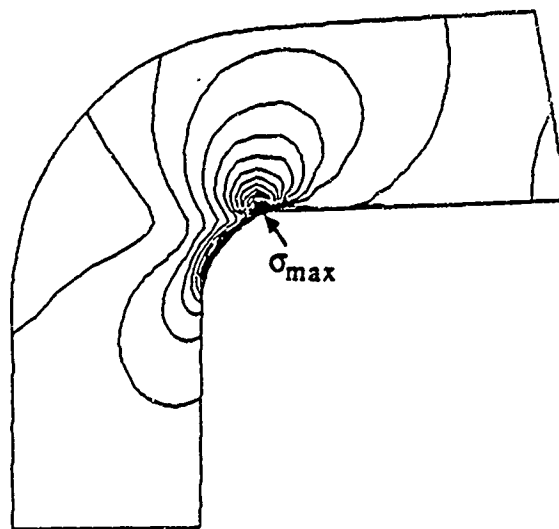
(a) Conventional groove
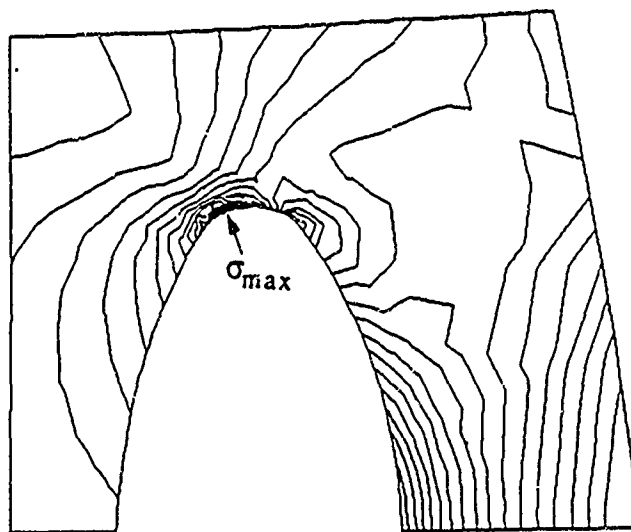
(b) Changed groove

Figure 4.4 Equivalent stress contours due to torsional loading near groove root region

208

Figure 4.5 Changed-groove geometry with different types of stress relief groove

```
            ┌─────────────────┐
            │  Start Routine  │
            └─────────────────┘
                    │
                    ▼
        ┌─────────────────────┐        Yes        ┌──────────────────────────────────┐
 ┌─────▶│  Sufficient Number  │─────────────────▶ │  Form Object Function Approximation│◀──┐
 │      │   of Design Sets ?  │                   └──────────────────────────────────┘   │
 │      └─────────────────────┘                              │                           │
 │                  │ No                                     ▼                           │
 │      ┌─────────────────────┐               ┌──────────────────────────────────┐       │
 │      │ Perform New Analysis│               │ Convert to Unconstrained Problem  │       │
 │      └─────────────────────┘               │ using Penalty Function            │       │
 │                  │                          └──────────────────────────────────┘       │
 │                  ▼                                        │                           │
 │      ┌─────────────────────┐               ┌──────────────────────────────────┐       │
 └──────│ Generate a Set of Random│           │ Search for Minimum of the Penalized│      │
        │ Design Variable Values  │           │ Objective Function Approximation   │      │
        └─────────────────────┘               └──────────────────────────────────┘       │
                                                           │                            │
                                                           ▼                            │
                                              ┌──────────────────────────────────┐      │
                                              │ Determine a New Set of Design     │      │
                                              │ Variable Values                   │      │
                                              └──────────────────────────────────┘      │
                                                           │                            │
                                                           ▼                            │
                                              ┌──────────────────────────────────┐      │
                                              │      Perform New Analysis         │      │
                                              └──────────────────────────────────┘      │
                                                           │                            │
                                  No                       ▼                            │
                              ┌────────────────────────────────────┐                    │
                              │           Converge ?               │────────────────────┘
                              └────────────────────────────────────┘
                                                │ Yes
                                                ▼
                                      ┌──────────────────┐
                                      │  Stop Routine    │
                                      └──────────────────┘
```

Figure 4.6 Quasi-optimization procedure used for groove shape optimization
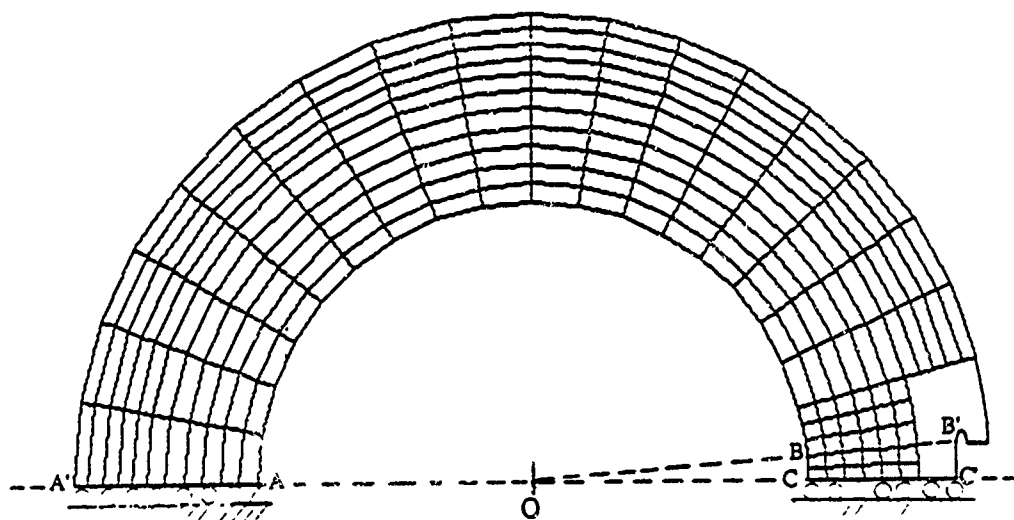
(a) Finite element mesh of model
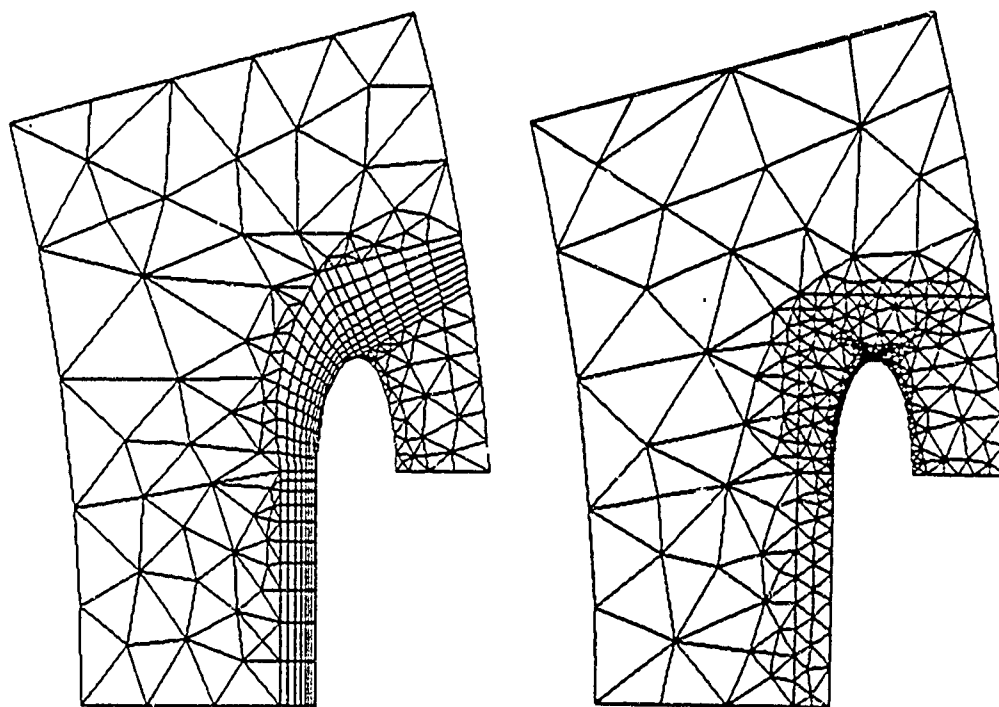
(b) Refined mesh near groove root

Figure 4.7 Finite element model of thick-walled pressure vessel used
for optimization of groove shape
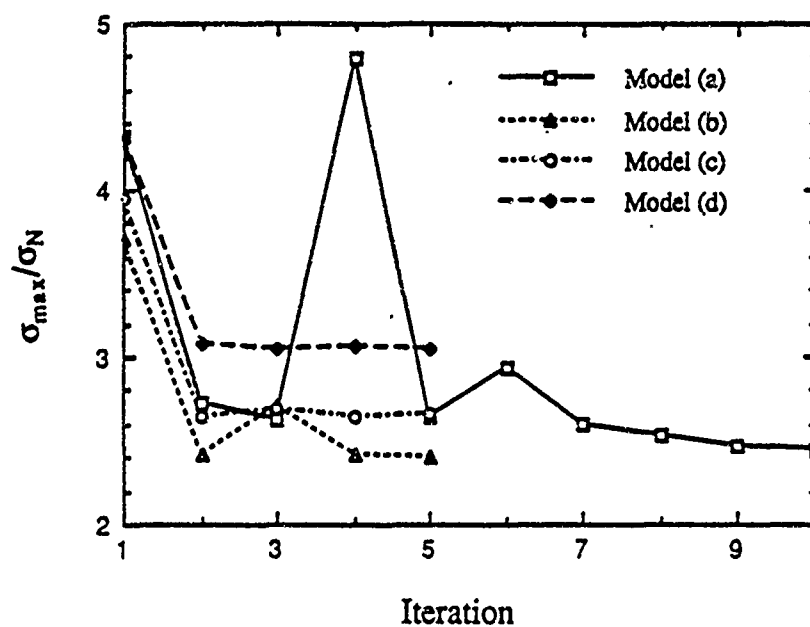
Figure 4.8 Minimization of stress concentration from optimization of each model in type I
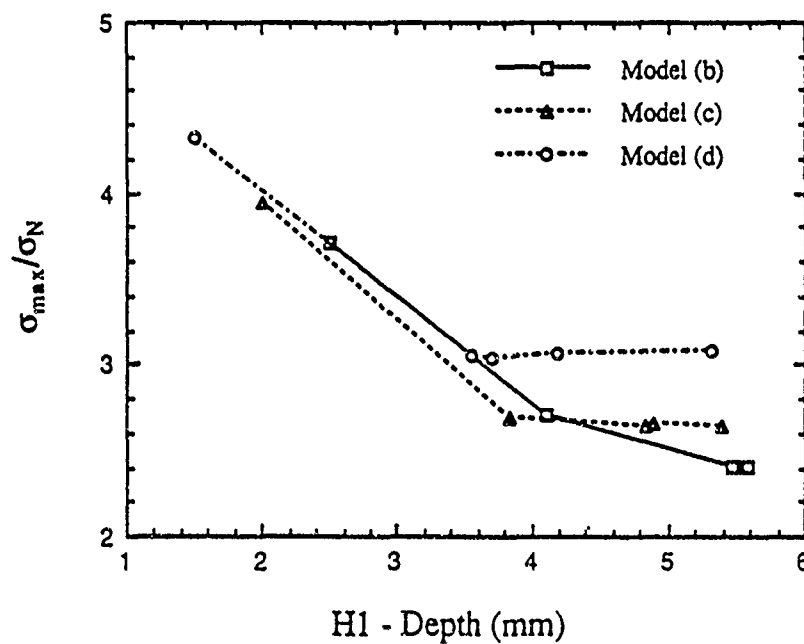
Figure 4.9 Stress concentration factors versus depth-of-stress relief groove in type I
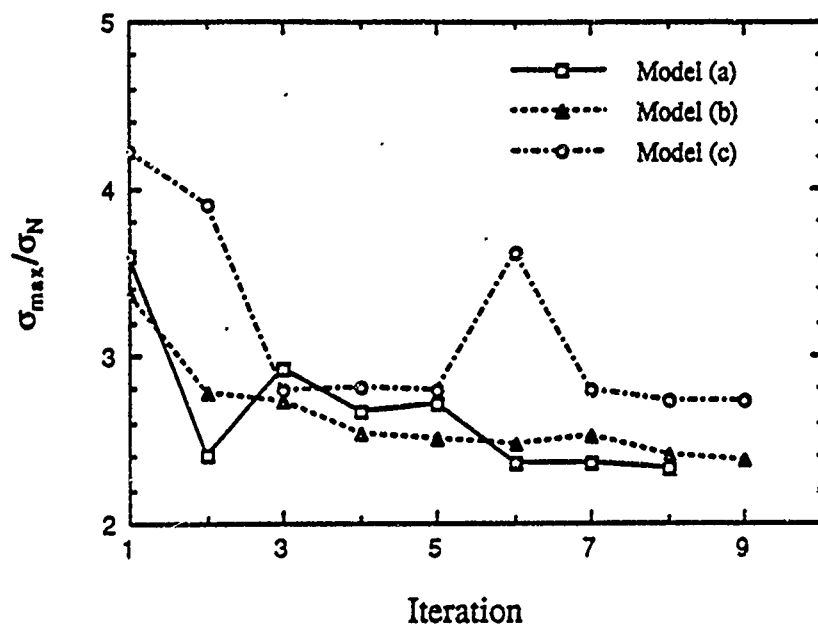
Figure 4.10 Minimization of stress concentration from optimization of each model in type II
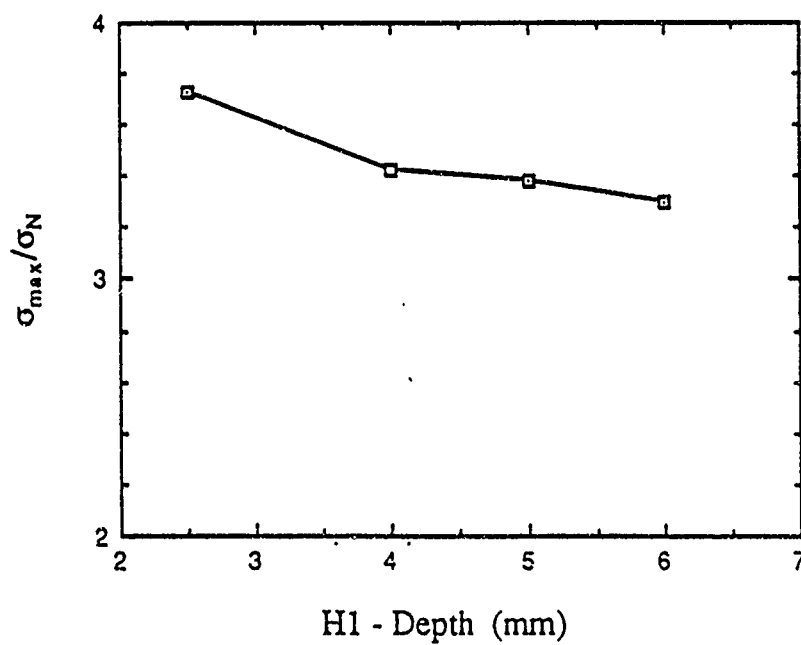
Figure 4.11 Stress concentration factor versus depth-of-stress relief groove in type III
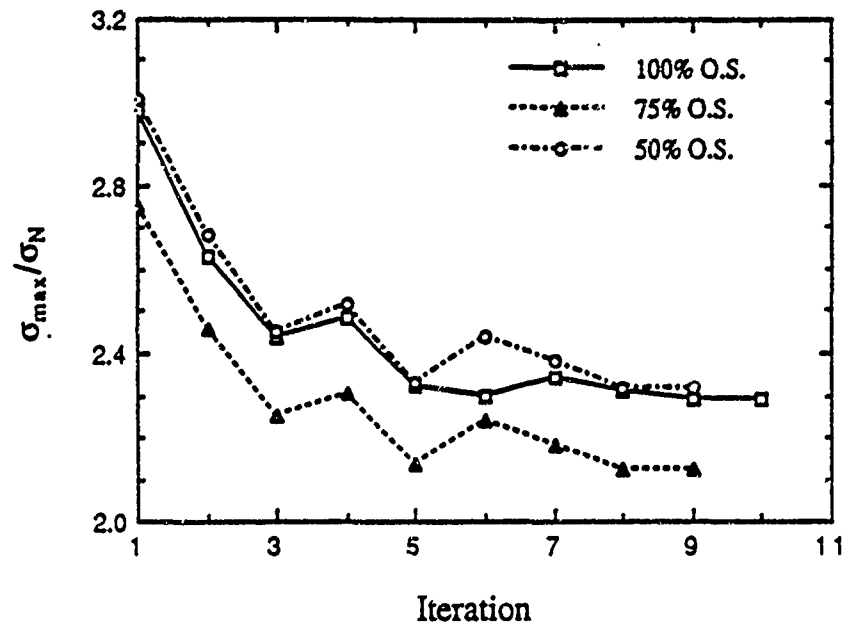
Figure 4.12 Minimization of stress concentration from optimization of stress groove of type IV for each overstrain loading case
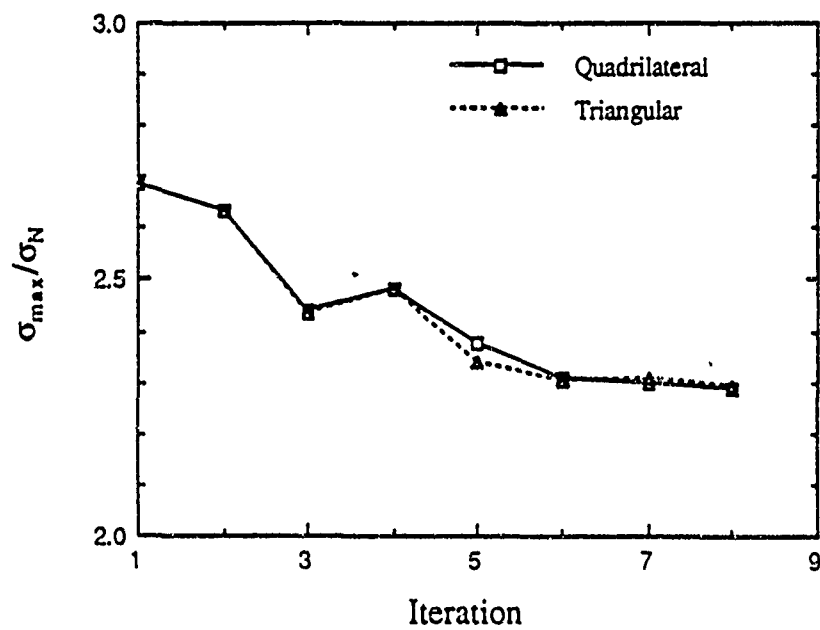
Figure 4.13 Comparison of element types in optimization of stress relief groove in type IV
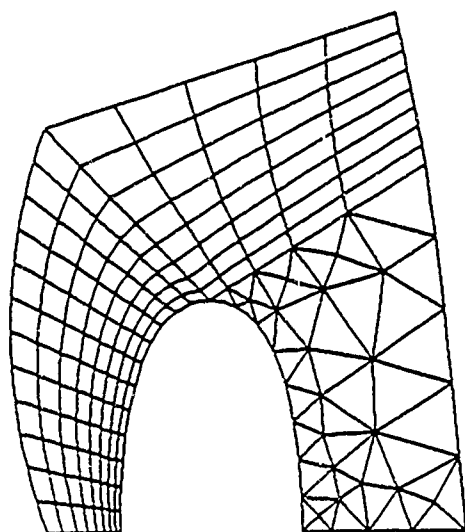
(a) type I
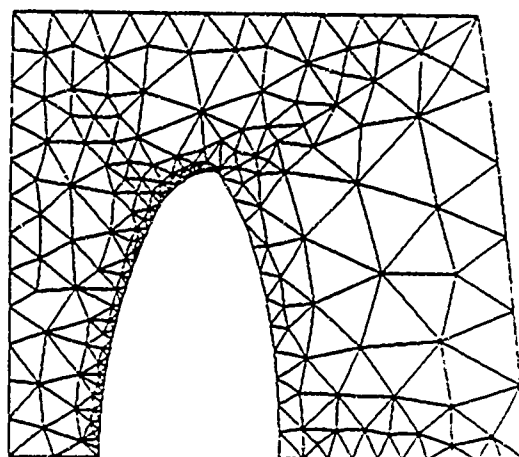
(b) type II
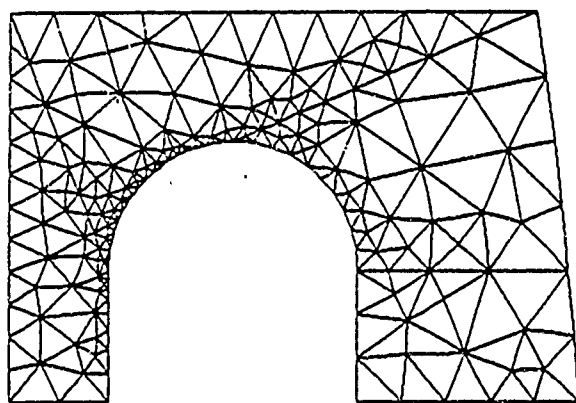
(c) type III
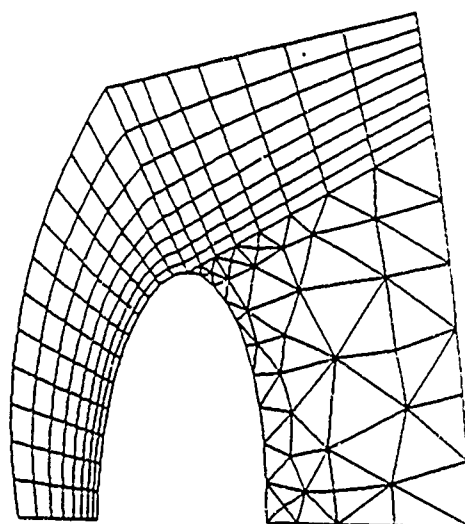
(d) type IV

Figure 4.14 Finite element mesh for each type of optimum stress relief groove
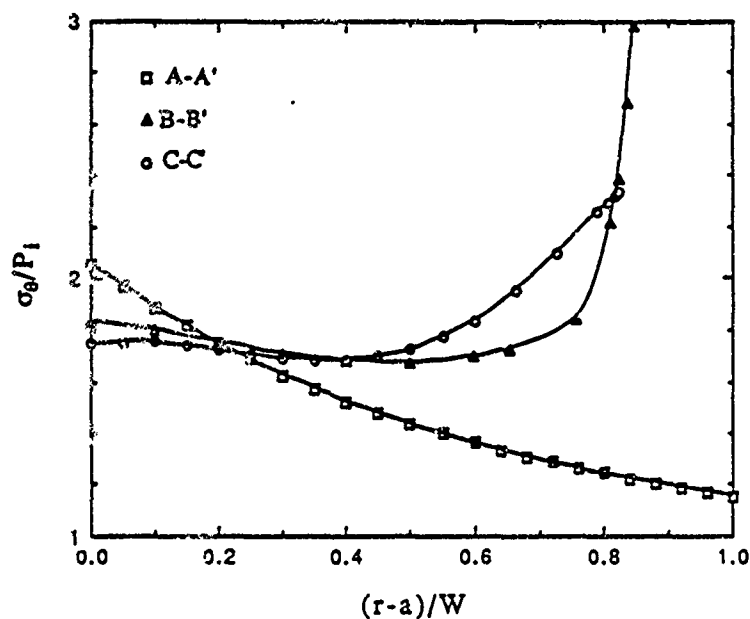
Figure 4.15 Tangential stress distribution in the thick-walled pressure vessel with the elliptic stress relief groove due to internal pressure only
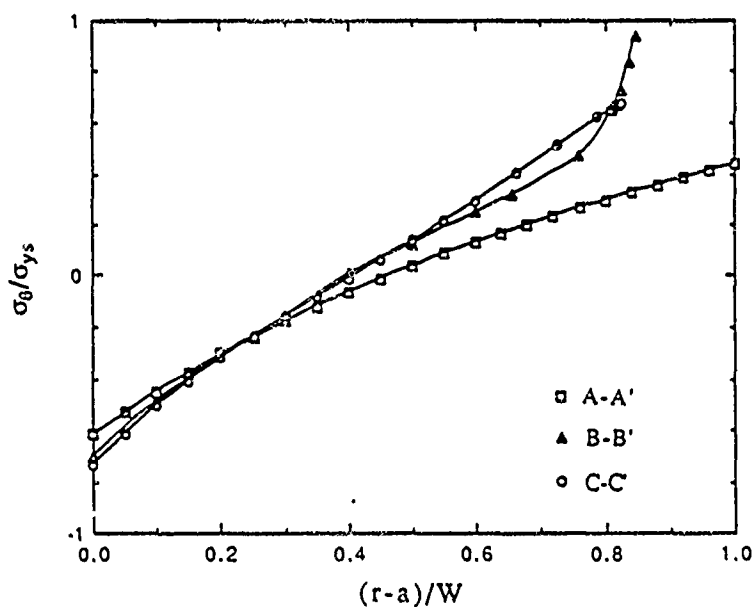
Figure 4.16 Tangential residual stress distribution in the thick-walled pressure vessel with the elliptic stress relief groove due to 100 percent overstrain loading only

216
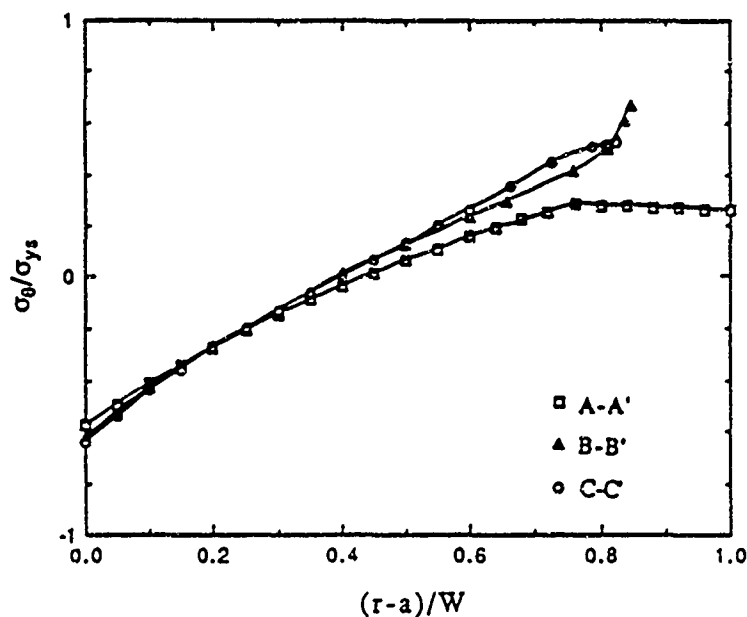
Figure 4.17 Tangential residual stress distribution in the thick-walled pressure vessel with the elliptic stress relief groove due to 75 percent overstrain loading only
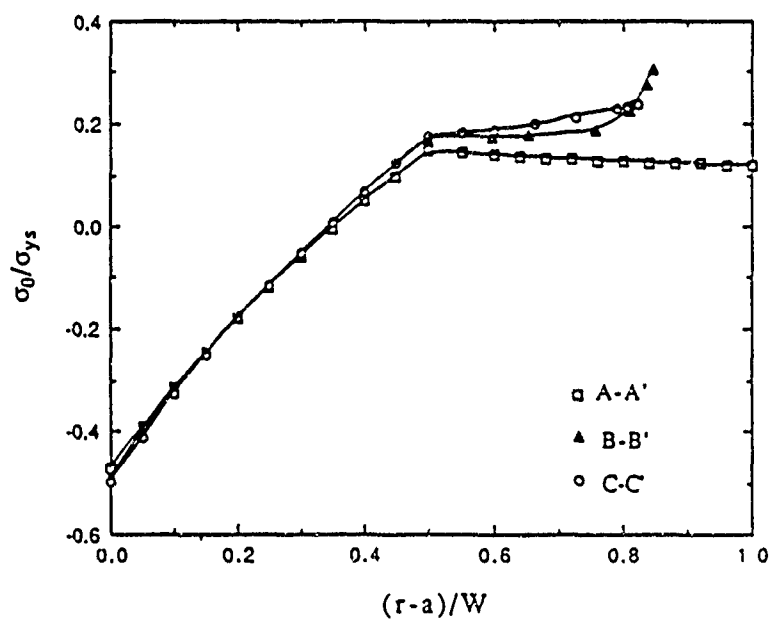
Figure 4.18 Tangential residual stress distribution in tne thick-walled pressure vessel with the elliptic stress relief groove due to 50 percent overstrain loading only
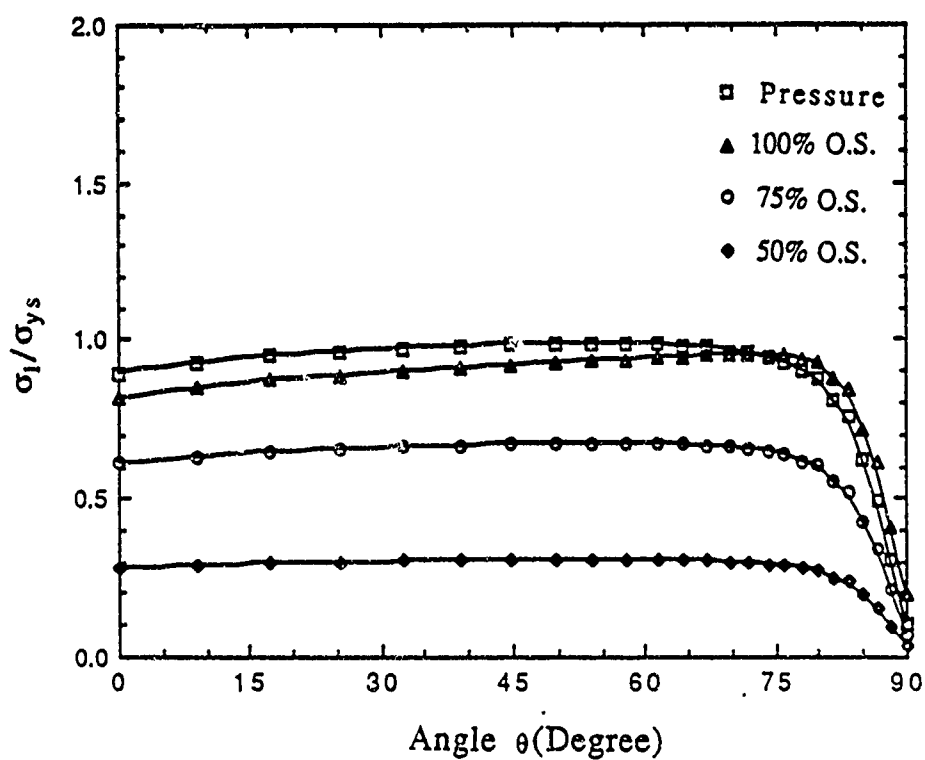
Figure 4.19 Maximum principal stress distribution along the elliptic stress relief groove contour for each loading condition
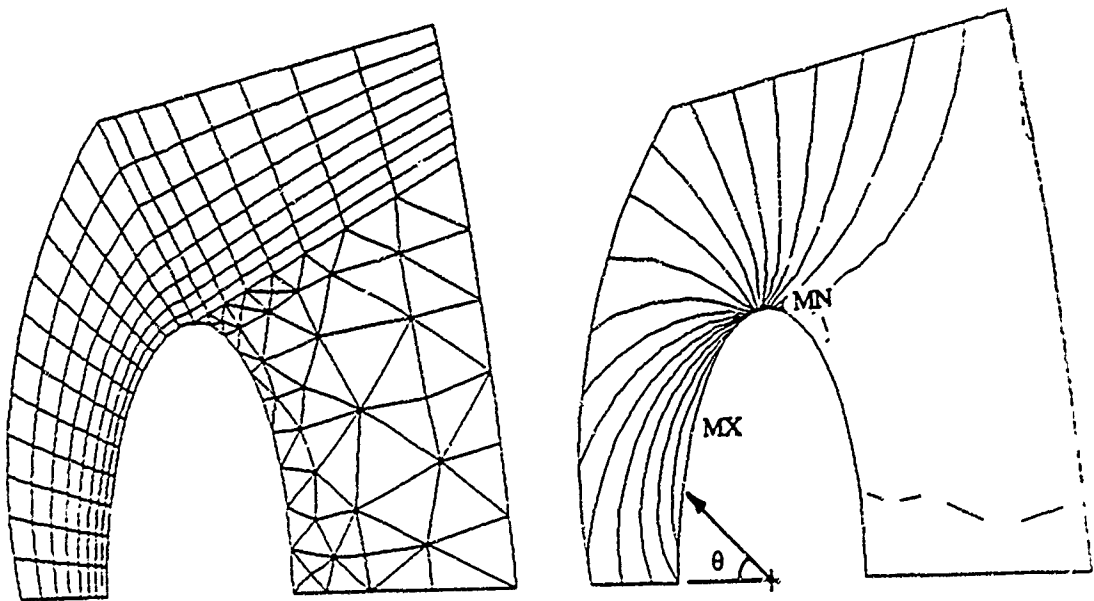
(a) 8-node isoparametric quadrilateral element
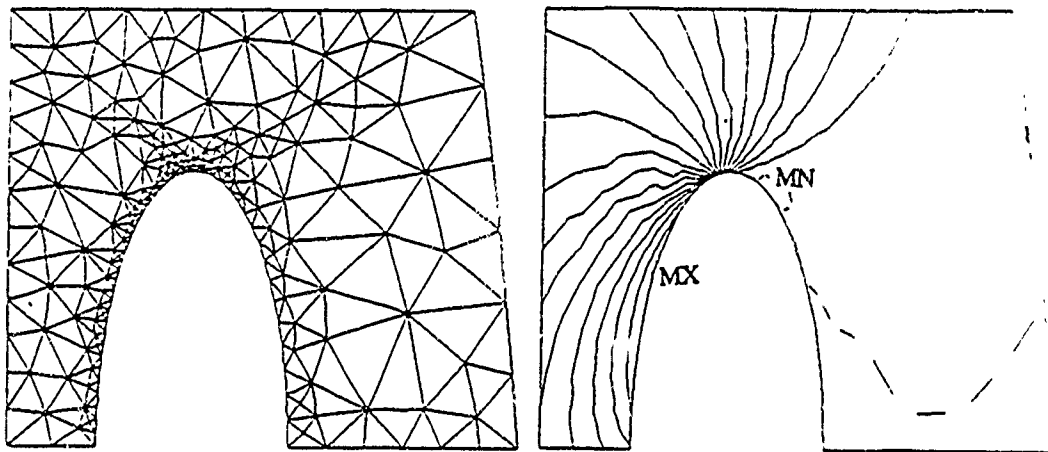
(b) 6-node isoparametric triangular element

Figure 4.20 Refined finite element mesh and maximum principal stress contours near the optimized elliptic stress relief groove
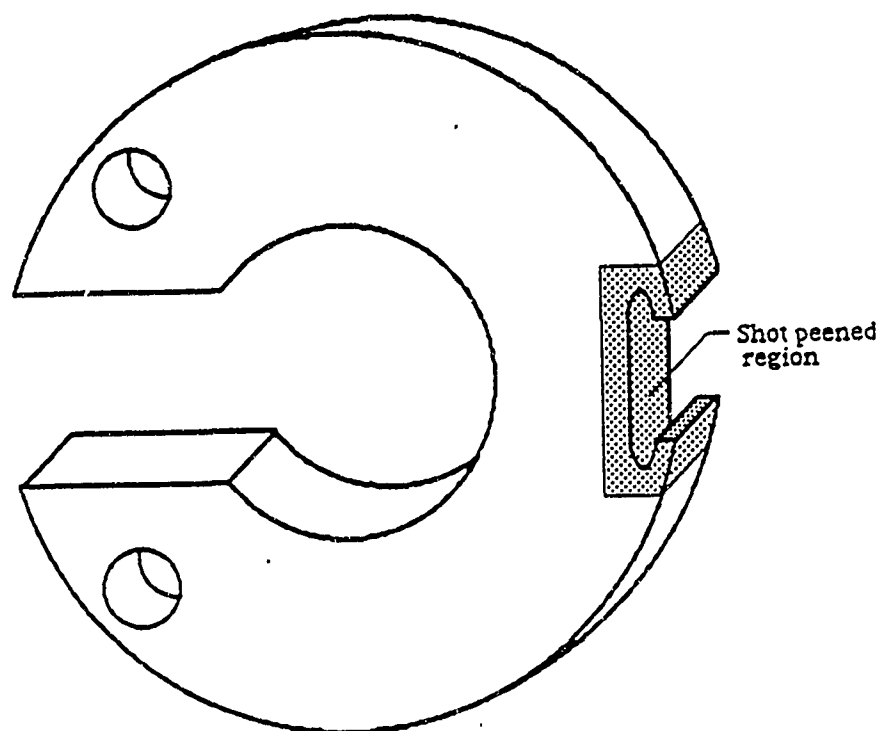
Figure 5.1 Schematic of shot peened region of changed external groove in simulation fatigue specimen
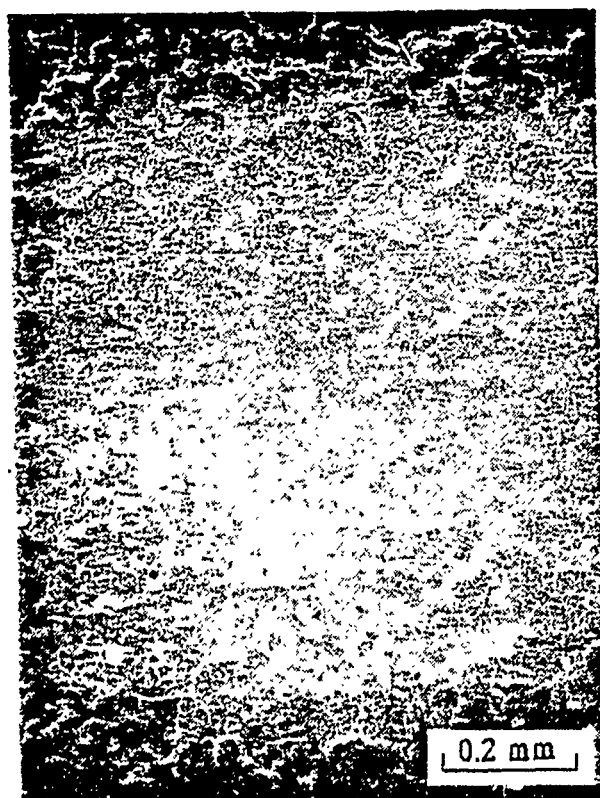
Figure 5.2 SEM photo of shot peened surface (100X)
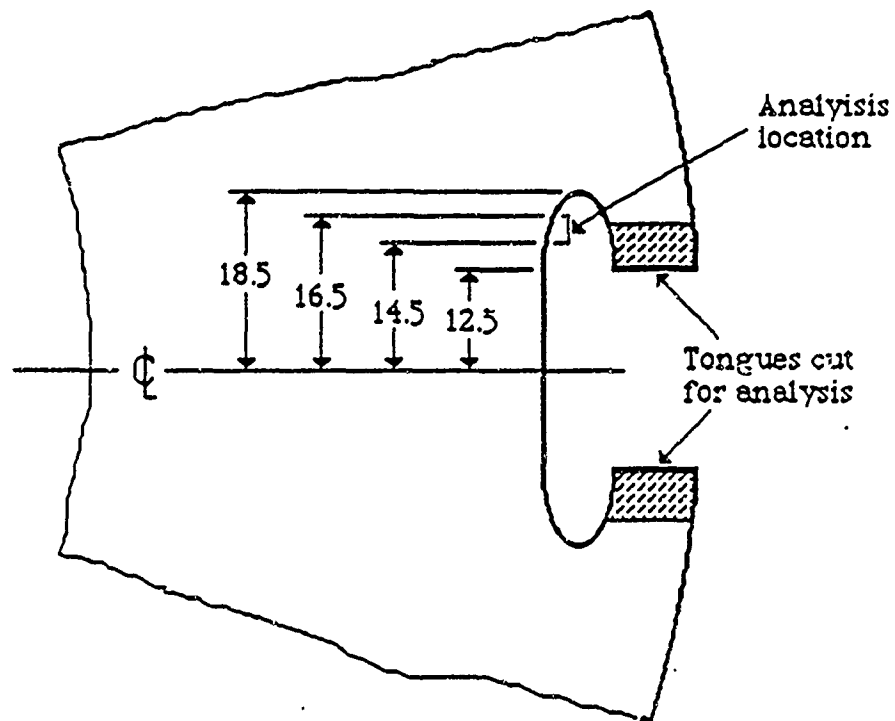
Figure 5.3 Location of X-ray diffraction analysis in changed external groove
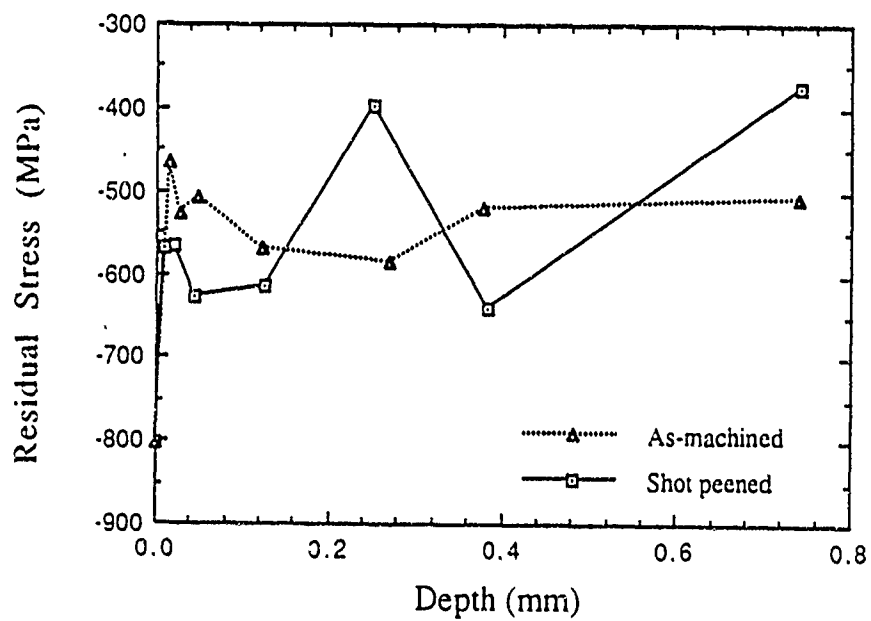
Figure 5.4 Residual stress distributions near the changed external groove using X-ray diffraction method
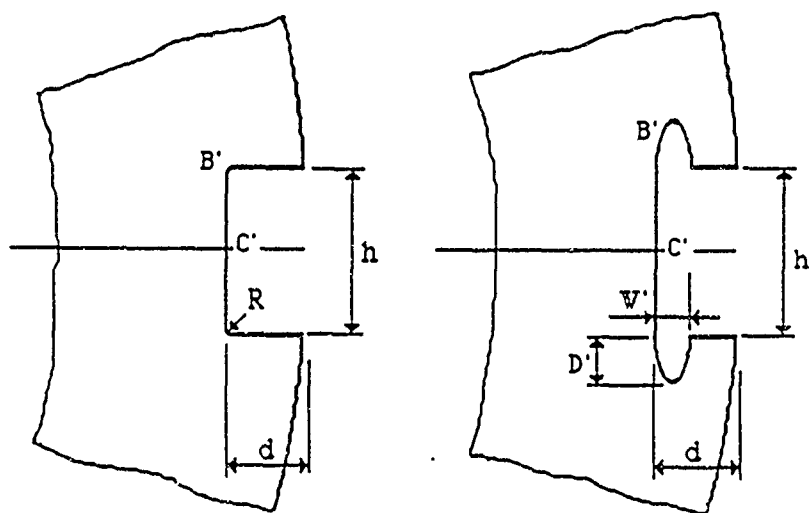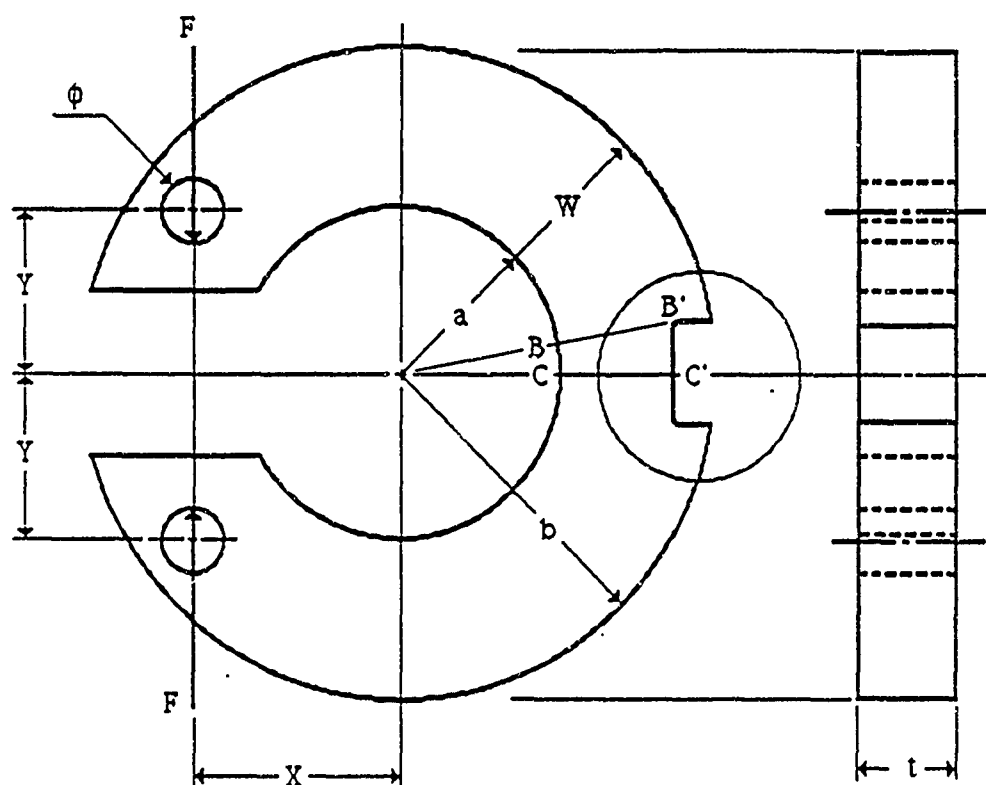
Figure 6.1 Simulation fatigue specimens with conventional and
changed external grooves (a=85, b=142, W=57, f=19, X=98,
Y=86, t=20, R=1.5, h=25, d=10, W'=4.3, D'=6.0, unit: mm)
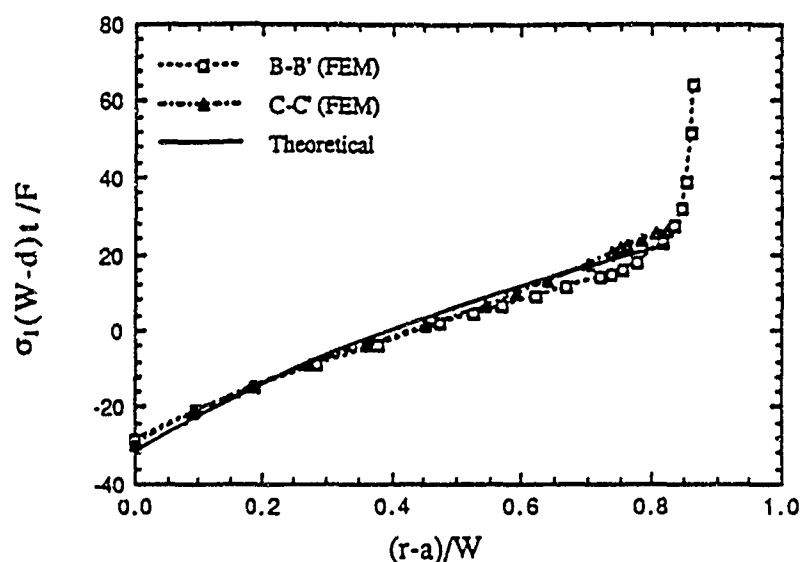
Figure 6.2 Maximum principal stress distributions along B-B' and C-C' in the simulation specimen with conventional external groove due to simulation loading
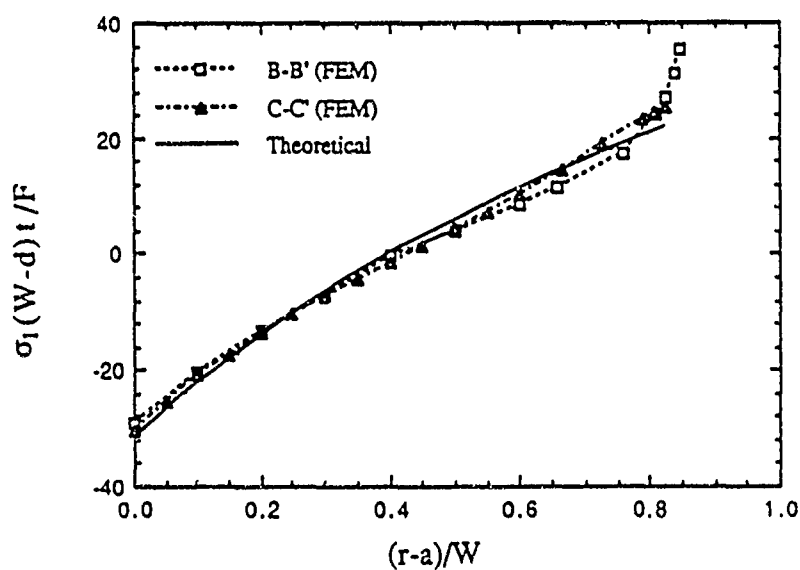
Figure 6.3 Maximum principal stress distributions along B-B' and C-C' in the simulation specimen with changed external groove due to simulation loading
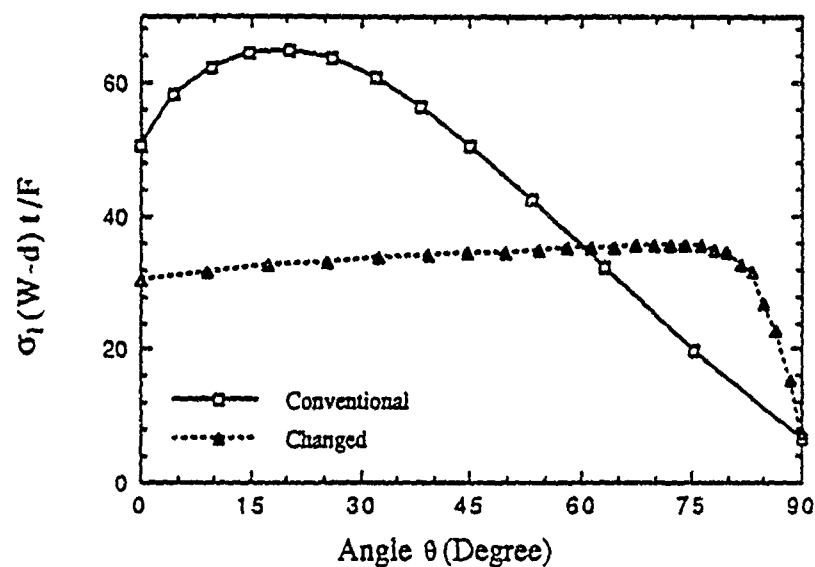
Figure 6.4 Maximum principal stress distributions along the external groove contours

Section G-G
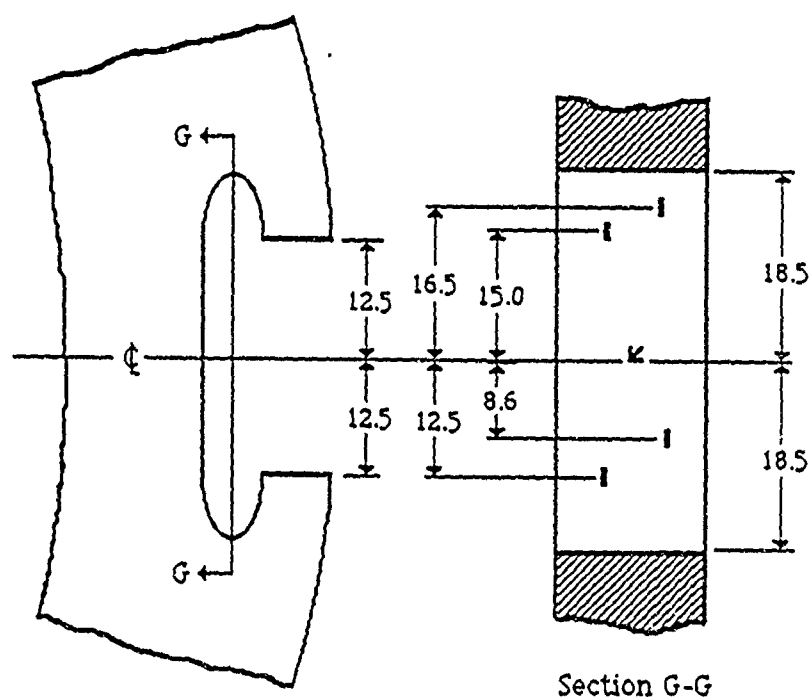
Figure 6.5 Strain gage locations for verification of finite element stress analysis results using simulation specimen with changed external groove
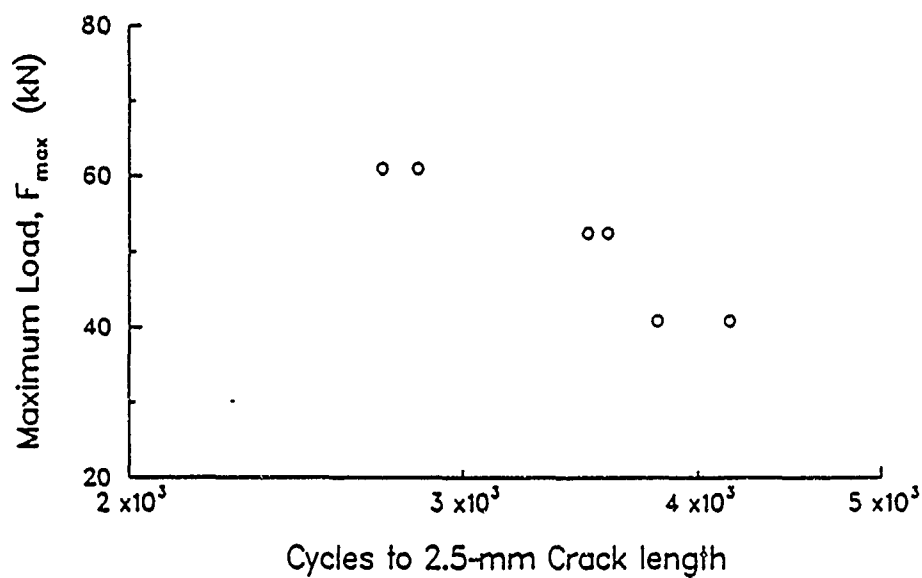
Figure 6.6 Simulation fatigue life to 2.5-mm crack length for conventional groove
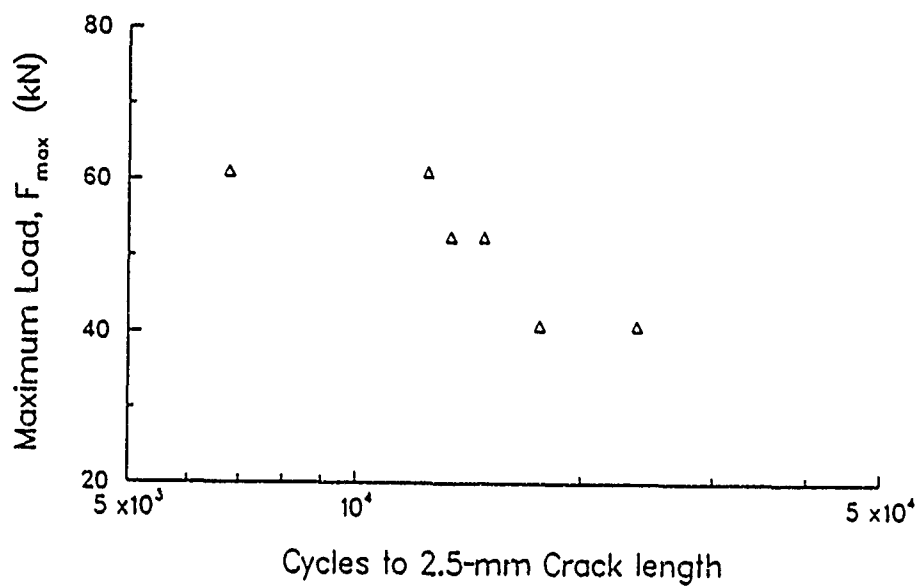
Figure 6.7 Simulation fatigue life to 2.5-mm crack length for changed groove
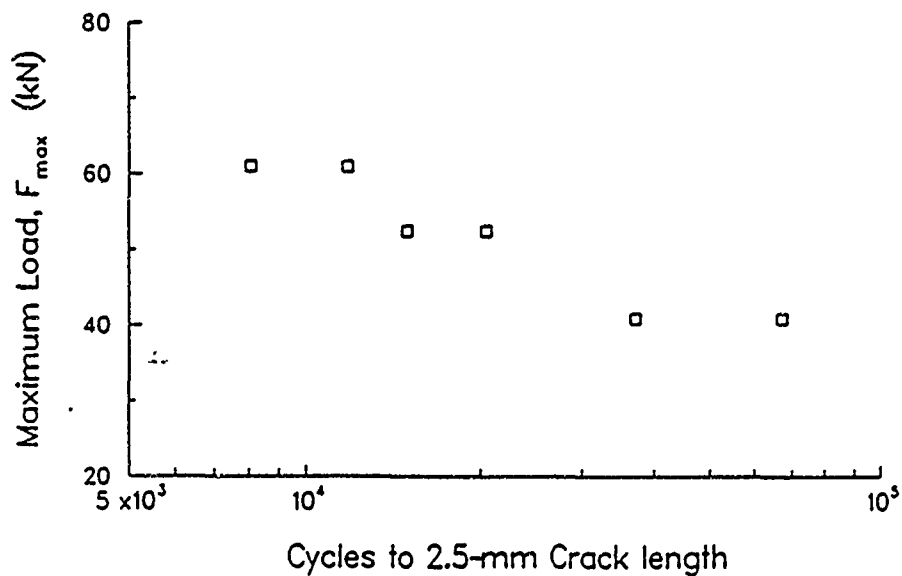
Figure 6.8 Simulation fatigue life to 2.5-mm crack length for shot peened-changed groove
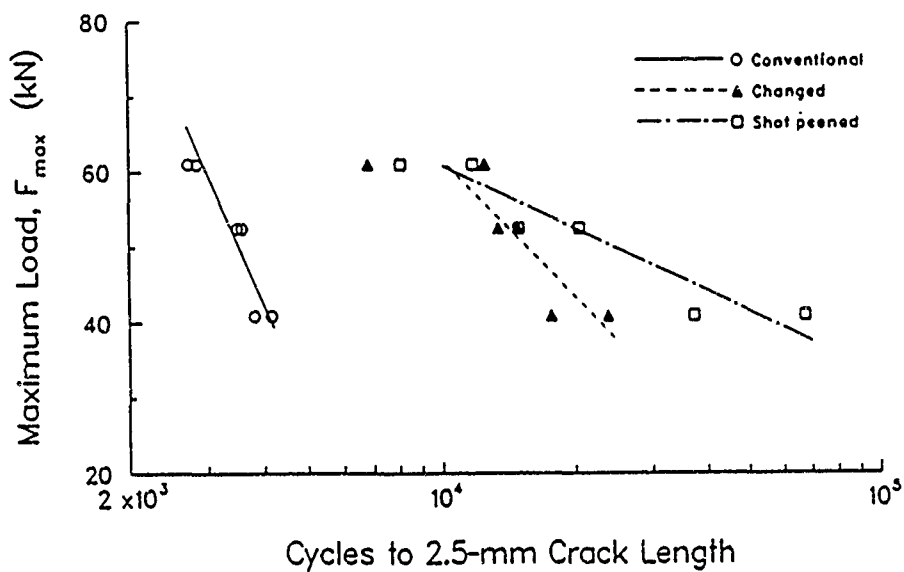
Figure 6.9 Simulation fatigue life to 2.5-mm crack length for all types of groove
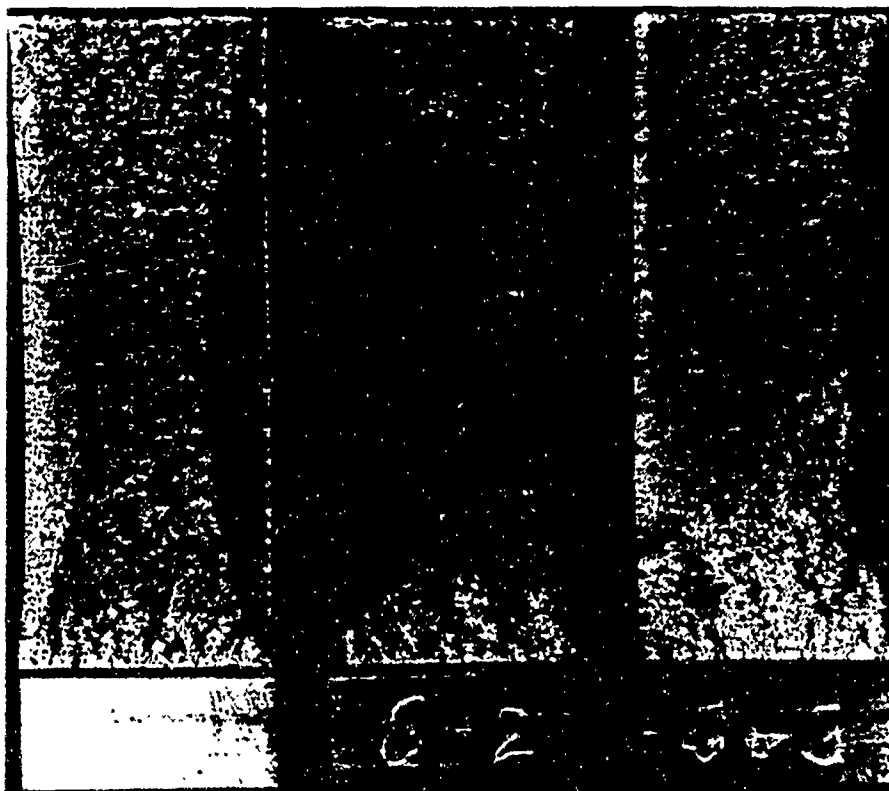
(a) 100 percent O. S.   (b) 75 percent O. S.   (c) 50 percent O. S.

Figure 6.10   Typical macrofracture surfaces(2X) of simulation
specimens with a conventional external groove
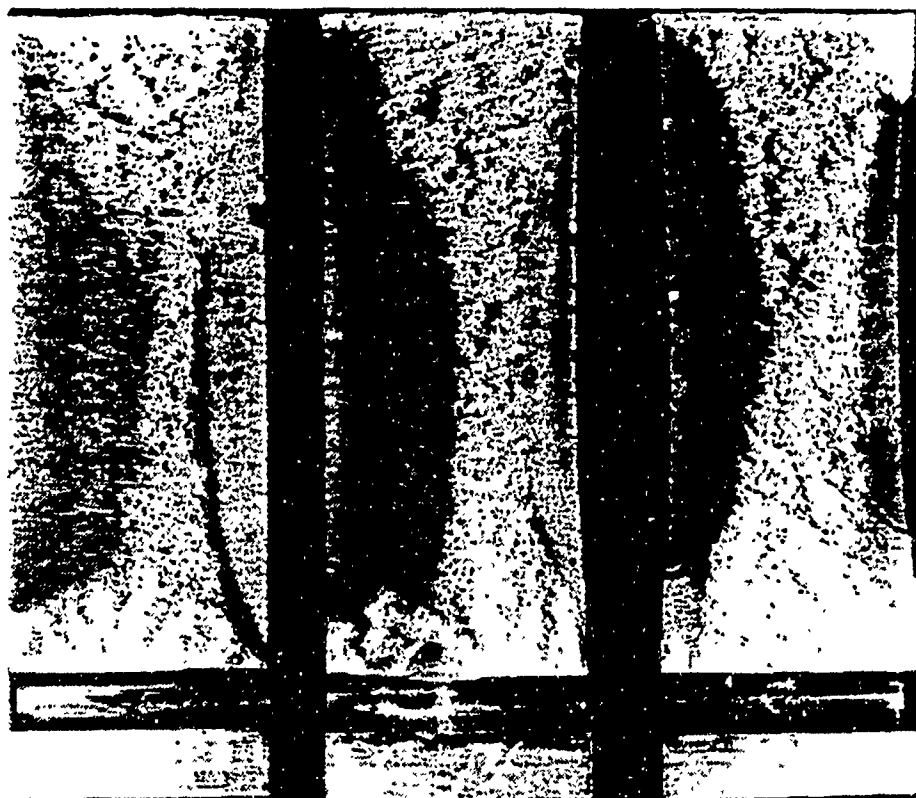
(a) 100 percent O. S.   (b) 75 percent O. S.   (c) 50 percent O. S.

Figure 6.11 Typical macrofracture surfaces(2X) of simulation
specimens with a changed external groove
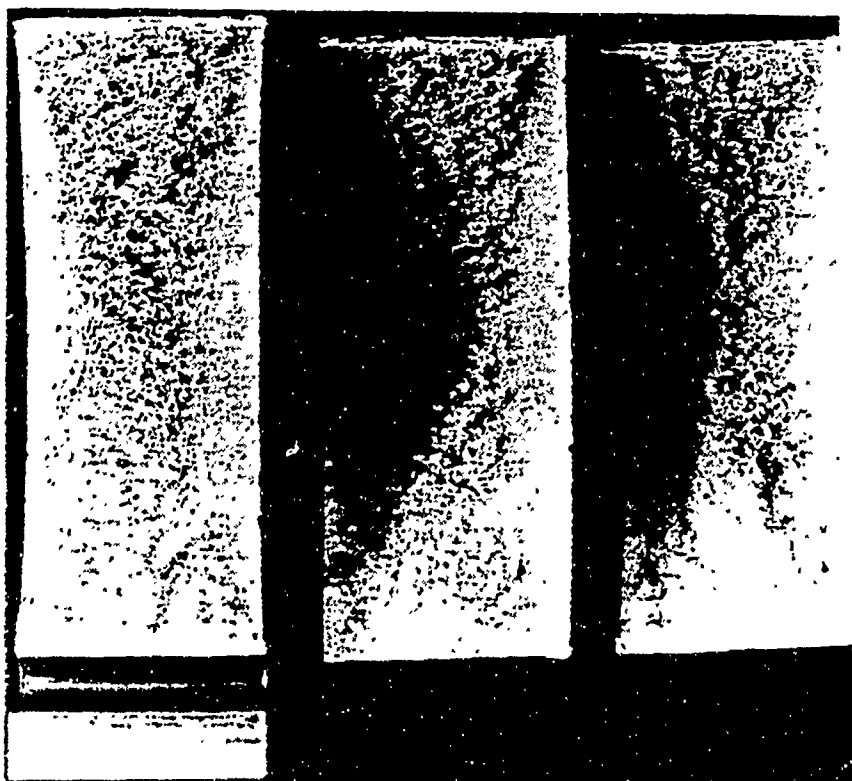
(a) 100 percent O. S.   (b) 75 percent O. S.   (c) 50 percent O. S.

Figure 6.12 Typical macrofracture surfaces(2X) of simulation
specimens with a shot peened-changed external groove
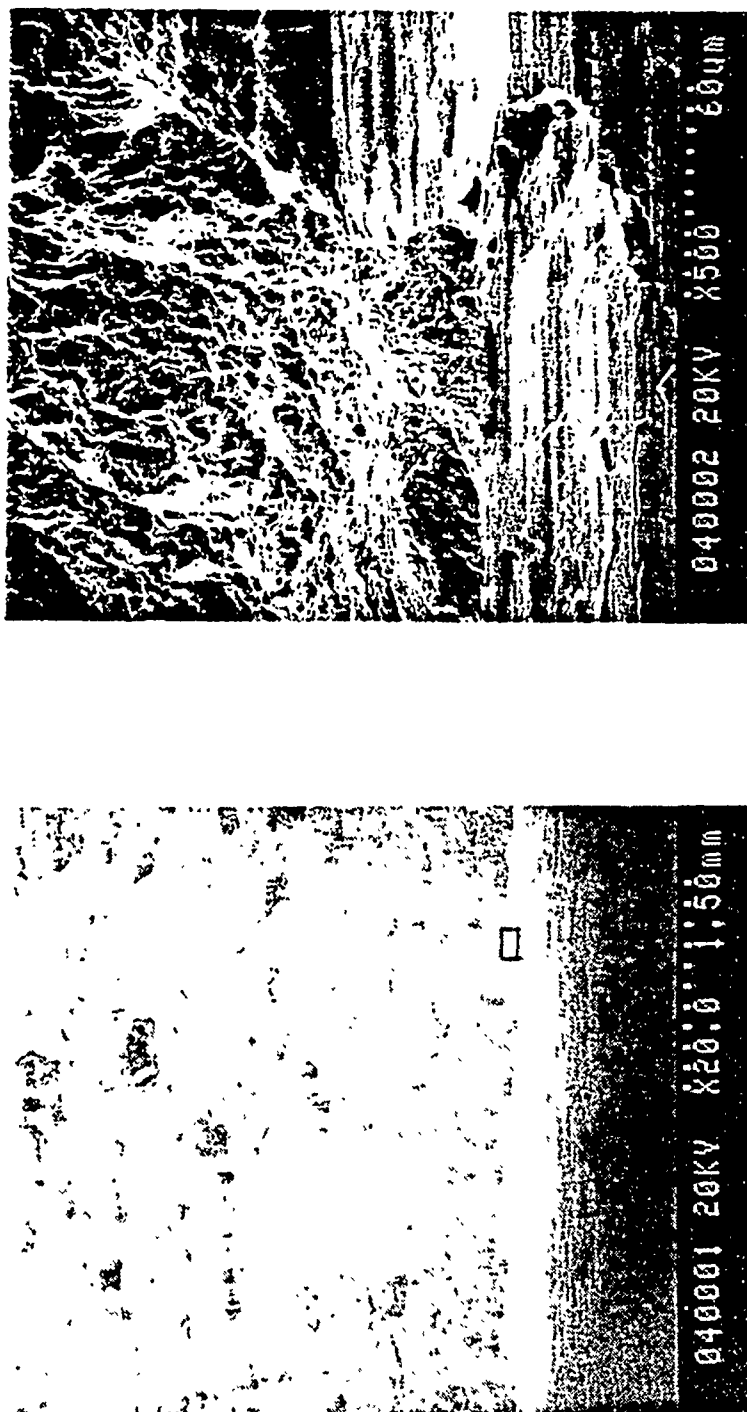
Figure 6.13 Typical fracture surface(20X and 500X) of fatigue crack formation and growth region of conventional groove
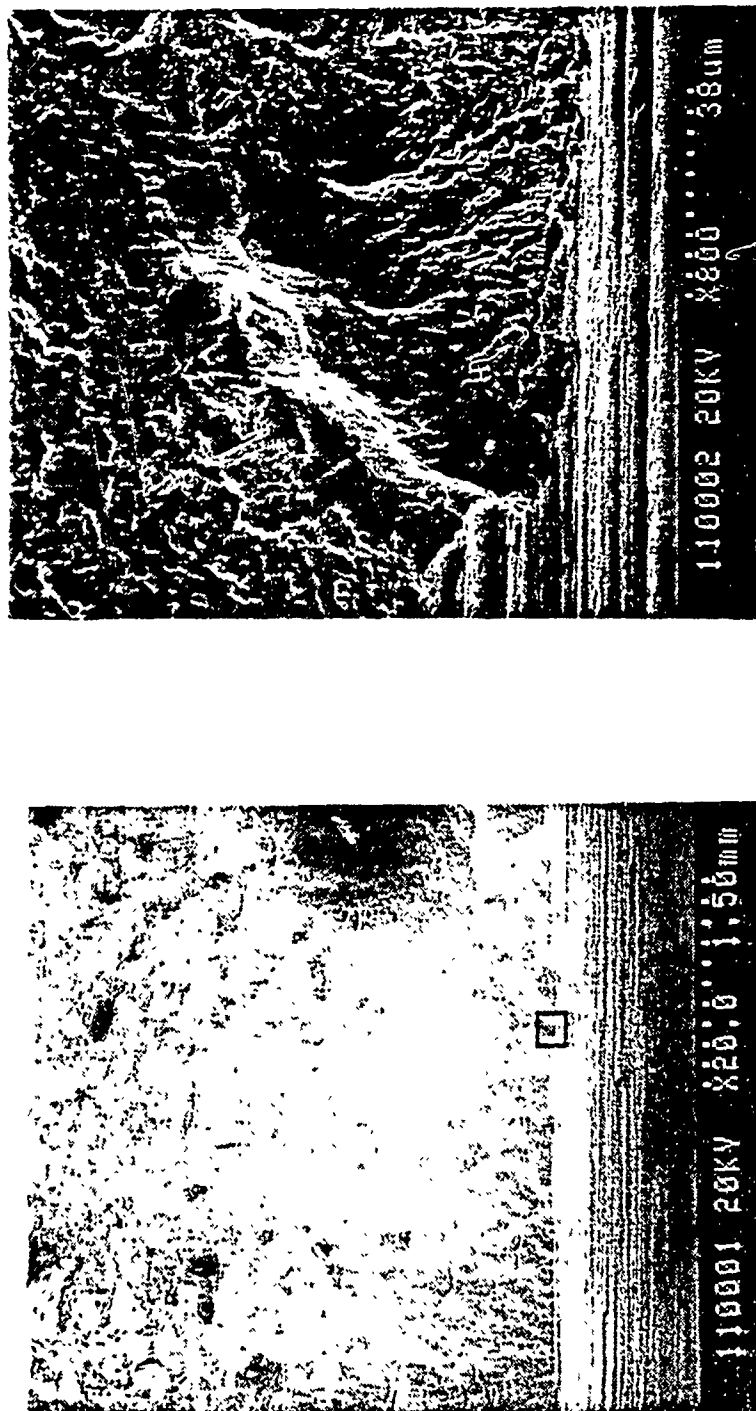
Figure 6.14 Typical fracture surface(20X and 800X) of fatigue crack formation and growth region of changed groove

232
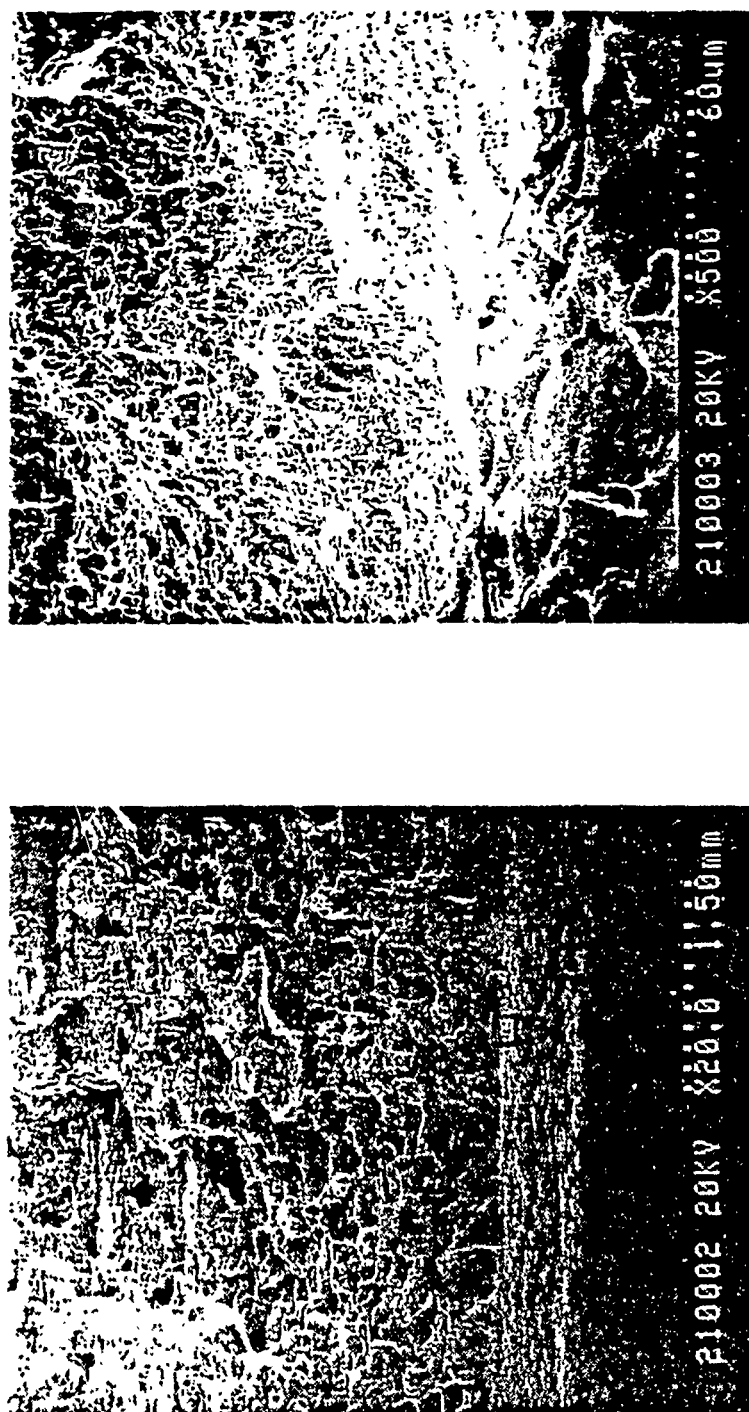
Figure 6.15 Typical fracture surface(20X and 500X) of fatigue crack formation and growth region of shot peened-changed groove

Figure 6.17 Typical final fracture region
(100X, 500X)

Figure 6.16 Typical fatigue crack growth
region(1000X)

234
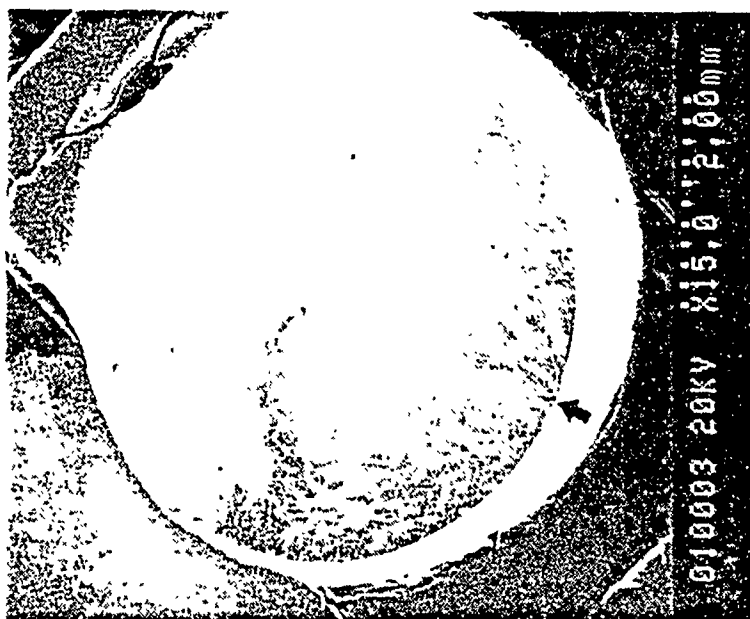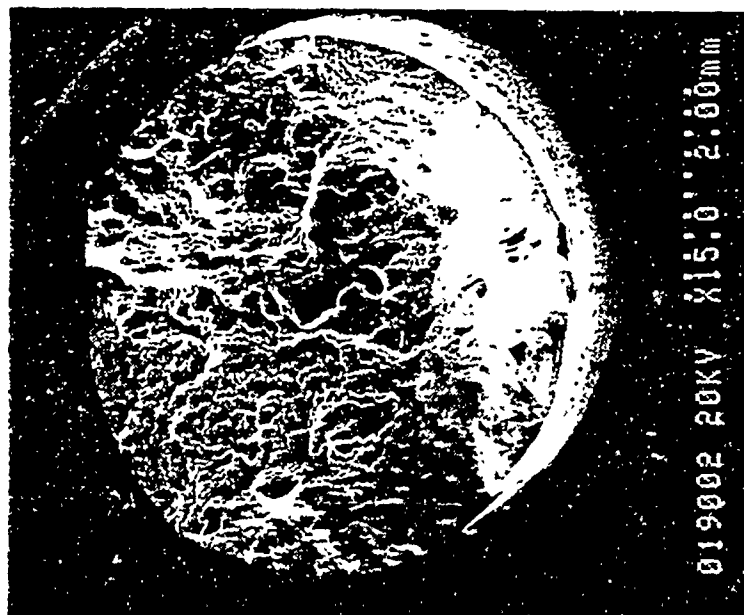
(b) $\Delta\varepsilon/2=0.008$

(a) $\Delta\varepsilon/2=0.003$

Figure 7.1 Typical fracture surfaces(15X) of R=-1
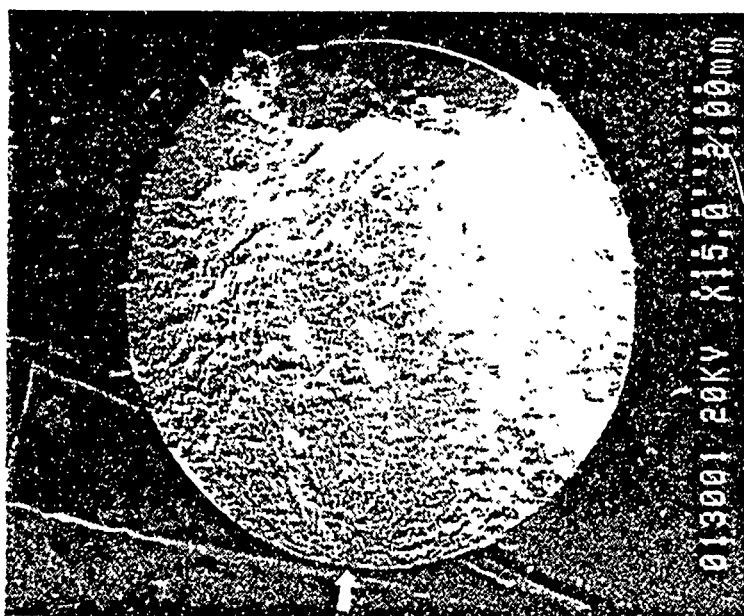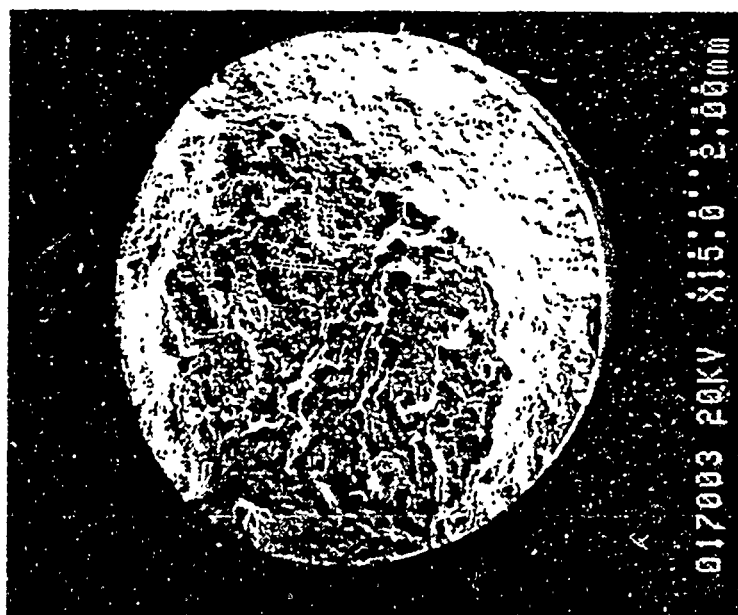
(b) $\Delta\varepsilon/2 = 0.010$

(a) $\Delta\varepsilon/2 = 0.003$

Figure 7.2 Typical fracture surfaces(15X) of R=-2
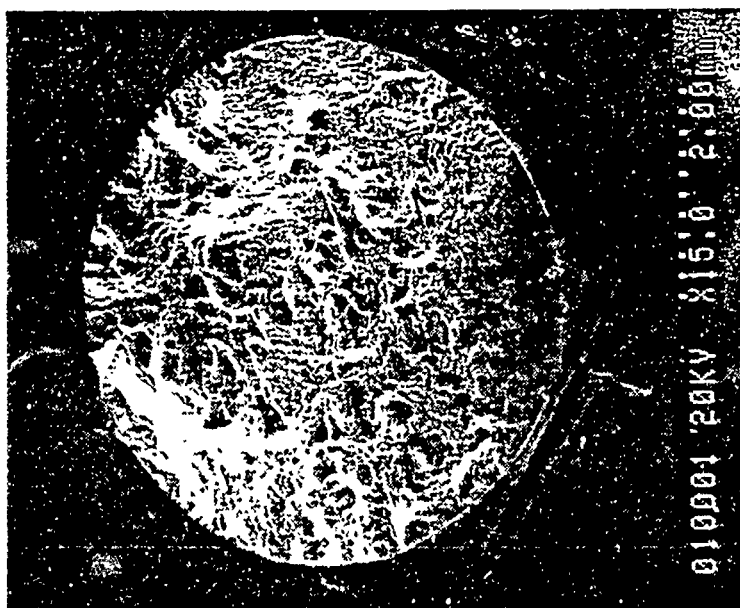
(b) $\Delta\varepsilon/2=0.009$, R=0.5
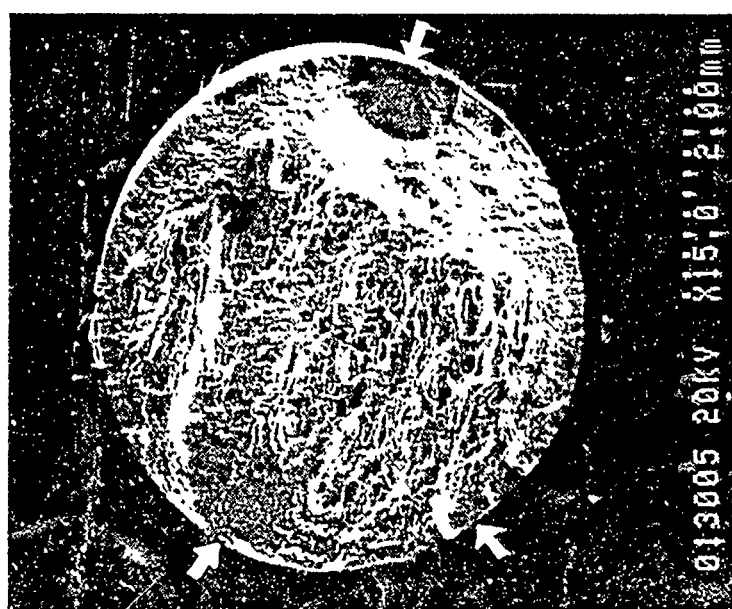
(a) $\Delta\varepsilon/2=0.0025$, R=0.75

Figure 7.3 Typical fracture surfaces(15X) of R $\geq$ 0
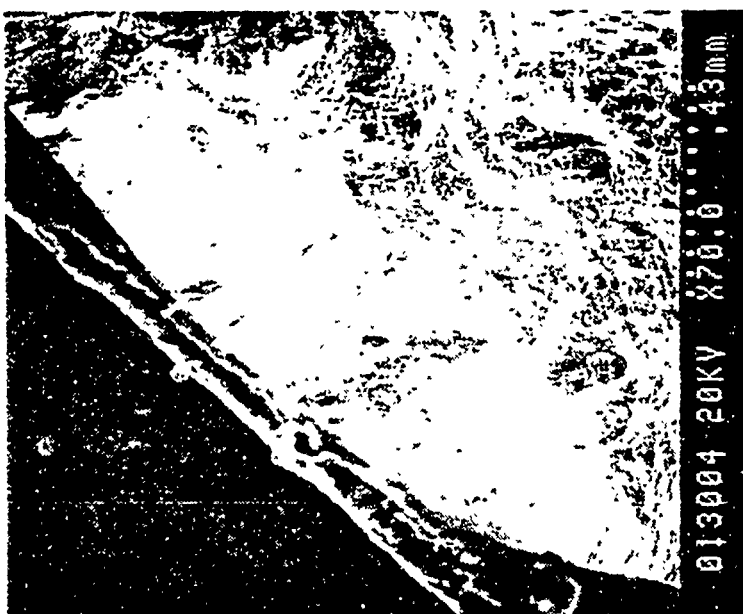
Figure 7.5 Fatigue crack formation site(70X)
from R=0.5, Δε/2=0.009
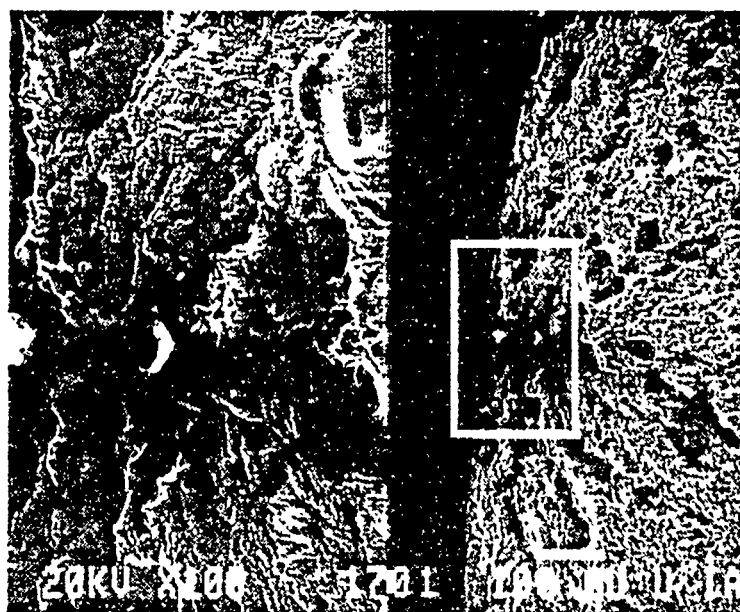
Figure 7.4 Fatigue crack formation site(100X
and 500X) from R=-2, Δε/2=0.003
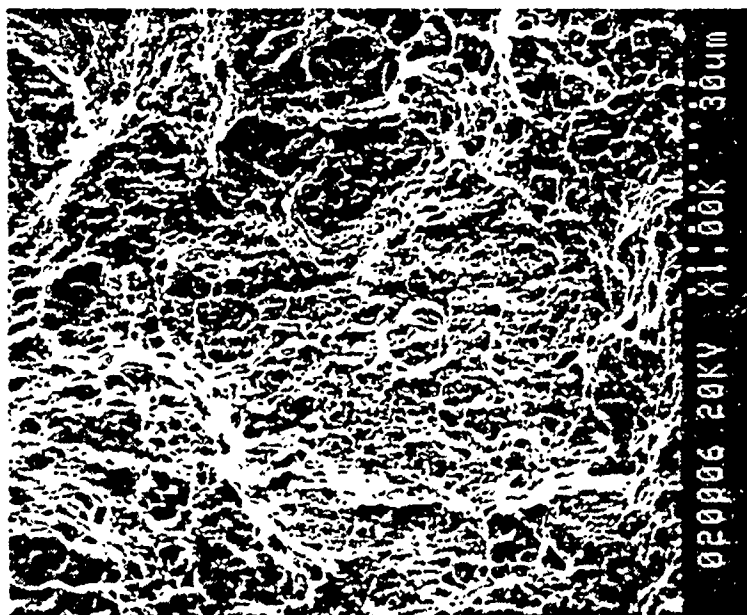
Figure 7.7 Final fracture region(1000X)
from R=-1, $\Delta\varepsilon/2=0.008$

Figure 7.6 Fatigue crack growth region(250X)
from R=-2, $\Delta\varepsilon/2=0.010$

(a) Δε/2=0.008
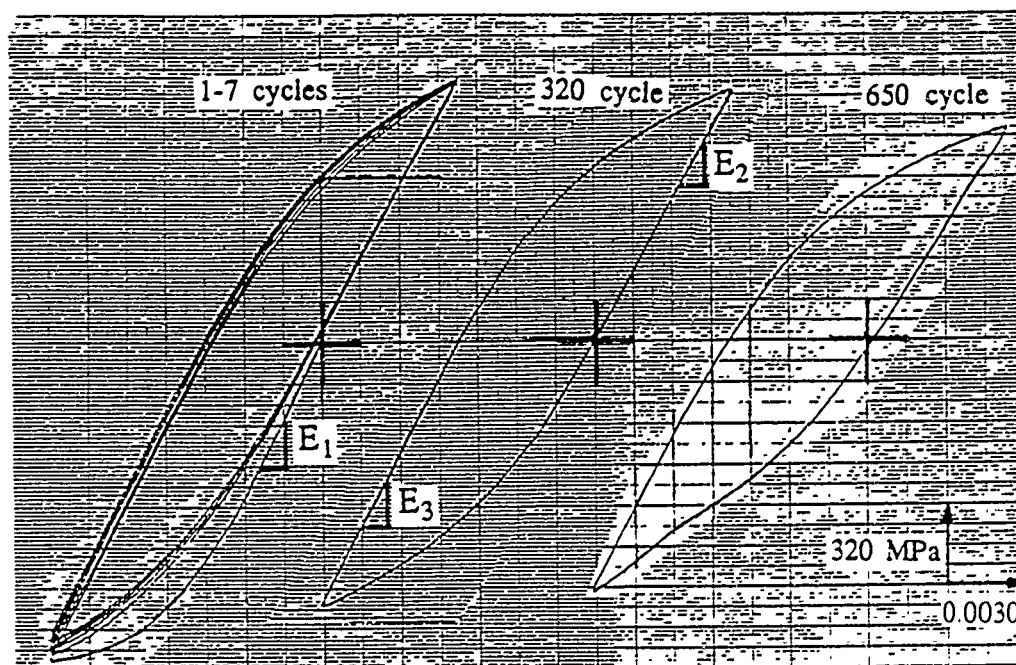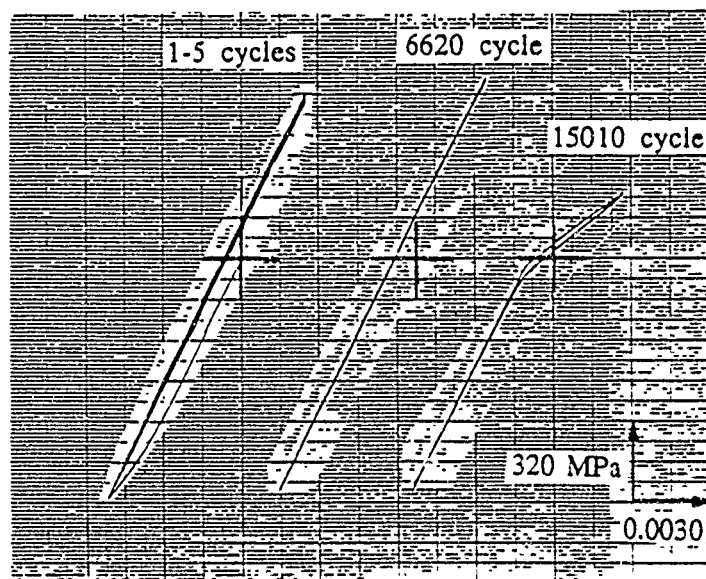
(b) Δε/2=0.004

Figure 7.8 Typical hysteresis loops for R=-2
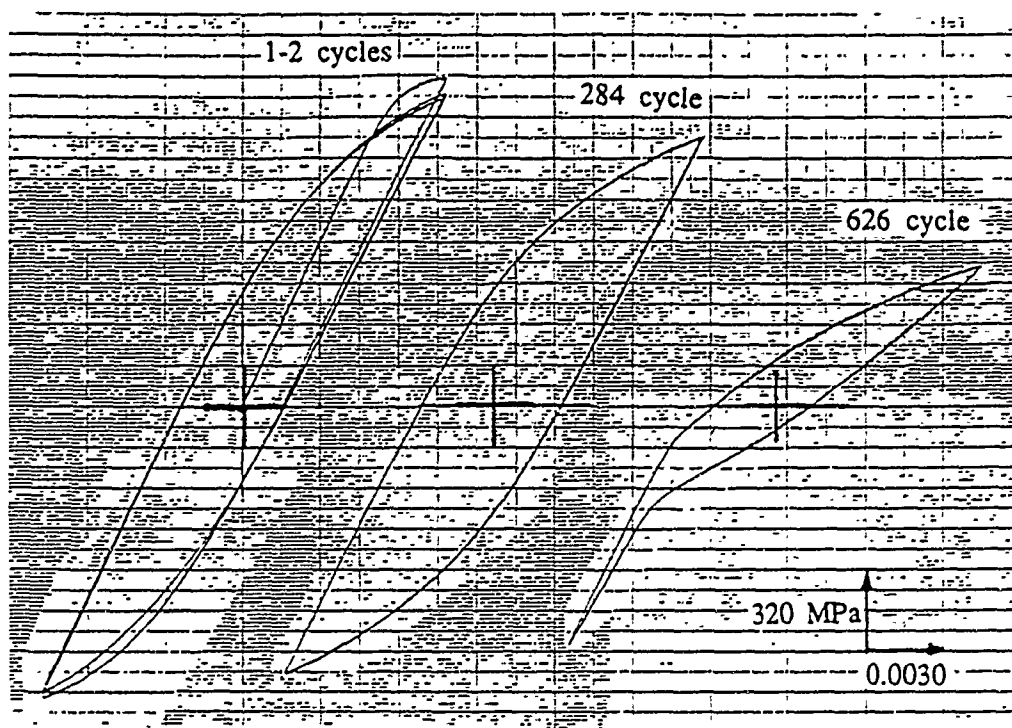
(a) $\Delta\varepsilon/2=0.008$
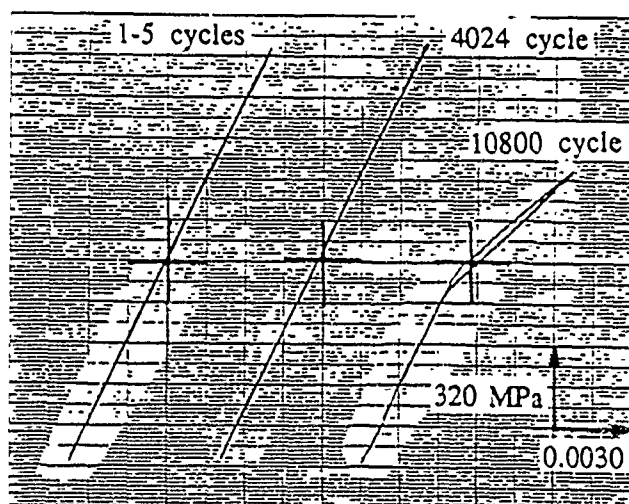
(b) $\Delta\varepsilon/2=0.004$

Figure 7.9 Typical hysteresis loops for R=-1
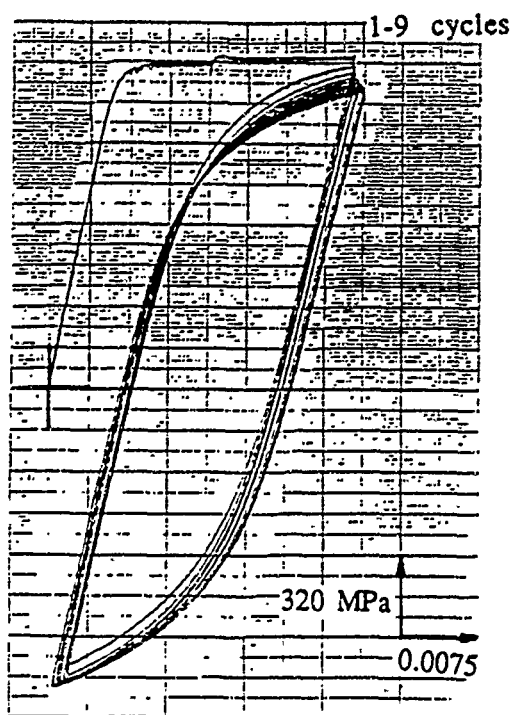
(a) $\Delta\varepsilon/2=0.015$
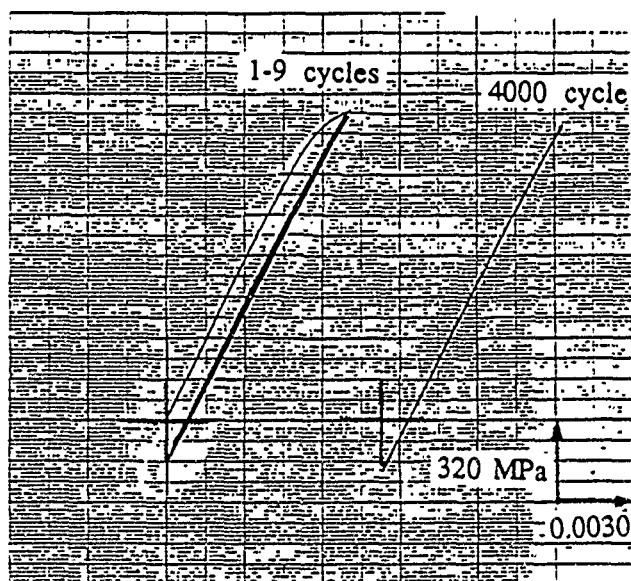
(b) $\Delta\varepsilon/2=0.0035$

Figure 7.10 Typical hysteresis loops for R=0
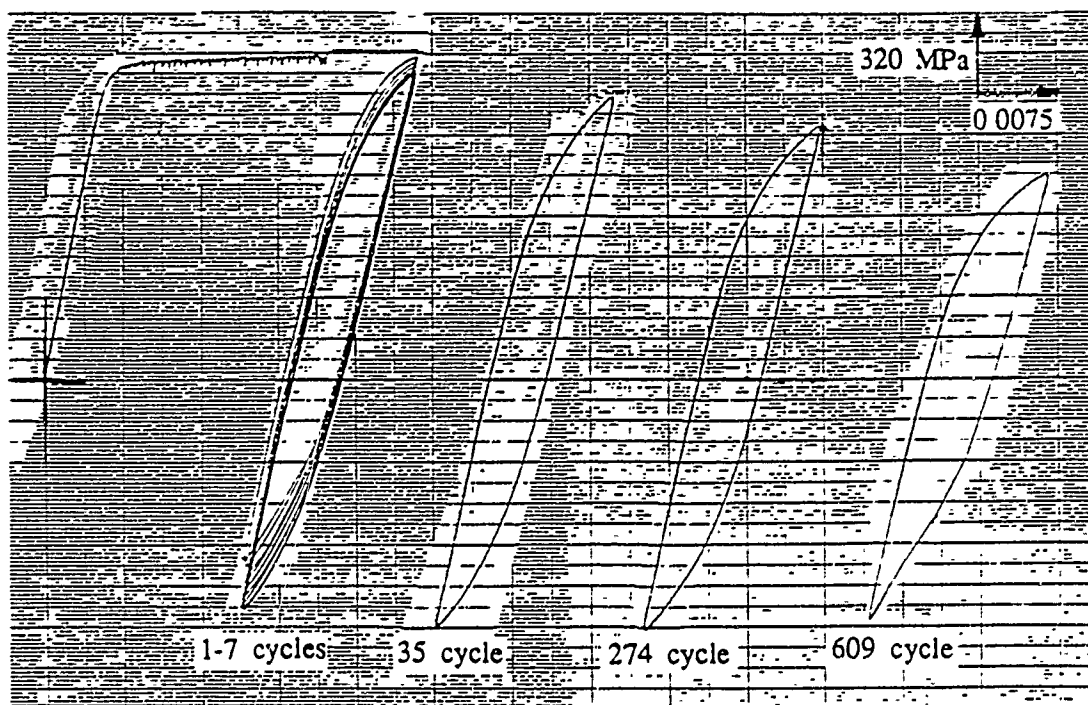
(a) $\Delta\varepsilon/2=0.009$
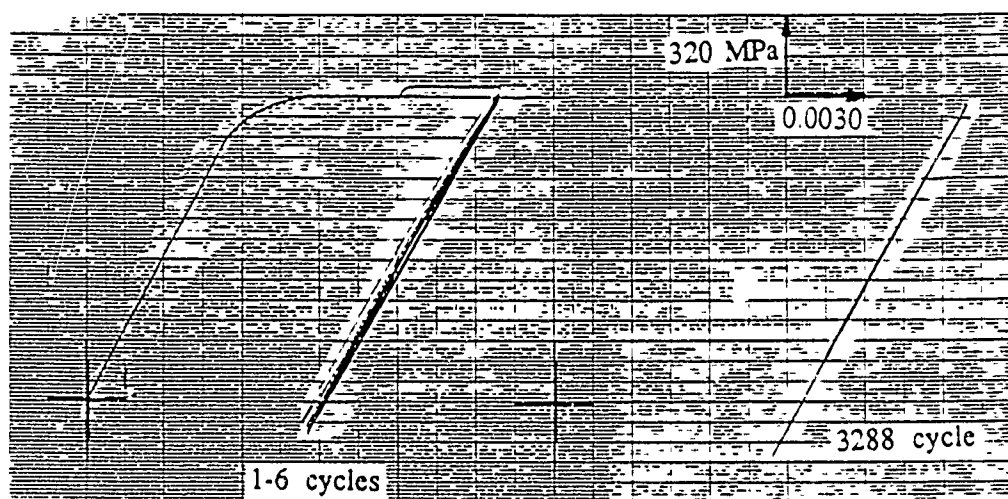
(b) $\Delta\varepsilon/2=0.004$

Figure 7.11 Typical hysteresis loops for R=0.5
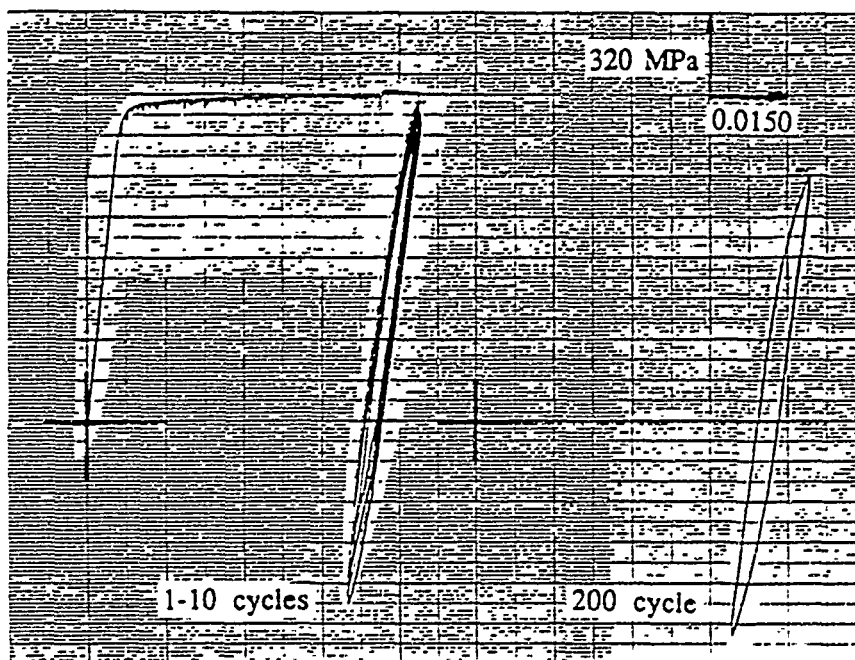
(a) $\Delta\varepsilon/2=0.008$
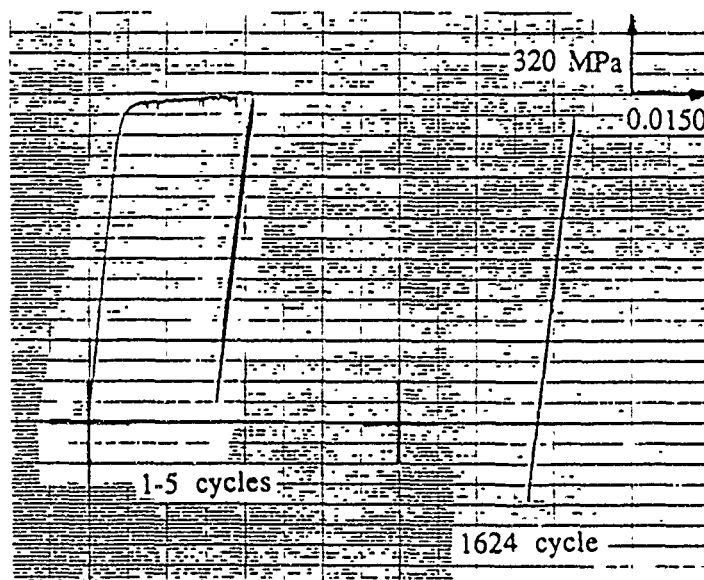
(b) $\Delta\varepsilon/2=0.004$

Figure 7.12 Typical hysteresis loops for R=0.75
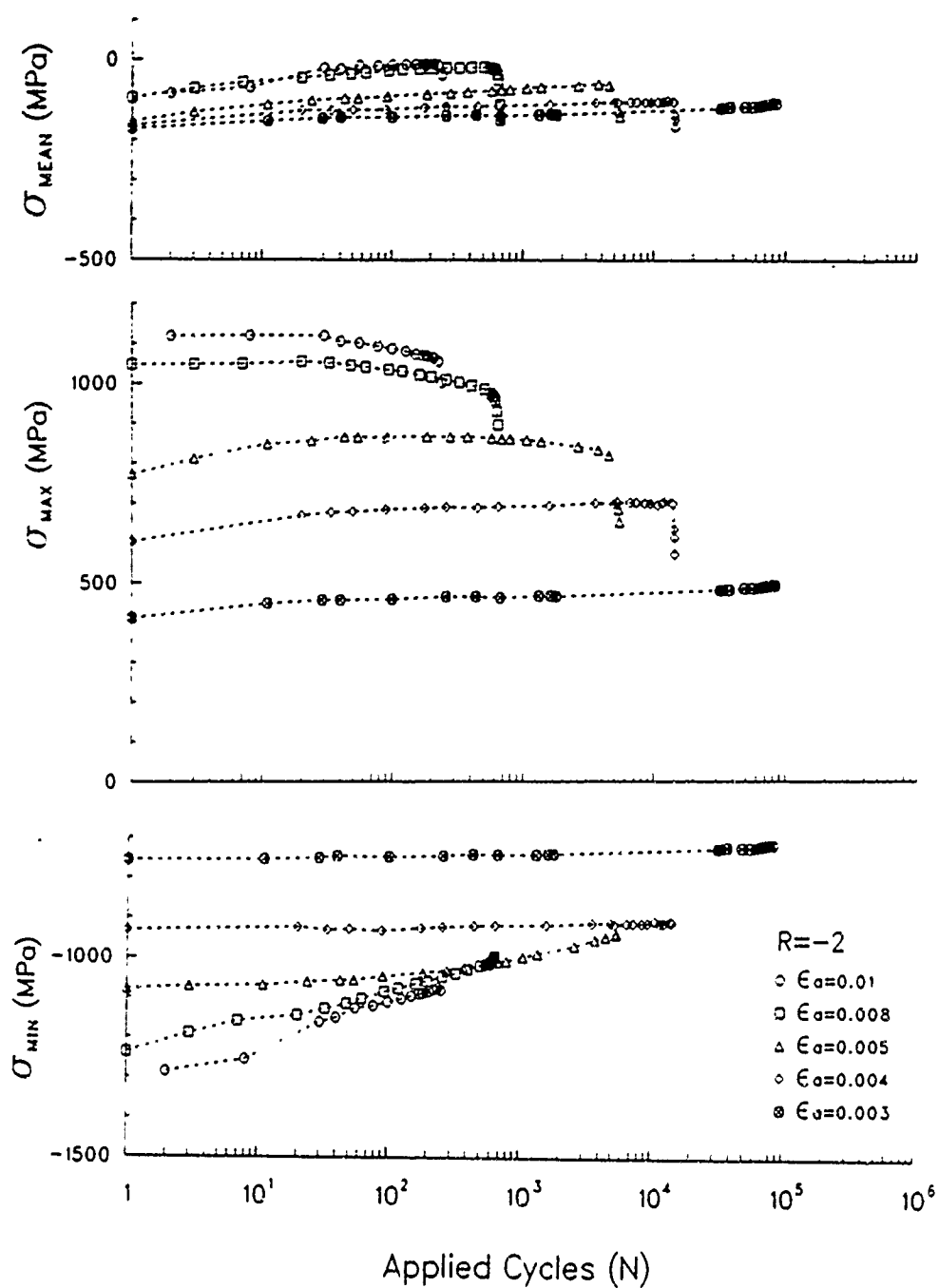
Figure 7.13 Stress versus applied cycles for R=-2
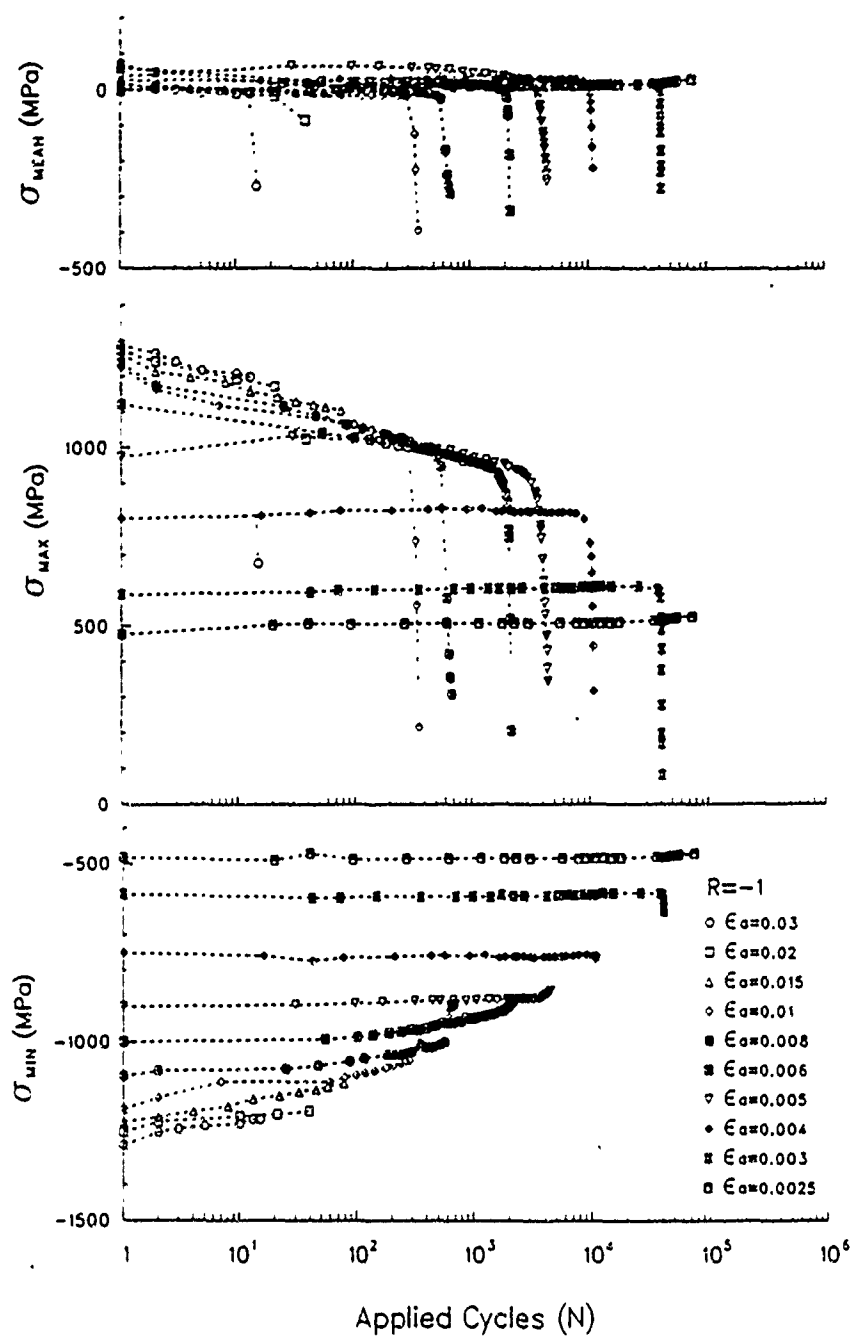
Figure 7.14 Stress versus applied cycles for R=-1
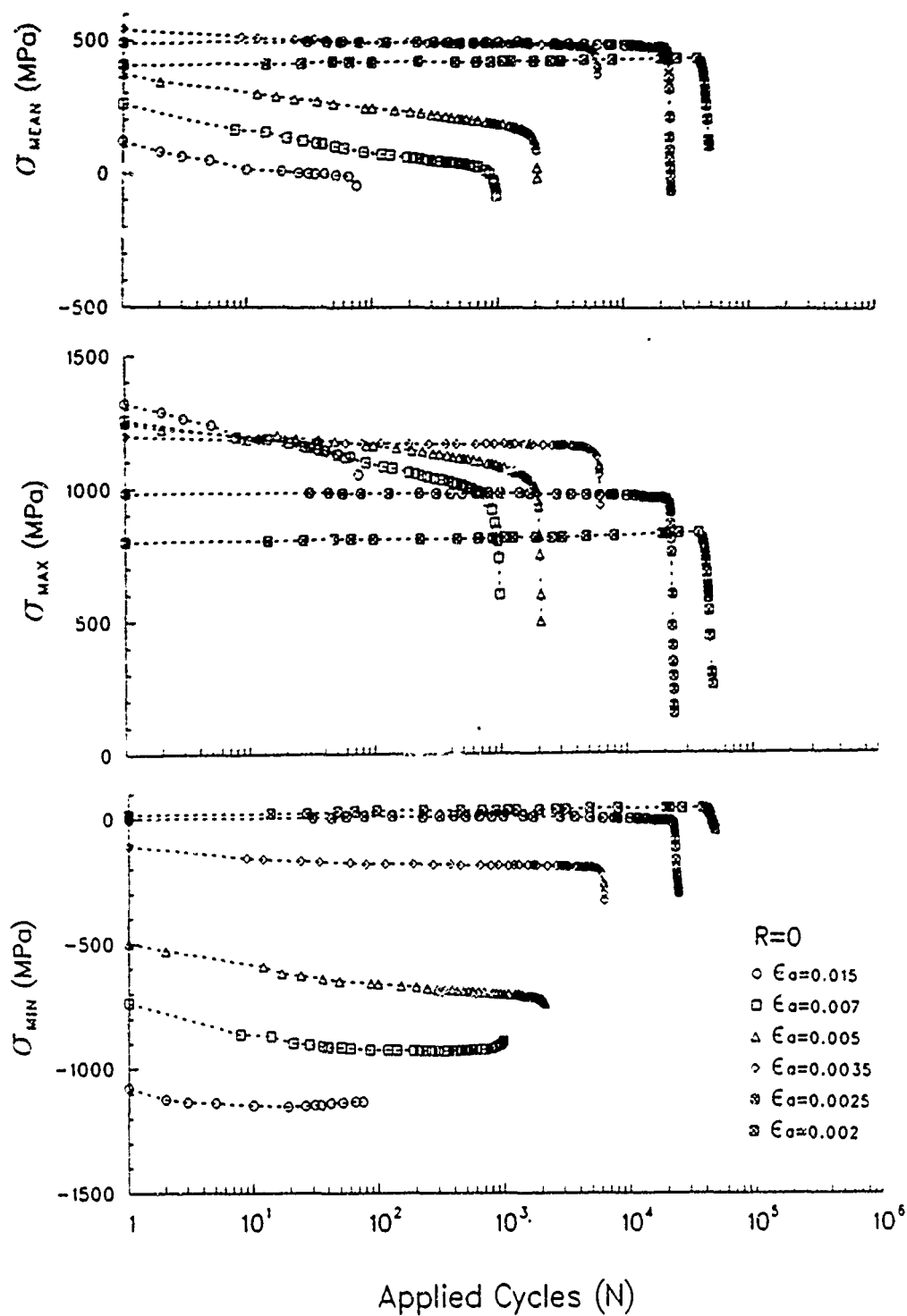
Figure 7.15 Stress versus applied cycles for R=0
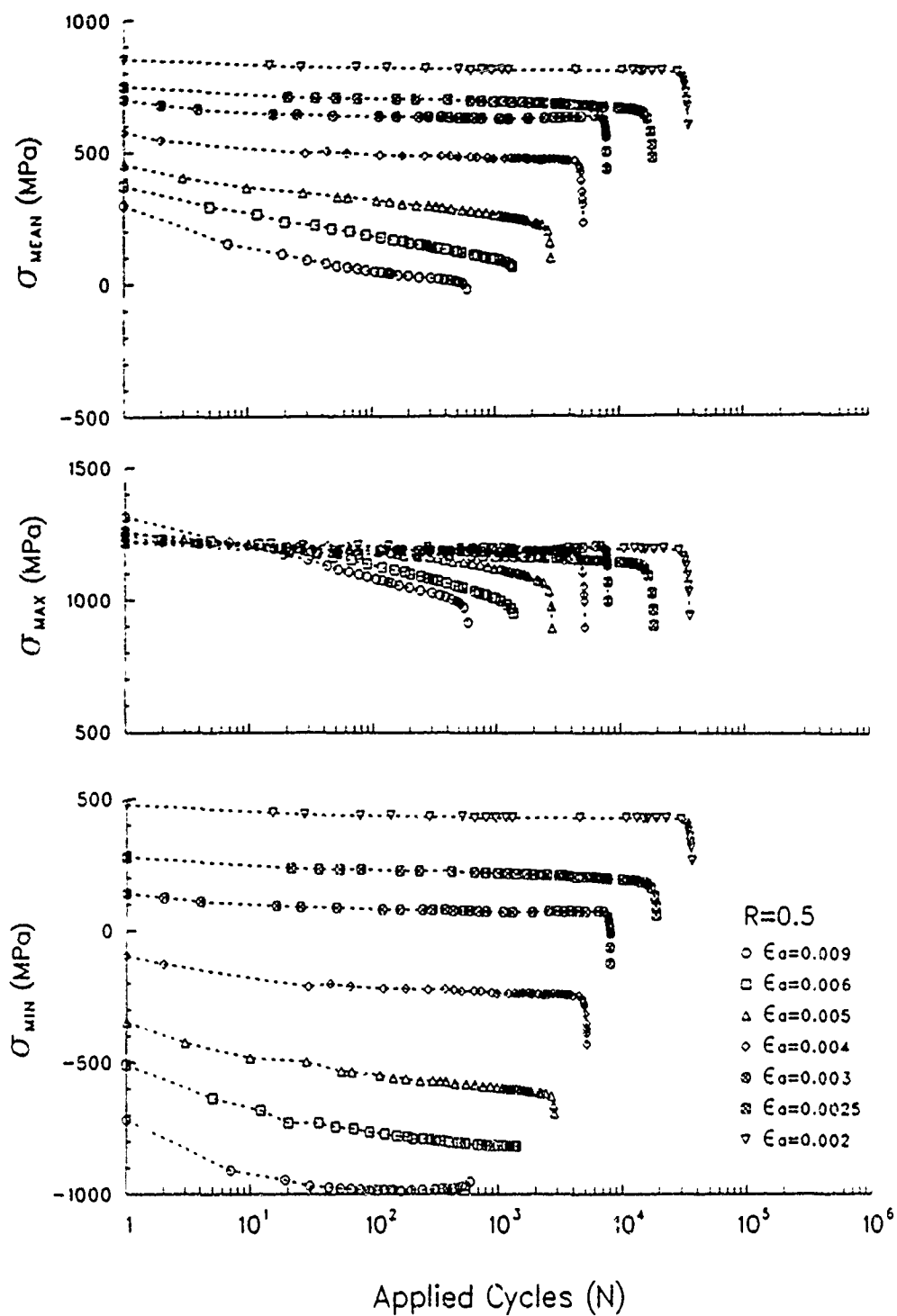
Figure 7.16 Stress versus applied cycles for R=0.5
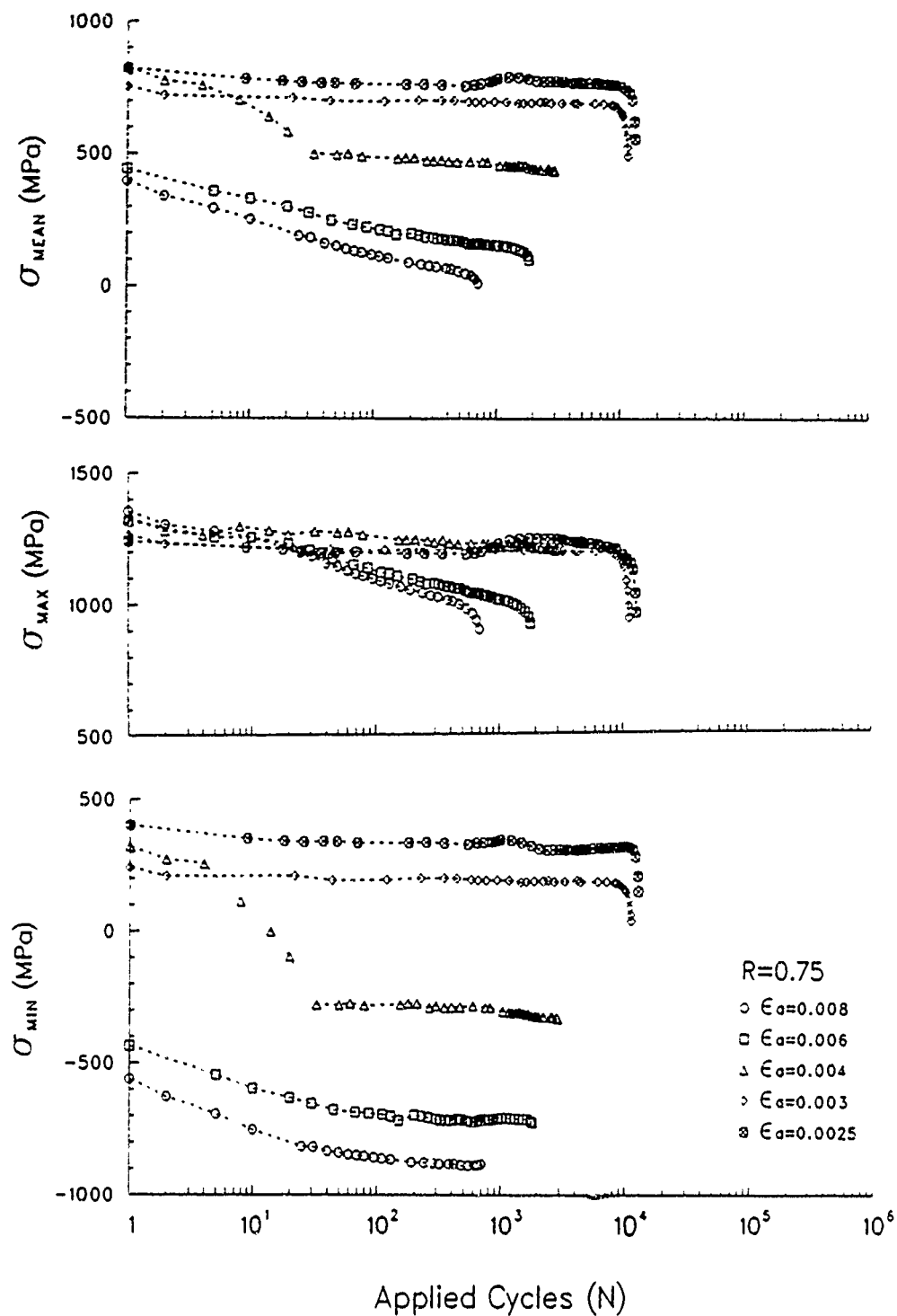
Figure 7.17 Stress versus applied cycles for R=0.75
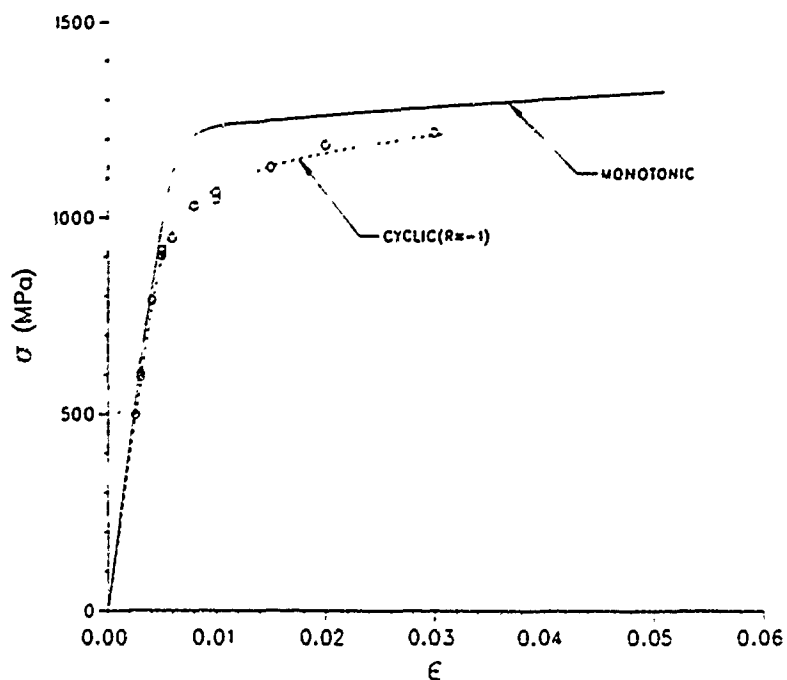
Figure 7.18 Monotonic stress-strain curve and cyclic stress-strain curve for R=-1
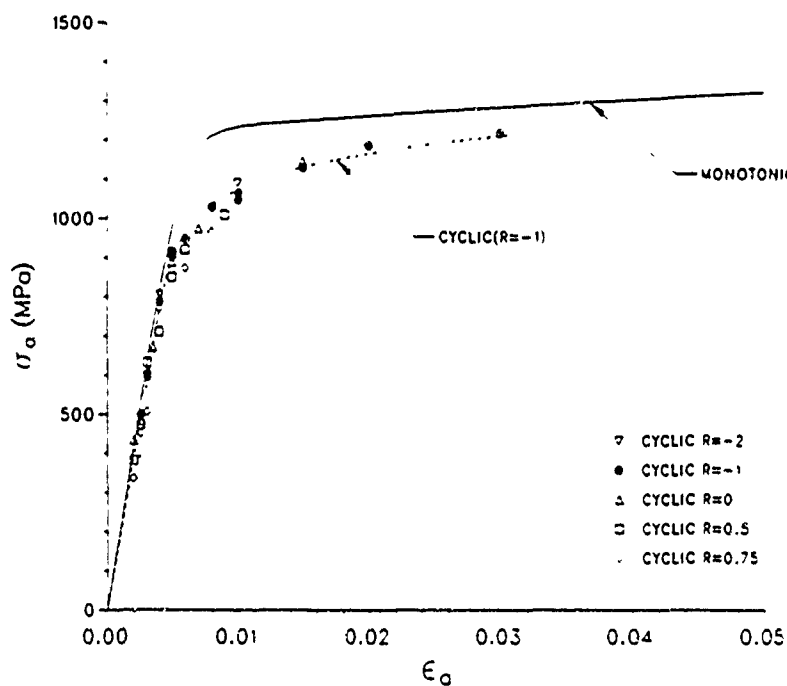
Figure 7.19 Monotonic stress-strain curve and cyclic stress-strain curve for all strain ratios

250
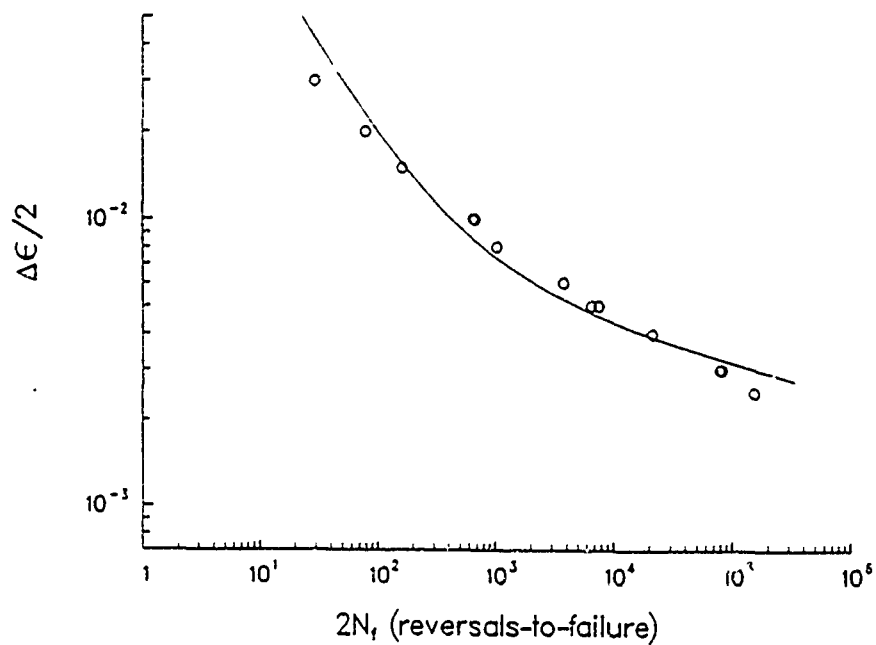
Figure 7.20 Strain amplitude versus reversals-to-failure for R=-1
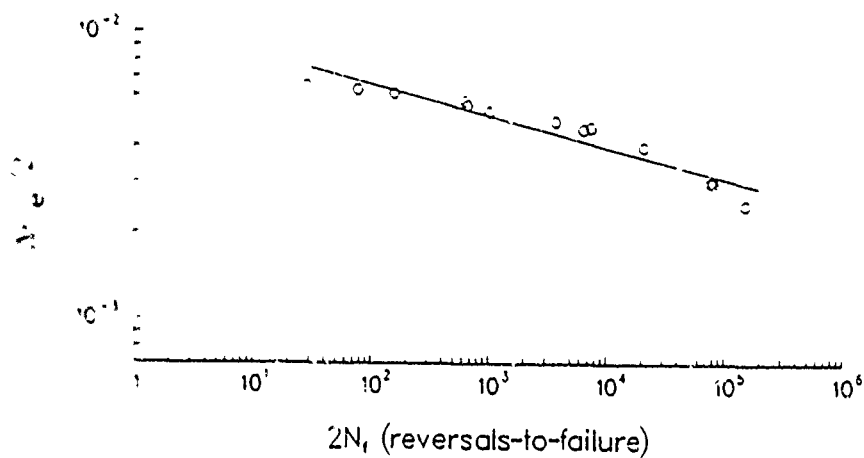
Figure 7.21 Elastic strain amplitude versus reversals-to-failure
for R=-1
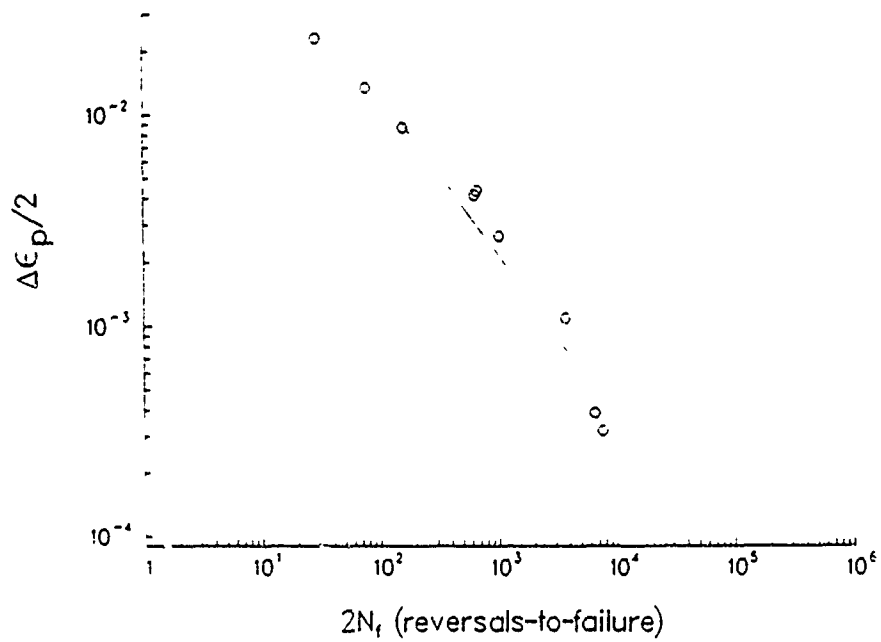
Figure 7.22 Plastic strain amplitude versus reversals-to-failure for R=-1
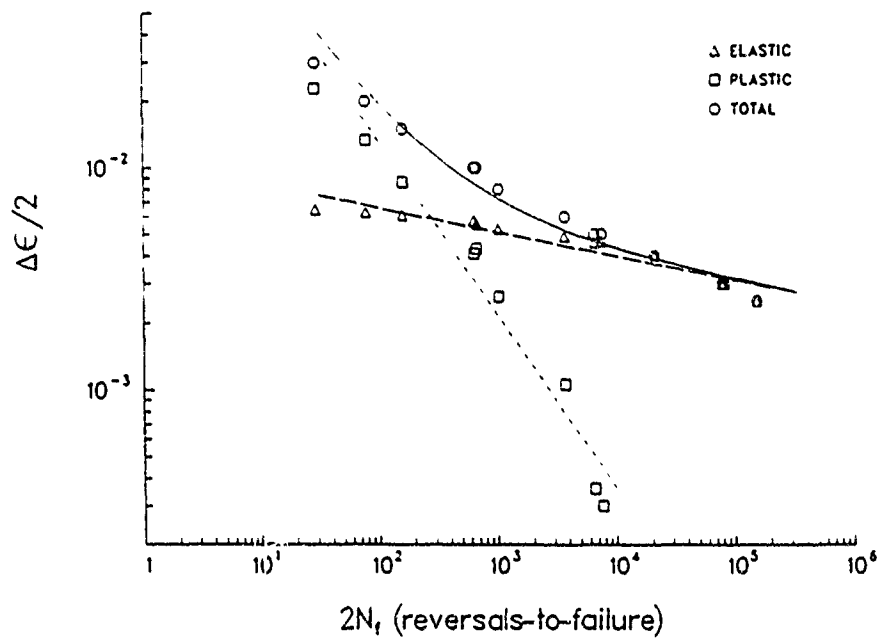
Figure 7.23 Resultant conventional low cycle fatigue behavior for R=-1
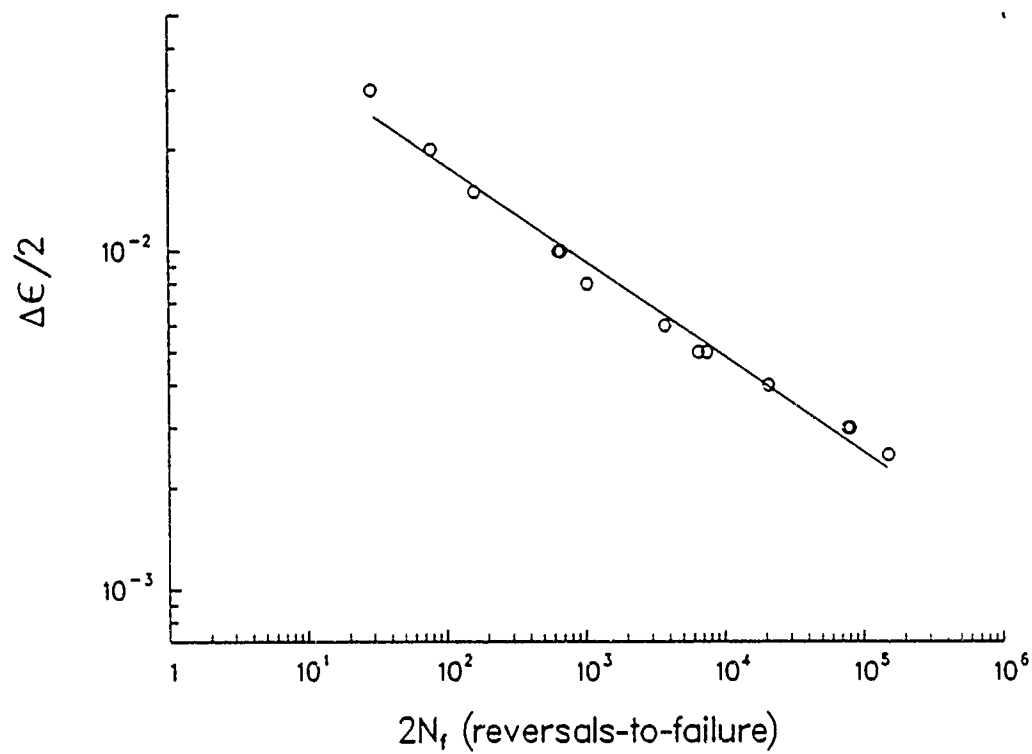
Figure 7.24 Log-log linear strain amplitude versus reversals-to-failure for R=-1
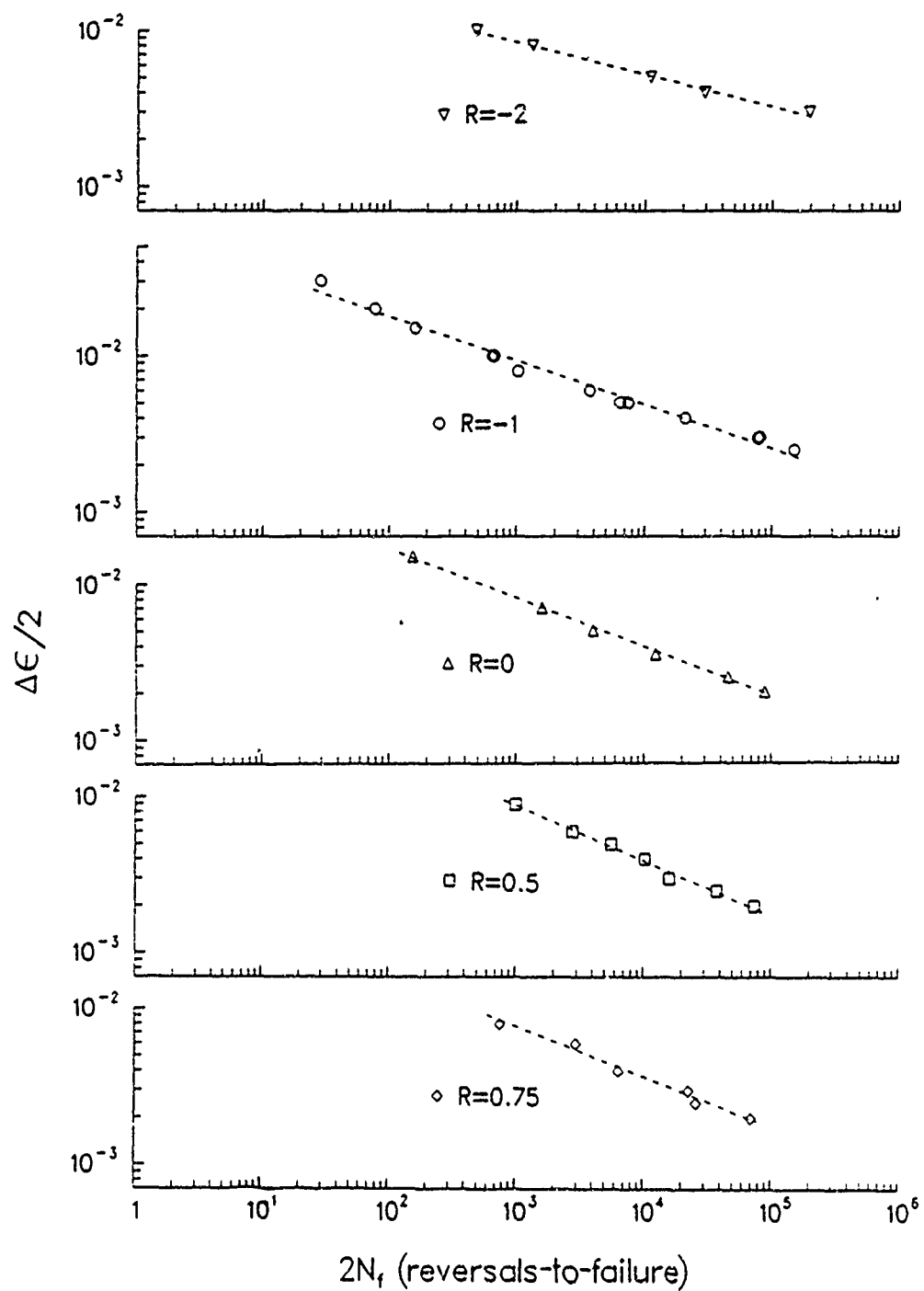
Figure 7.25 Strain amplitude versus reversals-to-failure for each strain ratio
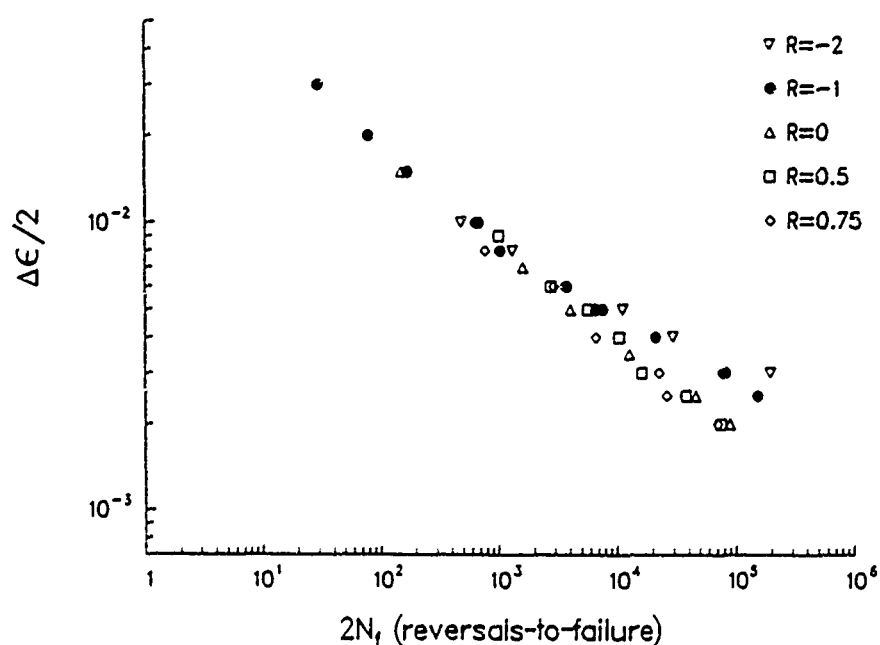
Figure 7.26 Strain amplitude versus reversals-to-failure for all strain ratios
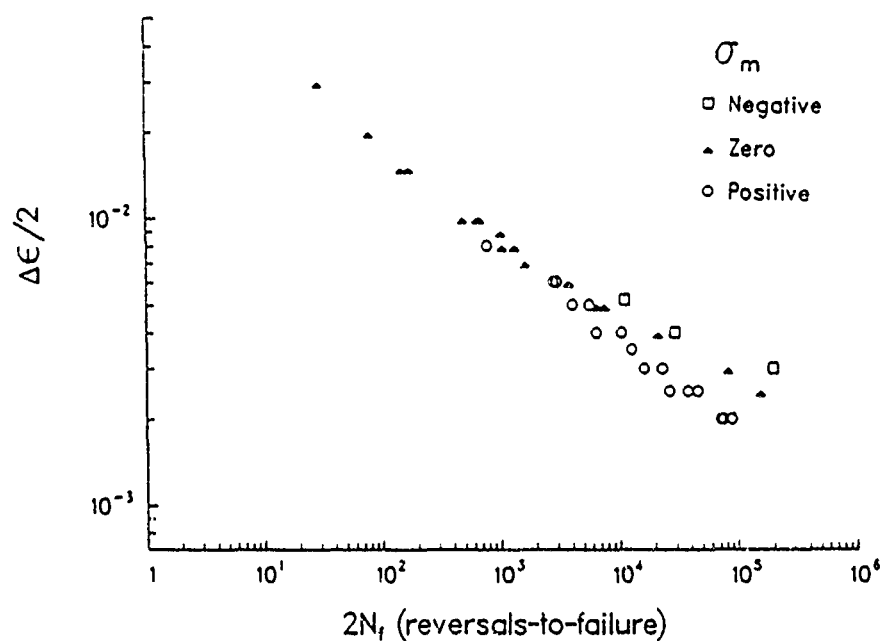
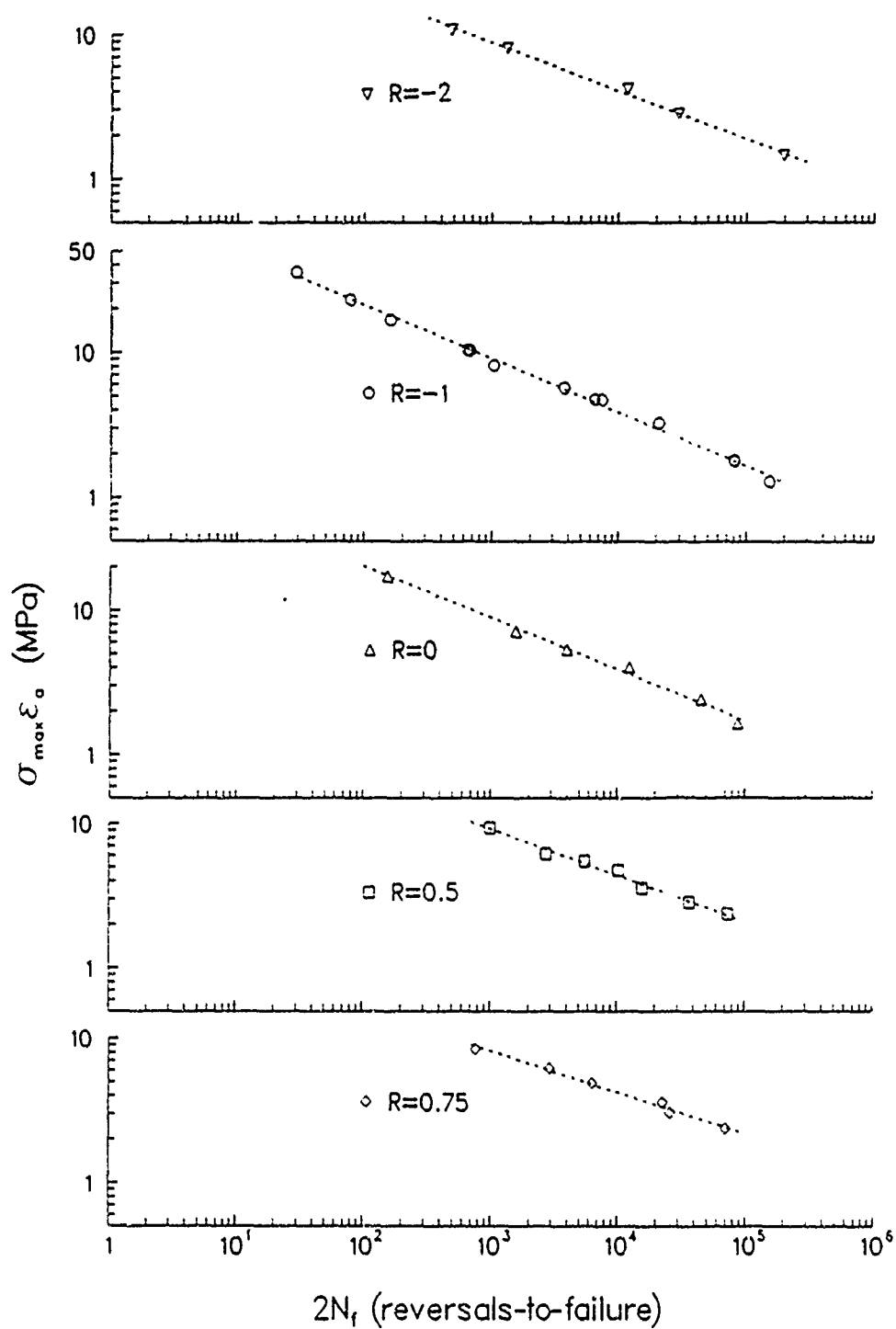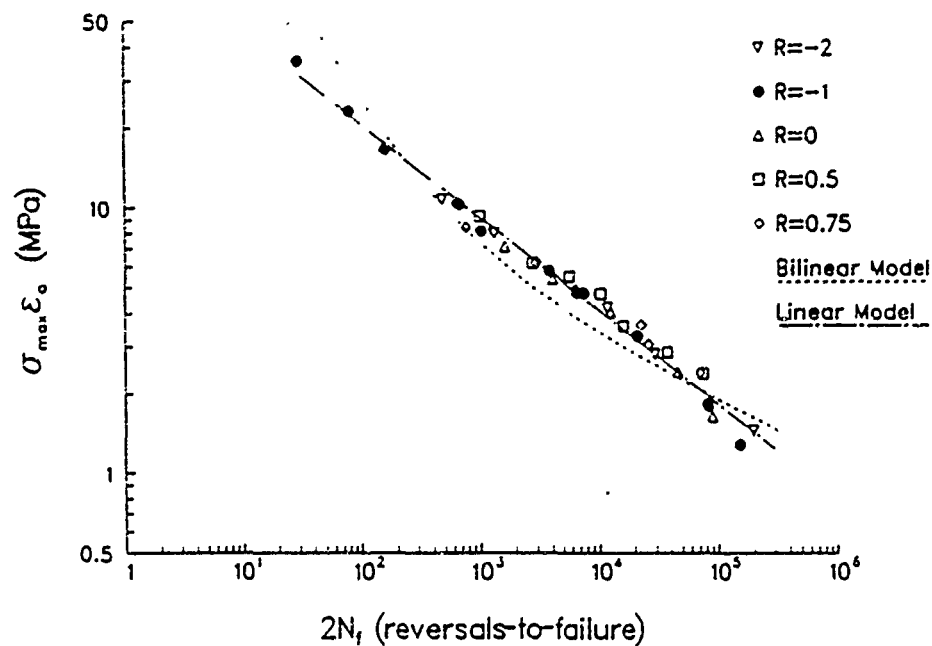Figure 7.27 Strain amplitude versus reversals-to-failure for all strain ratios with different mean stresses
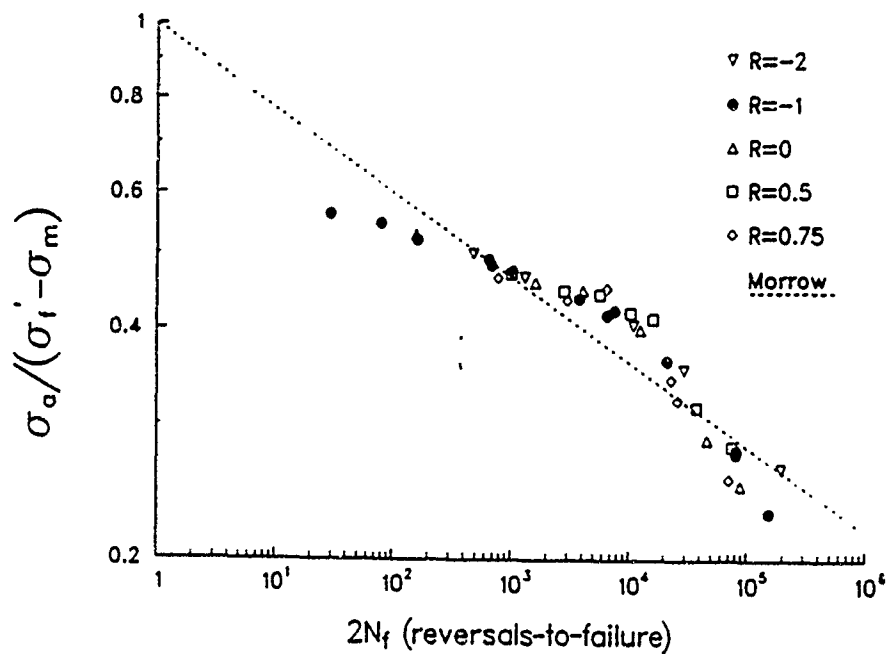
Figure 7.28 Correlation of Morrow's mean stress parameter
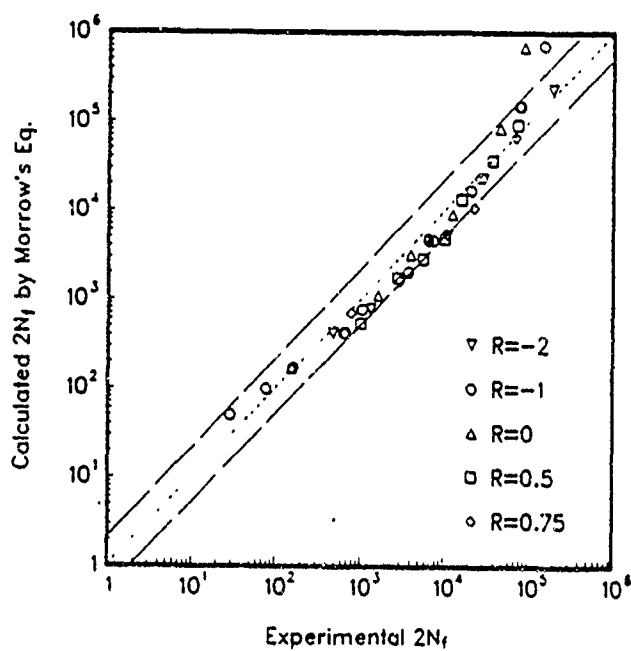
Figure 7.29 Experimental reversals-to-failure versus reversals-to-failure calculated using Morrow's equation
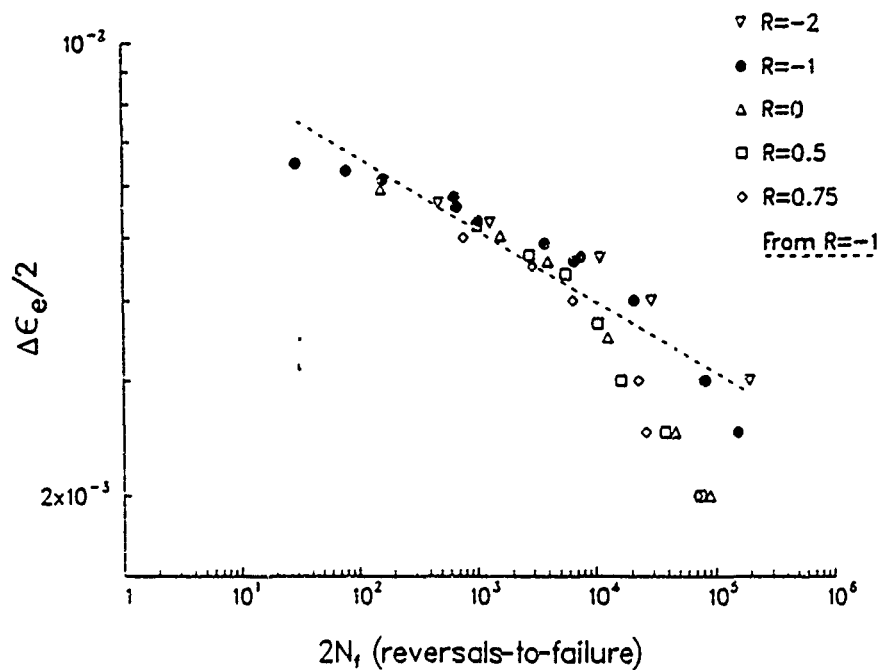
Figure 7.30 Elastic strain amplitude versus reversals-to-failure for all strain ratios
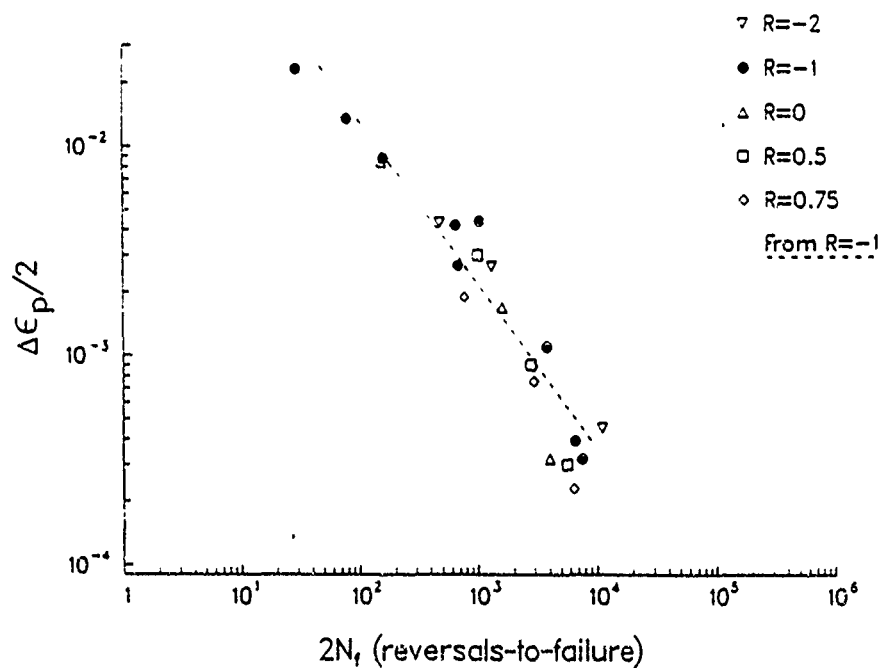
Figure 7.31 Plastic strain amplitude versus reversals-to-failure for all strain ratios

Figure 7.32 SWT parameter versus reversals-to-failure for each strain ratio

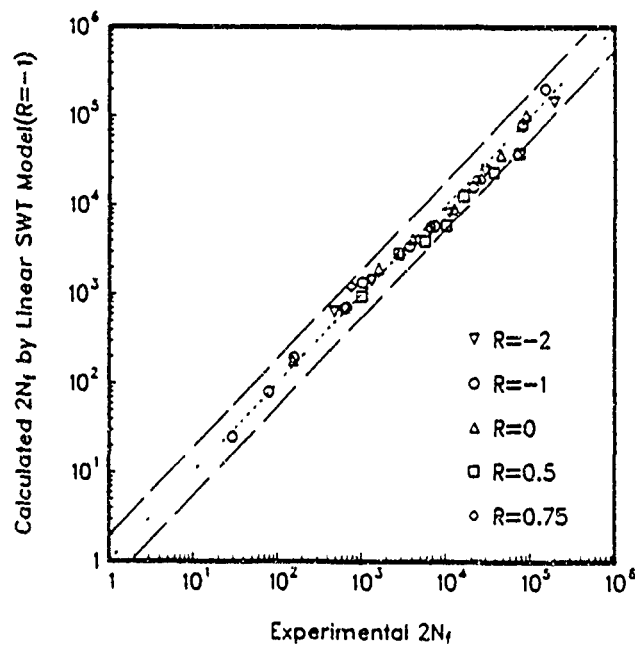Figure 7.33 Log-log bilinear and linear models of SWT parameter for all strain ratios

Figure 7.34 Experimental reversals-to-failure versus reversals-to-failure calculated using SWT parameter
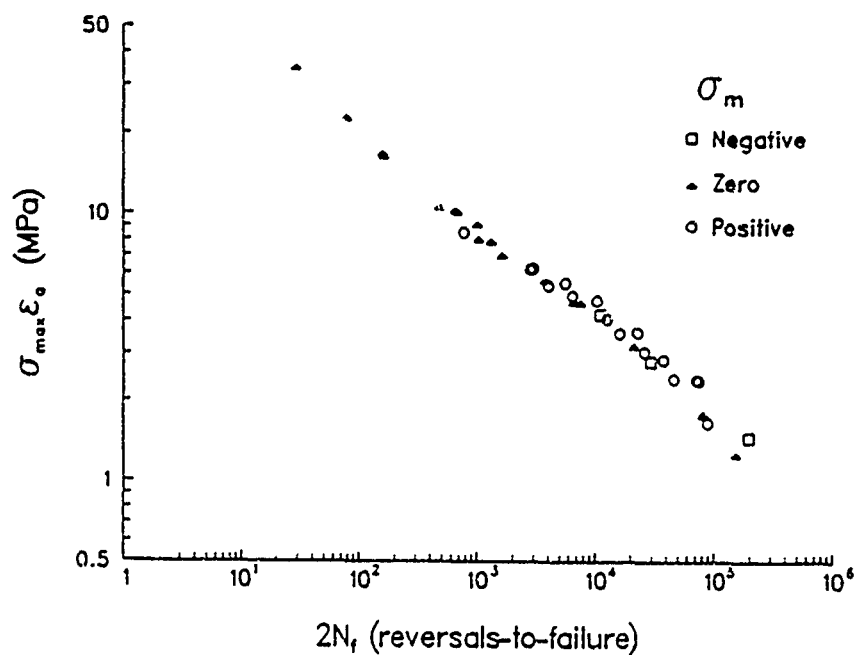
Figure 7.35 SWT parameter versus reversals-to-failure for all strain ratios with different mean stresses
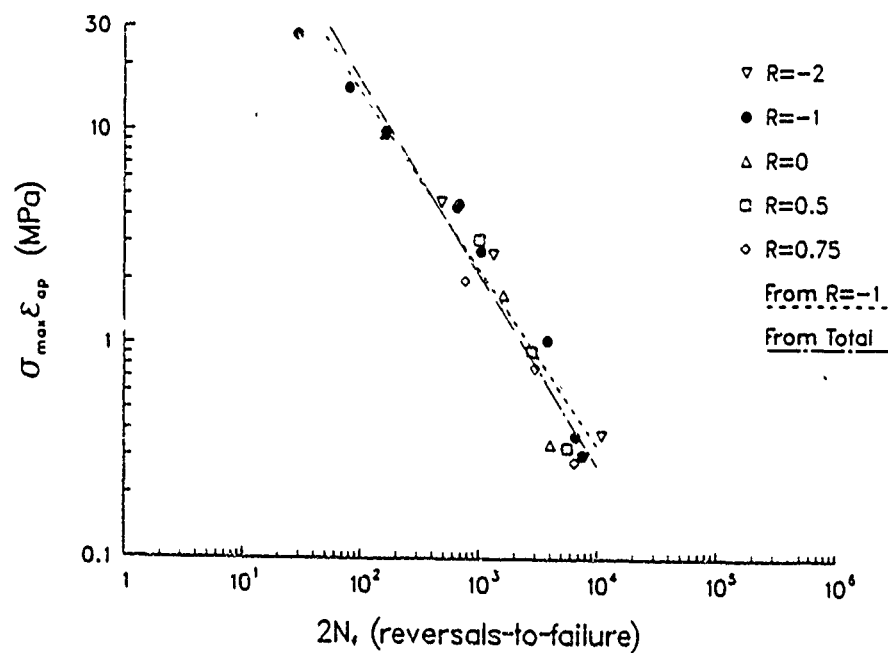

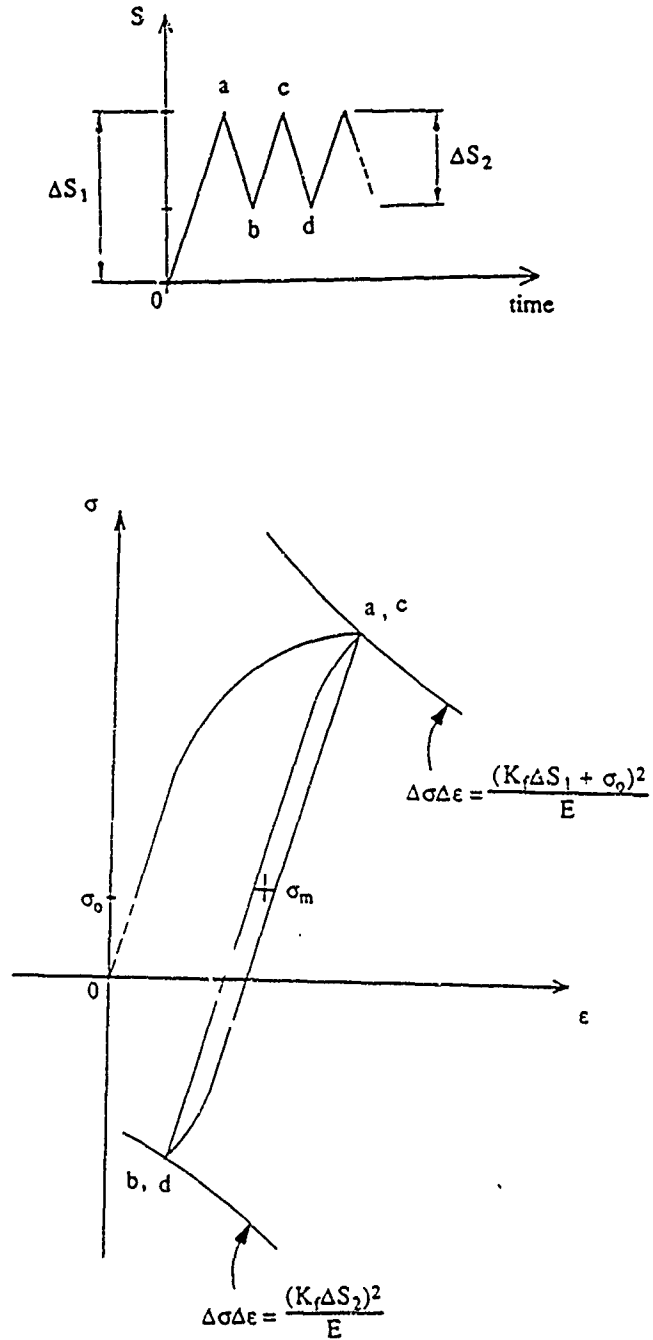Figure 7.36 Lorenzo-Laird model for all strain ratios

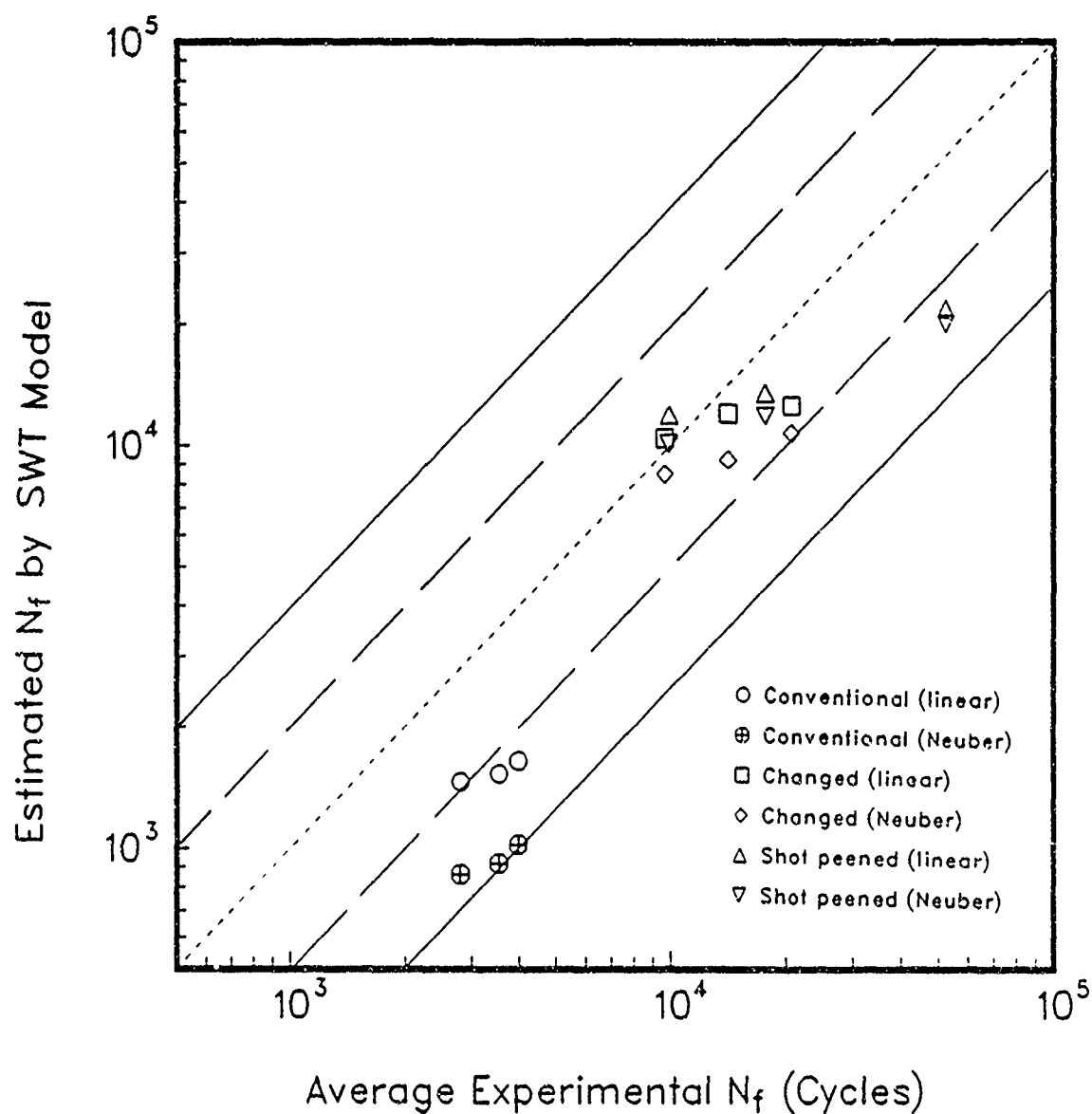Figure 8.1 Local strain and local stress determination using Neuber's rule

Figure 8.2 Estimated fatigue life of autofrettaged thick-walled pressure vessel versus average experimental fatigue life from simulation fatigue tests using SWT parameter
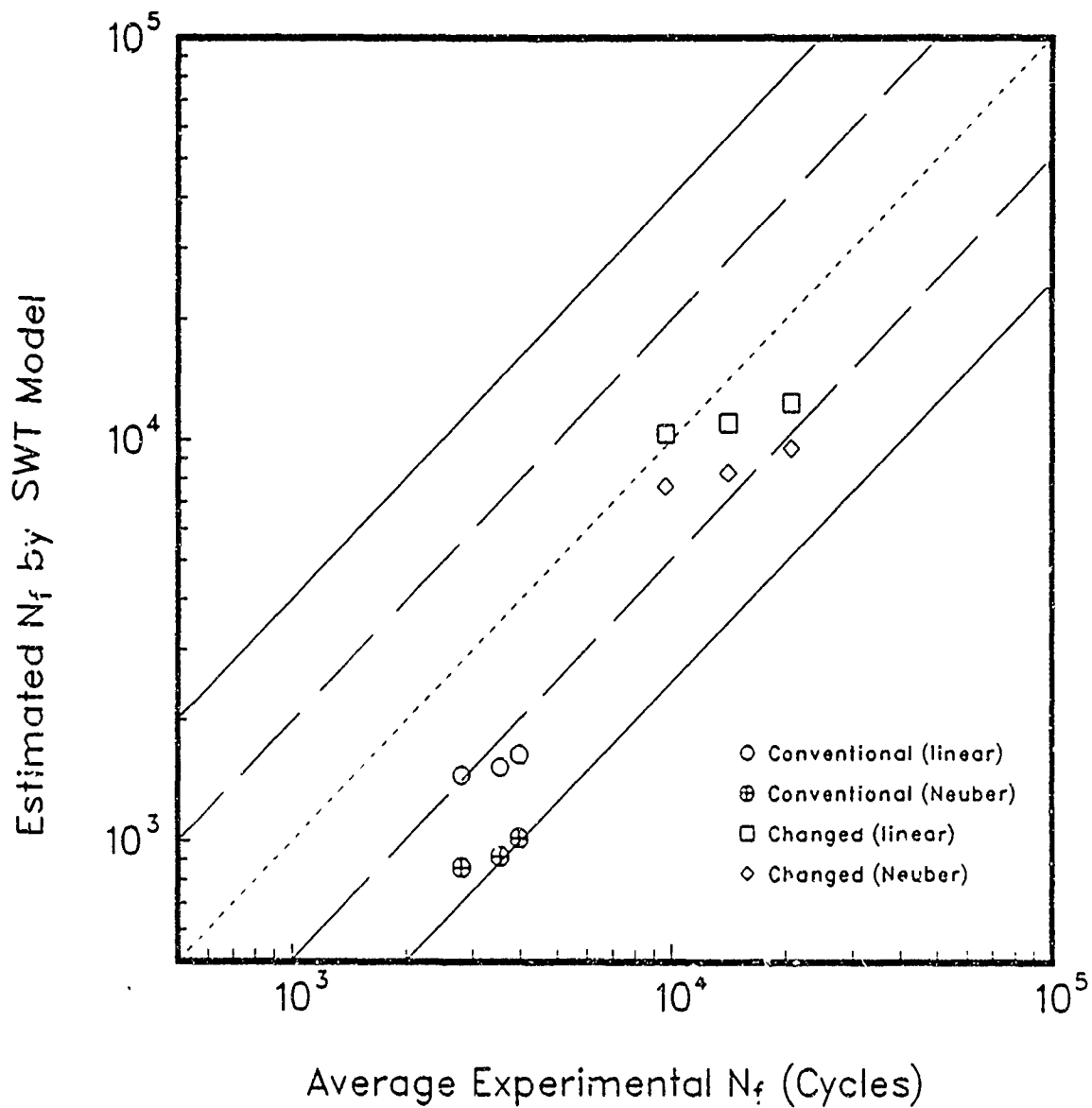
Figure 8.3 Estimated fatigue life of simulation specimen without considering residual stresses at the groove roots versus average experimental fatigue life from simulation fatigue tests using SWT parameter
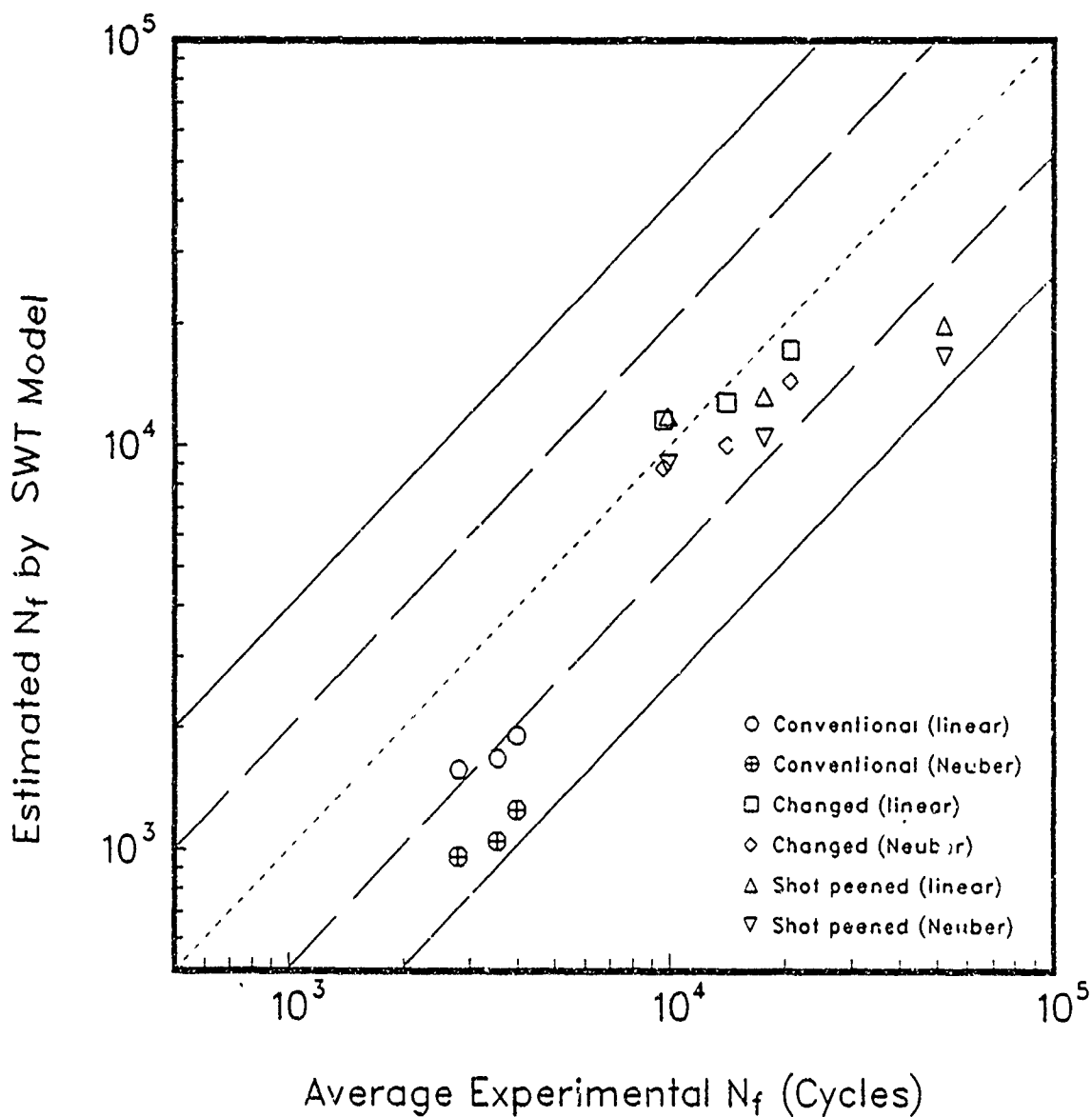
Figure 8.4 Estimated fatigue life of simulation specimen including residual stresses at the groove roots versus average experimental fatigue life from simulation fatigue tests using SWT parameter
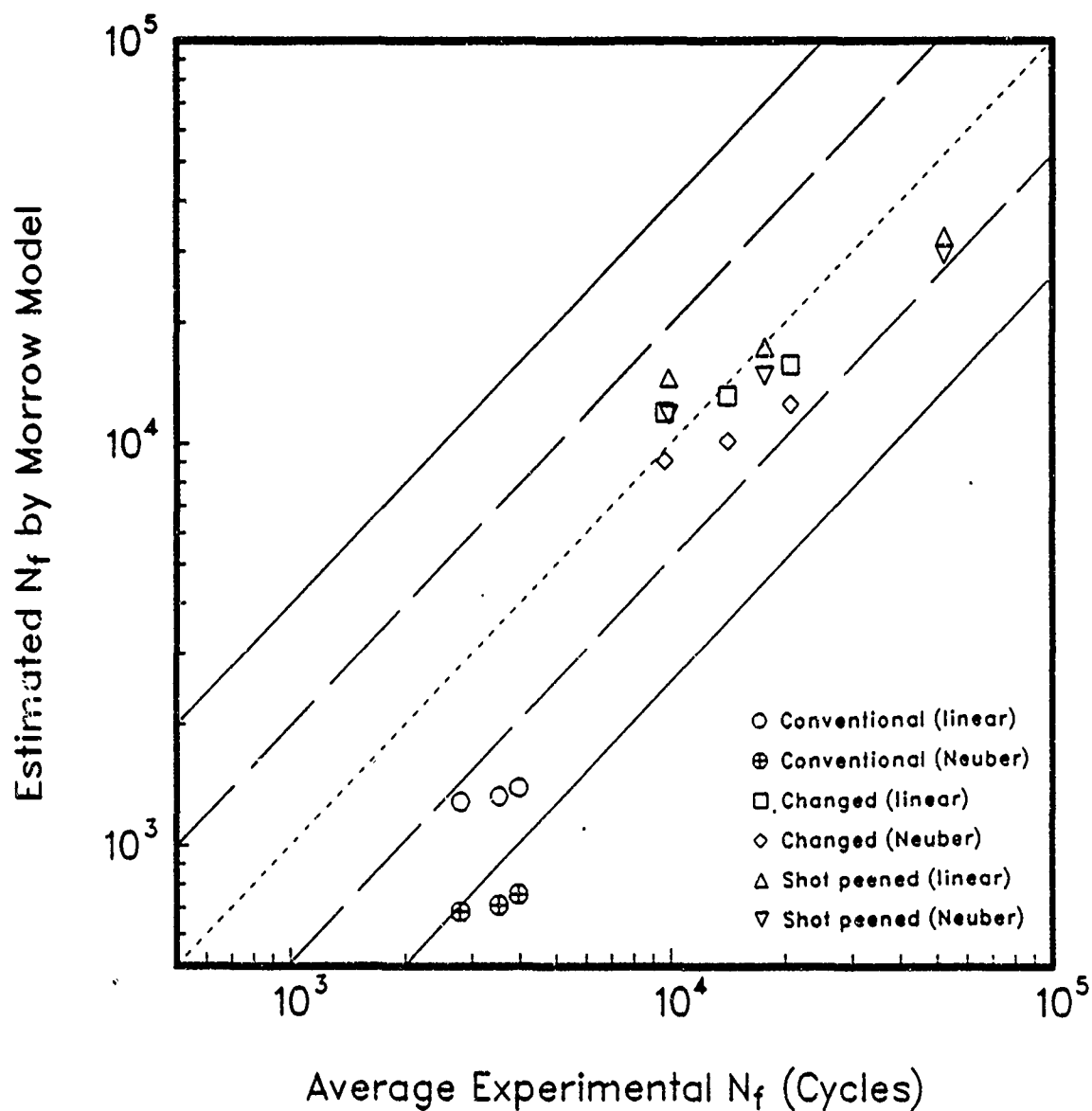
Figure 8.5 Estimated fatigue life of autofrettaged thick-walled pressure vessel versus average experimental fatigue life from simulation fatigue tests using Morrow's parameter

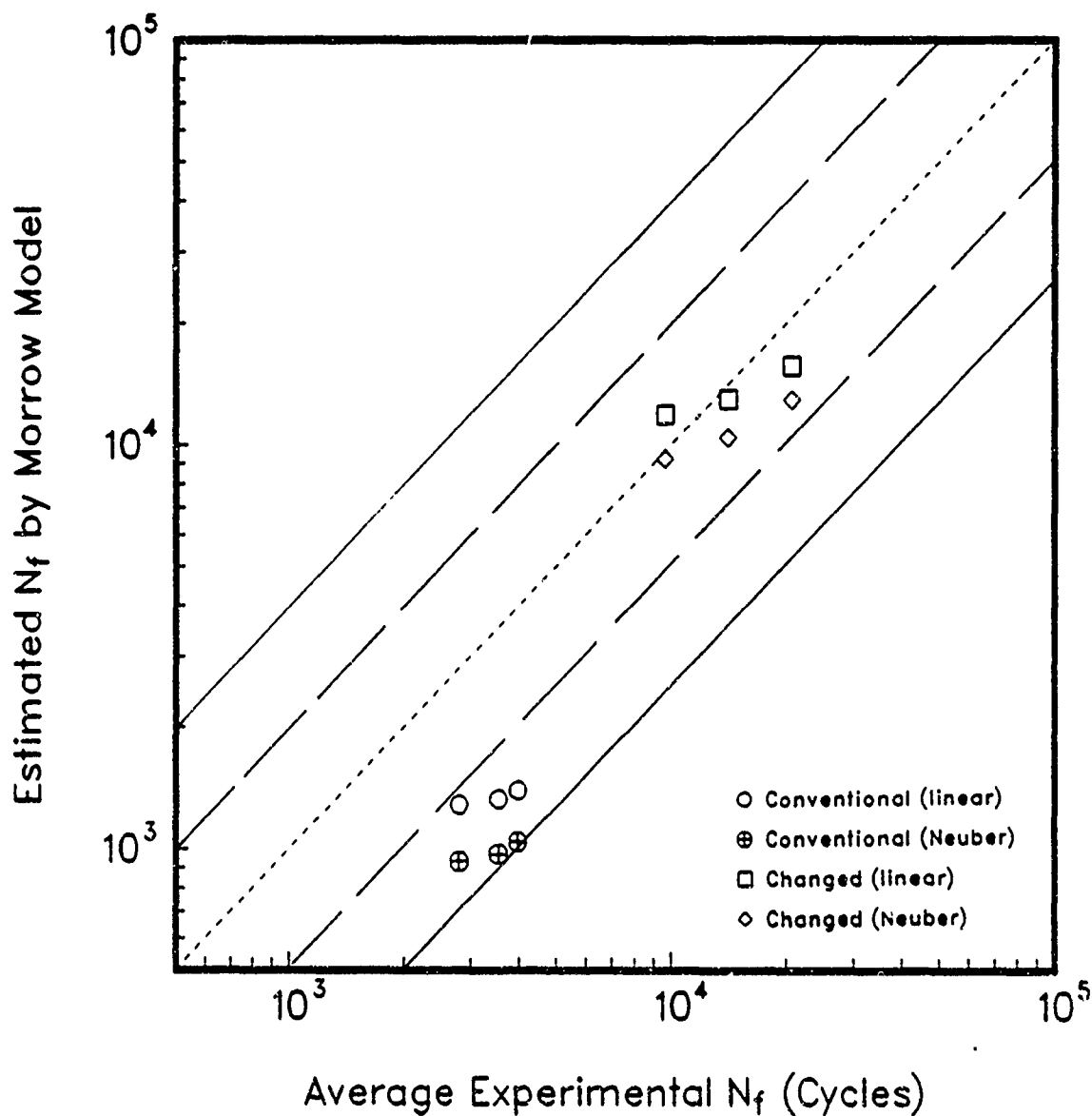Figure 8.6 Estimated fatigue life of simulation specimen without
considering residual stresses at the groove roots versus
average experimental fatigue life from simulation fatigue
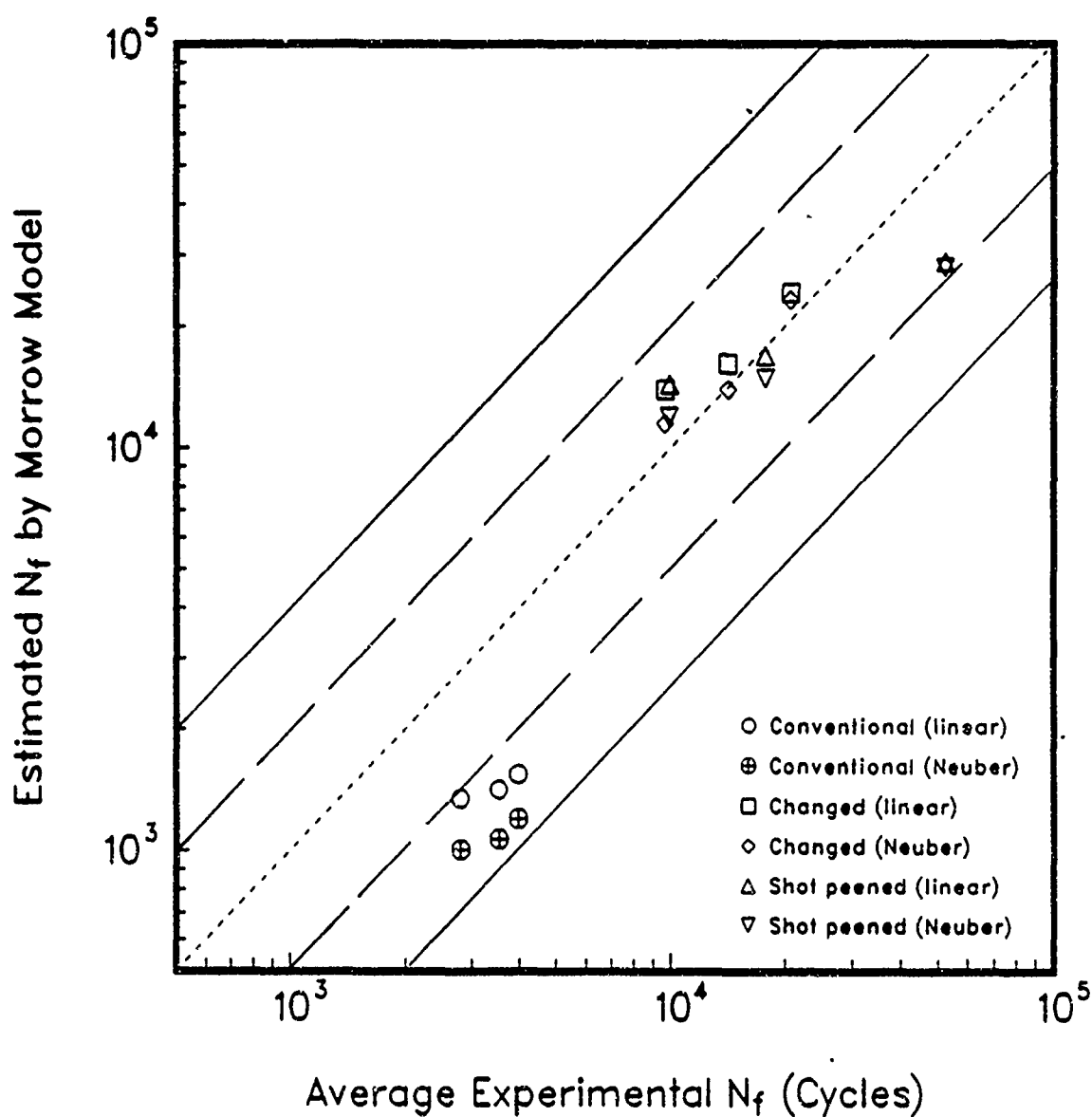tests using Morrow's parameter

Figure 8.7 Estimated fatigue life of simulation specimen inculding residual stresses at the groove roots versus average experimental fatigue life from simulation fatigue tests using Morrow's parameter

TECHNICAL REPORT INTERNAL DISTRIBUTION LIST

	NO. OF COPIES
CHIEF, DEVELOPMENT ENGINEERING DIVISION	
ATTN: SMCAR-CCB-DA	1
-DC	1
-DI	1
-DR	1
-DS (SYSTEMS)	1
CHIEF, ENGINEERING SUPPORT DIVISION	
ATTN: SMCAR-CCB-S	1
-SD	1
-SE	1
CHIEF, RESEARCH DIVISION	
ATTN: SMCAR-CCB-R	2
-RA	1
-RE	1
-RM	1
-RP	1
-RT	1
TECHNICAL LIBRARY	5
ATTN: SMCAR-CCB-TL	
TECHNICAL PUBLICATIONS & EDITING SECTION	3
ATTN: SMCAR-CCB-TL	
OPERATIONS DIRECTORATE	1
ATTN: SMCWV-ODP-P	
DIRECTOR, PROCUREMENT DIRECTORATE	1
ATTN: SMCWV-PP	
DIRECTOR, PRODUCT ASSURANCE DIRECTORATE	1
ATTN: SMCWV-QA	

NOTE: PLEASE NOTIFY DIRECTOR, BENET LABORATORIES, ATTN: SMCAR-CCB-TL, OF ANY ADDRESS CHANGES.

TECHNICAL REPORT EXTERNAL DISTRIBUTION LIST

	NO. OF COPIES		NO. OF COPIES
ASST SEC OF THE ARMY RESEARCH AND DEVELOPMENT ATTN: DEPT FOR SCI AND TECH THE PENTAGON WASHINGTON, D.C. 20310-0103	1	COMMANDER ROCK ISLAND ARSENAL ATTN: SMCRI-ENM ROCK ISLAND, IL 61299-5000	1
ADMINISTRATOR DEFENSE TECHNICAL INFO CENTER ATTN: DTIC-FDAC CAMERON STATION ALEXANDRIA, VA 22304-6145	12	DIRECTOR US ARMY INDUSTRIAL BASE ENGR ACTV ATTN: AMXIB-P ROCK ISLAND, IL 61299-7260	1

COMMANDER
US ARMY ARDEC
ATTN: SMCAR-AEE
     SMCAR-AES, BLDG. 321
     SMCAR-AET-O, BLDG. 351N
     SMCAR-CC
     SMCAR-CCP-A
     SMCAR-FSA
     SMCAR-FSM-E
     SMCAR-FSS-D, BLDG. 94
     SMCAR-IMI-I (STINFO) BLDG. 59
PICATINNY ARSENAL, NJ 07806-5000
	1
	1
	1
	1
	1
	1
	1
	1
	2
		COMMANDER
		US ARMY TANK-AUTMV R&D COMMAND
		ATTN: AMSTA-DDL (TECH LIB)
		WARREN, MI 48397-5000
		
		COMMANDER
		US MILITARY ACADEMY
		ATTN: DEPARTMENT OF MECHANICS
		WEST POINT, NY 10996-1792
		
		US ARMY MISSILE COMMAND
		REDSTONE SCIENTIFIC INFO CTR
		ATTN: DOCUMENTS SECT, BLDG. 4484
		REDSTONE ARSENAL, AL 35898-5241
			1
			
			1
			
			2

DIRECTOR US ARMY BALLISTIC RESEARCH LABORATORY ATTN: SLCBR-DD-T, BLDG. 305 ABERDEEN PROVING GROUND, MD 21005-5066	1	COMMANDER US ARMY FGN SCIENCE AND TECH CTR ATTN: DRXST-SD 220 7TH STREET, N.E. CHARLOTTESVILLE, VA 22901	1
DIRECTOR US ARMY MATERIEL SYSTEMS ANALYSIS ACTV ATTN: AMXSY-MP ABERDEEN PROVING GROUND, MD 21005-5071	1	COMMANDER US ARMY LABCOM MATERIALS TECHNOLOGY LAB ATTN: SLCMT-IML (TECH LIB) WATERTOWN, MA 02172-0001	2
COMMANDER HQ, AMCCOM ATTN: AMSMC-IMP-L ROCK ISLAND, IL 61299-6000	1		

NOTE: PLEASE NOTIFY COMMANDER, ARMAMENT RESEARCH, DEVELOPMENT, AND ENGINEERING CENTER, US ARMY AMCCOM, ATTN: BENET LABORATORIES, SMCAR-CCB-TL, WATERVLIET, NY 12189-4050, OF ANY ADDRESS CHANGES.

	NO. OF COPIES		NO. OF COPIES
COMMANDER US ARMY LABCOM, ISA ATTN: SLCIS-IM-TL 2800 POWDER MILL ROAD ADELPHI, MD 20783-1145	1	COMMANDER AIR FORCE ARMAMENT LABORATORY ATTN: AFATL/MN EGLIN AFB, FL 32542-5434	1
COMMANDER US ARMY RESEARCH OFFICE ATTN: CHIEF, IPO P.O. BOX 12211 RESEARCH TRIANGLE PARK, NC 27709-2211	1	COMMANDER AIR FORCE ARMAMENT LABORATORY ATTN: AFATL/MNF EGLIN AFB, FL 32542-5434	1
DIRECTOR US NAVAL RESEARCH LAB ATTN: MATERIALS SCI & TECH DIVISION CODE 26-27 (DOC LIB) WASHINGTON, D.C. 20375	1 1	MIAC/CINDAS PURDUE UNIVERSITY 2595 YEAGER ROAD WEST LAFAYETTE, IN 47905	1
DIRECTOR US ARMY BALLISTIC RESEARCH LABORATORY ATTN: SLCBR-IB-M (DR. BRUCE BURNS) ABERDEEN PROVING GROUND, MD 21005-5066	1		

NOTE: PLEASE NOTIFY COMMANDER, ARMAMENT RESEARCH, DEVELOPMENT, AND ENGINEERING CENTER, US ARMY AMCCOM, ATTN: BENET LABORATORIES, SMCAR-CCB-TL, WATERVLIET, NY 12189-4050, OF ANY ADDRESS CHANGES.